The Pennsylvania State University

The Graduate School

College of Earth and Mineral Sciences

THERMOMECHANICAL CONDITIONS AND STRESSES ON THE FRICTION STIR WELDING TOOL

A Dissertation in

Materials Science and Engineering

by

Amit Arora

Submitted in Partial Fulfillment
of the Requirements
for the Degree of

Doctor of Philosophy

December 2011

The dissertation of Amit Arora was reviewed and approved* by the following:

Tarasankar DebRoy
Professor of Materials Science and Engineering
Dissertation Adviser
Chair of Committee

Long-Qing Chen
Professor of Materials Science and Engineering

Kwadwo Osseo-Asare
Distinguished Professor of Metallurgy and Energy and Geo-environmental Engineering

Panagiotis Michaleris
Associate Professor of Mechanical Engineering

Todd Palmer
Research Associate and Assistant Professor of Materials Science and Engineering

Gary L. Messing
Distinguished Professor of Ceramic Science and Engineering
Head of the Department of Materials Science and Engineering;

*Signatures are on file in the Graduate School.

Abstract

Friction stir welding has been commercially used as a joining process for aluminum and other soft materials. However, the use of this process in joining of hard alloys is still developing primarily because of the lack of cost effective, long lasting tools.

Here I have developed numerical models to understand the thermo mechanical conditions experienced by the FSW tool and to improve its reusability. A heat transfer and visco-plastic flow model is used to calculate the torque, and traverse force on the tool during FSW. The computed values of torque and traverse force are validated using the experimental results for FSW of AA7075, AA2524, AA6061 and Ti-6Al-4V alloys. The computed torque components are used to determine the optimum tool shoulder diameter based on the maximum use of torque and maximum grip of the tool on the plasticized workpiece material. The estimation of the optimum tool shoulder diameter for FSW of AA6061 and AA7075 was verified with experimental results. The computed values of traverse force and torque are used to calculate the maximum shear stress on the tool pin to determine the load bearing ability of the tool pin. The load bearing ability calculations are used to explain the failure of H13 steel tool during welding of AA7075 and commercially pure tungsten during welding of L80 steel.

Artificial neural network (ANN) models are developed to predict the important FSW output parameters as function of selected input parameters. These ANN consider tool shoulder radius, pin radius, pin length, welding velocity, tool rotational speed and axial pressure as input parameters. The total torque, sliding torque, sticking torque, peak temperature, traverse force, maximum shear stress and bending stress are considered as the output for ANN models. These output parameters are selected since they define the thermo-mechanical conditions around the tool during FSW. The developed ANN models are used to understand the effect of various input parameters on the total torque and traverse force during FSW of AA7075 and 1018 mild steel. The ANN models are also used to determine tool safety factor for wide range of input parameters.

A numerical model is developed to calculate the strain and strain rates along the streamlines during FSW. The strain and strain rate values are calculated for FSW of AA2524. Three simplified models are also developed for quick estimation of output

parameters such as material velocity field, torque and peak temperature. The material velocity fields are computed by adopting an analytical method of calculating velocities for flow of non-compressible fluid between two discs where one is rotating and other is stationary. The peak temperature is estimated based on a non-dimensional correlation with dimensionless heat input. The dimensionless heat input is computed using known welding parameters and material properties. The torque is computed using an analytical function based on shear strength of the workpiece material. These simplified models are shown to be able to predict these output parameters successfully.

TABLE OF CONTENTS

Abstract iii
TABLE OF CONTENTS v
LIST OF TABLES viii
LIST OF FIGURES ix
Acknowledgement xiv

Chapter 1. Introduction 1
1.1. Friction stir welding 1
1.2. Important issues 2
1.3. Objectives 4
1.4. Research plan 5
1.5. Thesis layout 5
1.6. References 6

Chapter 2. Background 8
2.1. Tool-material interaction in FSW 9
2.1.1. Tool materials 9
2.2. Tool geometry 12
2.2.1. Tool shoulder 12
2.2.2. Tool pin 15
2.3. Thermo-mechanical environment around FSW tool 18
2.4. Selection of important unanswered questions 25
2.5. References 28

Chapter 3. Optimum friction stir welding tool shoulder diameter 32
3.1. Experiments 33
3.2. Numerical model 35
3.2.1. Assumptions 36
3.2.2. Governing equations 36
3.2.3. Boundary conditions 38
3.3. FSW of AA7075 41
3.4. AA 6061 53
3.5. Conclusions 59
3.6. References 60

Chapter 4. Load Bearing Capacity of Tool Pin 62
4.1. Numerical model 64
4.2. Results and Discussions 68
4.3. Conclusions 82
4.4. References 83

Chapter 5. Artificial neural networks in FSW 85
5.1. Artificial Neural Network (ANN) model: 87
5.2. Results and discussion 100
5.3. Conclusion 119
5.4. References 120

Chapter 6. Strains and strain rates 121
6.1. Numerical model 122
6.2. Results and discussion 123
6.3. Summary and conclusion 131
6.4. References 132

Chapter 7. Back of envelope calculations in FSW 133
7.1. Velocity field 134
7.2. Peak Temperature 136
7.3. Torque 137
7.4. Results and discussion 137
7.5. Summary and conclusion 142
7.6. References 143

Chapter 8. Concluding Remarks 145
8.1. Summary and conclusions 145
8.2. Future work 148

Appendix A. Sensitivity of uncertain parameters in flow stress equation 149
A.1. References 153

Appendix B. Recent calculations of fatigue failure in FSW tools 154
A.2. References 157

Appendix C. Artificial neural network models for 1018 mild steel 158

Appendix D. Analytical calculation of the flow field 169
D.1. References 171

LIST OF TABLES

Table 2.1 List of tool materials used for FSW of common alloys for a thickness range [3] ... 9

Table 2.2 Thermo-physical properties of commonly used FSW tool materials [2]..... 12

Table 3.1 Composition of work piece (AA 7075) and tool (EN24) materials [24-25]..... 34

Table 3.2 Tool dimensions, process parameters and material properties used for calculations 35

Table 3.3 Data used for calculation for FSW of AA6061 [22]..... 54

Table 3.4 The mechanical properties of welds made using tapered cylindrical pin profile [21]. 58

Table 4.1 Experimentally measured and corresponding computed values of tool traverse force during FSW of Ti-6Al-4V alloy at different welding conditions. 70

Table 4.2 The tool material, dimensions and welding variables used for calculation of force and torque..... 79

Table 5.1 Levels of the six input variables used for training and testing of the ANN models for FSW of AA7075..... 92

Table 5.2 Combinations of input variables and corresponding output parameters for the training of ANN models for FSW of AA7075..... 93

Table 5.3 Combinations of input variables and corresponding output parameters for the testing of ANN models for FSW of AA7075 98

Table 6.1 The experimental conditions and material properties used for calculating the temperature and velocity fields. 126

Table 7.1 Material properties and welding process parameters used in the velocity and torque estimation..... 135

Table 7.2 The data used for calculation of the peak temperature at different weld pitch values for various aluminum alloys. [50] 141

Table A.1 Reported values of the four uncertain parameters for selected aluminum alloys and steels with different heat treatments [2-4]..... 150

Table A.2 Data used for the calculation of temperature and velocity fields, torque and traverse force for FSW of AA7075..... 150

Table A.3 Nine different combinations of the four uncertain parameters for the sensitivity analysis..... 151

Table A.4 Calculated values of torque, traverse force, and peak temperature for the nine combinations of uncertain parameters in flow stress equation. 151

LIST OF FIGURES

Figure 1.1 A schematic representation of the friction stir welding process..... 1

Figure 1.2 A schematic diagram showing interrelation among various objectives of the research. 5

Figure 2.1 Ultimate tensile strength of some of the nickel- and cobalt-base alloys at elevated temperature. [72] 10

Figure 2.2 Ultimate tensile strength of tungsten-base alloys as function of temperature. [72] 11

Figure 2.3 Temperatures calculated from finite element model for FSW of AA6061 [80] 13

Figure 2.4 Experimentally measured weld properties for FSW of AA6061 as function of the tool shoulder diameter for 5 different tool pin shapes [81]..... 14

Figure 2.5 Some of the tool shoulder surface features considered by TWI for FSW of various different materials [3]..... 15

Figure 2.6 Commonly used tool pin geometries (a) cylindrical threaded, (b) three-flat threaded (c) triangular (d) trivex (e) threaded conical1 (f) four-flute threaded pin [2] 16

Figure 2.7 Different tool pin geometries proposed by The Welding Institute (a) Whorl™ (b) MX Triflute™ (c) A-Skew™ (d) Flared-Triflute – neutral flute, (e) Flared-Triflute – left hand flutes and (f) Flared-Triflute – right hand flute [3]..... 17

Figure 2.8 Ultimate tensile strength of 1050-H24 friction stir welds [12] 18

Figure 2.9 Distribution of teak temperature near the tool in FSW of 7075Al-T651. The line on the right side of figure shows the weld nugget boundary. [86] 19

Figure 2.10 Computed values of temperature, in K, in three different planes for FSW of AA6061 (a) XZ (longitudinal section), (b) YZ (transverse section) and (c) XY (top surface). The welding velocity is 1.59 mm/s and tool rotational speed is 344 rpm. [87]. 21

Figure 2.11 Peak temperatures as function of tool rotational speed for FSW of AA6063. [88]..... 22

Figure 2.12 measured values of torque as function of time for three different tool rotational speeds. [89]..... 23

Figure 2.13 Measured values of torque during FSW of AA2524-T351 as function of (a) tool rotational speed and (b) welding velocity. [90]..... 24

Figure 2.14 Measured values of traverse force (Fx), kN, as function of the welding speed for FSW of AA2524-T351. [90]..... 25

Figure 3.1 Comparison of the measured and computed peak temperatures during FSW of AA7075-T6 at rotational speeds of 355 and 560 RPM. The error bars shown represent the error in measurement estimated by repeated experimental measurements. [23]..... 42

Figure 3.2 Comparison of the computed and the measured time-temperature profile at a location 8.5 mm away from the butting surface and 0.75 mm from the top surface in the advancing side for the friction stir welding of AA7075-T6 with a 20 mm shoulder diameter tool at 355 RPM. [23] 43

Figure 3.3 Comparison of the measured and computed torque required for FSW of AA7075-T6 at rotational speeds of 355 and 560 RPM. The error bars shown represent the error in measurement estimated by repeated experimental measurements. [23] 44

Figure 3.4 Comparison of the measured and computed power required for FSW of AA7075-T6 at rotational speeds of 355 and 560 RPM. The error bars shown represent the error in measurement estimated by repeated measurements. [23] 45

Figure 3.5 Characteristic flow stress and temperature of the deforming material near the tool for various shoulder diameters and rotational speeds. The legends near the symbols are shoulder diameters in mm. 47

Figure 3.6 Computed values of sticking torque versus shoulder diameter for various tool rotational speeds. All other welding parameters, presented in Table 2, remain constant. 48

Figure 3.7 Variation of the objective function, O(f), as a function of tool shoulder diameter at various tool rotational speeds. [23] 50

Figure 3.8 Computed values of rate of mechanical work done at varying shoulder diameters for rotational speeds of 355, 560 and 710 RPM. 51

Figure 3.9 Ratio of the weld joint percent elongation, yield strength and ultimate tensile strength to the corresponding base metal properties. The weld was made using tool rotational speed 355 RPM and 0.67 mm/s. [23] 52

Figure 3.10 Flow stress and temperature combinations of the weld metal during FSW of AA60601 for various shoulder diameters at 1200 RPM. 55

Figure 3.11 The computed values of sticking, sliding and total torque for various shoulder diameters at 1200 RPM. 56

Figure 3.12 Total torque required during FSW of AA6061 as a function of the tool shoulder diameter for rotational speeds of 900, 1200 and 1500 RPM. 57

Figure 3.13 The computed values of the objective function, O(f), as a function of shoulder diameter at tool rotational speed of 900, 1200 and 1500 RPM. 59

Figure 4.1 Schematic of (a) force distribution on a straight cylindrical pin and (b) cross-section along S-S. 65

Figure 4.2 Schematic illustrations of (a) τ_T, (b) τ_B at section S-S and of (c) τ_T and τ_B at point A 67

Figure 4.3 A comparison of the experimental and computed traverse force values as a function of tool rotational speed during FSW of AA2524 at the welding speed of 2.11 mm/s. [22] 69

Figure 4.4 A comparison of the computed and corresponding experimentally measured total traverse force for FSW of Ti-6Al-4V alloy. The welding condition for the five samples are given in table 4.1. [23] 71

Figure 4.5 A comparison of experimentally measured and corresponding computed total traverse force as a function of the pin length for the FSW of AA6061. The welding velocity is 3.33 mm/s, tool rotational speed is 650 RPM and the pin diameter is 7.6 mm. [18] 72

Figure 4.6 A comparison of the computed and corresponding experimentally measured total traverse force for FSW of AA6061 as a function of pin diameter. [18] The welding velocity is 3.33 mm/s, tool rotational speed is 650 RPM and the pin length is 3.8 mm. [18] 73

Figure 4.7 A comparison of the force on the tool pin computed and the estimated values based on regression analysis model [18] for different pin lengths. The welding velocity is 3.33 mm/s, tool rotational speed is 650 RPM and the pin diameter is 7.6 mm. [18] 74

Figure 4.8 Typical distribution of traverse force from the root to the tip of a tool pin for a given pin geometry. The welding velocity is 3.33 mm/s, tool rotational speed is 650 RPM, the pin diameter is 7.6 mm and the pin length is 3.8 mm. 75

Figure 4.9 The computed maximum shear stress (τ_{max}) on the tool pin as a function of the pin length during FSW of AA6061. The welding velocity is 3.33 mm/s, tool rotational speed is 650 RPM and the pin diameter is 7.6 mm. 76

Figure 4.10 The computed maximum shear stress (τ_{max}) on the tool pin as a function of the pin diameter during FSW of AA6061. The welding velocity is 3.33 mm/s, tool rotational speed is 650 RPM and the pin length is 3.8 mm. 77

Figure 4.11 The force distribution on the tool pin during FSW of L80 steel. The welding velocity is 1.7 mm/s and the tool rotational speed is 170 RPM. [25] 78

Figure 4.12 Temperature dependent shear strength of the commercially pure tungsten as reported by Kravchenko et al. [26] 80

Figure 4.13 The tools used by Neilsen during FSW of AA7075 after the use. The tool pin in the second tool from the left sheared off during welding. [30] 81

Figure 4.14 The computed force distribution of the tool pin during FSW of AA7075 alloy. The tool rotational speed is 800 RPM and welding speed is 4.66 mm/s. 81

Figure 4.15 The temperature dependent shear strength of the H13 tool steel. [24] 82

Figure 5.1 Architecture of the artificial neural network (ANN) model. 88

Figure 5.2 Comparison of the predicted and the desired values of output parameters for FSW of AA7075, (a) total torque, (b) sliding torque, (c) sticking torque, (d) traverse force, (e) peak temperature, (f) maximum shear stress and (g) bending stress. 101

Figure 5.3 The predicted values of peak temperature (K) by ANN model for FSW of AA7075 as function of tool shoulder radius and tool rotational speed for the combinations of input variables listed in the table shown here. 104

Figure 5.4 Experimentally measured values of temperatures as function of the time for FSW of aluminum 6063 alloy at various tool rotational speeds. [26] 105

Figure 5.5 The predicted values of total torque (Nm) by ANN model for FSW of AA7075 as function of tool shoulder radius and tool rotational speed for the combinations of input variables listed in the table shown here. 107

Figure 5.6 Measured values of torque as function of tool rotational speed during FSW of AA2524 as the welding velocity is 2.11 mm/s and axial force is 42.3kN. [27] 108

Figure 5.7 The predicted values of traverse force (N) by the ANN model for FSW of AA7075 as function of tool shoulder radius and tool rotational speed for the combinations of input variables listed here. 110

Figure 5.8 The predicted values of maximum shear stress on the tool pin (MPa) by the ANN model for FSW of AA7075 as function of tool shoulder radius and tool rotational speed for the combinations of input variables listed here. 112

Figure 5.9 The predicted values of bending stress on the tool pin (MPa) by the ANN model for FSW of AA7075 as function of tool shoulder radius and tool rotational speed for the combinations of input variables listed here. 114

Figure 5.10 The temperature dependent shear strength of the H13 tool steel. [28]..... 116

Figure 5.11 Computed contours of safety factor for FSW of AA7075 alloy. 118

Figure 6.1 The strain values computed for the extrusion of an aluminum billet to verify the formulation of streamline integration method. The values shown by the squares are from the experimental results of Berghaus et al. [14] and the values shown by the triangles are from the methodology adapted in this work..... 124

Figure 6.2. The computed velocity fields and streamlines in two horizontal planes parellal to the work-piece top surface. (a) Plane 1 – 0.13mm away from top and (b) plane 2 – 2.0mm away from top. 125

Figure 6.3 Computed strain rate components (a) $\dot{\varepsilon}_{11}$, and (b) $\dot{\varepsilon}_{22}$. 128

Figure 6.4 Computed strain components (c) ε_{11}, and (d) ε_{22} 130

Figure 7.1 Schematic diagram showing the domain for velocity field calculation. An approximate thermomechanically affected zone (TMAZ) geometry is shown by cross hatched region in the figure. 135

Figure 7.2 The computed velocity fields in various horizontal planes for the FSW of AA2524. (a) results from a well tested numerical heat transfer and visco plastic flow code, and (b) from the proposed analytical solution. 138

Figure 7.3 The analytically computed velocities relative to the maximum velocity as a function of the dimensionless distance from the tool shoulder. (a) AA2524 (b) Ti-6Al-4V, (c) 304L SS. u' is the square root of sum of the three velocity components squared and u* is the maximum velocity. 139

Figure 7.4 Linear relationship between dimensionless temperature and log of dimensionless heat input. 140

Figure 7.5 Peak temperature against weld pitch for friction stir welding of various aluminum alloys. (a) Experimentally measured peak temperature [49] (b) Peak temperature from the proposed correlation. 141

Figure 7.6 Estimated and experimental torque values for FSW of (a) AA2524 [36] and (b) Ti-6Al-4V alloy. [51] The data used for the calculations are available in table 7.1. 142

Figure B.1 The calculated number of cycles for failure of the steel tool for toughness of 40 MPa-$m^{1/2}$. 155

Figure B.2 The calculated number of cycles for failure of the steel tool for toughness of 5 MPa-$m^{1/2}$. 157

Figure C.1 Comparison of desired and predicted values of output parameters for training and testing datasets for FSW of 1018 mild steel..... 158

Figure C.2 The predicted values of peak temperature (K) by ANN model for FSW of 1018 mild steel as function of tool shoulder radius and tool rotational speed for the combinations of input variables listed in the table shown here. 160

Figure C.3 The predicted values of total torque (Nm) by ANN model for FSW of 1018 mild steel as function of tool shoulder radius and tool rotational speed for the combinations of input variables listed in the table shown here. 162

Figure C.4 The predicted values of traverse force (N) by the ANN model for FSW of 1018 mild steel as function of tool shoulder radius and tool rotational speed for the combinations of input variables listed here. 164

Figure C.5 The predicted values of maximum shear stress on the tool pin (MPa) by the ANN model for FSW of 1018 mild steel as function of tool shoulder radius and tool rotational speed for the combinations of input variables listed here. 166

Figure C.6 The predicted values of bending stress on the tool pin (MPa) by the ANN model for FSW of 1018 mild steel as function of tool shoulder radius and tool rotational speed for the combinations of input variables listed here..... 168

Acknowledgement

This thesis is result of five years of work at Penn State whereby I have been accompanied and supported by many people. I would first like to express my deep appreciation and sincere gratitude to my advisor, Dr. Tarasankar DebRoy. He gave me many opportunities to advance my research as well as my professional development.

I would like to acknowledge Dr. Todd Palmer, Dr. Long-Qing Chen, Dr. Kwadwo Osseo-Asare, and Dr. Panagiotis Michaleris for their valuable advice and suggestions on my work while serving on my thesis committee. I am very grateful to them for giving their time to review and comment on this thesis. I would also like to express my thanks to Dr. Amitava De at Indian Institute of Technology, Bombay, Dr. Gour Gopal Roy at Indian Institute of Technology, Kharagpur, Dr. Anthony Reynolds at University of South Carolina, SC, Dr. Harry K.D.H. Bhadeshia at University of Cambridge, UK and Dr. Zhao Zhang at Dalian University of Technology, Dalian for their helpful discussions on various topics during the progress of my research work and also for their help in developing numerical models.

Many thanks to the senior members of my research group, Dr. Rituraj Nandan, Dr. Rohit Rai and Dr. Brandon Ribic who helped me get started with my research work and also helped me adjust in new environment. I would also like to thank my current colleague Mr. Ashwin Raghwan for his company at the workplace.

I am grateful to my family and friends for their love, support, patience and continued motivation for my work. My parents made many sacrifices and faced several hardships to support their children and provide them education which they could not obtain. I am greatly indebted to them and will keep working forever to fulfill their dreams. I would like to express my great appreciation to Ms. Charumani, Dr. Amit Kumar, Mr. Sudeep Sharma and Dr. Kokonad Sinha for their patient ears and sound advice over the course of this thesis work. I would also like to thank Association for India's Development, Penn State chapter for providing me a higher meaning in life and an opportunity to help people in need.

Finally, I am also grateful to Office of Naval Research for supporting my research at Penn State.

To my parents, Dilip Kumar Arora and Narbada Arora,
and my sister Punam Arora.

Chapter 1. Introduction

1.1. Friction stir welding

Friction stir welding (FSW) is a solid-state joining process where the joint forms because of mixing of the deforming plasticized material. [1,2] A solid tool consisting of a cylindrical shoulder and a smaller sized pin is placed in between the abutting metal plates. Figure 1.1 shows a schematic diagram of FSW setup. The tool is rotated at its axis and is moved along the welding line. The movement of the tool generates frictional and deformational heat at the tool workpiece interfaces (both shoulder-workpiece and pin-workpiece interfaces). The heat generated at the interfaces softens the workpiece material. The mixing of the materials occurs as the plasticized material deforms due to the rotating tool. The moving tool leaves behind a fine grained friction stir weld joint.

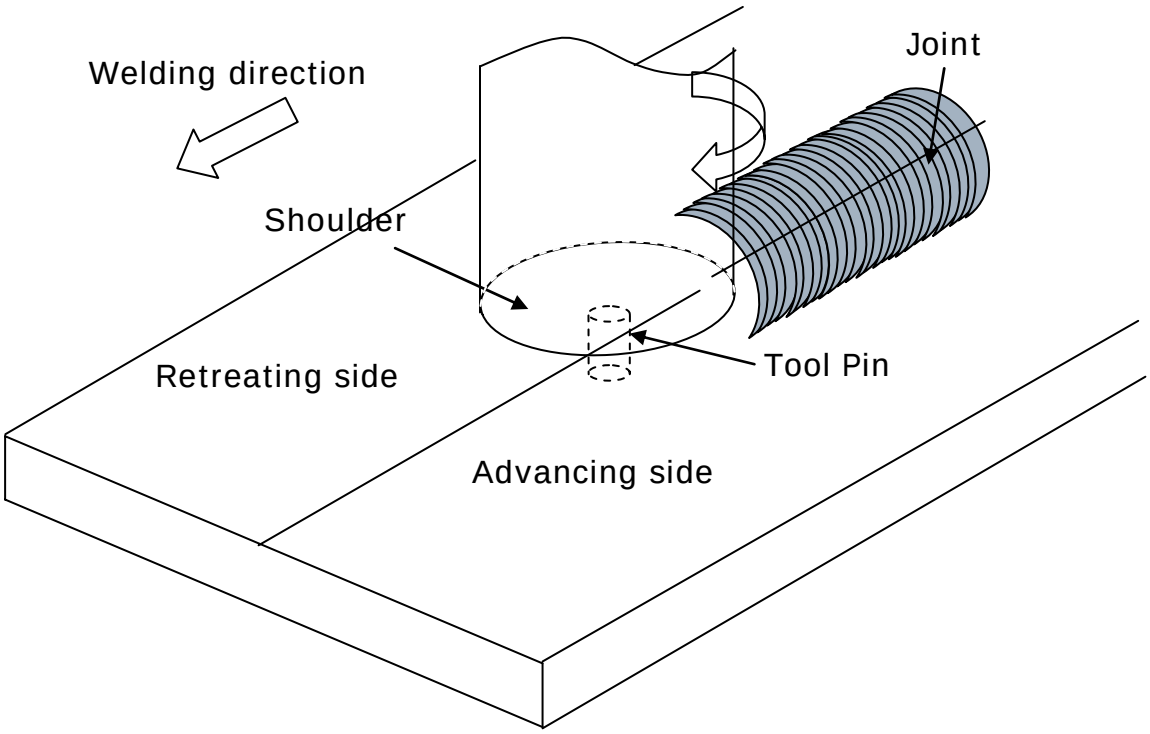

Figure 1.1 A schematic representation of the friction stir welding process.

In FSW, the material on either side of the welding line faces different thermal conditions. The asymmetry arises due to the simultaneous rotational and linear motion of the tool. The side where the direction of tool rotation is same as the direction of linear motion is called the 'advancing side'. The opposite side where the rotational and linear

motion are in opposite direction is called ‘retreating side’. This asymmetry leads to different temperatures and joint properties on the two sides of a butt weld. The advancing side experiences higher temperatures compared to the workpiece material in the retreating side.

Since there is no significant liquid formation during FSW, the process avoids the common fusion welding problems such as solidification and liquation cracking, porosity and the loss of alloying elements. These advantages have led to widespread commercial use of FSW to join aluminum alloys and other soft materials such as magnesium and copper alloys. [2] However, the lack of cost-effective long-lasting tools limits the commercial application of FSW to hard alloys. High temperatures and severe stresses experienced by the tool during welding of the FSW of the hard materials result in severe degradation and premature failure of tool. A quantitative understanding of the stresses on the FSW tool is required to further the development of tools to join hard materials. Since these stresses are directly and indirectly dependent on the thermo mechanical conditions around the tool, a detailed analysis of the thermo mechanical conditions around the tool is required.

1.2. Important issues

Since the discovery of the FSW process, researchers have greatly benefitted from the process understanding developed through numerical modeling. The currently available numerical models can provide a fair idea about the heat generation rate, heat transfer, material flow and temperature distribution during FSW. [3-13] Success of these models has significantly contributed to the development of FSW process for soft materials. However, further development of numerical models to understand the thermo mechanical conditions around the tool and the stresses on the tool is needed.

During FSW, the temperature, required torque and power are measure of the thermo mechanical environment experienced by the tool. A numerical model to predict the required torque for a given set of FSW parameters would be useful to understand the stresses on the tool. Even though numerical models of FSW have been developed to calculate the temperature distribution, material flow, weld microstructure, and, residual

stress. [3-13] A well tested numerical model to compute the required torque, power and energy is not available.

During FSW, the shoulder generates most of the heat, induces the flow of plasticized material, and prevents escape of the work piece material during welding. In order to achieve a long tool life, the shoulder diameter should be such that the work piece can be adequately softened for the ease of materials flow while requiring low power and torque. An optimal value of the shoulder diameter would be where the balance of these contrasting requirements can be achieved. A method to determine the optimum tool shoulder diameter based on scientific principles is needed and not available in the literature.

Although FSW is now widely used for the joining of aluminum and other soft alloys, its commercial application to hard materials, such as steels and titanium alloys, is still developing. [14-16] An important challenge is to improve the cost effectiveness and long term usability of the tools. [1,14-16] Due to the continuous linear and rotational motions through the deforming material, the tool is subjected to high temperatures, severe stresses and wear. Therefore, the tool must have adequate torsional stiffness and strength at high temperature so that it can endure large torque and bending moment without any significant distortion or premature failure. The tool pin in friction stir welding is subjected to continuous bending and twisting moments due to the simultaneous linear and rotational motions, respectively. Knowledge of the traverse force and the torque acting on the tool pin are thus critical factors in the design of tools, particularly for the welding of hard alloys. A method to determine tool pin geometry based on its load bearing ability would be helpful to design reliable tools with long service life.

Numerical models to estimate the temperature and material flow during FSW require the solution of the Navier Stokes equations and the energy equation together with the material constitutive equations. These calculations are complex and computationally intensive. Several sophisticated models exist to estimate thermal conditions for fusion welding along with simple but insightful analytical methods, such as the Rosenthal equation based temperature model. [2] These analytical methods are very simple and straight forward to use and are very popular to practicing welders. However, such

methods to estimate the thermo mechanical condition of material are not available for FSW.

Currently the three dimensional heat transfer and material flow model uses temperature dependent thermo-mechanical properties of the workpiece material. However, during FSW, these properties are also affected by the strains and strain rates imparted on the workpiece material by the process. The workpiece strains result in dynamic recrystallisation and change in mechanical properties of the workpiece. Development of a dynamic recrystallisation model will add these changes to the existing numerical models. The lack of computed values of strain and strain rates limit the development of a dynamic recrystallisation model for the prediction of the weld joint properties. The microstructure and mechanical properties of FSW joints are also affected by local gradients of strain and strain rates in the stir zone (SZ) and the thermo mechanically affected zone (TMAZ). [17] A numerical model which can estimate the local strain and strain rate values would be useful in determining the weld properties and development of a dynamic recrystallisation based numerical model.

1.3. Objectives

The objective of the proposed research is to improve the understanding of the thermo mechanical environment around the tool and provide a quantitative estimate of the load bearing ability of the tools during FSW. The specific objectives are listed below:

1. Develop numerical model to compute required torque, power and energy, and stir zone geometry during FSW.
2. Determine the optimal tool shoulder diameter based on the optimum use of torque and maximum grip of the tool on plasticized material.
3. Development of a numerical model to compute traverse force and load bearing ability of the tool.
4. Develop a neural network based model to design process maps of safe and optimum welding conditions.
5. Development of a methodology to compute local strains and strain rates in FSW from the computed material flow field.
6. Development of set of analytical methods to estimate the peak temperature, material flow field and torque.

1.4. Research plan

A schematic diagram showing interrelation among the aforementioned objectives is shown in figure 1.2. The inputs and outputs are shown in rectangular boxes and the models are presented in rounded boxes.

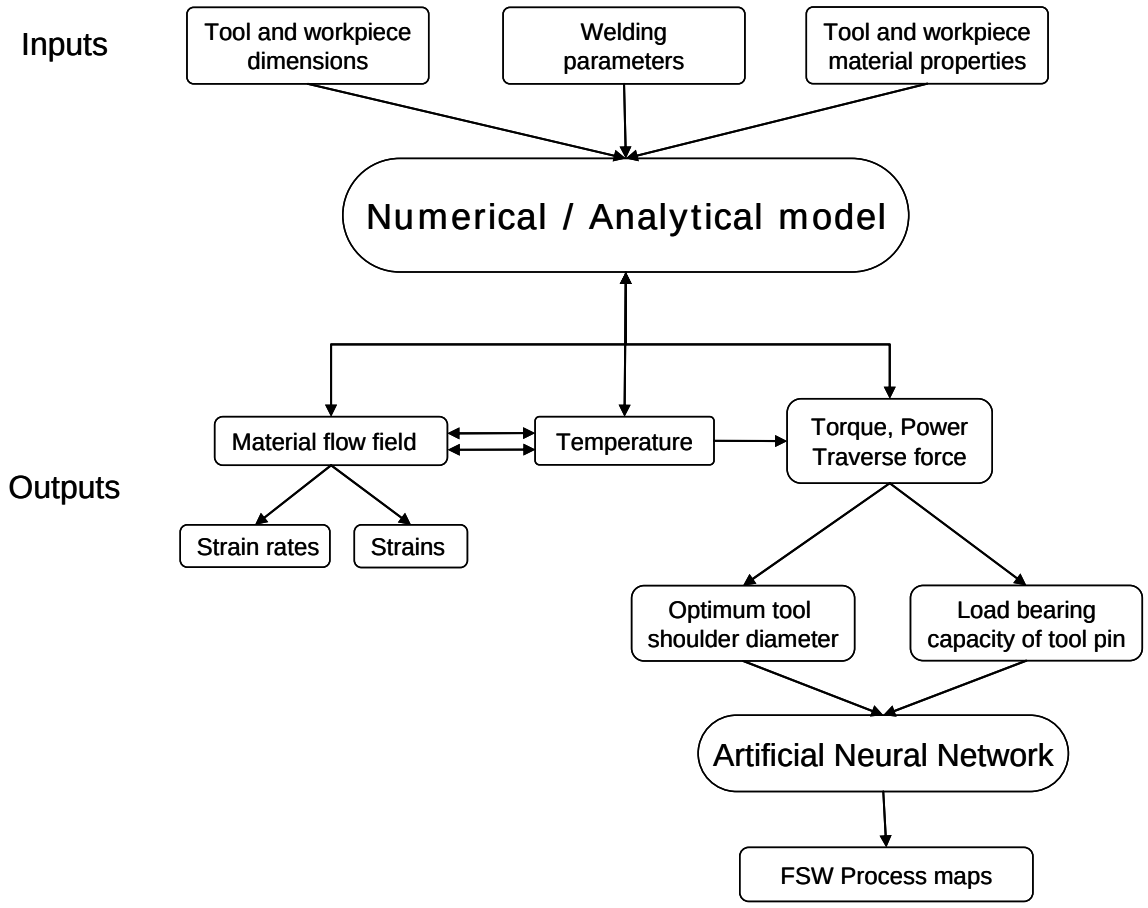

Figure 1.2 A schematic diagram showing interrelation among various objectives of the research.

1.5. Thesis layout

The thesis consists of eight chapters. The first chapter explains the friction stir welding process, introduces various important issues in the field of FSW and outlines the objectives of the research and the layout of the thesis. Chapter 2 reviews the existing literature related to the proposed research. The chapter also describes the existing numerical heat transfer and fluid flow models, and their respective inputs and outputs.

This chapter describes the evolution of quantitative understanding of FSW. A detailed model for calculating the torque, power and energy is described in Chapter 3. The concept of optimum shoulder diameter during FSW is also explained in this chapter. A calculation of traverse force on the tool shoulder and tool pin is presented in Chapter 4. The load bearing capability of a tool pin is also included in this chapter. Chapter 5 contains description of artificial neural network model and the FSW process maps developed using this model.

A new methodology is proposed and tested to calculate the strains and strain rates in chapter 6. The calculation procedure is presented and the calculations are shown for a system where independent experimental data is available and where the calculated values could be tested for the proposed procedure. The strains and strain rates for FSW of AA2524 are computed along the stream lines using the material flow field from the three dimensional heat transfer and visco-plastic flow model. In Chapter 7 simplified models for estimation of peak temperature, torque and material flow field during FSW are presented. A dimensionless expression is developed to predict the peak temperature in terms of the dimensionless heat input in the FSW of various alloys. Analytical solutions are described to calculate the required-torque and the material flow field. The important findings of this research are summarized in chapter 8 of this thesis.

1.6. References

1. W.M. Thomas, E.D. Nicholas, J.C. Needham, M.G. Murch, Temple-Smith P, Dawes CJ. Friction stir butt welding. International Patent Application No. PCT/GB92/02203; 1991.
2. R. Nandan, T. DebRoy and H.K.D.H. Bhadeshia, Prog. Mater Sci. 53(2008) 980-1023
3. O. Frigaard, Ø. Grong, O.T. Midling. Metall Mater Trans A 32(2001) 1189–200.
4. M. Song, R. Kovacevic, Int J Mach Tools Manuf 43(2003) 605–15.
5. M. Song, R. Kovacevic, J Eng Manuf 217(2003) 73–85.
6. H.W. Zhang, Z. Zhang, J.T. Chen, Mater Sci Eng A 403(2005) 340–8.
7. C.M. Chen, R. Kovacevic, Int J Mach Tools Manuf 43(2003) 1319–26.
8. H. Schmidt, J. Hattel, Int J Offshore Polar Eng 14(2004) 296–304.
9. M.Z.H. Khandkar, J.A. Khan, J Mater Process Manuf Sci 10(2001) 91–105.
10. M.Z.H. Khandkar, J.A. Khan, A.P. Reynolds Sci Technol Weld Join 8(2003) 165–74.
11. R. Nandan, G.G. Roy, T. DebRoy., Metall Mater Trans A 37(2006) 1247–59.
12. P.A. Colegrove, H.R. Shercliff, Sci Technol Weld Join 9(2004) 345–51.

13. A. Simar, J. Lecomte-Beckers, T. Pardoen, B. de Meester, Sci Technol Weld Join 11(2006) 170–7.
14. H.K.D.H. Bhadeshia, T. DebRoy, Sci. Technol. Weld. Join. 14(2009) 193-196.
15. R. Nandan, T.J. Lienert, T. DebRoy, Int. J. Mater. Res. 99(2008) 434-444.
16. R. Nandan, G.G. Roy, T.J. Lienert, T. DebRoy, Acta Mater. 55(2007) 883-895.
17. M.D. Fuller, S. Swaminathan, A.P. Zhilyaev, T.R. McNelley, Mater Sci Eng A 463(2007) 128–137

Chapter 2. Background

Friction stir welding (FSW) is a solid state joining process where a rotating tool moves along the line between the two pieces being joined. The tool is made of a shoulder and smaller size pin. The tool is rotated by external power and is pressurized along the tool axis to keep in firm contact with the workpiece top surface. Rotating tool in contact with the workpiece material generates large amount of heat which softens the workpiece material. Severe plastic deformation occurs and plasticized workpiece material flows with the tool forming weld joint behind the moving tool. Since the tool has to plastically deform the workpiece material for the weld to form, the FSW tools are subjected to high torsional and bending stresses at high temperatures. As a result, tool degradation and failure limit commercial application of FSW to hard alloys. The objective of the present thesis research is to understand the thermo-mechanical conditions around the tool during friction stir welding. In particular, the research work seeks to quantitatively predict the temperature, torque, optimal shoulder diameter, traverse force, load bearing ability of tool pin, workpiece strains and strain rates to seek an improved understanding of the thermo-mechanical environment of the FSW tools.

The current issues and problems in FSW have been reviewed recently [1-3] It was found from these reviews that the fundamental understanding of the thermo-mechanical environment of the FSW tools is still developing. As a result, currently there is no unified approach to understand how various welding variables and other factors such as the tool geometry affect the severity of the thermo-mechanical conditions experienced by the FSW tools. The goal of this chapter is to examine the available research related to the thermo-mechanical conditions around the tool and effect of various welding variables on these thermo-mechanical conditions.

The following topics are covered in this chapter:

(1) FSW process uses a tool that is usually made of a large size shoulder and a smaller sized pin. The tool is responsible for heat generation and material flow during the process. This generated heat and material flow in FSW affects both the thermo-mechanical environment of the tool and the weld properties. Researchers have examined

several tool geometries to obtain better material flow and weld properties during FSW. Also, to weld various types of alloys, different kinds of tool materials are used. This sections reviews some of the available tool materials and tool geometries for friction stir welding of common alloys.

(2) Thermo-mechanical conditions around the tool affects the stresses on the tool pin. These thermo-mechanical conditions include the temperatures, strain and strain rates in workpiece, and torque, force, stresses on the tool. Geometry of the tool, both shoulder and pin, contribute to these thermo-mechanical and also affect the weld properties. Some of the literature related to the thermo-mechanical environment of the tool.

At the end of this chapter, a selection of important unanswered questions related to the thermo-mechanical conditions around FSW tool is identified. Solving these unanswered questions is an important goal of the present thesis study, and details of the solution are presented in subsequent chapters.

2.1. Tool-material interaction in FSW

2.1.1. Tool materials

In laboratory system, FSW has been used to join a wide variety of materials, such as magnesium alloys [4-8], aluminum alloys [9-19], titanium alloys [20-31], ferrous alloys [32-45], copper alloys [46-52], metal matrix composites [53-59], dissimilar alloys [60-71]. The commonly used tool materials are tool steels, commercially pure tungsten, tungsten-25% rhenium, tungsten carbide, titanium carbide, silicon nitride, and polycrystalline cubic boron nitride. Common tool materials used to join specific alloys are listed in table 2.1. [3]

Table 2.1 List of tool materials used for FSW of common alloys for a thickness range [3]

Alloy	Thickness, mm	Tool material
Aluminum alloys	<12	Tool steel, WC-Co
	<26	MP159
Magnesium alloys	<6	Tool steel, WC
Copper and copper alloys	<50	Nickel alloys, pcBN, tungsten alloys
	<11	Tool steel
Titanium alloys	<6	Tungsten alloys
Stainless steels	<6	pcBN, tungsten alloys
Low-alloy steels	<10	WC, pcBN
Nickel alloys	<6	pcBN

Since most of the published research is for soft alloys, such as aluminum, magnesium alloys, the most commonly used tool material is tool steel. Easy availability and machinability, low cost and established material characteristics make the tool steels as a preferred choice for FSW tools. In case of joining copper alloys, research has shown that tool steel FSW tool could weld 3 mm thick copper alloy but in case of welding 10 mm thick sheet, the workpiece material softened the tool material and distorted the pin profile. [48] Some of the other common tool materials are nickel and cobalt based alloys, tungsten based alloys, polycrystalline cubic boron nitride, and metal carbides (TiC).

Nickel- and cobalt based alloys were initially designed for use in aircraft engine components due to high strength, ductility, creep resistance and corrosion resistance at high temperatures. However, these alloys are difficult to machine especially in high alloying conditions. Some of the nickel based alloys used for FSW of copper alloys are IN738LC, IN939, MAR-M-002, Stellite 12, IN-100, PM 3030, Nimonic 90, Inconel 718, Waspalloy and Nimonic 105. Cobalt-nickel-base alloy MP159 has been used as FSW tool material to weld aluminum alloys. [72] Ultimate tensile strength of some of these alloys is shown as function of temperature in Figure 2.1. [72]

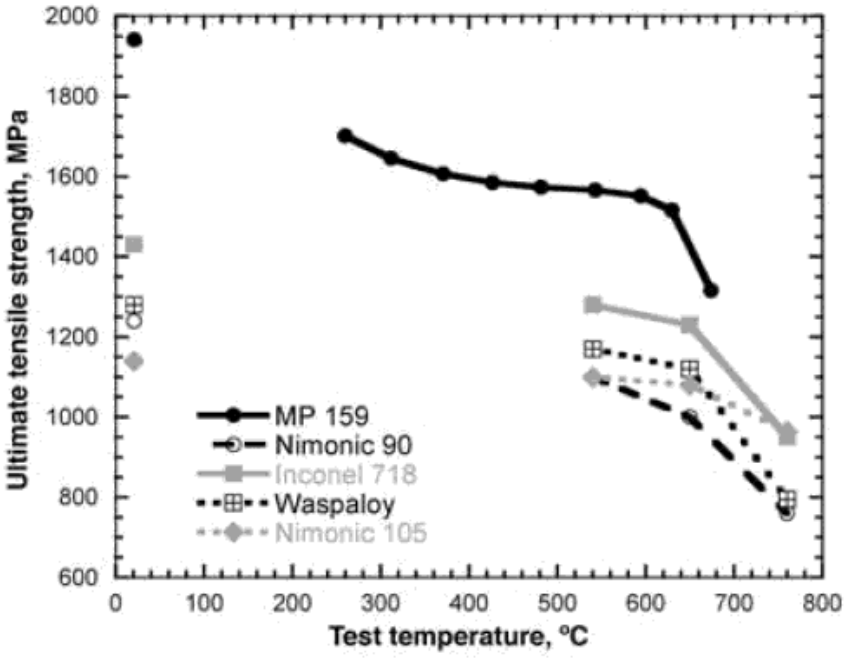

Figure 2.1 Ultimate tensile strength of some of the nickel- and cobalt-base alloys at elevated temperature. [72]

Another commonly used tool material category is refractory metals, such as tungsten, molybdenum, niobium, and tantalum. Since these alloys are produced in single phase, they keep their strength at high temperature. However, niobium and tantalum have high oxygen solubility at high temperatures which results in sharp reduction in ductility. Lack of material availability, high cost and difficult machining limits the use of these materials for FSW tools. Four common tungsten-base alloys used for FSW tools are commercially pure W, W-25%Re, Densimet (W spheres in Ni-Fe or Ni-Cu matrix) and W-1%LaO_2. These alloys have high operational temperatures. The ultimate tensile strength of these alloys at elevated temperatures is shown in Figure 2.2. [72]

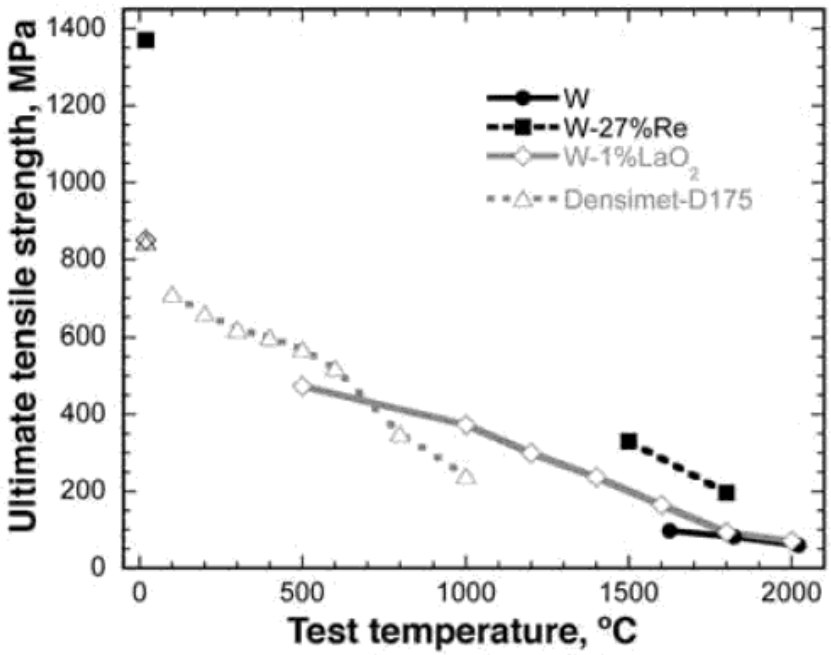

Figure 2.2 Ultimate tensile strength of tungsten-base alloys as function of temperature. [72]

Another hard commonly considered for FSW tools is polycrystalline cubic boron nitride (pcBN). This alloy was originally developed for the machining of tool steels, cast irons and superalloys. Based on the success of pcBN as a machining tool material for high temperature materials, it has been accepted for application in FSW tool manufacturing. Extreme pressure and temperatures required to produce pcBN limits the size of the tools made from pcBN. Thus only tool shoulder and pin are made of pcBN, and are fitted to tungsten carbide tool shank using a superalloy locking collar. **[**72**]** The

important thermo-physical properties of some of these commonly used tool materials are listed in Table 2.2. [2]

Table 2.2 Thermo-physical properties of commonly used FSW tool materials [2]

	Coefficient of thermal expansion 10^{-6}/K	Thermal conductivity W/m-K	Yield strength MPa	Hardness HV
pcBN	4.6-4.9 [73]	100-250 [73]		2600-3500
cp-W	~4.6 @20-1000 C [74]	167 @20 C [74] 111 @1000 C	~ 100 @ 1000 C [75]	360-500 [74]
W-25%Re		55-65 [76]	~ 500-800 @1000 C [75]	
WC	4.9-5.1 [73]	95 [73]		1300-1600 [73]
4340 Steel	11.2-14.3 [73]	48 [73]		280 [73]
TiC	8.31 [77]	5-31 [77]	20,000 [77]	2800-3400 [77]
Si_3N_4	3.9@20 C 6.7@1000 C [78]	20-70 [79]		1580

2.2. Tool geometry

2.2.1. Tool shoulder

Friction stir welding tools are mostly made of a shoulder and a smaller size pin. Simplest form of a friction tool is a cylindrical tool shoulder along with a cylindrical tool pin. However, researchers have experimented with various tool designs and geometrical features to improve the material flow and weld qualities. Important geometrical features for the tool shoulder are shoulder diameter, shoulder surface angle and nature of the shoulder surface.

Tool shoulder diameter size significantly contributes to the heat generation at the tool-workpiece interface. Zhang [80] used commercial finite element software to show that larger shoulder diameter results in higher peak temperatures. Figure 2.5 shows the calculated values of temperature, in °C, as function of the distance along the welding direction. [80] As the tool shoulder diameter increases, the temperatures in the workpiece also increases at all the places. The computed temperatures are for the three tool shoulder diameters 16mm, 20mm and 24mm.

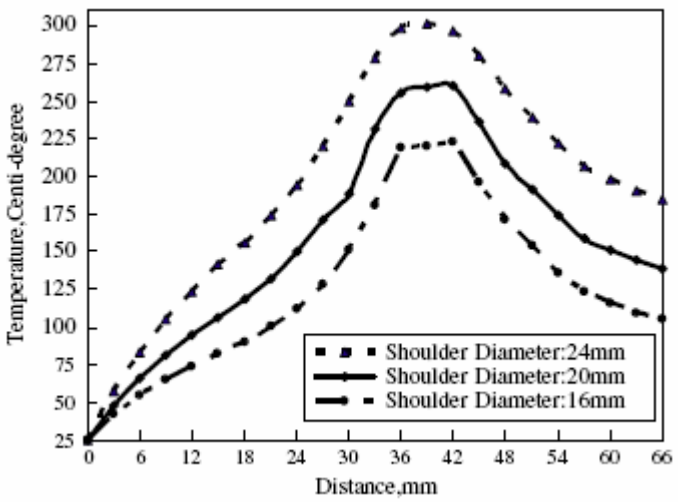

Figure 2.3 Temperatures calculated from finite element model for FSW of AA6061 [80]

FSW tool Shoulder diameter also affect the material based on its grip on the plasticized workpiece material. This effect can be seen in terms of the mechanical properties of the friction stir welds using tool with different shoulder diameters. Elangovan and Balasubramanian [81] studied the effect of tool shoulder diameter on the mechanical properties of welds. For FSW of AA6061 they [81] considered three shoulder diameters, 15mm, 18mm and 21mm, for five different kind of tool pin geometries. Tool with one of the three shoulder diameters, 18mm, resulted in superior weld tensile properties for all the tool pin geometries used. Figure 2.6 shows the measured weld properties for FSW of AA6061 for three different tool shoulder diameter values. [81]

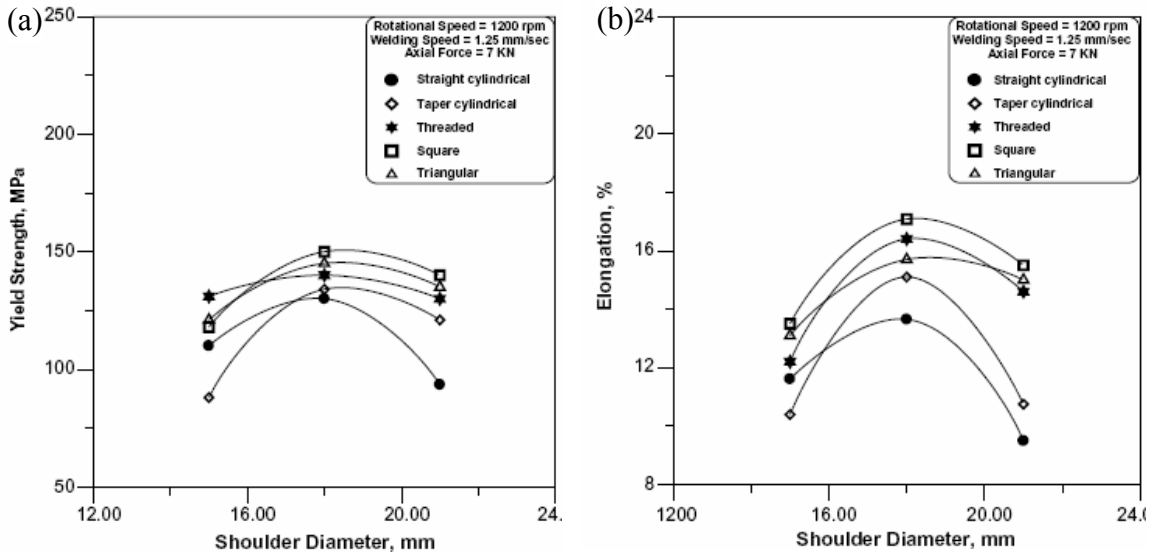

Figure 2.4 Experimentally measured weld properties for FSW of AA6061 as function of the tool shoulder diameter for 5 different tool pin shapes [81]

Considering the tool shoulder surface angle, two possible tool shoulder are convex and concave. The concave tool surface is the most common tool surface for FSW tools. [3] An angle of 6°-10° between the edge of the shoulder and the pin is considered to produce the shoulder surface concavity. The concavity in the shoulder surface absorbs the material displaced by the tool pin during plunge of the tool at the start of the welding. [3] Some researchers have also used FSW tools with convex surface, where the convex tool shoulder was mainly used with scrolls on the surface.

Scialpi et al [19] used three tools with three different shoulder surfaces, (a) scroll, (b) cavity and (c) fillet. The tool with cavity in the shoulder surface was found to produce the best weld surface where the flash from the weld was held by the cavity in the tool shoulder surface. Leal et al [82] also showed that the weld surface was best when a tool with conical cavity was used as compared to the weld made with a scrolled convex tool. Badrinarayan et al [83] measured strength of the welds for tools with three different shoulder surfaces, namely concave, flat and convex. They showed that the weld strength is highest for the welds made with concave shoulder tool and the tool with convex shoulder resulted in lowest weld strength. [83]

Further, various tool shoulder surface features, such as scrolls, ridges or knurling, grooves, and concentric circles, have been designed to improve the grip of the tool

shoulder surface on the plasticized workpiece material. [3] These shoulder surface designs improve the tool grip and material flow by entrapping the plasticized material within special re-entrant features. [3] Figure 2.2 shows an example of some of the tool shoulder surface features considered by TWI to suit different materials and conditions. [3]

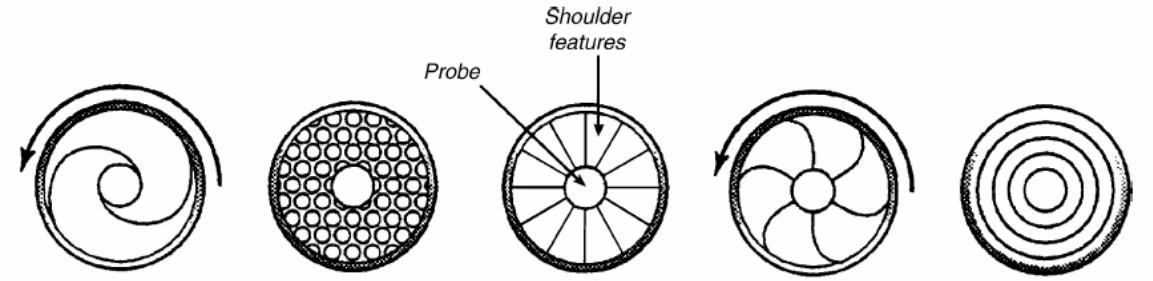

Figure 2.5 Some of the tool shoulder surface features considered by TWI for FSW of various different materials [3]

2.2.2. Tool pin

Friction stir welding tool pin is responsible for the material flow around the tool. Researchers have designed several tool pin geometries to improve the stirring and the material flow during FSW. The important geometrical features of a tool pin are the length, pin diameter/thickness, cross section shape, tapering angle, and surface features. Length of a FSW tool pin is determined by the thickness of the plate to be welded, where the pin length is considered as 90-95% of the plate thickness for near full penetration. The pin cross section shapes experimented are circle, triangle, and square, where circular cross section is the most common tool pin geometry used. Threads on the tool pin vertical surface are added to improve the vertical flow of the material for better mixing. The threads can be circular, spiral or stepped spiral. Some of these tool pin shapes are shown in Figure 2.3. [2]

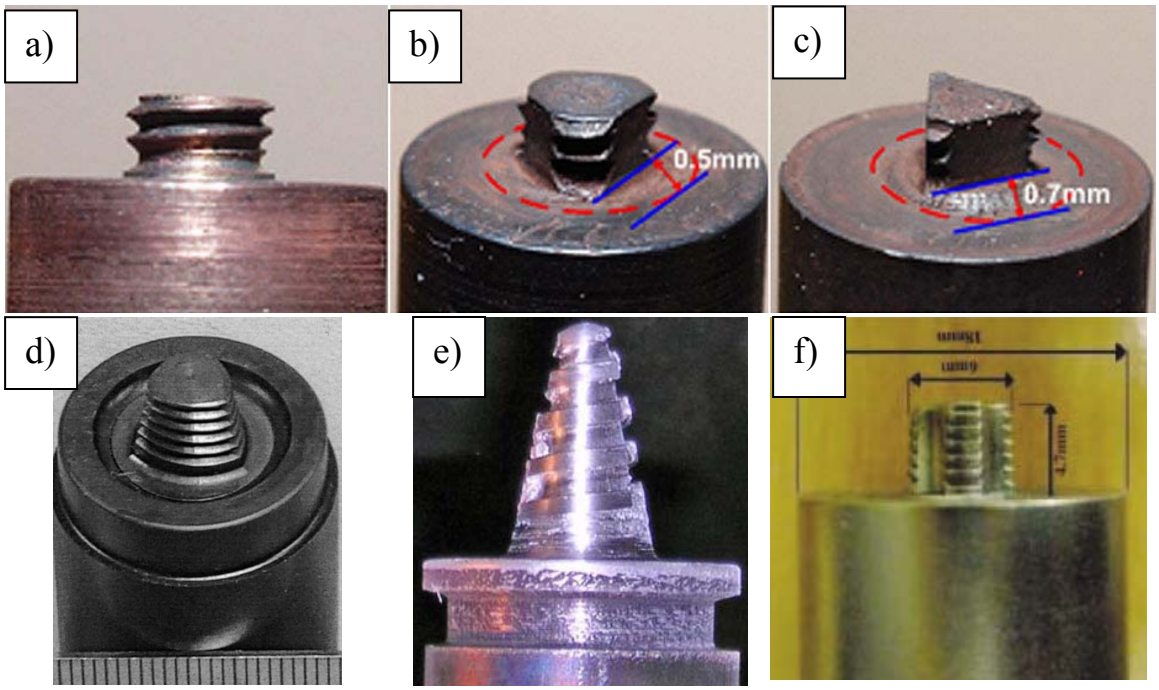

Figure 2.6 Commonly used tool pin geometries (a) cylindrical threaded, (b) three-flat threaded (c) triangular (d) trivex (e) threaded conical1 (f) four-flute threaded pin [2]

Researchers at The Welding Institute (TWI), UK showed that addition of flat surfaces on the tool pin improved the material flow. These flat surfaces added to the tool pin acts as paddle when the pin rotates and thus the material flow improves. Some of the proposed schematic tool pin geometries are shown in Figure 2.4. [3] Since most of these designs are patented by TWI, more research about the performance and life of these tool pins is not currently available.

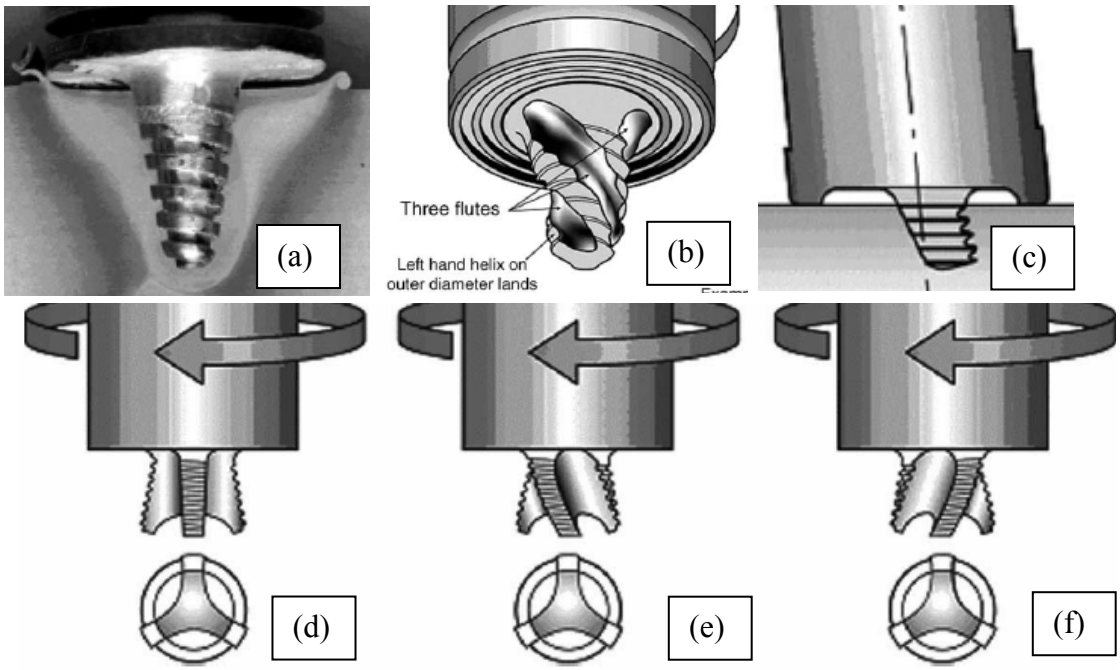

Figure 2.7 Different tool pin geometries proposed by The Welding Institute (a) Whorl^{TM} (b) MX Triflute^{TM} (c) A-Skew^{TM} (d) Flared-Triflute – neutral flute, (e) Flared-Triflute – left hand flutes and (f) Flared-Triflute – right hand flute [3]

The geometrical profile of the tool pin affects the material flow in the stir zone (SZ) of friction stir welds. This material flow determines the defects in the welds and the mechanical properties of the welds. Fujii et al [12] used three tool pin profiles to weld three types of aluminum alloys 1050-H24, 6061-T6, 5083-O to examine the effect of tool pin profile on the weld mechanical properties. As shown in Figure 2.7, the cylindrical tool with threads obtained the best weld mechanical properties in 1050-H24 welds. For revolutionary pitch (tool advance per rotation) of 0.2 and small, the UTS of the weld made with the threaded tool was same as for the weld made with the tool without thread. However, as the revolutionary pitch increased, larger defects were found in the welds made using tool without thread. Thus the UTS of the weld made by threaded tool was measured to be higher than the one for the tool without threads. In case of triangular tool pin of defects were very large except when the revolutionary pitch was near 0.25 mm/rpm, when the defects were small. This means that the strength of the welds made with triangular pin was small at all revolutionary pitch except at 0.25 mm/rpm. [12]

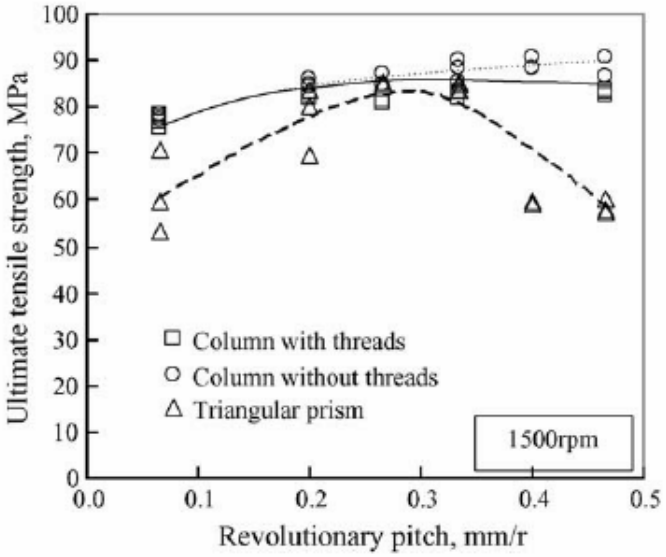

Figure 2.8 Ultimate tensile strength of 1050-H24 friction stir welds [12]

Hirasawa et. al [84] studied the plastic flow during friction stir welding for various tool geometries using particle movement method. They [84] showed that the shape of the hook, which is a material formation near the edge of tool shoulder, can be estimated by the numerical calculations. They [84] concluded that the triangular pin tool results in enhanced material flow that results in suppressed upward rising hook geometry. Badrinarayan et. al [83] studied the effect of tool pin geometry during friction stir spot welding of AA5754-O. They [83] showed that the welds made using the tool with triangular pin had cross tension strength almost twice of the same for welds made using tool with circular pin. Elangovan and Balasubramanian [85] considered various tool pin profiles to study the effect on the friction stir processing zone and showed that for all considered welding speeds the tools with a square pin profile resulted in defect free welds.

2.3. Thermo-mechanical environment around FSW tool

FSW results in severe plastic deformation of the workpiece around the tool and friction between the tool and the workpiece. These two factors generate heat and contribute to the increase in workpiece temperatures in and around the stir zone. The

temperature distribution in the workpiece around the tool affects the material properties which determine the stresses on the tool during FSW. Temperature measurement in the stir zone during FSW is very difficult, since the thermocouples applied would move away with the deforming material. Most of the experimental measurements of the workpiece temperatures have been near the tool shoulder edge. The development of numerical models have helped to better understand the temperature distributions in the stir zone and thermo-mechanically affected zone during FSW.

Mahoney et al [86] welded 6.35mm thick plates of AA7075-T651 using FSW and measured the temperature distribution as function of the distance from the end of the stir zone. These temperatures were measured at the surface and through the thickness of the workpiece material. Figure 2.1 shows the peak temperatures, in °C, as function of the distance from the nugget and distance from the top surface. The measured temperatures are highest near the FSW nugget and decreases away from the FSW nugget. [86]

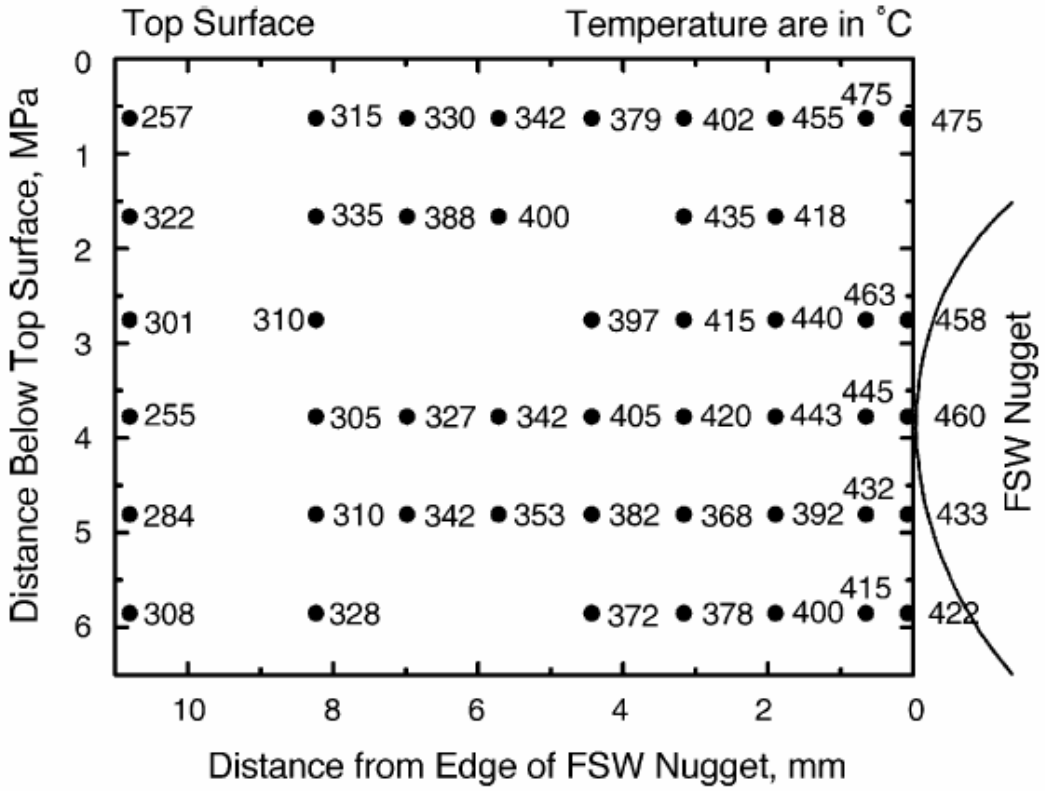

Figure 2.9 Distribution of teak temperature near the tool in FSW of 7075Al-T651. The line on the right side of figure shows the weld nugget boundary. [86]

Nandan et al [87] used a three dimensional heat transfer and visco-plastic flow model to calculate the temperatures during FSW of AA6061. The computed temperatures for welding speed of 1.59 mm/s and tool rotational speed 344 rpm are shown in Figure 2.8. The three planes shown in Figures (a), (b) and (c) are longitudinal section, transverse section and top surface planes, respectively. The tool axis is represented by the origin (x=0 and y=0) for the calculation grid. In Figure 2.8(a), the temperature is maximum near the welding tool at the top surface, and decreases with the distance from the tool axis. The computed temperatures in the transverse section, Figure 2.8(b) show an asymmetry in the temperatures around the tool. The temperatures in the advancing side are relatively higher compared to the temperatures in retreating side. According to the definition, the direction of tool linear velocity and rotational velocity are in the same direction in advancing side and are in opposite direction in retreating side. Since the heat generated at the interface is proportional to the tool-workpiece relative velocity, more heat is generated at the tool workpiece interface. Thus the temperatures around the tool axis show an asymmetry. In figure 2.8(c) the calculated temperatures show the effect of linear velocity, where the temperature contours are densely populates in front of the tool and are sparsely distributed behind the tool. [87]

The temperatures during FSW are affected by welding variables, such as tool rotational speed, welding velocity, axial pressure. The heat generation rate increases with increase in rotational speed, and axial pressure, thus resulting in higher temperatures during FSW. Higher welding velocity will result in lower heat input per unit length and thus the temperatures would decrease. Figure 2.9 shows the effect of tool rotational speed on the peak temperatures during FSW of AA6063. [88]

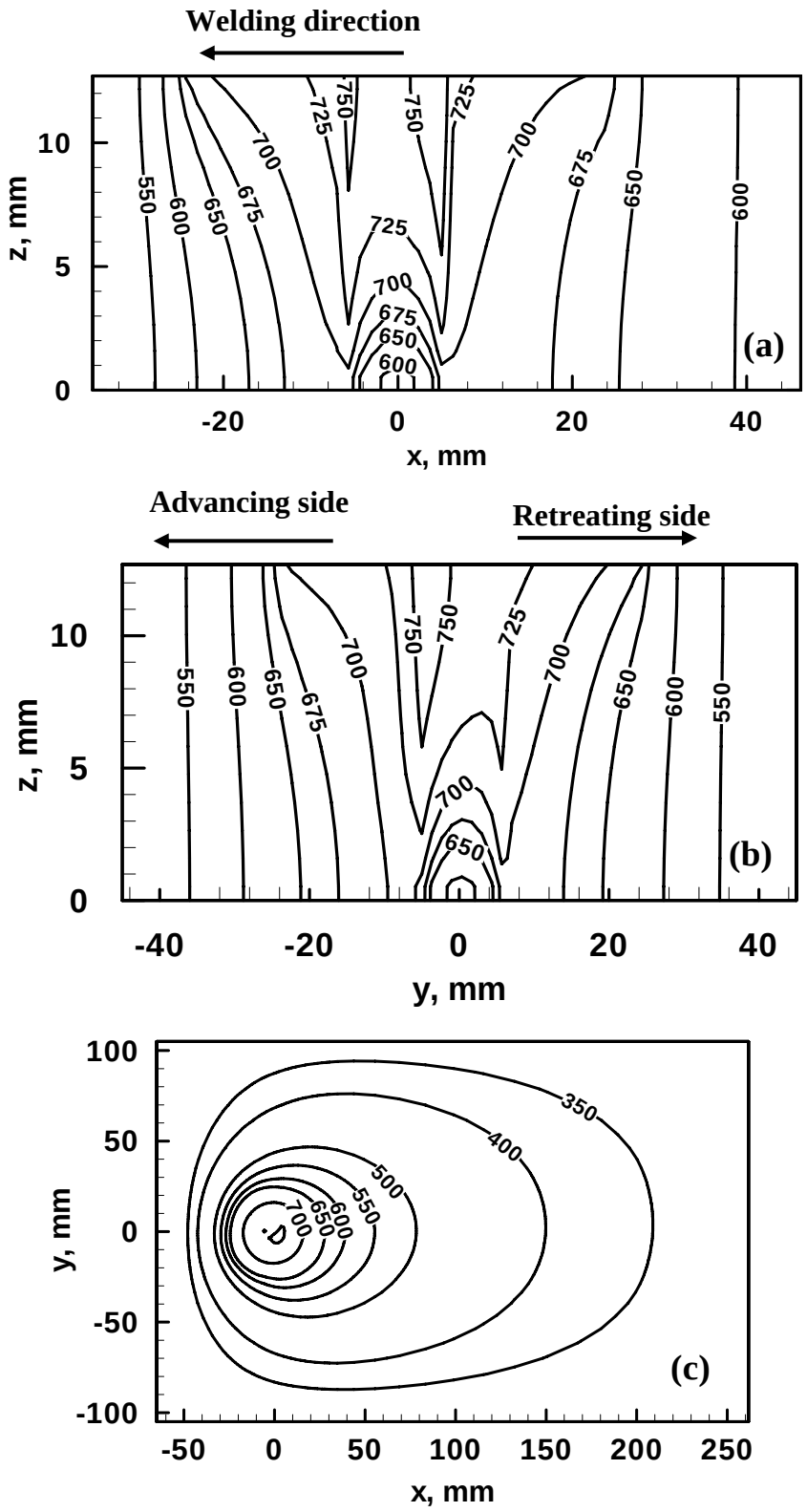

Figure 2.10 Computed values of temperature, in K, in three different planes for FSW of AA6061 (a) XZ (longitudinal section), (b) YZ (transverse section) and (c) XY (top surface). The welding velocity is 1.59 mm/s and tool rotational speed is 344 rpm. [87]

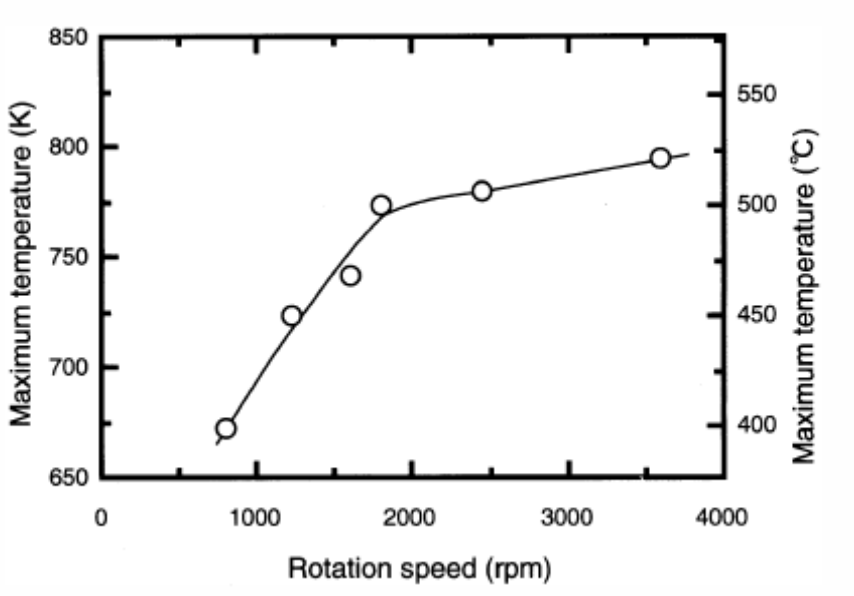

Figure 2.11 Peak temperatures as function of tool rotational speed for FSW of AA6063. [88]

Workpiece material resists any movement of the FSW tool, either rotational or linear, during welding. The resistance to the tool rotational movement is measured as the torque on the FSW tool. Torque on the tool is much higher at the start of the process when the tool comes into contact and is inserted into the workpiece (plunge phase). As the workpiece is heated subsequently (dwell phase), the torque decreases with time. Gemme et al [89] measured the torque during FSW of 2 mm thick AA7075-T6 plates. They used a smooth concave shoulder tool with a flat fixed FSW pin. The measurement of torque was made at three tool rotational speeds, 600, 900 and 1200 rpm. These torque values recorded are shown in Figure 2.12. [89] They showed that the torque increases as the tool in inserted in the workpiece, and is maximum during the plunge phase. During dwell phase, as the continuous rotation of FSW generates more heat the workpiece softens and thus the torque continuously decreases during dwell phase. This value of torque reaches a plateau in around 16-18 seconds, beyond which the torque is at its lowest value and does not decrease anymore with time. The process can be considered as a steady state process beyond this point in time. Figure 2.12 also shows the effect of tool rotational speed on the measured values of torque during FSW of AA7075-T6. Since more heat is generated at higher tool rotational speeds, as tool rotational speed increases the measured torque decreases.

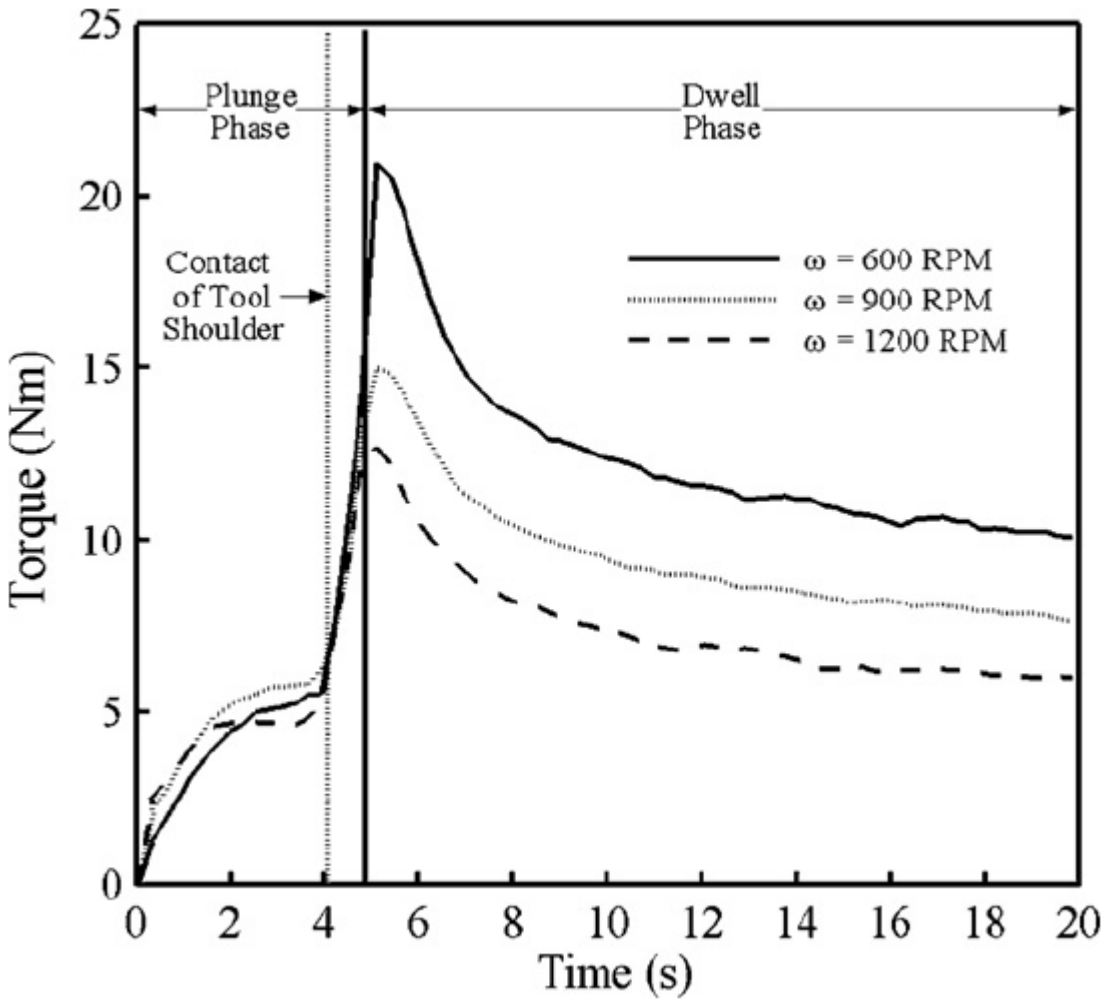

Figure 2.12 measured values of torque as function of time for three different tool rotational speeds. [89]

Yan et al [90] also measured torque during FSW of AA2524-T351 as function of the tool rotational speed and welding speed. Figure 2.13(a) shows the effect of tool rotational speed on the torque during FSW of AA2524-T351 at welding speed of 2.11 mm/s and axial force of 43.2kN. The torque continuously decreases with increase in tool rotational speed. Decrease in the torque is far more at low rotational speeds compared to high rotational speeds. Figure 2.13(b) shows the effect of welding velocity on the torque at tool rotational speed of 300 rpm and axial force of 43.2kN. As the welding speed increase, there is very small increase in the measured value of torque for FSW of AA2524-T351. [90]

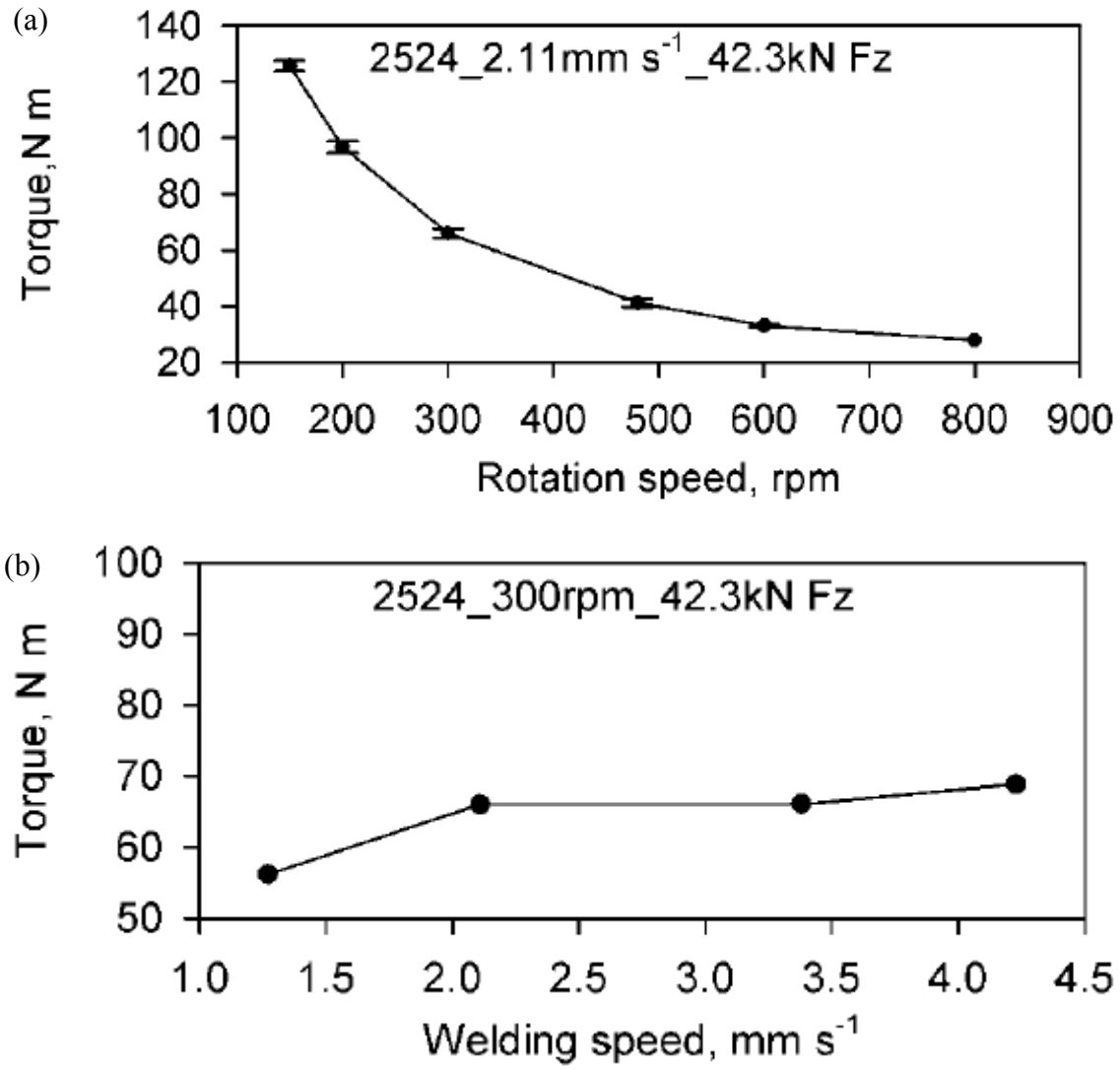

Figure 2.13 Measured values of torque during FSW of AA2524-T351 as function of (a) tool rotational speed and (b) welding velocity. [90]

Linear motion of the FSW tool experiences resistance from the workpiece material in form of force, this force is called traverse force. The traverse force opposes the linear motion of the tool along the weld line and is thus is opposite to the direction of the tool movement. Yan et al [90] measured the traverse force for FSW of AA2524-T351 alloy for various welding velocities when the tool rotational speed is 300 rpm and axial force is 42.3kN. The measured values of traverse force as function of the welding velocity is shown in Figure 2.14. [90] Since the amount of heat generated decreases with increase in welding velocity, the traverse force increases with increase in welding velocity.

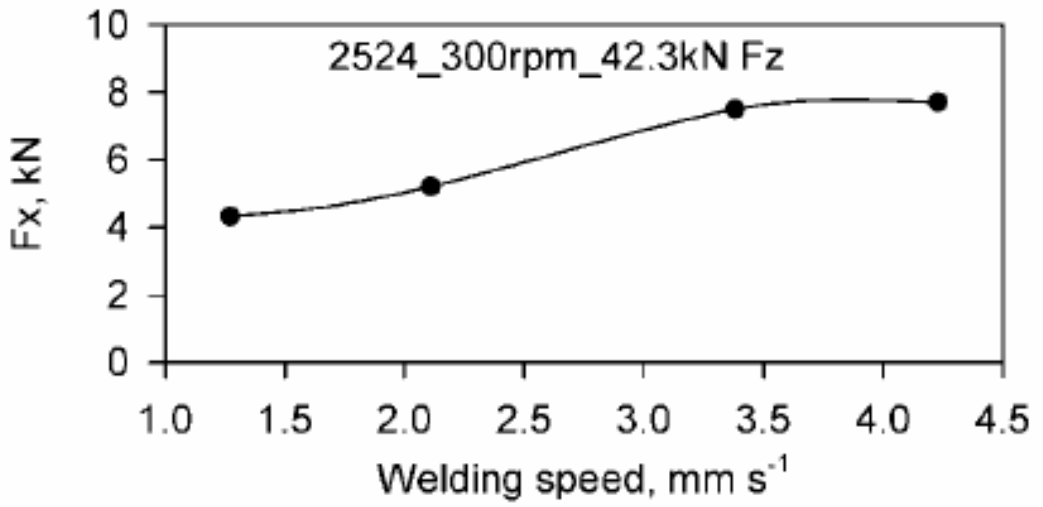

Figure 2.14 Measured values of traverse force (Fx), kN, as function of the welding speed for FSW of AA2524-T351. [90]

2.4. Selection of important unanswered questions

Friction stir welding is commercially being adopted as common method of joining aluminum and other soft alloys. However, the commercial application of this technique to join other hard materials is still not common. [1-2] Understanding of the thermo-mechanical conditions around FSW tools is required to develop reliable and long lasting FSW tools for welding of hard alloys. Heat transfer and visco-plastic flow model has been developed to understand the heat generation and material flow during FSW, however, important questions related to thermo-mechanical conditions around tool still remain unanswered. The following is a selection of important unanswered questions that are addressed in the present thesis study.

(A) Optimal tool shoulder diameter

In FSW, tool shoulder is major source of the heat generation and significantly affects the plastic flow of workpiece material. Experimental measurement of weld properties as function of the tool shoulder diameter has shown possibility of an optimal tool shoulder diameter in FSW. [81] It is important to understand the origin of such an optimal tool shoulder diameter and if this optimal shoulder can be estimated using heat transfer and visco-plastic flow model for FSW.

In order to answer these questions, a numerical model is developed to calculate the sticking and sliding torque components during FSW. The computed values of sticking torque are analyzed to determine the effect of tool shoulder diameter on tool grip on the workpiece material. An objective function is proposed for calculation of optimal tool shoulder diameter and computed values of the objective function are presented for FSW of AA7075 and AA6061.

(B) Load bearing ability of the tool pin

Severe degradation of the tool pin during FSW limits the reliable, long term use of the FSW tool for welding of hard alloys. The mechanical degradation of the tool pin results from the stresses on the pin during FSW. The maximum shear stress on the tool pin is computed due to both bending and torsion. It is important to answer the following questions: (1) Can numerical model estimate the stresses on the tool pin because of both bending and torsion, (2) how does the maximum shear stress vary as function of the tool pin dimensions, (3) can the computed maximum shear stress explain few tool pin degradation cases reported in literature.

A numerical model to calculate the traverse force on the tool is developed and tested against the available experimental results. The numerical models to calculate torque and force on the tool pin are used to compute the stresses on the tool pin due to both bending and torsion. The computed maximum shear stress is shown to be a much higher fraction of the temperature dependent shear strength of the tool material for the reported FSW tool pin degradation.

(C) Artificial neural network for FSW

Artificial neural networks have been developed to understand the complex relationships of input and output variables for various welding process. The thermo-mechanical conditions around the FSW tool are complex functions of important input variables parameters, such as tool shoulder radius, pin radius, pin length, tool rotational speed, welding velocity and axial pressure. The important questions to be answered are: (1) can ANN models be developed to exhibit the complex relationship between input and output variables for FSW, (2) can the developed ANN models explain various thermo-

mechanical conditions around FSW tool for a vast range of input parameters, (3) how can these ANN models be used to develop tool durability maps for FSW.

In order to answer these questions, several ANN models are developed to predict the thermo-mechanical conditions, such as total torque, sliding torque, sticking torque, traverse force, peak temperature, maximum shear stress and bending stress during FSW. These models are used to explain the trends of some of these output variables as function of vast range of input variables. These developed ANN models are used to develop tool durability maps where contours of calculated safety factor are plotted for large range of input parameters.

(D) Strains and strain rates

The strains and strain rates during FSW affect the grain structure and weld properties for friction stir welds. These calculated values will also be useful to estimate the material properties of the plastically deformed material. The material flow velocities computed from the heat transfer and visco-plastic flow model are used to calculate the strain rates during FSW. The calculated strain rates are integrated along the streamlines to estimate the strain values in the workpiece material.

(E) Simplified models

Along with phenomenological models, simple but insightful models exist for fusion welding processes. In case of FSW, simplified models can developed to explain some of the thermo-mechanical conditions. Simplified models are developed for quick estimation of important FSW parameters, such as material flow fields, peak temperature and torque. The material flow fields are estimated by adopting an existing analytical model for the steady state flow of incompressible fluid between two discs, one rotating and other stationary. The non-dimensional peak temperature is estimated as function of non-dimensional heat input, which is calculated from the available welding variables and material properties. The torque is calculated as integration of the total shear stress on the tool shoulder-workpiece surface.

2.5. References

1. R. Nandan, T. DebRoy, H.K.D.H. Bhadeshia, Prog Mater Sci 53(2008) 980-1023.
2. R. Rai, A. De, H.K.D.H. Bhadeshia, T. DebRoy, Sci Technol Weld Join 16(2011) 325-342.
3. R.S. Mishra, Z.Y. Ma, Mater Sci Eng R 50(2005) 1-78.
4. N. Sun, Y. H. Yin, A. P. Gerlich, T. H. North, Sci. Technol. Weld. Join. 8(2009) 747-752.
5. S. M. Chowdhury, D. L. Chen, S. D. Bhole, X. Cao, Mater. Sci. Eng. A 527(2010) 6064-6075.
6. Y. H. Yin, N. Sun, T. H. North, S. S. Hu, Sci. Technol. Weld. Join.15(2010) 81-86.
7. G. Padmanaban, V. Balasubramanian, Mater. Des. 30(2009) 2647-2656.
8. X. Cao, M. Jahazi, Mater. Des. 32(2011) 1-11.
9. N. A. Rodriguez, E. Almanza, C. J. Alvarez, L. E. Murr, J. Mater. Sci. 40(2005) 4307-4312.
10. O. Lorrain, V. Favier, H. Zahrouni, D. Lawrjaniec, J. Mater. Process. Technol. 210(2010) 603-609.
11. K. Kumar, S. V. Kailas, T. S. Srivatsan, Mater. Manuf. Processes 23(2008) 189-195.
12. H. Fujii, L. Cui, M. Maeda, K. Nogi, Mater Sci Eng A 419(2006) 25-31.
13. H. Badarinarayan, Y. Shi, X. Li, K. Okamoto, Int. J. Mach. Tools Manuf 49(2009) 814-823.
14. H. Atharifar, D. C. Lin, R. Kovacevic, J. Mater. Eng. Perform. 18(2009) 339-350.
15. C. D. Sorensen, A. L. Stahl, Metall. Mater. Trans. B 38(2007) 451-459.
16. P. A. Colegrove, H. R. Shercliff, Sci. Technol. Weld. Join. 9(2004) 345-351.
17. D. Bakavos, P. B. Prangnell, Sci. Technol. Weld. Join., 2009, 14, (5), 443-456.
18. 1P. A. Colegrove, H. R. Shercliff, Sci. Technol. Weld. Join. 8(2003) 360-368.
19. A. Scialpi, L. A. C. De Filippis, P. Cavaliere, Mater. Des. 28(2007) 1124-1129.
20. Y. Zhang, Y. S. Sato, H. Kokawa, S. H. C. Park, S. Hirano, Mater. Sci. Eng. A 488(2008) 25-30.
21. K. Reshad Seighalani, M. K. Besharati Givi, A. M. Nasiri, P. Bahemmat, J. Mater. Eng. Perform. 19(2010) 955-962.
22. P. Edwards, M. Ramulu, Sci. Technol. Weld. Join. 14(2009) 669-680.
23. W. B. Lee, C. Y. Lee, W. S. Chang, Y. M. Yeon, S. B. Jung, Mater. Lett. 59(2005) 3315-3318.
24. S. Mironov, Y. S. Sato, H. Kokawa, Mater. Sci. Eng. A 527(2010) 7498-7504.
25. P. Edwards, M. Ramulu, J. Eng. Mater. Technol. (ASME) 132(2010) Article# 031006.
26. P. D. Edwards, M. Ramulu, Sci. Technol. Weld. Join. 14(2009) 476-483.
27. P. Edwards, M. Ramulu, Sci. Technol. Weld. Join. 15(2010) 468-472.

28. H. Liu, K. Nakata, N. Yamamoto, J. Liao, Sci. Technol. Weld. Join. 15(2010) 428-432.
29. A. P. Reynolds, E. Hood, W. Tang, Scr. Mater. 52(2005) 491-494.
30. L. Zhou, H. J. Liu, P. Liu, Q. W. Liu, Scr. Mater. 61(2009) 596-599.
31. K. E. Knipling, R. W. Fonda, Scr. Mater. 60(2009) 1097-1100.
32. Y. S. Sato, H. Yamanoi, H. Kokawa and T. Furuhara, Scr. Mater. 57(2007) 557-560.
33. Y. S. Sato, T. W. Nelson, C. J. Sterling, R. J. Steel and C. O. Pettersson, Mater. Sci. Eng. A 397(2005) 376-384.
34. M. Santella, Y. Hovanski, A. Frederick, G. Grant and M. Dahl, Sci. Technol. Weld. Join. 15(2010) 271-278.
35. S. Park, Y. Sato, H. Kokawa, K. Okamoto, S. Hirano and M. Inagaki, Metall. Mater. Trans. A 40(2009) 625-636.
36. Y. Hovanski, M. L. Santella and G. J. Grant, Scr. Mater. 2007, 57, (9), 873-876.
37. Y. S. Sato, N. Harayama, H. Kokawa, H. Inoue, Y. Tadokoro and S. Tsuge, Sci. Technol. Weld. Join 14(2009) 202-209.
38. M. I. Khan, M. L. Kuntz, P. Su, A. Gerlich, T. North and Y. Zhou, Sci. Technol. Weld. Join. 12(2007) 175-182.
39. T. Weinberger, N. Enzinger and H. Cerjak, Sci. Technol. Weld. Join. 14(2009) 210-215.
40. P. Reynolds, W. Tang, T. Gnaupel-Herold and H. Prask, Scr. Mater. 48(2003) 1289-1294.
41. D. H. Choi, C. Y. Lee, B. W. Ahn, J. H. Choi, Y. M. Yeon, K. Song, H. S. Park, Y. J. Kim, C. D. Yoo and S. B. Jung, Int. J. Refract. Met. Hard Mater. 27(2009) 931-936.
42. R. Ohashi, M. Fujimoto, S. Mironov, Y. S. Sato and H. Kokawa, Sci Technol Weld Join 14(2009) 221-227.
43. T. J. Lienert, W. L. Stellwag, B. B. Grimmett and R. W. Warke, Weld. J. 82(2003) 1S-9S.
44. L. Cui, H. Fujii, N. Tsuji and K. Nogi, Scr. Mater. 56(2007) 637-640.
45. H. Fujii, L. Cui, N. Tsuji, M. Maeda, K. Nakata and K. Nogi, Mater. Sci. Eng. A 429(2006) 50-57.
46. Y. D. Chung, H. Fujii, R. Ueji and K. Nogi, Sci. Technol. Weld. Join. 14(2009) 233-238.
47. T. Hautala and T. Tianien, Proc. 6th Int. Conf. on 'Trends in welding research', (ed. S. A. David et al.) 324(2003)
48. L. Cederqvist and T. Oberg: Reliab. Eng. Syst. Saf. 93(2008) 1491–1499.
49. C.G. Andersson, R.E. Andrews, in: Proceedings of the First International Symposium on Friction Stir Welding, Thousand Oaks, CA, USA, June, 1999.
50. C.G. Andersson, R.E. Andrews, B.G.I. Dance, M.J. Russell, E.J. Olden, R.M. Sanderson, in: Proceedings of the Second Symposium on Friction Stir Welding, Gothenburg, Sweden, June 2000.
51. T. Hautala, T. Tianien, in: S.A. David, T. DebRoy, J.C. Lippold, H.B. Smartt, J.M. Vitek (Eds.), Proceedings of the Sixth International Conference on

Trends in Welding Research, Pine Mountain, GA, ASM International, 2003, p. 324.
52. W.B. Lee, S.B. Jung, Mater. Lett. 58(2004) 1041–1046.
53. H.S. Park, T.K. Kimura, T. Murakami, Y. Nagano, K. Nakata, M. Ushio, Mater. Sci. Eng. A 371(2004) 160–169.
54. R. A. Prado, L. E. Murr, K. F. Soto, J. C. McClure, Mater. Sci. Eng. A, 2003, 349, (1-2), 156-165.
55. R. A. Prado, L. E. Murr, D. J. Shindo, K. F. Soto, Scr. Mater. 45(2001) 75-80.
56. G. J. Fernandez, L. E. Murr, Mater. Charact. 52(2004) 65-75.
57. H. Nami, H. Adgi, M. Sharifitabar, H. Shamabadi, Mater. Des. 32(2011) 976-983.
58. D. J. Shindo, A. R. Rivera, L. E. Murr, J. Mater. Sci. 37(2002) 4999-5005.
59. S. J. Vijay, N. Murugan, Mater. Des. 31(2010) 3585-3589.
60. S. Gopalakrishnan, N. Murugan, Mater. Des. 32(2011) 462-467.
61. T. P. Chen and W. B. Lin, Sci. Technol. Weld. Join. 15(2010) 279-285.
62. U. Dressler, G. Biallas, U. A. Mercado, Mater. Sci. Eng. A 526(2009) 113-117.
63. Y. C. Chen, K. Nakata, Mater. Des. 30(2009) 469-474.
64. R. Ayer, H. W. Jin, R. R. Mueller, S. Ling, S. Ford, Scr. Mater. 53(2005) 1383-1387.
65. C. P. Cheng, H. M. Lin, J. C. Lin, Sci. Technol. Weld. Join. 15(2010) 706-711.
66. Y. C. Chen, K. Nakata, Mater. Des. 30(2009) 3913-3919.
67. Y. C. Chen, K. Nakata, Sci. Technol. Weld. Join. 15(2010) 293-298.
68. Y. S. Sato, A. Shiota, H. Kokawa, K. Okamoto, Q. Yang, C. Kim, Sci. Technol. Weld. Join. 15(2010) 319-324.
69. M. Fazel-Najafabadi, S. F. Kashani-Bozorg, A. Zarei-Hanzaki, Mater. Des. 31(2010) 4800-4807.
70. A.A.M. da Silva, E. Aldanondo, P. Alvarez, E. Arruti, A. Echeverria, Sci. Technol. Weld. Join. 15(2010) 682-687.
71. R. Heideman, C. Johnson, S. Kou, Sci. Technol. Weld. Join. 15(2010) 597-604.
72. M. Aonuma, K. Nakata, Mater. Sci. Eng. B 161(2009) 46-49.
73. R. S. Mishra, M. W. Mahoney, Friction stir welding and proessing, ASM International, Materials Park, OH USA, 7-35.
74. B. K. Agarwala, B. P. Singh, S. K. Singhal, J. Mater. Sci. 21(1986) 1765-1768.
75. H. Sumiya, S. Uesaka, S. Satoh, J. Mater. Sci. 35(2000) 1181-1186.
76. S. Gimenez, O. Van der Biest, J. Vleugels, 16(2007) 435-445.
77. M. Collier, R. Steel, T. Nelson, C. Sorensen, S. Packer, Thermec'2003, Pts 1-5, 426(2003) 3011-3016.
78. M. P. D'Evelyn and T. Taniguchi, Diamond, Related Materials 8(1999) 1522-1526.
79. C. A. M. Casanova, N. M. Balzaretti, G. Voronin, J. A. H. da Jornada, Diamond and Related Materials 8(1999) 1451-1454.

80. T. K. Harris, E. J. Brookes, C. J. Taylor, Int. J. Refract. Met. Hard Mater. 22(2004) 105-110.
81. Z. Zhang, Y.L. Liu, J.T. Chen, Int J Adv Manuf Technol 45(2009) 889-895.
82. K. Elangovan, V. Balasubramanian, Mater Des 29(2008) 362-373.
83. R. M. Leal, C. Leitao, A. Loureiro, D. M. Rodrigues, P. Vilaca, Mater Sci Eng A 498(2008) 384-391.
84. H. Badarinarayan, Y. Shi, X. Li, K. Okamoto, Int. J. Mach. Tools Manuf. 49 (2009) 814-823.
85. S. Hirasawa, H. Badarinarayan, K. Okamoto, T. Tomimura, T. Kawanami, J Mater Process Technol 210(2010) 1455-1463.
86. K. Elangovan, V. Balasubramanian, J Mater Process Technol 200(2008) 163-175.
87. M.W. Mahoney, C.G. Rhodes, J.G. Flintoff, R.A. Spurling, W.H. Bingel, Metall. Mater. Trans. A 29(1998) 1955.
88. R. Nandan, G. G. Roy, T. DebRoy, Metall. Mater. Trans. A 37(2006) 1247-1259.
89. Y.S. Sato, M. Urata, H. Kokawa, Metal. Mater. Trans. A 33A(2002) 625-635.
90. F. Gemme, Y. Verreman, L. Dubourg, M. Jahazi, Mater. Sci. Eng. A 527(2010) 4152-4160.
91. J. H. Yan, M. A. Sutton and A. P. Reynolds, Sci Techno Weld Join 10(6) (2005) 725–736.

Chapter 3. Optimum friction stir welding tool shoulder diameter

Although friction stir welding (FSW) is now widely used for the joining of aluminum and other soft alloys, its commercial application to hard materials, such as steels and titanium alloys, is still developing. [1-5] An important challenge is to develop reliable cost effective tools with long service life. [1,6] No unified approach for tool design that is based on scientific principles is now available. [1] The current practice for tool design involves the selection and testing of tool materials with higher softening temperatures and tensile strength than those of the workpiece material. This practice does not always lead to the design of optimum tools that would result in good welds.

Most of the previous research on the geometry of the tool has focused on the design of the tool pin. These studies aim to design tool pin for good weld properties. Buffa et al. [7] showed by finite element calculations that an increase in pin taper angle resulted in higher peak temperatures. Fujii et al. [8] showed that a columnar tool pin without any thread resulted in defect free welds in soft alloys, such as AA1050, while a triangular prism shaped tool pin was appropriate for hard alloys, such as AA5083. Kumar and Kailas [9] suggested that the material flow induced by the pin is important to achieve a cavity-free weld joint. Zhao et al. [10-11] showed that a threaded tapered pin profile produced welds with minimum defects in AA2014. Hattingh et al. [12] suggested a relation between the thread pitch, pin diameter and the plate thickness to achieve sound welds for tri-fluted tapered pins. Thomas et al. [13-14] suggested that the tapered threads in Whorl^{TM} pin design induce a vertical material flow. Furthermore, the larger surface of the MX Triflute^{TM} tool leads to higher heat generation rates and improved material flow. [13-14] Colegrove and Shercliff [15-16] suggested that the Triflute pin increased the downward material flow based on modeling. Although the role of pin geometry has been addressed in several studies, the effect of the tool shoulder geometry during FSW is not well understood.

Among the various geometric features of an FSW tool, the size of the shoulder is by far the most important. [1,6] The shoulder generates most of the heat, induces flow of

plasticized materials and prevents its escape from the work piece during welding. [3-5] The stronger the work piece material, the greater is the need for the shoulder to generate heat for adequate softening and ease of material flow around the tool pin. [1,6-17] Larger shoulder diameter also requires higher spindle power and torque. In order to achieve a long tool life, the tool shoulder should facilitate adequate softening and ease of flow of workpiece materials while requiring low power and torque. A unified method to determine the optimum shoulder diameter considering such contrasting requirements has not been reported so far in literature.

Zhang [18], using a commercial finite element software, suggested that larger shoulder diameters would result in higher peak temperatures. The shoulder roughness is also thought to be important in preventing the escape of flush from the weld. [19-20] Elangovan and Balasubramanian [21] studied the effect of tool shoulder diameter on the mechanical properties of welds and found that one of the three diameters resulted in superior weld tensile properties during FSW of AA6061. Although the reason for this behavior is not well understood, it was found that welds with the best properties corresponded to the maximum utilization of the supplied torque in overcoming sticking. [22-23] In short, the previous research [18-23] has established the importance of shoulder geometry in both the operation of the FSW process and the resulting properties of the welded joints. However, an approach for estimating optimum tool shoulder size is not available to the FSW community. Here a criterion that balances the need for low flow stress for good material flow and the contrasting requirement for the tool to have a good grip on the plasticized material is used to identify an optimum shoulder diameter.

3.1. Experiments

FSW machines are large capital intensive machines and are not available in very many places. To analyze the proposed hypothesis of an optimum shoulder diameter an experimental plan was developed in collaboration with researchers Indian Institute of Technology (IIT), Bombay. The experiments were planned in collaboration and were conducted independently at IIT Bombay, India by Mr. Manish Mehta and Prof. Amitava De. Aluminum alloy AA7075-T6 plates 172 mm long, 97 mm wide and 3.5 mm thickness are welded in square butt joint configuration. A 25 mm thick AISI316 back-up

plate is used which reduces the heat loss from the bottom of the workpiece because of its low thermal conductivity (around 16 W/m-K at 100°C and 21 W/m-K at 500°C). Table 3.1 shows the compositions of the work piece and tool materials. Five tools with different shoulder diameters with the same cylindrically tapered pin geometry were used for the welds. Table 3.2 lists the tool shoulder and the pin dimensions. A tool shoulder diameter of 35 mm is selected, since a tool with larger shoulder diameter than 35 mm results in melting of the workpiece material. The tools with shoulder diameter less than 15 mm do not produce a weld. All welds were made with a tool tilt angle of 2°. An axial pressure of 30 MPa is maintained constant to keep the tool shoulder in contact with the workpiece with an average plunge depth of 0.2~0.4 mm. These parameters were selected based on the stable weld formation observed in preliminary experiments. Transient temperature during welding was measured at three monitoring locations, two on the advancing side and one on the retreating side, positioned at a transverse distance of 8.5 mm from the butting surface and depth of 0.75 mm from the top surface. The two K-type thermocouples in the advancing side were kept 50 mm apart in the direction of welding to examine the accuracy of the measured temperature profiles. The tool spindle power was measured using two watt-meters. The torque utilized by the tool was obtained by dividing the spindle power with the corresponding tool rotational speed (radian/s). The ultimate tensile strength, yield strength and percent elongation (at break) were determined from transverse section of the welded specimens.

Table 3.1 Composition of work piece (AA 7075) and tool (EN24) materials [24-25]

AA7075	Element	Al	Cu	Mg	Zn	Cr
	weight (%)	90	1.6	2.5	5.6	0.23
EN24	Element	C	Mn	Ni	Cr	Mo
	weight (%)	0.35~0.45	0.45~0.70	1.30~1.80	0.90~1.40	0.20~0.35

Table 3.2 Tool dimensions, process parameters and material properties used for calculations

Workpiece material	AA 7075
Tool material	EN24 tool steel
Tool shoulder diameter, mm	15, 20, 25, 30, 35
Pin diameter at root, mm	6.0
Pin diameter at tip, mm	4.66
Pin length, mm	3.325
Workpiece thickness, mm	3.5
Tool rotational speed, RPM	355, 450, 560, 710
Welding speed, mm s^{-1}	0.67
Axial pressure, MPa	30.0
Workpiece material	
Solidus temperature, K [24]	749
Density, kg cm^{-3}	2800
Specific heat*, J kg^{-1} K^{-1} [24]	$0.20 - 3.0\times10^{-4}T + 1.0\times10^{-7}T^2 - 3.0\times10^{-12}T^3$
Thermal conductivity*, W m^{-1} K^{-1} [24]	$0.18 + 6.0\times10^{-4}T - 1.0\times10^{-7}T^2$
Yield stress, MPa [25]	$6.97\times10^{3}\times e^{(-0.0087\times T)}$ for $T < 644$ K $0.245\times(749-T)$ for $644 < T < 749$ K
Tool material	
Density, kg cm^{-3} [25]	7860
Specific heat*, J kg^{-1} K^{-1} [25]	460
Thermal conductivity*, W m^{-1} K^{-1} [25]	25

3.2. Numerical model

The accomplishment of the objectives of this thesis required use of an existing heat transfer and visco-plastic flow model for FSW as the main engine. [26-29] During the research presented in this thesis several new components were added to this model. The model solves the equations of conservation of mass, momentum and energy in three dimensions. The model can successfully estimate the temperature fields, cooling rates, the plastic flow fields, and the geometry of the thermo mechanically affected zone (TMAZ). [26-29] The heat generation in the model is considered as spatially variable and tool design dependent. The heat generated from friction, plastic deformation and viscous dissipation is considered in the model. Temperature dependent properties such as thermal conductivity, specific heat and yield strength and non-Newtonian viscosity as a function of local strain rate are considered in the calculations. The model has been tested for FSW

of various alloys such as AA6061, 1018 Mn Steel, 304L stainless steel and Ti-6Al-4V. [26-29] The numerically computed temperature fields, TMAZ geometry and peak temperatures have been compared with corresponding experimental results to validate the numerical model.

3.2.1. Assumptions

The following assumptions were made in the development of the numerical model:

- The FSW process reaches quasi steady state soon after the beginning. The weld geometry, structure and properties display quasi steady state behavior during the process.
- The FSW tool rotates at a constant rotation speed and maintains a constant plunge depth during welding.
- The material flow is non-Newtonian, incompressible and visco-plastic in nature.
- The maximum shear stress at yielding is $\tau = \sigma_y / \sqrt{3}$, where σ_y is the yield stress.
- Boussinesq's approximation is followed and the density variation is not considered.

3.2.2. Governing equations

The pseudo-steady state temperature and velocity fields are computed by solving the equations of conservation of mass, momentum and energy. An incompressible single phase flow is considered for the solution of these equations. The steady state energy equation can be given as following: [26-29]

$$\rho C_p \frac{\partial (u_i T)}{\partial x_i} = -\rho C_p U \frac{\partial T}{\partial x_1} + \frac{\partial}{\partial x_i}\left(k \frac{\partial T}{\partial x_i} \right) + S_b + S_{in} \qquad (3.1)$$

where i=1,2,3 in represent x, y and z directions, u_i is the material velocity in i^{th}-direction, T is the temperature, ρ is the density, x_i is the distance in i-direction, C_p is the specific heat capacity at constant pressure, U is the welding velocity, k is the thermal conductivity, S_{in} is the interfacial heat generation rate per unit volume and S_b (= $\beta\mu\phi$) is the heat generation rate per unit volume due to plastic deformation in the workpiece away from the interface. The symbol β is the fraction of plastic deformation work dissipating as heat, μ is the non-Newtonian viscosity and the symbol ϕ is given as: [26-29]

$$\phi = 2\sum_{i=1}^{3}\left(\frac{\partial u_i}{\partial x_i}\right)^2 + \left(\frac{\partial u_1}{\partial x_2} + \frac{\partial u_2}{\partial x_1}\right)^2 + \left(\frac{\partial u_1}{\partial x_3} + \frac{\partial u_3}{\partial x_1}\right)^2 + \left(\frac{\partial u_3}{\partial x_2} + \frac{\partial u_2}{\partial x_3}\right)^2 \tag{3.2}$$

The source term due to the interfacial heat generation rate per unit volume at the tool workpiece interface, S_{in}, is calculated as: [26-29]

$$S_{in} = [(1-\delta)\eta\tau + \delta\mu_f P_N](\omega R_P - U \sin\theta)\frac{A_r}{V} \tag{3.3}$$

where δ is the spatially variable fractional slip between the tool and work piece interface, η is the mechanical efficiency, i.e. the fraction of mechanical energy converted into heat, τ is the maximum shear stress for yielding, μ_f is the spatially variable coefficient of friction, P_N is the axial pressure on the interface, ω is the tool rotational speed, R_P is the tool pin radius, A_r is a small area on the interface and V is the control volume enclosing the area A_r. A mechanical efficiency or the fraction of plastic work which is converted to heat is a material dependent parameter which is a complex function of strain, strain rate and temperature and can range from 0.3 to 0.95. [26]

The incompressible flow continuity equation is given as following:

$$\frac{\partial u_i}{\partial x_i} = 0 \tag{3.4}$$

The coordinate system for the solution of the momentum equation is considered such that the origin is attached to the tool axis and is moving with the tool at a constant speed U along the x-axis. The momentum equation for such a coordinate system is given as: [26-29]

$$\rho\frac{\partial u_i u_j}{\partial x_i} = -\frac{\partial P}{\partial x_i} + \frac{\partial}{\partial x_i}\left(\mu\frac{\partial u_i}{\partial x_j} + \mu\frac{\partial u_j}{\partial x_i}\right) - \rho U\frac{\partial u_j}{\partial x_1} \tag{3.5}$$

where P is the pressure. In contrast to the axial pressure P_N on the tool workpiece interface, P is a relative pressure which drives the flow.

The non-Newtonian viscosity μ as function of the strain rate and the temperature can be estimated using the material specific constitutive equations determined by experimental flow stress data. The viscosity, μ, as function of effective flow stress, σ_e and effective strain rate, $\dot{\varepsilon}$, can be calculated using following relation: [26]

$$\eta = \frac{\sigma_e}{3\dot{\varepsilon}} \quad \text{where} \quad \dot{\varepsilon} = \left(\frac{2}{3}\dot{\varepsilon}_{ij}\dot{\varepsilon}_{ij}\right)^{\frac{1}{2}} \text{ and } \dot{\varepsilon}_{ij} = \frac{1}{2}\left(\frac{\partial u_i}{\partial x_j} + \frac{\partial u_j}{\partial x_i}\right) \tag{3.6}$$

The flow stress as function of the temperature and strain rate can be calculated using the Zener-Hollomon relationship as following: [26]

$$\sigma_e = \frac{1}{\alpha}\sinh^{-1}\left[\left(\frac{1}{A}\dot{\varepsilon}\exp\left(\frac{Q}{RT}\right)\right)^{1/n}\right] \tag{3.7}$$

where T is temperature in K, $\dot{\varepsilon}$ is the effective strain rate, and α, A, Q and n are temperature independent material specific constants determined by fitting the constitutive equation for the experimentally determined flow stress values.

3.2.3. Boundary conditions

For the sake of heat generation and distribution, the tool surface is divided in three parts, the tool shoulder, the pin vertical and the pin horizontal surface. The heat generated at the tool shoulder workpiece interface is distributed between the tool and the workpiece. This partition of the generated heat is done on the basis of the thermo physical properties of the two materials.

The ratio, f, of heat entering into the workpiece to the ratio of heat entering into tool is calculated as [26-29]

$$f = \frac{J_W}{J_T} = \frac{(k\rho C_P)_W^{1/2}}{(k\rho C_P)_T^{1/2}} \tag{3.8}$$

where J_W is the portion of the generated heat entering the workpiece, J_T is the portion of the generated heat entering the tool, k is the thermal conductivity, r is the density and C_P is the specific heat. The subscript W represent the properties of workpiece material whereas the subscript T represent the tool material properties. This partition of heat among the tool and the workpiece material is based on their thermo-physical properties. Equation 3.8 assumes steady-state, one-dimensional heat flow from the tool shoulder workpiece interface. Lienert et al. have experimentally tested this expression and have found it to be reliable. [30] The heat flux continuity at the shoulder matrix interface is considered as following: [26-29]

$$k\left.\frac{\partial T}{\partial z}\right|_{top} = \frac{J_W}{J_W + J_T}\dot{q} \qquad \text{in the range} \qquad R_P \le r \le R_S \tag{3.9}$$

where $\dot{q}$ is the rate of heat generation at the shoulder workpiece interface due to both friction and plastic deformation, and is given by: [26-29]

$$\dot{q} = [(1-\delta)\eta\tau + \delta\mu_f P_N](\omega r - U \sin\theta) \tag{3.10}$$

Beyond the shoulder workpiece interface, both convective and radiative heat transfer is considered for heat exchange between the top surface of the workpiece and the surroundings. [26-29]

$$-k\left.\frac{\partial T}{\partial z}\right|_{top} = \sigma\varepsilon(T^4 - T_a^4) + h(T - T_a) \tag{3.11}$$

where σ is the Stefan-Boltzmann constant (5.67×10^{-16} W K^{-4} m^{-2}), ε is the emissivity, T_a is the ambient temperature and h is the heat transfer coefficient at the top surface.

A temperature dependent heat transfer coefficient is considered for the heat transfer into the backing plate from the workpiece: [26-29]

$$k\left.\frac{\partial T}{\partial z}\right|_{bottom} = h_b(T - T_a) \qquad \text{where} \qquad h_b = h_{b0}(T - T_a)^{0.25} \tag{3.12}$$

where h_b is the enhanced heat transfer coefficient at the bottom surface and h_{b0} is a numerical constant.

The numerical model considers spatially variable values of fractional slip and friction coefficient at the tool workpiece interface. The spatial variations of fractional slip, δ, and the coefficient of friction, μ_f, are derived from the trend of the reported data on accumulated slip during cross-wedge rolling as: [31]

$$\delta = 0.2 + 0.6\left(1 - \exp\left(-\delta_0 \frac{\omega r}{\omega_0 R_S}\right)\right) \tag{3.13}$$

$$\mu_f = \mu_0 \exp\left(-\delta_0 \frac{\omega r}{\omega_0 R_S}\right) \tag{3.14}$$

where ω is the tool rotational speed in rad/s and r is distance from tool axis in m, δ_0 and μ_0 are adjustable modeling fitting parameters. Equations (3.13) and (3.14) are valid for ωr from 0.1 to 1.6 m/s. [31]

The boundary values of material velocities at the tool workpiece interface are determined based on the partial slip condition. The x and y component of velocities at the top surface are given as u and v respectively: [26-29]

$$u = (1-\delta)(\omega r \sin\theta - U) \tag{3.15}$$

$$v = (1-\delta)\omega r \cos\theta \tag{3.16}$$

At the shoulder workpiece interface the z component of velocity, w, is assumed to be zero whereas at the tool pin workpiece interface w is given as:

$$w = \psi\omega \tag{3.17}$$

where ψ is the thread pitch. The velocities at all other boundaries are considered to be zero and the temperature at all boundaries is assumed to be 298K.

Apart from the welding variables and material properties the model introduces five modeling parameters in the above equations. The constant for heat transfer coefficient at the bottom surface, h_{b0}, coefficient for slip, δ_0, friction coefficient, μ_0, mechanical efficiency, η, and the fraction of plastic deformational heat generation, β, are the five modeling parameters which are used in this numerical model. The values of these modeling parameters are uncertain because they cannon be prescribed by scientific principles or by straight forward experiments. The values of these parameters were optimized by fitting the available experimental data for the FSW model for various alloys. [26, 32] However, the sensitivity of the four material constants, α, Q, A, n in Equation (3.7) are not yet studied. The sensitivity of these variables is examined in appendix A.

The torque (M) required during FSW is computed as:

$$M = M_T + M_L \tag{3.18}$$

where M_T and M_L are the fractions of the total torque responsible for material flow by overcoming sticking and frictional heating by sliding, respectively. Hereafter, M_T and M_L are referred as sticking torque and sliding torque, respectively, and are computed as follows:

$$M_T = \oint_A r_A \times (1-\delta)\tau \times dA \tag{3.19}$$

$$M_L = \oint_A r_A \times \delta\mu_f P_N \times dA \tag{3.20}$$

where r_A is the distance of any infinitesimal area element, dA, from the tool axis, δ is the spatially variable fractional slip between the tool and work piece interface, τ is the maximum shear stress for yielding, μ_f is the spatially variable coefficient of friction, and P_N is the axial pressure on the interface. As indicated in Equation (3.19), both

components of the torque contribute to heat generation. The spindle power is calculated as follows:

$$P = \omega M \tag{3.21}$$

where ω is the tool rotational speed.

3.3. FSW of AA7075

A three dimensional heat transfer and visco-plastic flow model for FSW is used to calculate the temperature and material velocity distribution. Figure 3.1 shows a comparison between the computed and the corresponding measured values [23] of peak temperatures at various shoulder diameters for rotational speeds of 355 and 560 RPM. The peak temperatures are measured at 8.5 mm away from the tool center and 7.5 mm below the top surface where the thermo couples are located in the experiments. The tool dimensions, welding conditions and material properties used for the calculation are presented in Table 3.2. It is observed that the peak temperature increases with increase in shoulder diameter and tool rotational speed. A larger shoulder diameter provides greater contact area resulting in higher frictional and mechanical work, thus leading to higher temperatures. Both the computed and the experimental temperatures also show that the effect of shoulder diameter is more pronounced than that of the rotational speed.

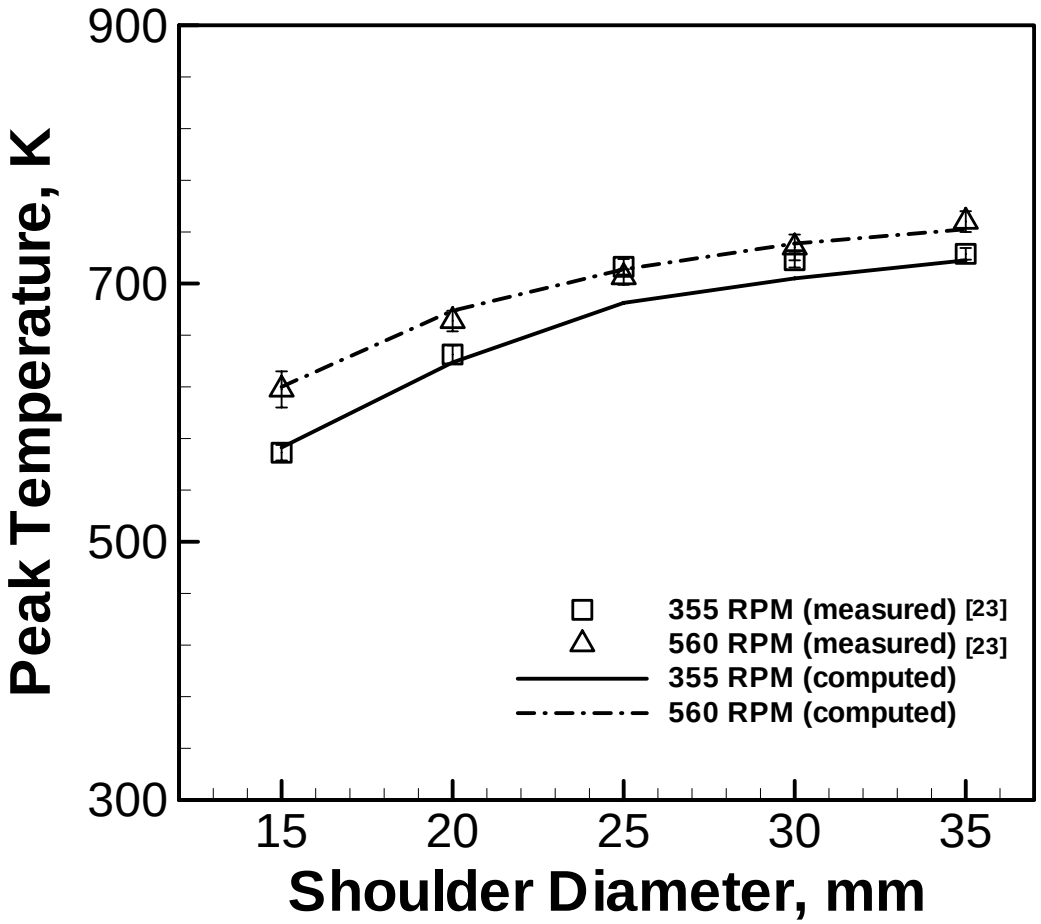

Figure 3.1 Comparison of the measured and computed peak temperatures during FSW of AA7075-T6 at rotational speeds of 355 and 560 RPM. The error bars shown represent the error in measurement estimated by repeated experimental measurements. [23]

Figure 3.2 shows a comparison between the experimentally measured and the corresponding computed thermal cycles for a tool shoulder diameter of 20 mm and a rotational speed of 355 RPM. A fair agreement between the computed and the corresponding measured peak temperature and thermal cycles indicates that the model is capable of predicting these variables correctly for FSW of AA7075 alloy.

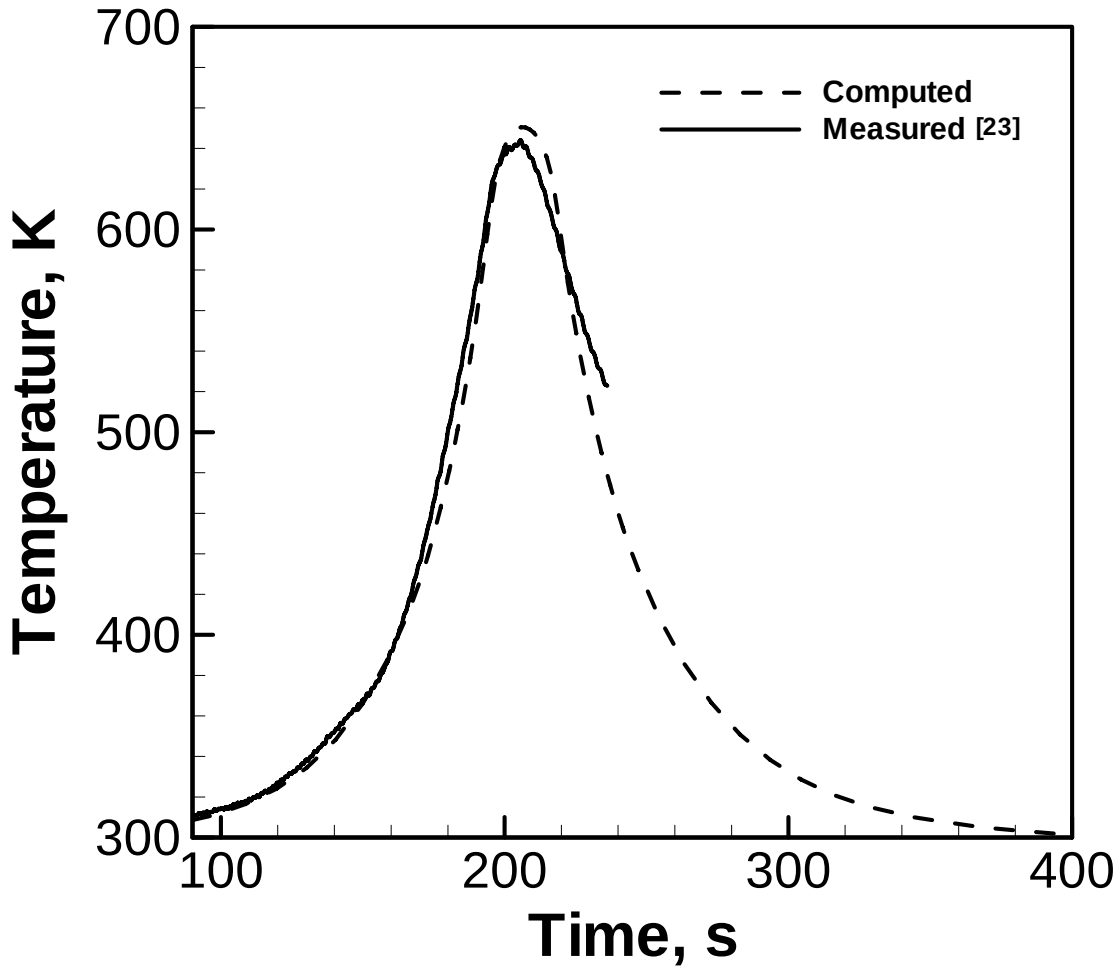

Figure 3.2 Comparison of the computed and the measured time-temperature profile at a location 8.5 mm away from the butting surface and 0.75 mm from the top surface in the advancing side for the friction stir welding of AA7075-T6 with a 20 mm shoulder diameter tool at 355 RPM. [23]

Figures 3.3 shows a comparison of the computed and the corresponding measured torque required during FSW of AA7075. The torque increases with increase in the shoulder diameter and decrease in the rotational speed. The effect of rotational speed is more prominent at larger shoulder diameters. Increase in the tool-workpiece contact area with shoulder diameter leads to a higher torque requirement as shown in Equations (3.19) and (3.20). The fractional slip, δ, increases significantly with rotational speed and shoulder radius. However, the friction coefficient, μ_f, decreases exponentially as fractional slip, rotational speed and shoulder diameter increase. With increase in rotational speed the fractional slip increases and, as a result, the sticking torque decreases

significantly. The increased rotational speed and fractional slip also leads to lower friction coefficient and reduction in sliding torque.

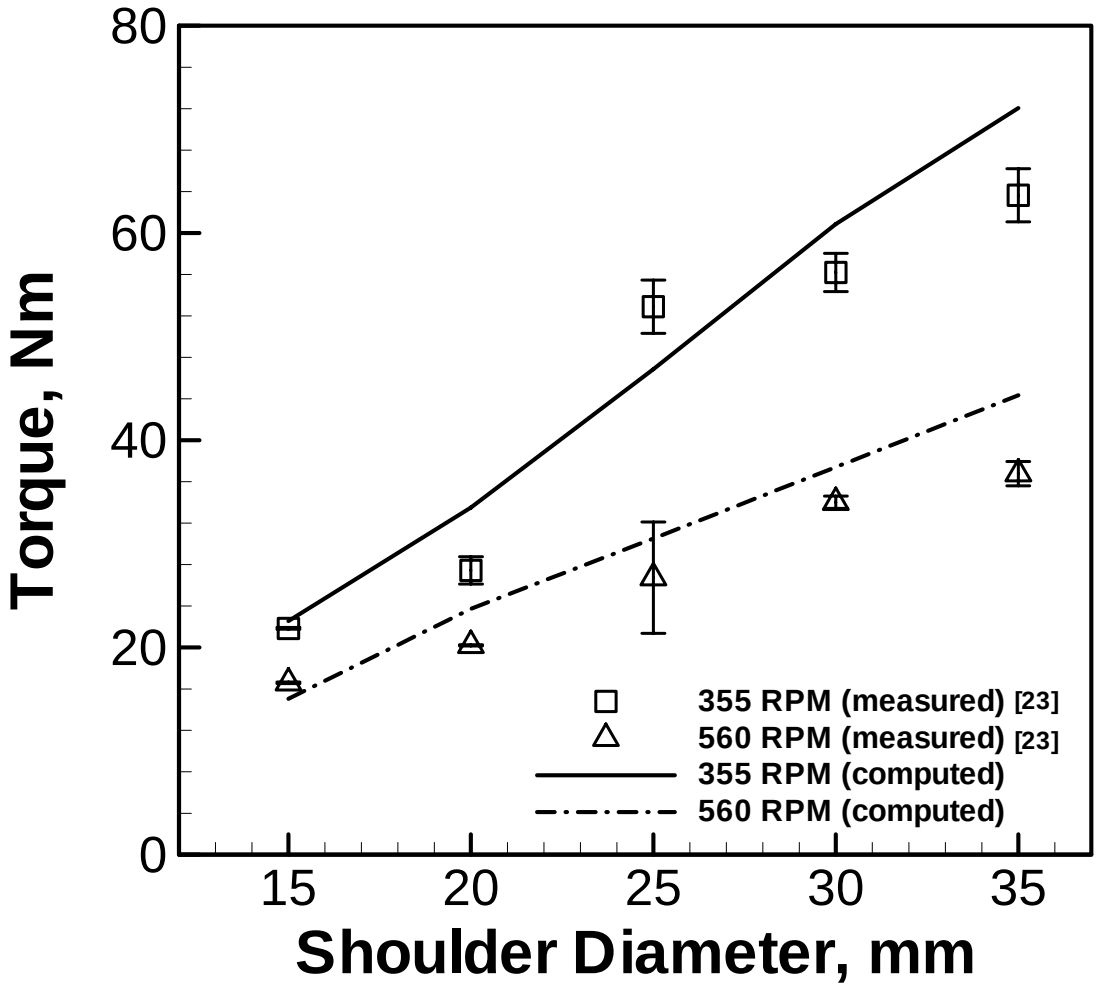

Figure 3.3 Comparison of the measured and computed torque required for FSW of AA7075-T6 at rotational speeds of 355 and 560 RPM. The error bars shown represent the error in measurement estimated by repeated experimental measurements. [23]

Figure 3.4 shows the computed and the corresponding measured values of spindle power as function of shoulder diameter. The power requirement increases with shoulder diameter due to increase in the tool workpiece contact area. In contrast, there is no significant effect of rotational speed on the spindle power. Figures 3.3 and 3.4 show a fair agreement between the measured and the corresponding computed values of torque and power required for welding. Friction stir welding is a very complex process and the measurement of temperatures and torques are very difficult. The numerical model for FSW considers unknown variables whose values cannot be experimentally measured and

must be estimated through the application of complex optimization schemes. The difference in the measured and the computed values can arise from either experimental inaccuracies or inaccuracies in the values of the numerical model unknown variables.

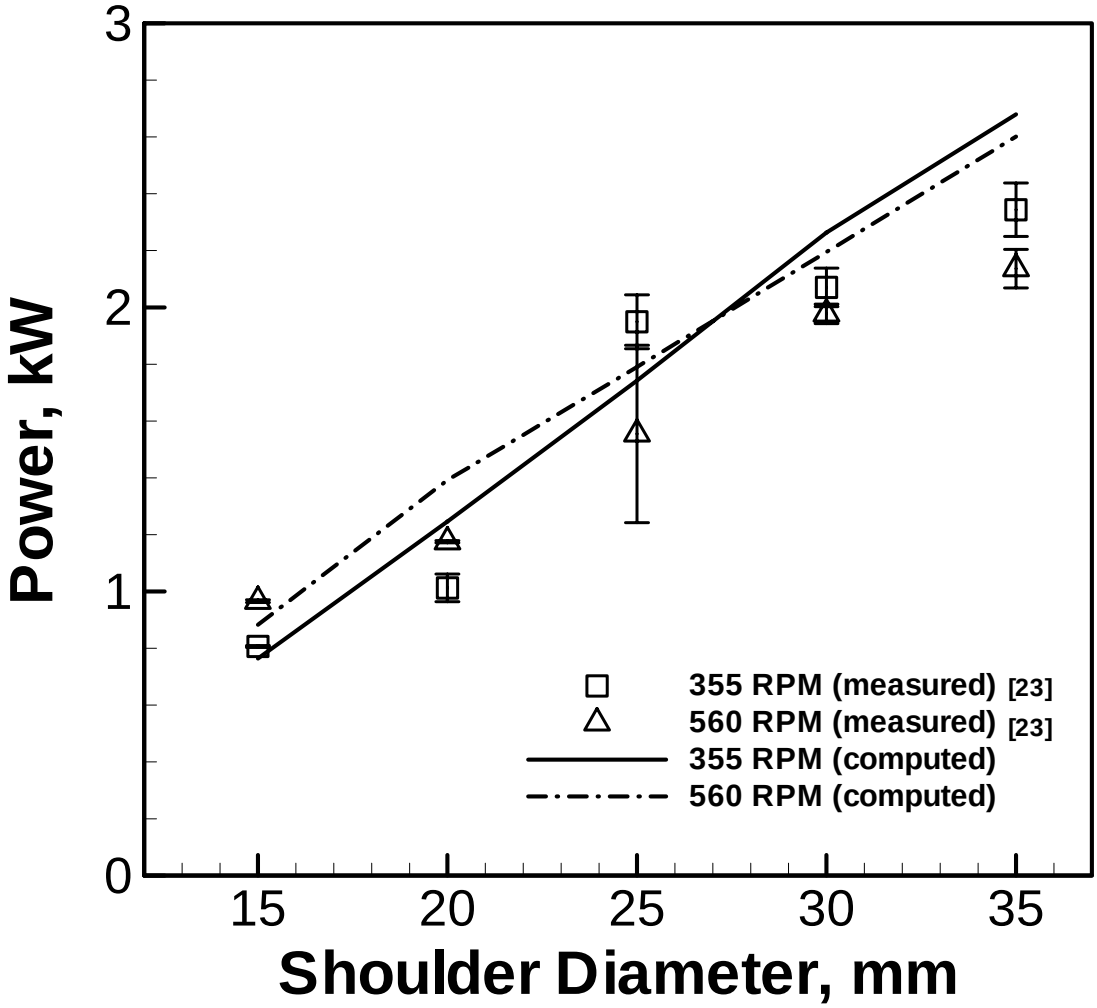

Figure 3.4 Comparison of the measured and computed power required for FSW of AA7075-T6 at rotational speeds of 355 and 560 RPM. The error bars shown represent the error in measurement estimated by repeated measurements. [23]

The tool life is affected by the flow stress and temperature of the deforming material near the tool. [33-34] The volume averaged characteristic flow stress, σ_z, and temperature, T_z, of the deforming material can be calculated as:

$$\sigma_z = \frac{\sum \sigma \times V}{\sum V} \tag{3.22}$$

$$T_z = \frac{\sum T \times V}{\sum V} \tag{3.23}$$

where, σ and T are the flow stress and temperature of a location in the deforming zone, respectively and V is the corresponding cell volume. Figure 3.5 shows the characteristic flow stress and temperature combinations experienced by the deforming material at various shoulder diameters and rotational speeds. It is observed that the characteristic temperature increases with increase in shoulder diameter. This trend is similar to the observed trend in the peak temperature with shoulder diameter shown in Figure 3.1. Consequently the characteristic flow stress reduces with increase in shoulder diameter. Figure 3.5 suggests lower resistance to a larger shoulder diameter tool during deformation of the work piece material. However, the torque required is comparatively higher for larger shoulder diameter tools as shown in Figure 3.3. Thus, when the shoulder diameter is increased, the lower resistance to deformation is achieved at the expense of higher total torque requirement.

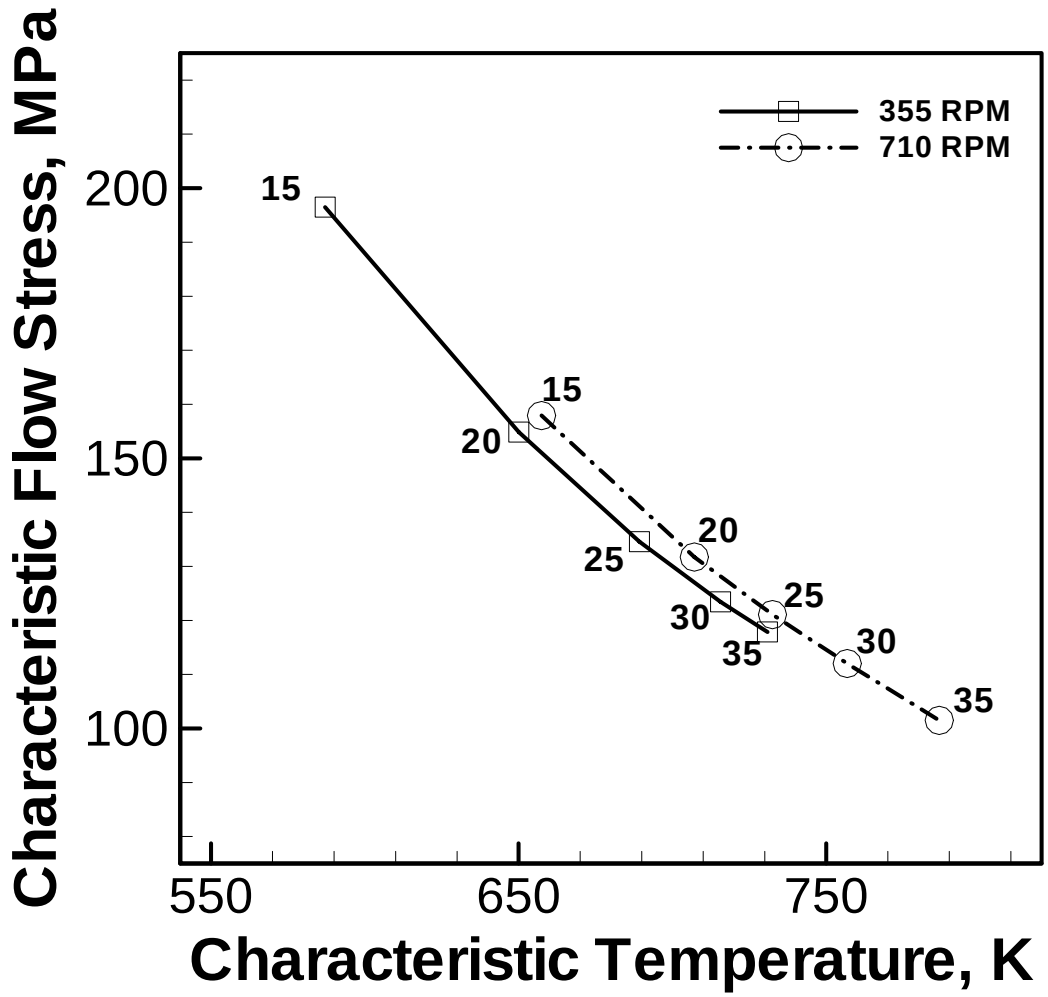

Figure 3.5 Characteristic flow stress and temperature of the deforming material near the tool for various shoulder diameters and rotational speeds. The legends near the symbols are shoulder diameters in mm.

The torque provided by the tool is used for sliding and to overcome sticking during welding. The sliding torque continuously increases with shoulder diameter due to the larger contact area as indicated in Equation (3.20). The sticking torque is affected by both contact area and shear strength, τ, as shown in Equation (3.19). With an increase in the shoulder diameter, the contact area increases while the shear strength decreases. Thus, with an increase in shoulder diameter, the sticking torque first increases, reaches a maxima and then decreases because the shear strength decreases with increase in temperature. Figure 3.6 shows the sticking torque versus shoulder diameter for various tool rotational speeds. The shoulder diameter corresponding to the maximum sticking torque is taken as the optimum shoulder diameter for each RPM. All other welding

variables were kept constant. Figure 3.6 shows that the optimum values of the shoulder diameter are 30, 25 and 20 mm corresponding to the rotational speeds 355, 560 and 710 RPM, respectively. Since the torque components are dependent on various parameters apart from the tool rotational speed, these estimated optimum shoulder diameter values are only valid for the process parameters considered here. The values of peak temperature corresponding to these optimum conditions are 713, 705 and 719 K, respectively. All these peak temperatures lie in the range of 0.94-0.96 TS, where TS is the solidus temperature (749K). This range lies well within the suggested working temperatures for FSW. [1,6,13,33-34]

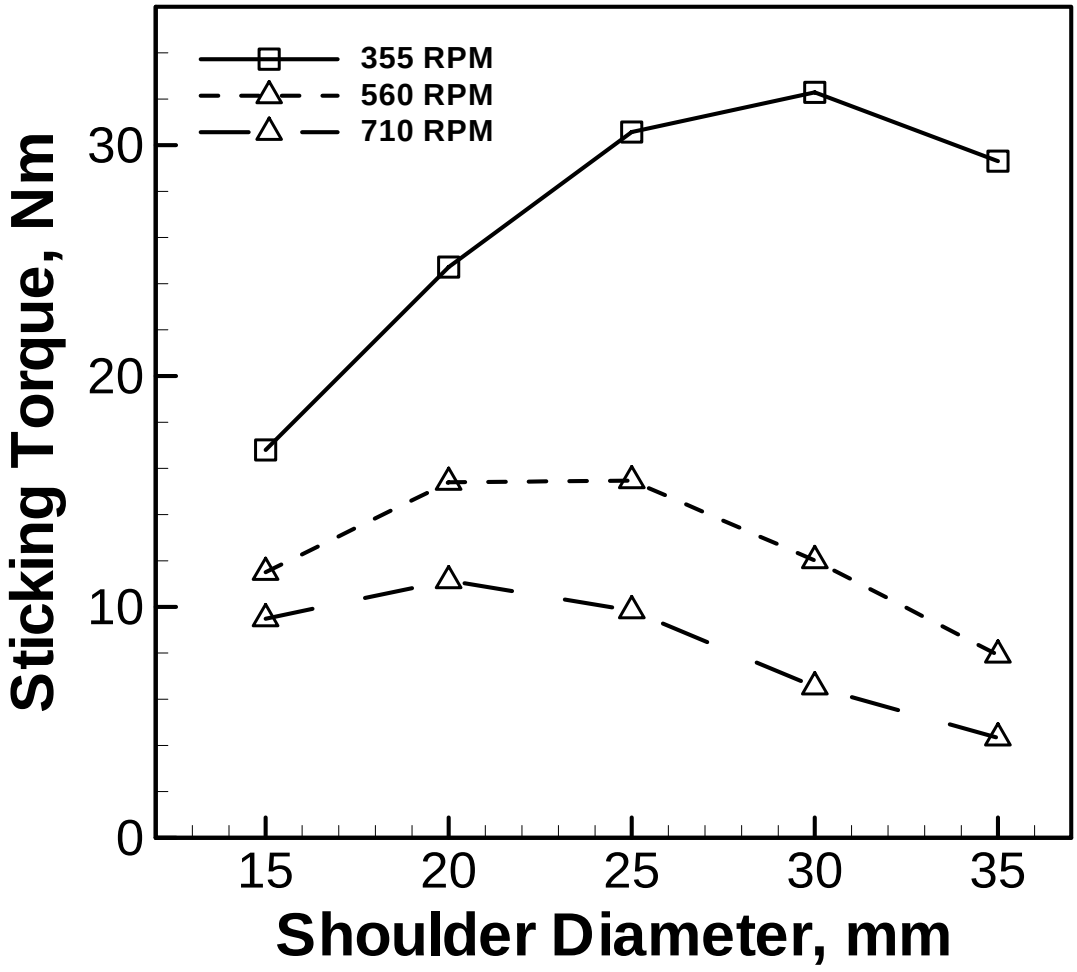

Figure 3.6 Computed values of sticking torque versus shoulder diameter for various tool rotational speeds. All other welding parameters, presented in Table 2, remain constant.

During the torque calculations, we observed that the two torque components are equal when the sticking torque is maximum. Although the reason for this equality is not

known, the following discussion will show that an objective function based on the two torque components gives the same optimum shoulder diameter as given by the maximum sticking torque. The objective function, O(f), can be defined as shown below: [22-23]

$$O(f) = \left(\frac{M_T}{M_T + M_L} \times \frac{M_L}{M_T + M_L} \right) \tag{3.24}$$

where M_T and M_L are the sticking and sliding torques defined by Equations (3.19) and (3.20) respectively. The two terms in the right hand side of Equation (3.7) represent the sticking and sliding fractions of the total torque. Figure 3.7 shows the computed values of O(f) as a function of the tool shoulder diameter for three rotational speeds. The function O(f) has a maximum value of 0.25 when the sticking and sliding torques are equal. The figure shows the O(f) is maximum at the shoulder diameter of 30, 25 and 20 mm corresponding to the rotational speeds 355, 560 and 710 RPM, respectively. These values of shoulder diameter for the given rotational speeds are the same as optimum shoulder diameter obtained from maximizing the sticking torque.

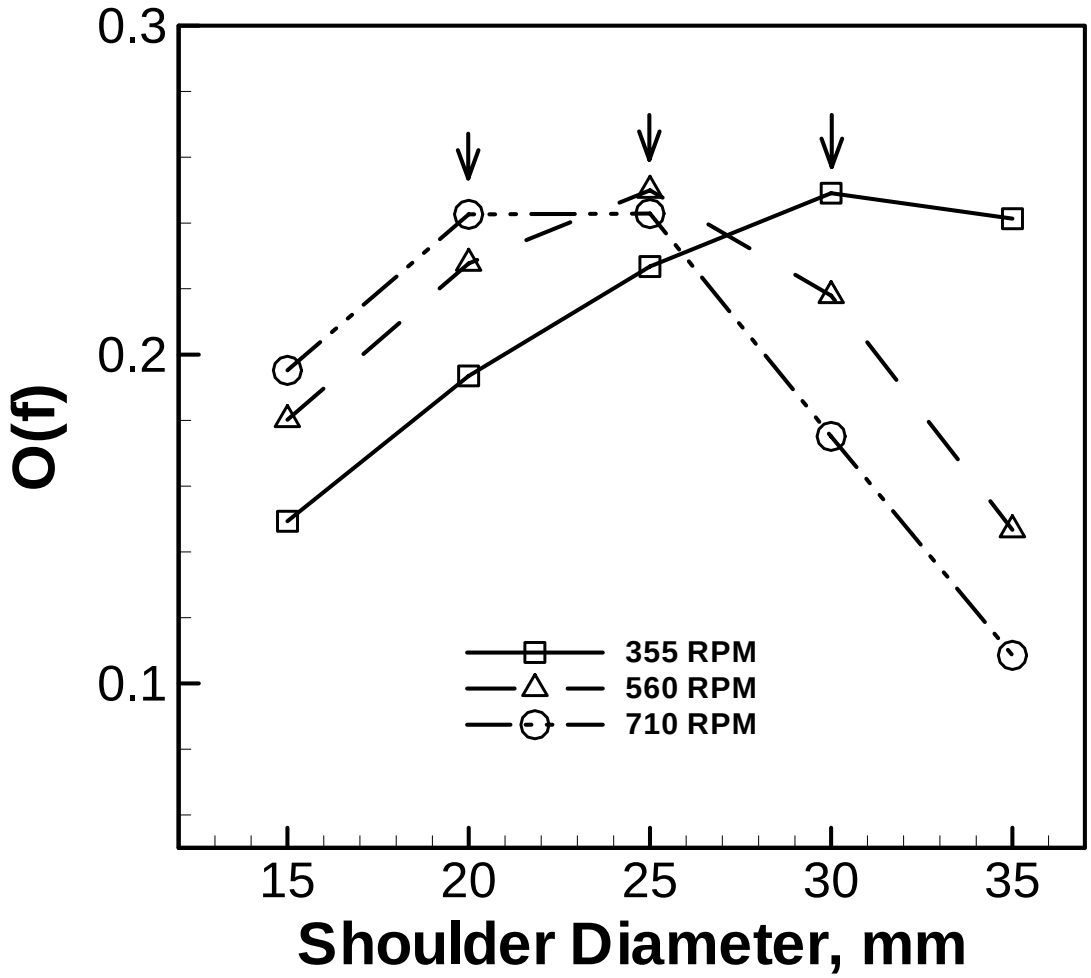

Figure 3.7 Variation of the objective function, O(f), as a function of tool shoulder diameter at various tool rotational speeds. [23]

The value of optimum shoulder diameter decreases with the increase in the tool rotational speed. For higher tool rotational speeds a smaller tool shoulder diameter is sufficient to provide enough heat to soften the material and induce the flow. However, a larger tool shoulder is required for the same purpose at lower rotational speeds. As the tool shoulder diameter increases beyond the optimum shoulder diameter, the relative velocity of the tool and workpiece increase, leading to higher slip. This increased value of slip leads to lower sticking torque and reduced grip of the tool on the workpiece.

The role of shoulder diameter can be further studied by evaluating the computed rate of mechanical work which is calculated by the term $[(1-\delta)\eta\tau(\omega r - U_1 \sin\theta)]$. Figure 3.8 shows that the maximum rate of mechanical work is done when the shoulder diameter is optimum. Beyond the optimum shoulder diameter, the rate of mechanical work

decreases. However, the total power increases continuously with shoulder diameter, as shown in Figure 3.4, due to increase in the rate of sliding frictional work.

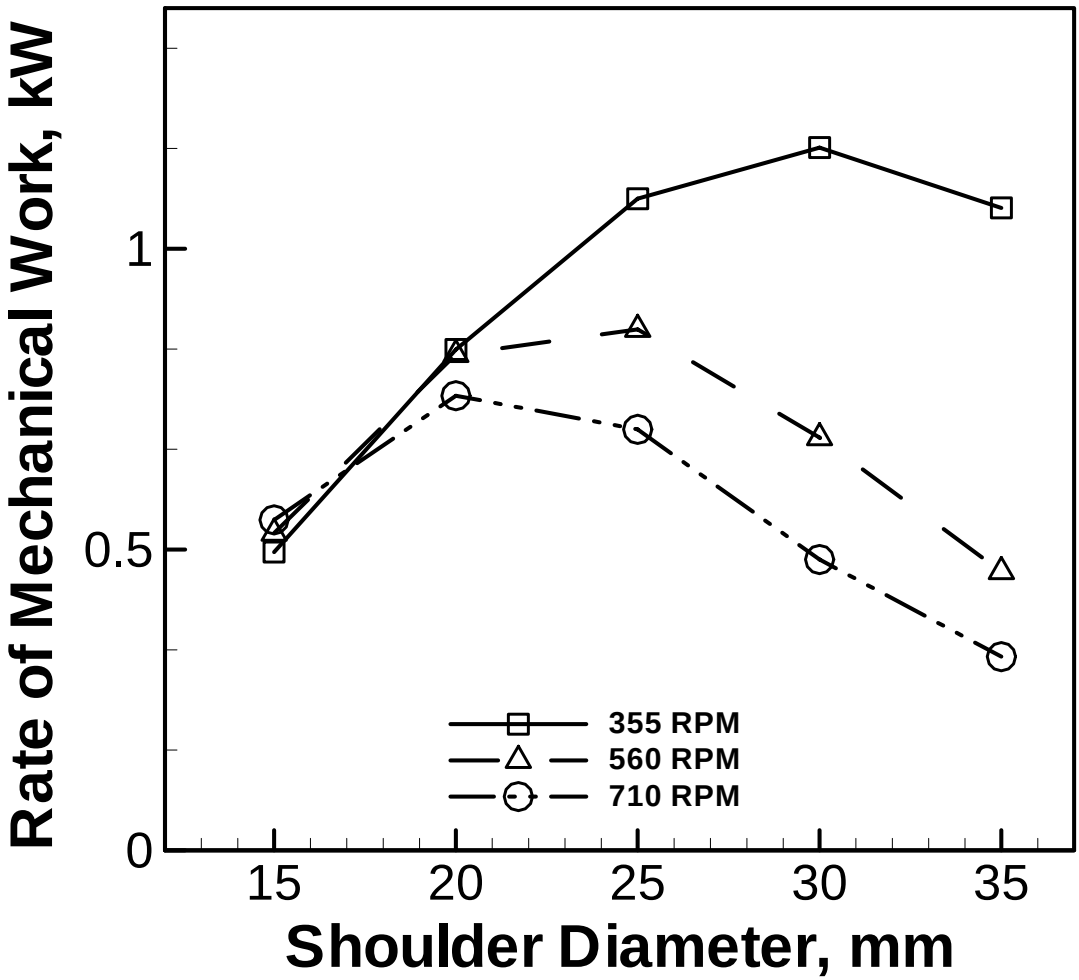

Figure 3.8 Computed values of rate of mechanical work done at varying shoulder diameters for rotational speeds of 355, 560 and 710 RPM.

Loss of the yield strength and the ductility of the welded joints in comparison with the corresponding properties of the base material are important for aluminum alloys. For example, Mahoney et al. [35] reported a moderate to significant loss in the ultimate tensile strength (UTS) and yield strength (YS) in FSW of AA7075-T651. Figure 3.9 shows the influence of shoulder diameter on the YS and UTS of the welds and the percent elongation (at break), welded at a tool rotational speed of 355 RPM and a welding velocity of 0.67mm/s. The ratio of the weld joint property to the corresponding base material property is shown in the figure for various tool shoulder diameters. The

percent elongation at break, YS and UTS for the AA7075-T6 base material are 11~12%, 503 MPa and 572 MPa, respectively.

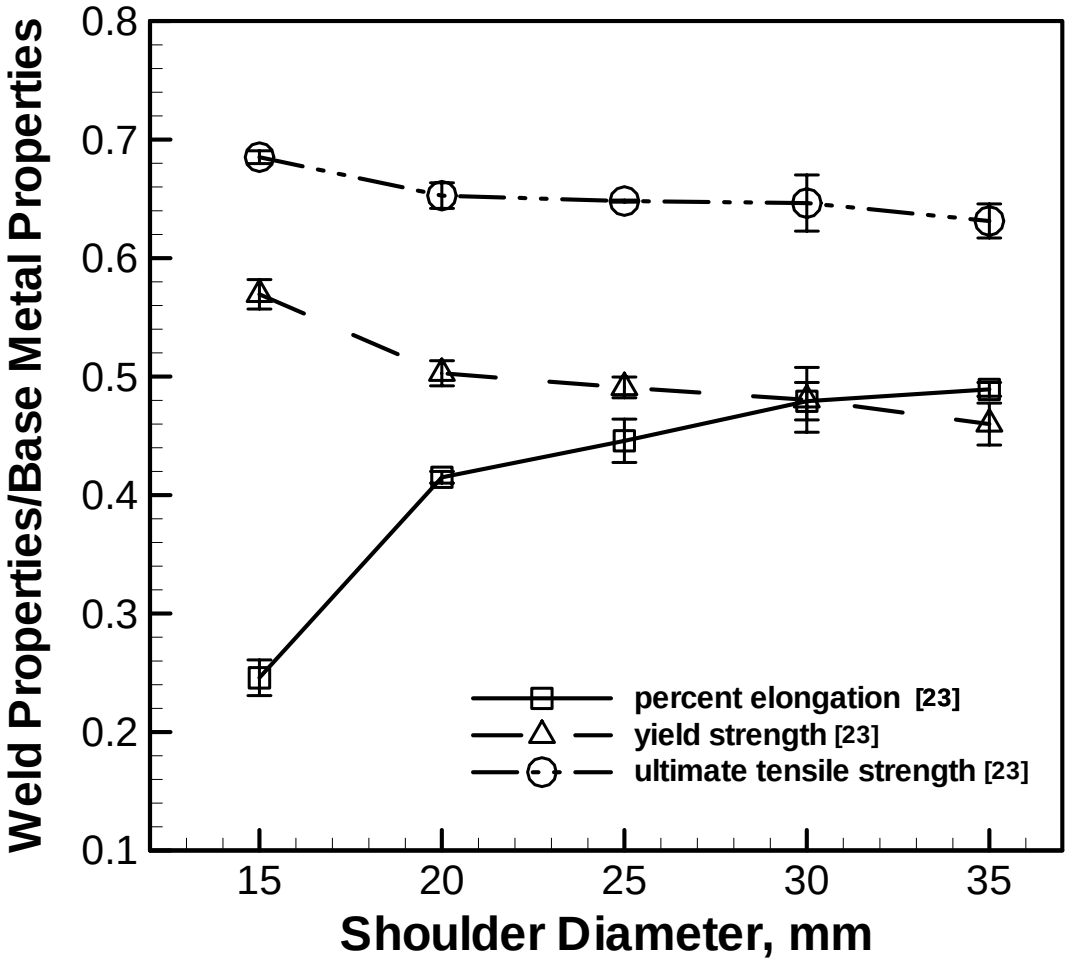

Figure 3.9 Ratio of the weld joint percent elongation, yield strength and ultimate tensile strength to the corresponding base metal properties. The weld was made using tool rotational speed 355 RPM and 0.67 mm/s. [23]

As shown in figure 3.9, the YS of the weld joint is 57% of the base material YS when the 15 mm shoulder diameter tool is used and is about 46% of the base material YS when the 35 mm shoulder diameter tool is used. The percent elongation changes from 25% to 49% of the base material as the shoulder diameter is increases from 15 mm to 35 mm. The YS and percent elongation of the weld joint is 48% of the base material properties when the tool with optimum shoulder diameter of 30 mm is used. These weld properties obtained from the use of the tool with optimum shoulder diameter are within the range of commonly obtained weld properties. [35]

Considering the FSW tool as a solid circular shaft, the computed total torque for the optimum shoulder diameter can be compared with the maximum permissible torque. For a solid shaft with circular cross-section, the maximum permissible torque, M_{max}, is given as follows: [36]

$$M_{max} = \frac{\tau \times J}{R} \tag{3.25}$$

where τ is the shear strength, J is the polar second moment of inertia, and R is the radius of the shaft. Considering the tool shoulder and tool pin as circular shafts, the polar second moment of inertia can be computed as follows: [36]

$$J = \int_A r^2 dA = \frac{\pi R^4}{2} \tag{3.26}$$

where r is the distance from the axis for a small area element dA. The tool pin is structurally the weakest part of the tool as it has the smallest diameter. The maximum permissible torque for the cylindrically tapered tool pin with an average diameter of 5.33 mm, as used here, is about 16.1 Nm considering the shear strength [37] of the tool material as 540 MPa at 613 K. The shear strength values were not available at higher temperatures. Among the three optimum tool geometries, the maximum value of the computed torque on the pin is about 4.1 Nm. These values indicate that the tools with suggested optimum geometries can be used safely with a fairly high factor of safety. The tool design criterion, considered here, provides a reliable basis for the selection of an optimum tool shoulder diameter for a given rotational speed.

3.4. AA 6061

Elangovan and Balasubramanian [21] studied FSW of 6 mm thick AA6061 plates with 15, 18 and 21 mm shoulder diameter tools, each with five pin profiles at a constant rotational speed of 1200 RPM and linear velocity of 1.25 mm/s. They reported that the tool with 18 mm shoulder diameter produced defect free welds irrespective of pin geometries. Furthermore, the tool with square pin profile provided superior weld joint tensile properties. However, the authors did not explain why the 18 mm shoulder diameter resulted in superior welds.

In order to evaluate the effect of shoulder diameter, a well tested heat transfer and materials flow model is used to compute the temperature and velocity fields, and the torque for several shoulder diameters (12-27 mm) and rotational speeds (900-1500 RPM). The data used for the calculations are presented in Table 3.3. The model was able to predict peak temperatures and torques within an error of ±5% for the FSW of several aluminum alloys, steels and titanium alloys [3-5,38-41]. As expected, the peak temperature increases with shoulder diameter for a given tool rotational speed. As a result, the flow stress of the alloy in the weld region decreases with increase in shoulder diameter.

Table 3.3 Data used for calculation for FSW of AA6061 [22]

Alloy	AA-6061
Shoulder diameter, mm	15, 18, 21
Pin diameter, mm	6
Pin length, mm	5.5
Rotational velocity, RPM	900, 1200, 1500
Welding speed, mm s^{-1}	1.25
Axial pressure, MPa	30
Workpiece material	
Density, kg m^{-3}	2700
*Yield Strength, MPa [38]	$13.52 + 263.25 \times \left(1 + \exp\left(\frac{T - 456.5}{29}\right)\right)^{-1}$
*Specific heat, J kg^{-1} K^{-1} [38]	$9.29\times10^{2} - 6.27\times10^{-1}T + 1.48\times10^{-3}T^{2} - 4.33\times10^{-8}T^{3}$
*Thermal conductivity, W m^{-1} K^{-1} [38]	$2.52\times10^{1} + 3.98\times10^{-1}T + 7.36\times10^{-6}T^{2} - 2.52\times10^{-7}T^{3}$
Tool material	
Density, kg m^{-3} [38]	7860
Specific heat, J kg^{-1} K^{-1} [38]	$9.29\times10^{2} - 6.27\times10^{-1}T + 1.48\times10^{-3}T^{2} - 4.33\times10^{-8}T^{3}$
Thermal conductivity, W m^{-1} K^{-1} [38]	25

*(Temperature, *T* in K)

Colegrove and Shercliff [33] used the temperature and flow stress combinations experienced by the material near the tool to evaluate the effects of different pin profiles. They suggested that the combination of flow stress and temperature indicate the state of the material during welding and this knowledge of state of the material would be useful

to understand the design of the tool [33]. In order to examine how the shoulder diameter affects the state of the material, the computed flow stress and temperature combinations experienced by the materials are plotted in Figure 3.10 for various tool shoulder diameters. In this figure, the darker shades indicate that the specific combination of temperature and flow stress is experienced more frequently by many locations within the weld zone. Figure 3.10 shows that for smaller shoulder diameters, the material deforms at low temperatures and high flow stresses and vice versa. In the hot working literature, a temperature range between $0.8T_S$ and T_S, where T_S is the solidus temperature, has been often considered for good results[6,16-17,22]. Because of the monotonous trend shown in Figure 3.1, the flow stress versus temperature plot alone is insufficient to identify an optimal shoulder diameter among the ones considered here.

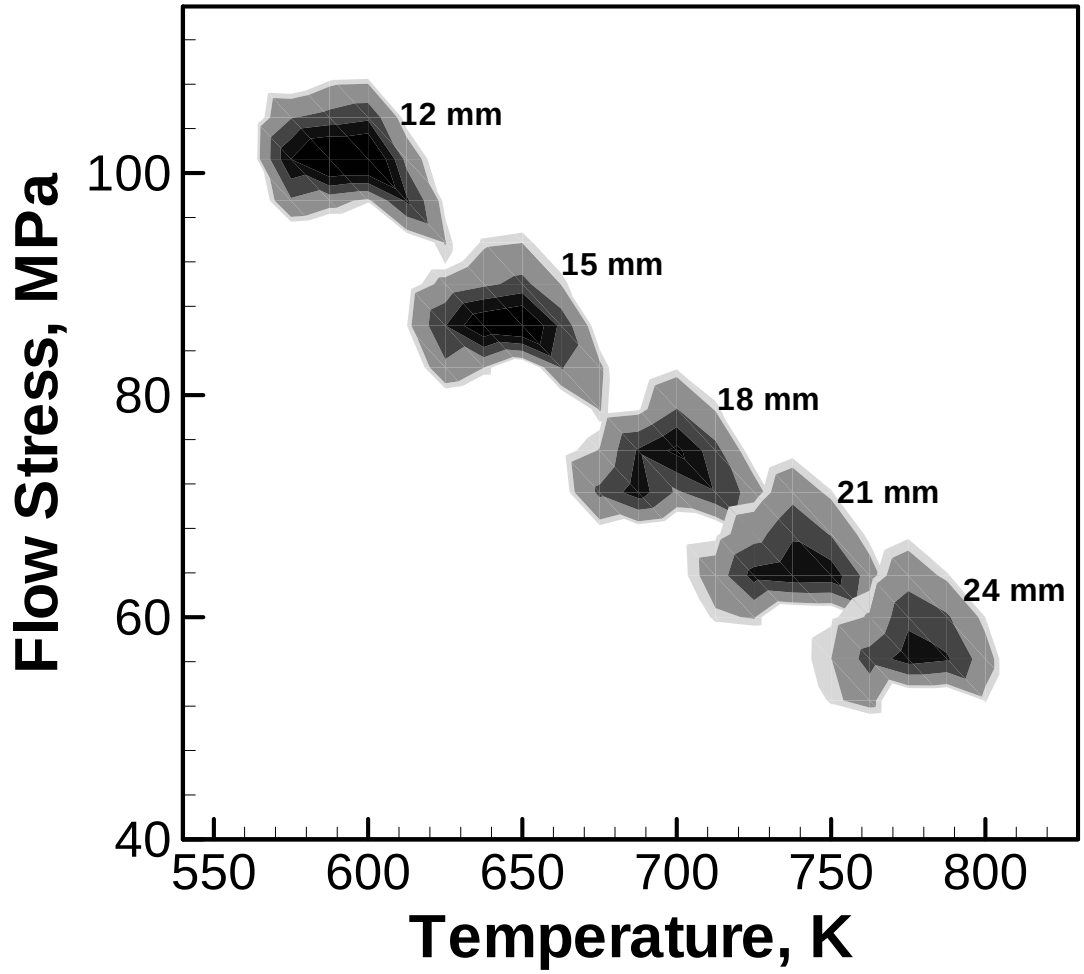

Figure 3.10 Flow stress and temperature combinations of the weld metal during FSW of AA60601 for various shoulder diameters at 1200 RPM.

In order to determine the optimum tool geometry, the two components of the torque are plotted in Figure 3.11 for various shoulder diameters. As the shoulder diameter increases, the sticking torque, M_T, increases, reaches a maximum and then decreases. This behavior can be explained using equation (3.2), which shows that there are two main factors that affect the value of the sticking torque. First, the strength of the material, τ, decreases with increase in temperature due to increase in shoulder diameter. Second, the area over which the torque is applied increases with shoulder diameter. As a result, the product of these two components shows the trend indicated in Figure 3.12. The sliding torque, M_L, increases continuously with increase in shoulder diameter due to larger contact area. With the increase in shoulder diameter the total torque increases continuously even when the sticking torque decreases for large shoulder diameters. In this regime, the extent of decrease in sticking torque is smaller than the increase in the sliding torque. As a result, the total torque increases continuously with shoulder diameter. This behavior is also observed for other tool rotational speeds as shown in Figure 3.12. The variation of sticking torque with shoulder diameter can be used to find an optimum tool shoulder diameter as explained below.

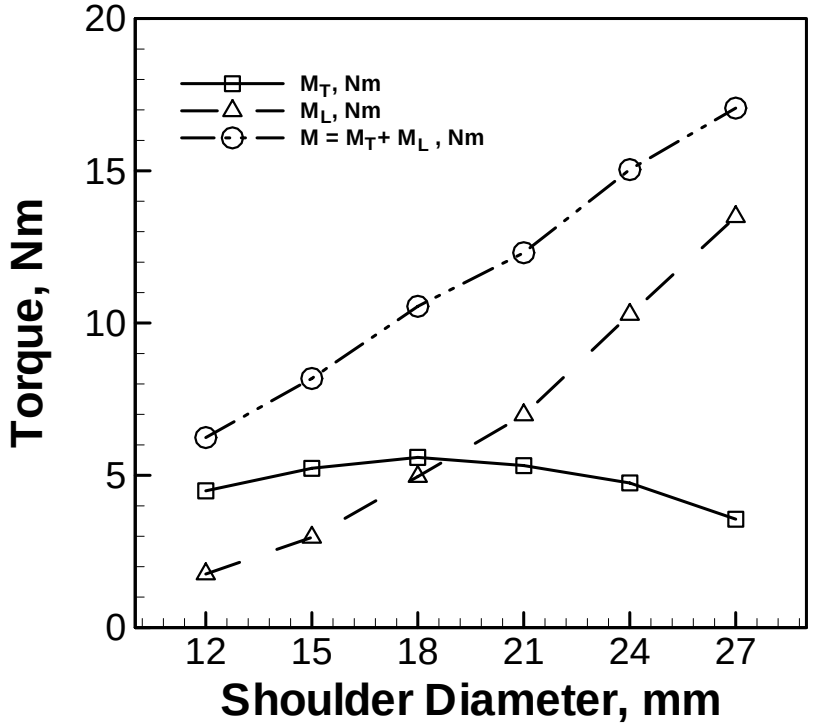

Figure 3.11 The computed values of sticking, sliding and total torque for various shoulder diameters at 1200 RPM.

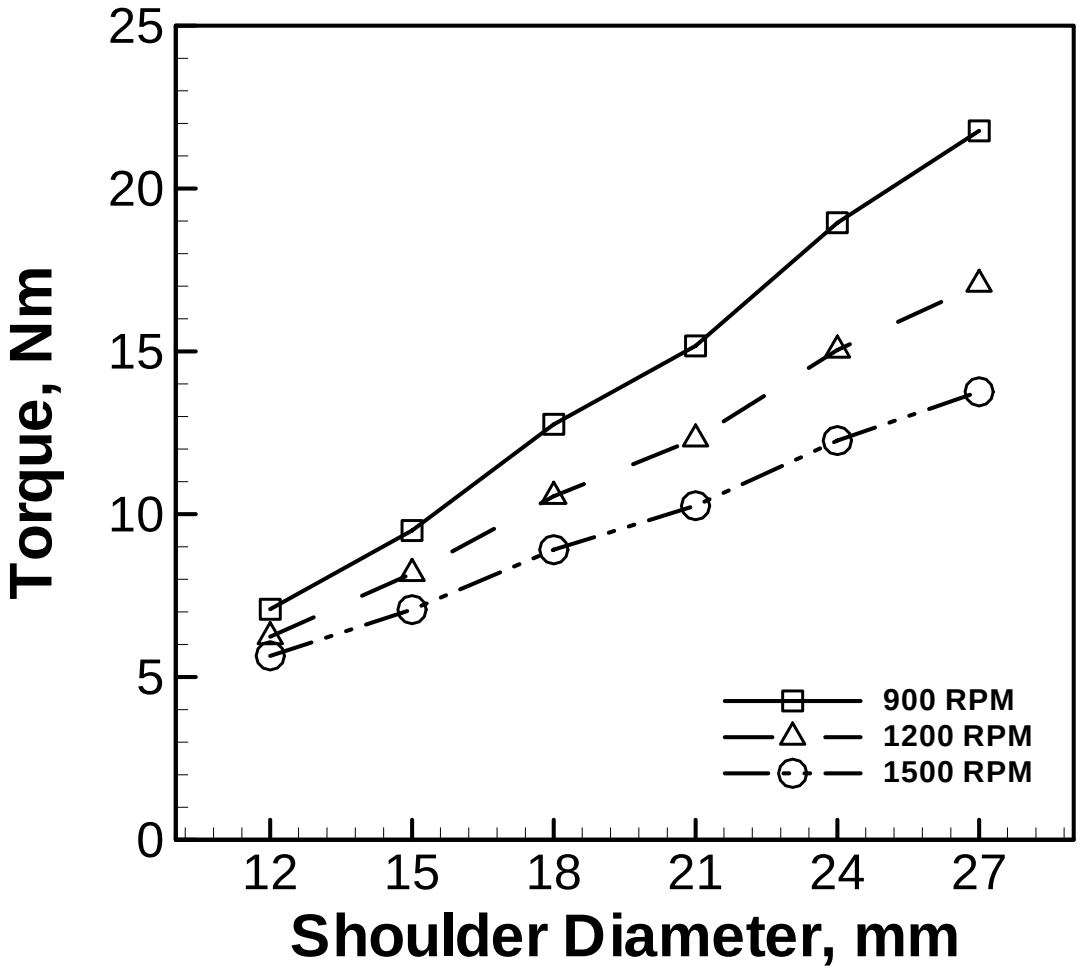

Figure 3.12 Total torque required during FSW of AA6061 as a function of the tool shoulder diameter for rotational speeds of 900, 1200 and 1500 RPM.

During FSW the tool must have adequate traction on the plasticized material so that material flow occurs from the leading to the trailing edge of the tool. The shape of the sticking torque versus shoulder diameter discussed above indicates that the sticking torque is maximum at a certain critical shoulder diameter. Beyond this shoulder diameter further increase in torque does not result in any improved traction of the tool because of the increase in temperature and the resulting decrease in the flow stress. The sticking torque represents the resistance of the plasticized material against flow around the tool. An optimum amount of material flow around the tool with minimum resistance is needed for a good weld and better tool life in FSW. With increase in shoulder diameter beyond the maximum sticking torque, the material reduces its resistance against flow because of

increased temperature and, as a result, the rotating tool loses its ability to influence the movement of the material. Figure 3.11 indicates that both the sticking and the sliding components of the total torque tend to be equal at a particular shoulder diameter where the sticking torque is maximum. The optimum shoulder diameter corresponds to the maximum value of an objective function, O(f), defined in Equation 3.24.

An optimum tool shoulder diameter should correspond to the criterion when O(f) is closest to its maximum possible value (=0.25). Figure 3.13 shows the variations in the computed values of O(f) as a function of shoulder diameter at three tool rotational speeds. It can be observed that the optimum tool shoulder diameter (mm) and rotational speed (rpm) combinations are (21, 900), (18, 1200) and (18, 1500) for the range of welding parameters considered in the present study. Elangovan and Balasubramanian [21] have also reported that the tool with 18 mm shoulder diameter provided the best weld joint strength at rotational speed of 1200 RPM as shown in Table 3.4. This shoulder diameter is three times the plate thickness, and the shoulder diameter commonly used in industry is about 2.5 to 3 times the thickness of the aluminum alloy plates [22]. The computed peak temperatures for the optimized shoulder diameters were in the range of $0.87T_s$ to $0.90T_s$ where T_s is the solidus temperature. This temperature range is well within the range of peak temperature commonly used in the FSW of AA6061.

Table 3.4 The mechanical properties of welds made using tapered cylindrical pin profile [21].

Diameter (mm)	Yield Strength (MPa)	Ultimate Tensile Strength (MPa)
15	88	112
18	134	168
21	121	154

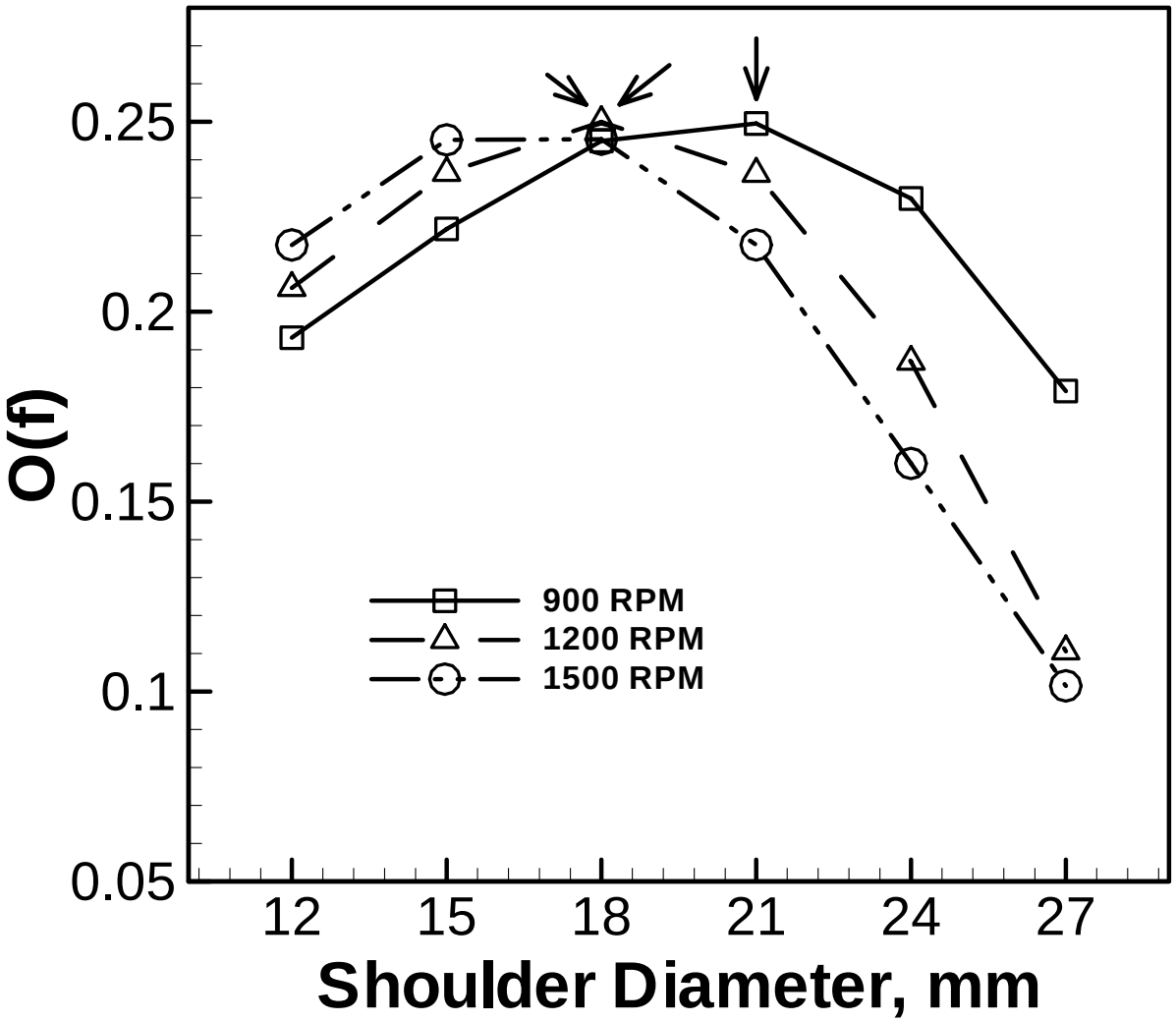

Figure 3.13 The computed values of the objective function, O(f), as a function of shoulder diameter at tool rotational speed of 900, 1200 and 1500 RPM.

3.5. Conclusions

A three dimensional heat transfer and visco-plastic flow model was used to understand the effect of tool shoulder diameter on peak temperature, torque and spindle power requirements in the FSW of AA7075-T6 and AA6061 at various rotational speeds. The increase in shoulder diameter resulted in higher peak temperature, spindle power and torque requirements for all rotational speeds considered. As the shoulder diameter increases, the state of the deforming material changes from high flow stress and low temperature to low flow stress and high temperature. A design criterion for the selection

of an optimum tool shoulder diameter is considered. The optimum tool shoulder diameter identified for 355, 560 and 710 RPM are 30 mm, 25 mm, and 20 mm, respectively for FSW of AA7075. The mechanical energy provided by the tool is also shown to have a maximum for these combinations of optimal shoulder diameter and rotational speed. The computed peak temperature for these optimum tool shoulder diameters are found to lie well within the commonly used working range for FSW. The welds made at the optimum shoulder diameter and the corresponding RPM have showed acceptable yield strength and percent elongation (at break). The optimum shoulder diameters were determined for rotational speeds of 900, 1200 and 1500 RPM for FSW of AA6061. The 18 mm optimum shoulder diameter at 1200 RPM has resulted in superior tensile properties in independent tests reported in the literature. The computed peak temperatures for all three optimized shoulder diameters were in the range of peak temperatures commonly encountered in the FSW of AA6061.

3.6. References

1. H.K.D.H. Bhadeshia, T. DebRoy, Sci Technol Weld Join 14(2009) 193-196.
2. T. DebRoy, H.K.D.H. Bhadeshia, Sci Technol Weld Join 15(2010) 266-270.
3. R. Nandan, T.J. Lienert, T. DebRoy, Int J Mater Res 99(2008) 434-444.
4. R. Nandan, G.G. Roy, T.J. Lienert, T. DebRoy, Acta Mater 55(2007) 883-895.
5. R. Nandan, G.G. Roy, T.J. Lienert, T. DebRoy, Sci Technol Weld Join 11(2006) 526-537.
6. W. M. Thomas, E. D. Nicholas, J. C. Needham, M. G. Murch, P. Templesmith, C. J. Dawes, “Friction stir butt welding”, Int. Patent Appl. no. PCT/GB92/02203 and GB Patent Appl. no. 9125978.8, Dec.1991, U.S. Patent Appl. No. 5460317, Oct.1995.
7. G. Buffa, J. Hua, R. Shivpuri, Mater Sci Eng A 419(2006) 381-388.
8. H. Fujii, L. Cui, M. Maeda, Mater Sci Eng A 419(2006) 25-31.
9. K. Kumar and S. V. Kailas, Mater Sci Eng A 485(2008) 367-374.
10. Y.H. Zhao, S.B. Lin, L. Wu, F.X. Qu, Mater Lett 59(2005) 2948-2952.
11. Y.H. Zhao, S.B. Lin, F.X. Qu, L. Wu, Mater Sci Technol 22(2006) 45-50.
12. D.G. Hattingh, C. Bignaut, T.I.van Niekerk and M.N. James, J Mater Process Technol 203(2008) 46-57.
13. W.M. Thomas, K.I. Johnson, C.S. Wiesner, Adv Eng Mater 5(2003) 485-490.
14. W.M. Thomas, Mater Sci Forum 426-432(2003) 229-236.
15. P.A. Colegrove, H.R. Shercliff, Sci Technol Weld Join 9(2004) 345-351.
16. P.A. Colegrove, H.R. Shercliff, Sci Technol Weld Join 9(2004) 352-361.
17. R. Nandan, T. DebRoy, H.K.D.H. Bhadeshia, Prog Mater Sci 53(2008) 980-1023.
18. Z. Zhang, Y.L. Liu, J.T. Chen, Int J Adv Manuf Technol 45(2009) 889-895.
19. A. Scialpi, L. A. C. De Filippis, P. Cavaliere, Mater Des 28(2007) 1124-1129.

20. R. M. Leal, C. Leitao, A. Loureiro, D. M. Rodrigues, P. Vilaca, Mater Sci Eng A 498(2008) 384-391.
21. K. Elangovan, V. Balasubramanian, Mater Des 29(2008) 362-373.
22. A. Arora, A. De, T. DebRoy, Scr Mater 64(2011) 9-12.
23. M. Mehta, A. Arora, A. De, T. DebRoy, Metall Mater Trans A, DOI: 10.1007/s11661-011-0672-5.
24. J.G. Sessler, V. Weiss, Aerospace structural metals handbook, vol. II, Wright-Patterson Air Force Base, Ohio, pp. 3207(1-3).
25. E.A. Brandes and G.B. Brook, eds., Smithells Metals Reference Book, 7th ed., Butterworth Heinemann, Woburn, MA, 1992, pp. 8–51.
26. R. Nandan, Computational modeling of heat transfer and visco-plastic flow in fraction stir welding, Ph.D. Thesis, 2008.
27. R. Nandan, T.J. Lienert, T. DebRoy, Int. J. Mater. Res. 99(2008) 434-444.
28. R. Nandan, G.G. Roy, T.J. Lienert, T. DebRoy, Acta Mater. 55(2007) 883-444.
29. R. Nandan, G. G. Roy, T.J. Lienert, T. DebRoy, Sci Technol Weld Join 11(2006) 526-537.
30. T.J. Lienert, W.L. Stellwag, Jr. B.B. Grimmeett, R.W. Warke, Weld J 83(2003) 1s-9s.
31. Q. Li, M. Lovell, J. Mater. Process. Technol. 160 (2005) 245-256.
32. R. Nandan, B. Prabu, A. De and T. DebRoy, Weld J 86(2007) 313s-322s.
33. P.A. Colegrove, H. R. Shercliff, Sci Technol Weld Join 11(2006) 429-441.
34. P.A. Colegrove, H. R. Shercliff, R. Zetter, Sci Technol Weld Join 12(2007) 284-297.
35. M.W. Mahoney, C.G. Rodes, J.G. Flintoff, R.A. Spurling, W.H. Bingel, Metall Mater Trans A 29(1998) 1955-1964.
36. E.J. Hearn, Mechanics of materials 1, 3rd ed., Oxford: Butterworth Heinemann, 1997, pp. 179-181.
37. J. Woolman, R.A. Mottram, The mechanical and physical properties of the British Standard En steels (B.S. 970-1955). volume 2, New York: Pergamon, 1964, pp. 107.
38. R. Nandan, G.G. Roy, T. DebRoy, Metall Mater Trans A 37(2006) 1247-1259.
39. R. Nandan, B. Prabu, A. De, T. DebRoy, Weld J 86(2007) 313s-322s.
40. A. Arora, R. Nandan, A. P. Reynolds, T. DebRoy, Scr Mater 60(2009) 13-16.
41. A. Arora, Z. Zhang, A. De, T. DebRoy, Scr Mater 61(2009) 863-866.

Chapter 4. Load Bearing Capacity of Tool Pin

An FSW tool, in general, consists of a shoulder and a cylindrical threaded pin. The tool pin, which is structurally the weaker of the two, experiences severe stresses due to both bending and torsion. These stresses result from the continuous linear and rotational motion of the tool in the plasticized material. The FSW tools are currently designed by trial and error. A systematic study to examine the mechanical behavior of the tools under various FSW conditions is not available. Since the tool pin failure is a main reason for the FSW tool failures, understanding of the stresses on the tool pin is needed to develop long lasting FSW tools.

The geometrical features of FSW tool pin and shoulder affect the material flow and weld joint properties during FSW. Several researchers [1-17] have studied the effect of various features of tool pin and shoulder geometry on the material flow and weld properties. Bhadeshia and DebRoy [1] reviewed the commonly used tool materials for FSW of steels and highlighted the inadequacies in the present tool design practices for hard materials. Nandan et. al [2] have reviewed several commonly used tools and tool geometrical features for FSW of various alloys. Hirasawa et. al [3] studied the plastic flow during friction stir welding for various tool geometries using particle movement method. Elangovan and Balasubramanian [4] considered various tool pin profiles to study the effect on the friction stir processing zone and showed that for all considered welding speeds the tools with square pin profile resulted in defect free welds. Hattingh et. al [5] showed that a relation can be determined between the thread pitch, pin diameter and the plate thickness to obtain defect free welds while using tools with tri-fluted tapered pin. Badrinarayan et. al [6] studied the hook (a geometrical defect originating at the interface of the two welded sheets) formation during friction stir spot welding of AA5754-O for various tool geometries. They [6] showed that the welds made using the tool with triangular pin had higher static strength compared to the same for welds made using tool with circular pin. Tozaki et. al [7] studied the effect of tool pin length on the microstructure and static strength of AA5083 friction stir spot welds. Thomas et. al [8]

and Thomas [9] suggested new tool pin profiles for higher heat generation and improved material flow. Zhao et al [10-11] showed that among various tool pin profiles a threaded tapered tool pin would result in weld with minimum defects. Buffa et al [12] studied the effect of pin taper angle on the peak temperature during FSW. Fujii et al [13] showed that a triangular prism shaped pin results in defect free friction stir welds and the same is obtained by a threadless columnar pin in case of AA1050. Kumar and Kailas [14] studied the effect of material flow due to tool pin on the defect formation in friction stir welds. Colegrove and Shercliff [15-16] used a mathematical model to show the increased material flow by use of a Triflute tool pin. Colegrove and Shercliff [17] also estimated FSW traverse force using a mathematical model. However, the estimated values of the traverse force were one order of magnitude lower than those from independent experimental measurement. They [17] suggested that the agreement can be improved by considering appropriate slip between tool and material or by considering appropriate viscosity near the solidus. Although the effect of tool pin geometrical features on the weld properties and material flow has been studied by various researchers, its effect on the stresses on the tool pin due to bending and torsion is not yet understood. Since real time measurement of the stresses on the tool pin is difficult, a recourse is to use a well tested and reliable mathematical model to estimate the tool pin stresses. Sorensen and Stahl [18] proposed a mathematical relationship to estimate the forces on tool pin based on the regression analysis of the overall forces on the tool experimentally measured during FSW of AA6061. The proposed relationship was shown to be valid for tool pins of 5.6 mm or shorter.

In recent times, the heat transfer and visco-plastic flow models for FSW are used to explain the effect of tool shoulder diameter on the heat generation, material flow, peak temperature, torque and power requirements. [19-20] Furthermore, the model has been used to estimate an optimum shoulder diameter for given welding conditions to have maximum grip of the tool on the material while adequately softening the material to move it easily. The mathematical model has been used to estimate the optimum tool shoulder diameter. However, a scientific methodology is not available to determine suitable tool pin dimensions. An analysis of the effect of the tool pin dimensions on the stresses on the pin will be useful for improving tool design.

In this chapter, a method to compute the traverse force during FSW for various tool geometries and welding conditions for different aluminum and titanium alloys is proposed and tested. The maximum shear stress experienced by the tool pin is computed using the calculated distribution of the traverse force and the torque on the tool pin. The calculation of the maximum shear stress considers the combined action of bending and torsion on the tool pin. For a given set of welding variables, suitable tool pin dimensions can be prescribed based on the load bearing ability of the pin. The load bearing ability of the tool pin is then used to explain the deformation and failure of the tool pin during FSW of AA7075 and L80 steel. The low values of the factor of safety based on the computed load bearing ability of the tool pin is determined to be the reason for the premature failure of the tool pin in these cases. The proposed model for load bearing ability in combination with an appropriate factor of safety will be a very useful method to determine tool pin dimensions for long lasting FSW tools for given tool/workpiece material and welding conditions.

4.1. Numerical model

The stresses on the tool pin arises due to both bending and torsion because of the linear and rotational motion, respectively. Figure 4.1(a) shows a schematic distribution of the force, q(z), of a straight cylindrical FSW tool pin. The direction of the force is opposite to the welding direction. Figure 4.1(b) shows a transverse cross section of the tool pin along the S-S plane in Figure 4.1(a).

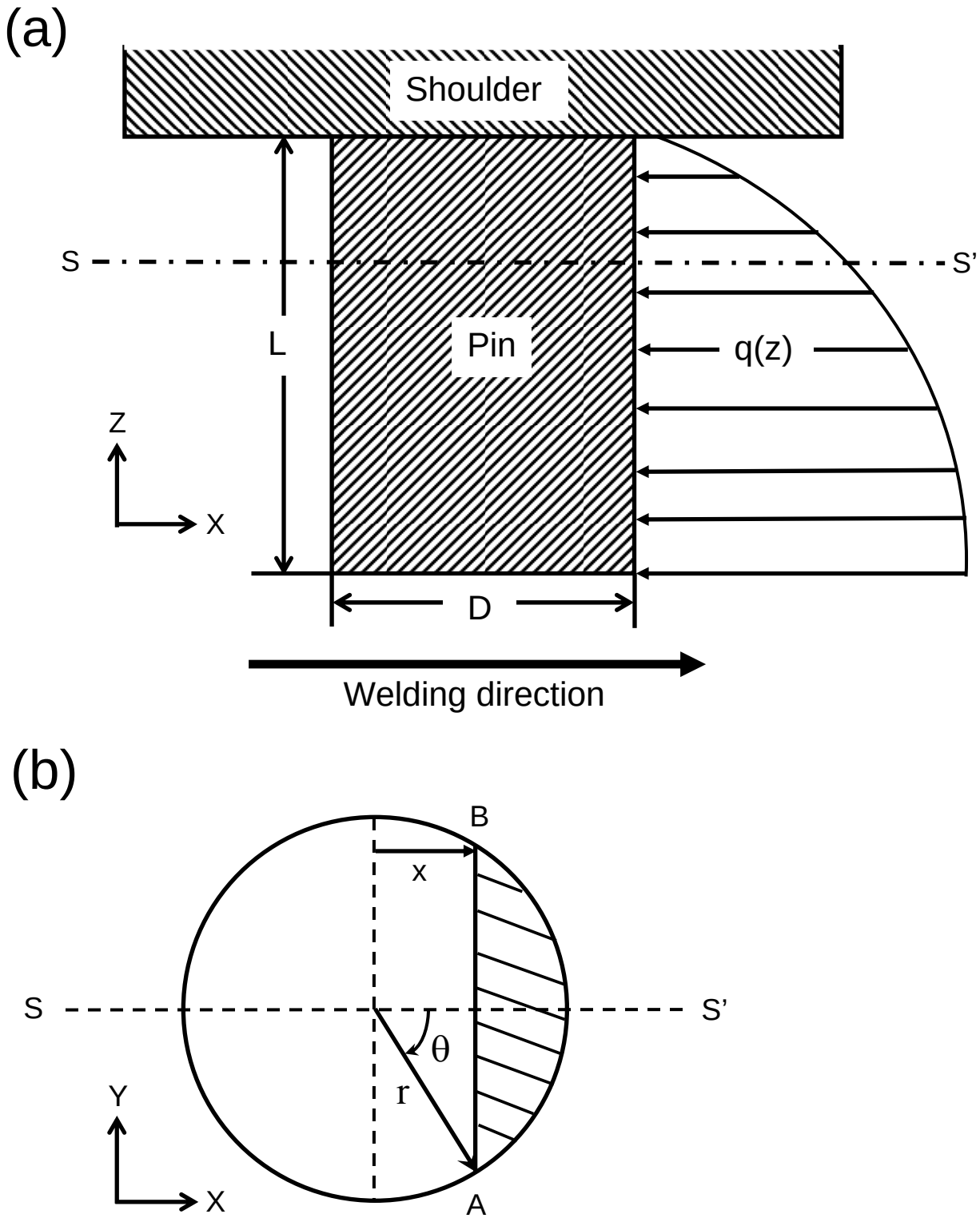

Figure 4.1 Schematic of (a) force distribution on a straight cylindrical pin and (b) cross-section along S-S

At a point A on the transverse cross section of the tool pin in Figure 4.1(b), the bending moment, M_y, can be computed as [21]

$$M_y = \int_{z_1}^{L} z\, q(z)\, dz \tag{4.1}$$

where L is the length of pin, z_1 is the distance of the point A from the root of the pin, q(z) is the force on the infinitesimal section of the pin, dz, at a distance z from the root of the pin. The normal stress due to bending, σ_B, is calculated as [21]

$$\sigma_B = \frac{M_y\, x}{I_{yy}} = \frac{M_y\, (r\cos\theta)}{\pi r^4/4} = \frac{4\cos\theta}{\pi r^3}\int_{z_1}^{L} z\, q(z)\, dz \tag{4.2}$$

where x is the normal distance of the cord AB from the neutral axis of the pin, I_{yy} is the second moment of area, r is the radius of the pin, and θ is the angle of the point A from the welding direction. The shear stress, τ_T, at point A due to torsion can be estimated as [21]

$$\tau_T = \frac{M_T\, \mathbf{r}}{\mathbf{J_{zz}}} = \frac{M_T\, \mathbf{r}}{\pi \mathbf{r^4/2}} \tag{4.3}$$

where M_T is the sticking torque experienced at point A and J_{ZZ} is the polar moment of inertia of the pin. Since the ratio of the pin length to the pin diameter is less (<20), the shear stress due to bending, τ_B, should be considered for the load bearing of the pin. [21] An estimation of the shear force, V, on the pin and of Q, the first moment of area of the section beyond chord AB (Figure 4.1(b)) about the neutral axis (y-axis) is required for the calculation of shear stress for bending. The terms, V and Q are computed, respectively, as [21]

$$V = \int_{z_1}^{L} q(z)\, dz \tag{4.4}$$

$$Q = \int_{x}^{r} gx\, dx \tag{4.5}$$

where $g = 2\sqrt{r^2 - x^2}$ is the length of the chord AB, $x\,dx = -(g\,dg)/4$ and since $x = r\cos\theta$, Q is rewritten as

$$Q = \int_{g}^{0} g\left(-g\frac{dg}{4}\right) = \int_{0}^{g} \frac{g^2}{4} dg = \frac{g^3}{12} = \frac{(2\sqrt{r^2 - x^2})^3}{12} = \frac{2}{3}(r\sin\theta)^3 \tag{4.6}$$

The shear stress, τ_B, at A due to bending can now be computed as [21]

$$\tau_B = \frac{VQ}{I_{yy}g} = \frac{4}{3}\frac{\sin^2\theta}{\pi r^2}\int_{z_1}^{L} q(z)\,dz \tag{4.7}$$

The typical nature of the stress distribution due to torsion and bending at several locations on the section SS is shown schematically in figures 4.2(a) and (b), respectively. The two stresses on any element located at point A is shown in Figure 4.2(c).

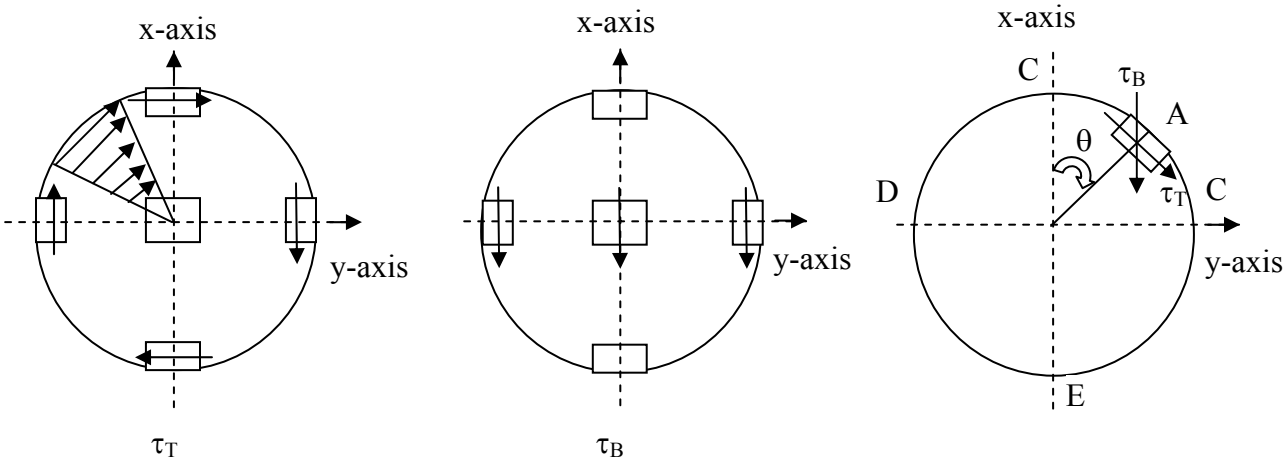

Figure 4.2 Schematic illustrations of (a) τ_T, (b) τ_B at section S-S and of (c) τ_T and τ_B at point A

At a point A, the maximum and minimum principal stresses, σ_1 and σ_2 respectively, due to combined bending and torsion loading can be written as [21]

$$\sigma_{1,2} = \frac{\sigma_B}{2} \pm \sqrt{\left(\frac{\sigma_B}{2}\right)^2 + (\tau_B + \tau_T\sin\theta)^2 + (\tau_T\cos\theta)^2} \tag{4.8}$$

The maximum shear stress, τ_{max}, at A can be obtained using the Tresca's criteria [21]

$$\tau_{max} = \frac{\sigma_1 - \sigma_2}{2} = \sqrt{\left(\frac{\sigma_B}{2}\right)^2 + (\tau_B + \tau_T\sin\theta)^2 + (\tau_T\cos\theta)^2} \tag{4.9}$$

The maximum shear stress, τ_{max}, is an estimate of the stresses applied on the tool pin at any point during FSW. As shown in Equations 4.2 and 4.3, the computation of the maximum shear stress requires the calculation of the force distribution, q(z), and torque, M_T, on the tool pin.

The total torque (M) is the sum of the sticking and sliding components of the torque as shown below: [19-20]

$$M = M_T + M_L \tag{4.10}$$

where M_T and M_L are the sticking and sliding components of the total torque, respectively. The values of torque components M_T and M_L are computed as follows: [19-20]

$$M_T = \oint_A r_A \times (1-\delta)\ \tau\ \times dA \tag{4.11}$$

$$M_L = \oint_A r_A \times \delta\ \mu\ P\ \times dA \tag{4.12}$$

where r_A is the distance of any infinitesimal area element, dA, from the tool axis, δ is the spatial fractional slip, μ is the coefficient of friction, P is the normal pressure, τ is the temperature dependent shear strength. The three dimensional heat transfer and fluid flow model is used to compute the temperature and material flow required for determination of the shear strength of the deforming material. The tool traverse force (F) during FSW is the sum of the force on the shoulder, F_S, and the force on the pin, F_P, and are computed as

$$F = F_S + F_P \tag{4.13}$$

The values of F_S and F_P are computed as:

$$F_S = \oint_A \delta \times \mu\ P \times dA \tag{4.14}$$

$$F_P = \oint_A \sigma \times dA \tag{4.15}$$

where σ is the temperature dependent yield strength of the deforming material, dA is the projected contact area of the tool pin.

4.2. Results and Discussions

The traverse force on the tool is computed using Equation 4.13. Figures 4.3 and 4.4 show the computed and the corresponding experimentally measured values of tool traverse force, obtained from independent experiments [22-23] for FSW of AA2524 and Ti-6Al-4V alloys, respectively. For FSW of AA2524, the welding velocity is 2.11 mm/s and the plunge force is 42.3 kN. The rotational speed for these cases varies from 150 to

800 RPM. When the tool rotational speed is increased, the computed values of the traverse force decreases. The faster rotation of the tool results in a greater rate of heat generation and softening of the work piece.

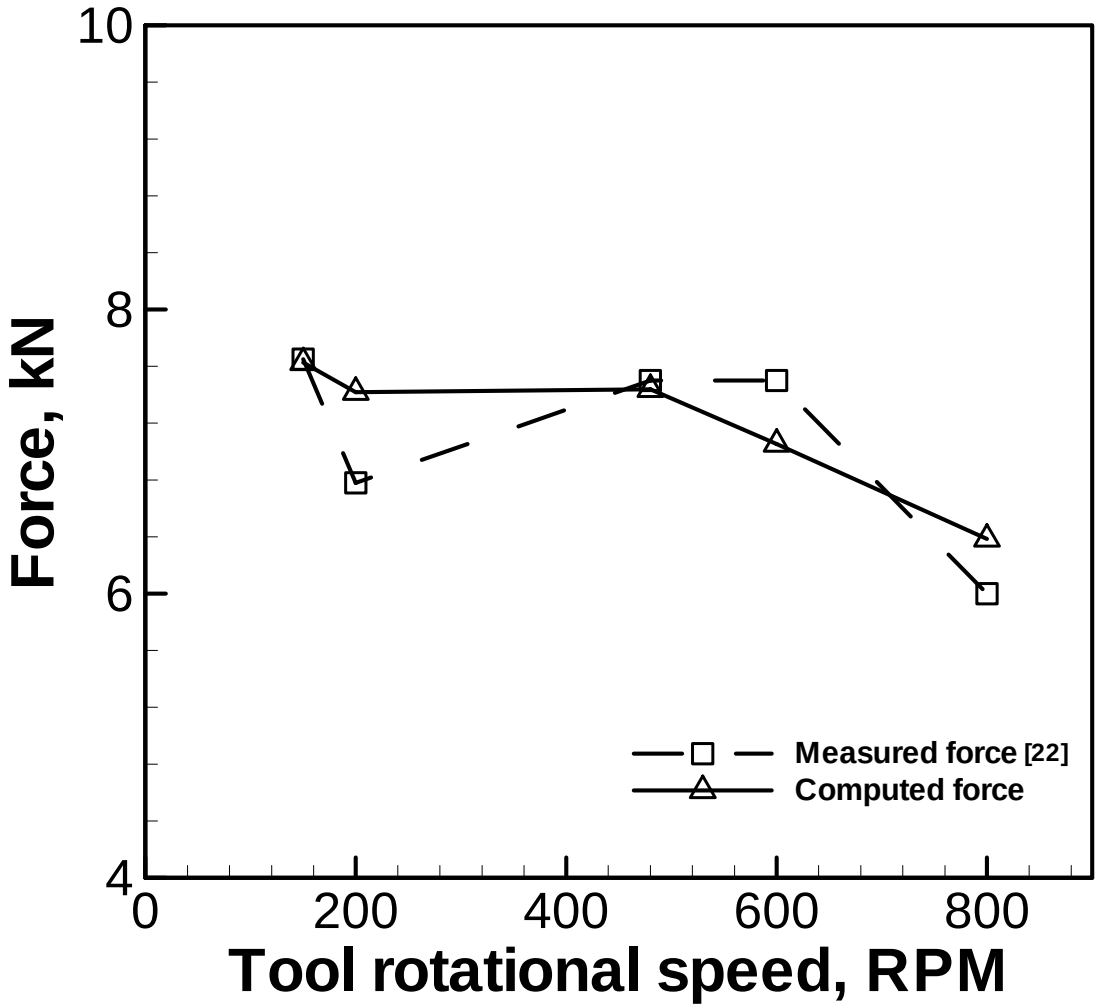

Figure 4.3 A comparison of the experimental and computed traverse force values as a function of tool rotational speed during FSW of AA2524 at the welding speed of 2.11 mm/s. [22]

Figure 4.4 shows the computed and the corresponding measured values of traverse force during FSW of Ti-6Al-4V alloy at different combinations of rotational speed, plunge force and welding speed. Table 4.1 gives the specific values of tool rotational speed, welding speed, plunge force for the cases shown in Figure 4.3. The standard deviation in the measurement of experimental values as reported in literature is shown in the error bars. For a constant welding speed the tool traverse force decreases with an increase in the rotational speed and with a decrease in the plunge force (cases #1,

#2 and #3) as shown in Figure 4.4. Increased plunge force increases the friction force on the tool shoulder and thus results in higher traverse force. For cases #4 and #5 where the tool rotational speed is higher than other cases, the plunge force and welding speed also increases, thus also increasing the traverse force. The increased welding speed reduces the amount of heat generated per unit length of the weld and, as a result, the material is not adequately softened leading to greater traverse force. However, the effect of higher welding speed is also accompanied by the higher tool rotational speeds for these two cases, and the measured forces are the combined effects of the two welding speed and the tool rotational speed.

Table 4.1 Experimentally measured and corresponding computed values of tool traverse force during FSW of Ti-6Al-4V alloy at different welding conditions.

Data set index	RPM	Welding speed (mm/s)	Plunge force (kN)	Tool traverse force (kN)	
				Measured	Computed
1	120	0. 85	32.920	8.200	7.663
2	150	0.85	21.320	6.410	6.060
3	200	0.85	9.050	0.849	4.196
4	400	1.70	6.220	0.471	3.613
5	800	3.40	9.620	1.792	3.759

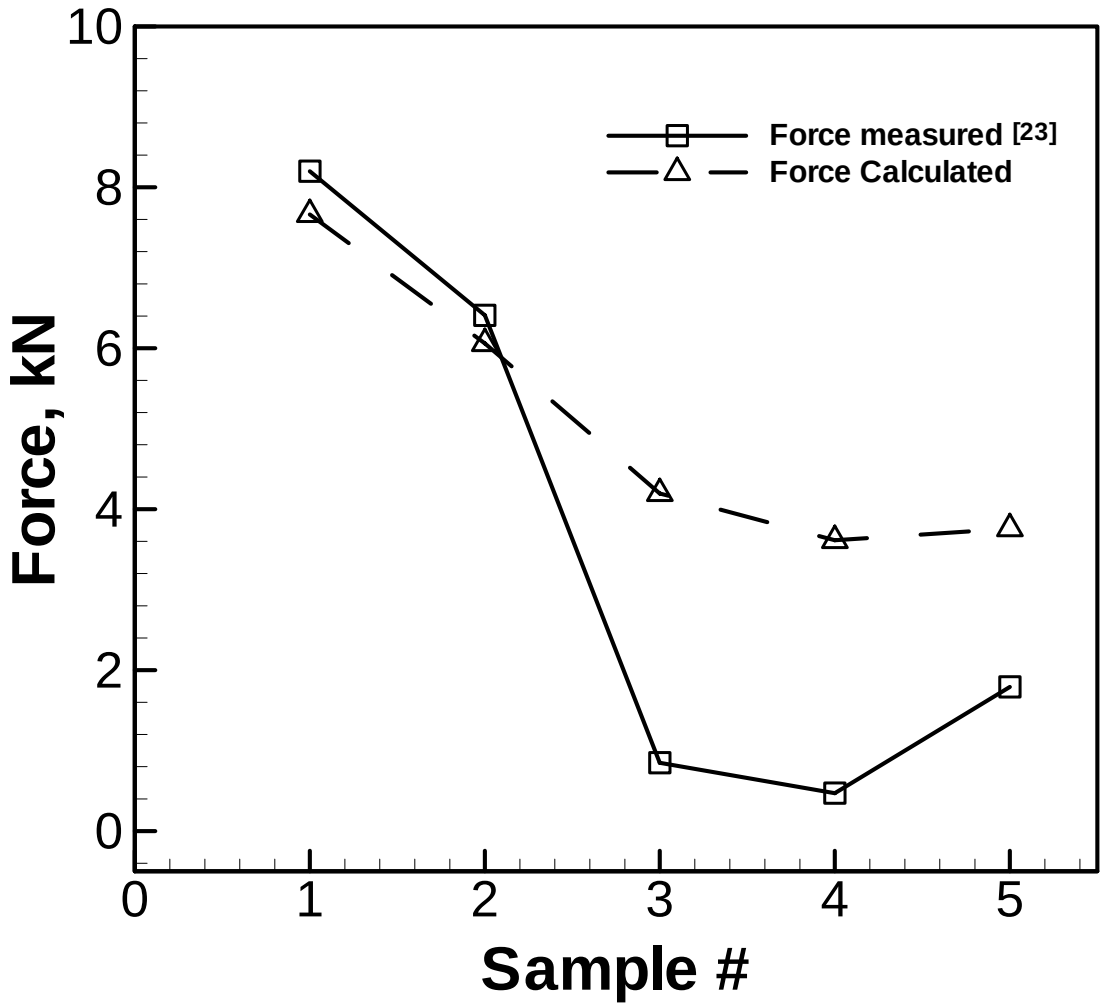

Figure 4.4 A comparison of the computed and corresponding experimentally measured total traverse force for FSW of Ti-6Al-4V alloy. The welding condition for the five samples are given in table 4.1. [23]

Figure 4.5 and 4.6 show the measured values of tool traverse force for FSW of AA6061 alloy as a function of pin length and diameter, respectively. The tool welding speed is 3.33 mm/s and rotational speed is 650 rpm. The error bars in Figures 4.5 and 4.6 show the estimated error in the experimentally measured values as reported in the literature [18]. The traverse force increases with tool pin length for a given workpiece thickness, whereas it remains unaffected with change in pin diameter. For the fact that most of the heat is generated at the tool shoulder – workpiece interface, the temperature of the workpiece is high at the shoulder workpiece interface and decreases downwards. As the pin length increases, the end of the tool pin faces the workpiece material with lower temperature. Thus, the tools with longer pins experience higher traverse force. An

increase in the pin diameter has much lower influence on the softening of the work piece material and allows only marginal increases in the interaction between the tool pin and work piece. Thus, the effect of pin length is much greater than the effect of pin diameter on the computed traverse force. A fair agreement of the computed tool traverse force with the corresponding experimentally measured values is shown in Figures 4.3 through 4.6 for the various welding conditions, tool dimensions and different workpiece materials.

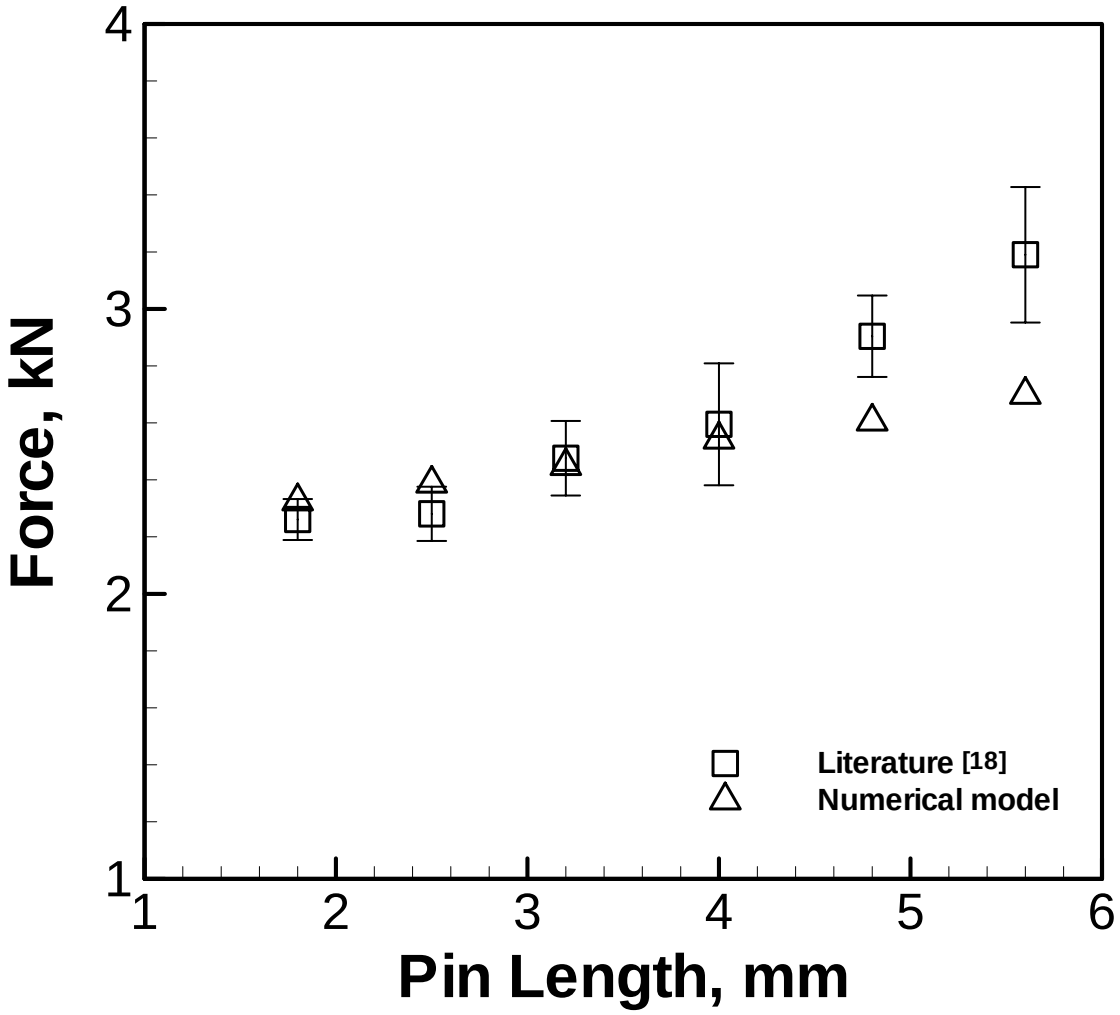

Figure 4.5 A comparison of experimentally measured and corresponding computed total traverse force as a function of the pin length for the FSW of AA6061. The welding velocity is 3.33 mm/s, tool rotational speed is 650 RPM and the pin diameter is 7.6 mm. [18]

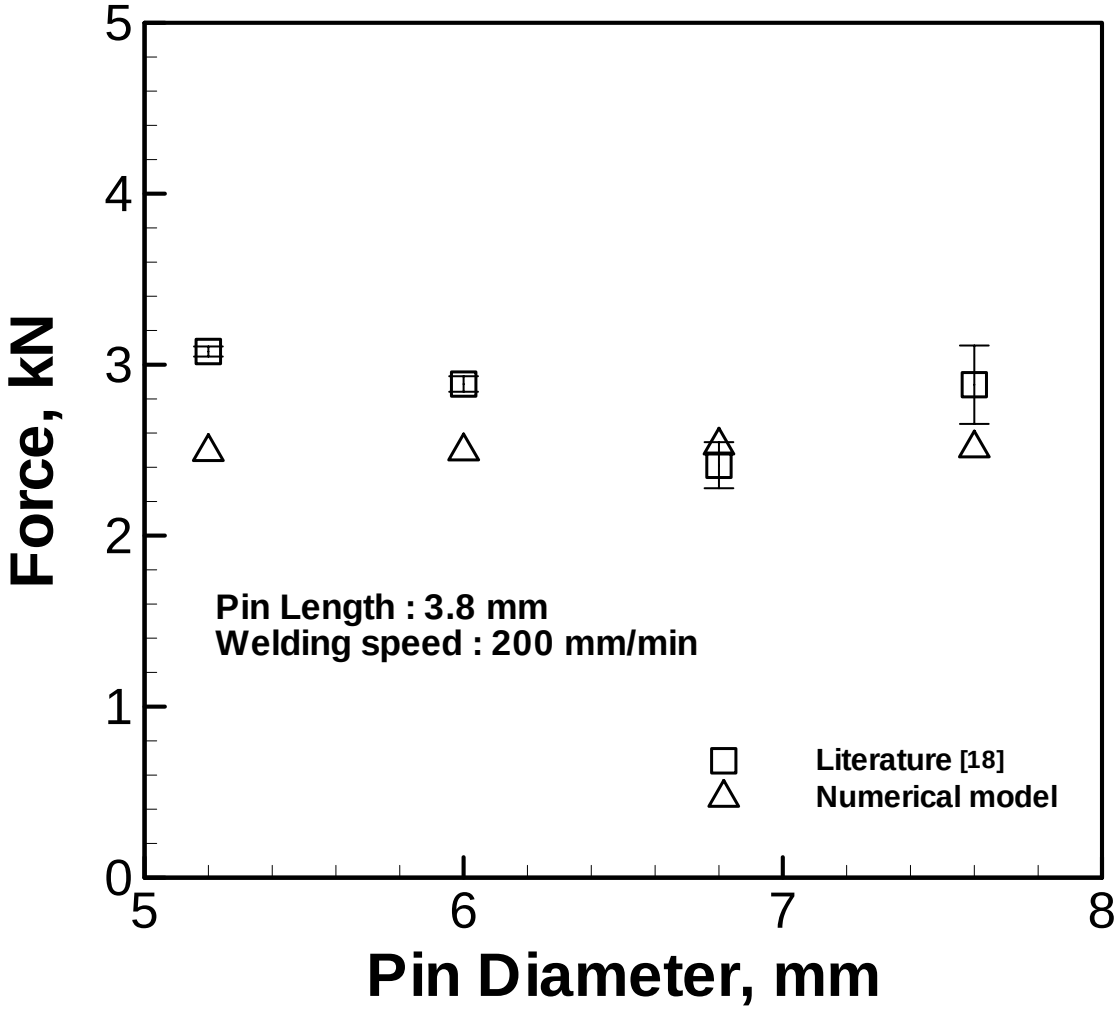

Figure 4.6 A comparison of the computed and corresponding experimentally measured total traverse force for FSW of AA6061 as a function of pin diameter. [18] The welding velocity is 3.33 mm/s, tool rotational speed is 650 RPM and the pin length is 3.8 mm. [18]

Figure 4.7 shows the computed values of the tool pin force with respect to the tool pin length calculated from Equation 4.15. The pin force increases with an increase in the tool pin length. The experimentally measured traverse force does not mention individual values of the force on the shoulder and the pin. However, the computed values of pin force give an insight about the thermo-mechanical environment around the tool pin during FSW. Since most of the tool failures occur at the tool pin, the knowledge of the force distribution on the tool pin is very important. Sorensen and Stahl [18] presented a regression based model to estimate the pin force values for the FSW of AA6061 for pin lengths between 2.5 mm and 5.5 mm. Figure 4.7 also shows the pin force values estimated from the regression model. The estimated values from the regression model are

of similar order of magnitude to the numerically computed pin force values. The difference in the two sets of values can be attributed to the fact that the regression model is not based on the experimentally measured values of pin force. Although there are differences in the estimates pin force values, the computed total force values using the numerical model are in good agreement with the experimentally measured values.

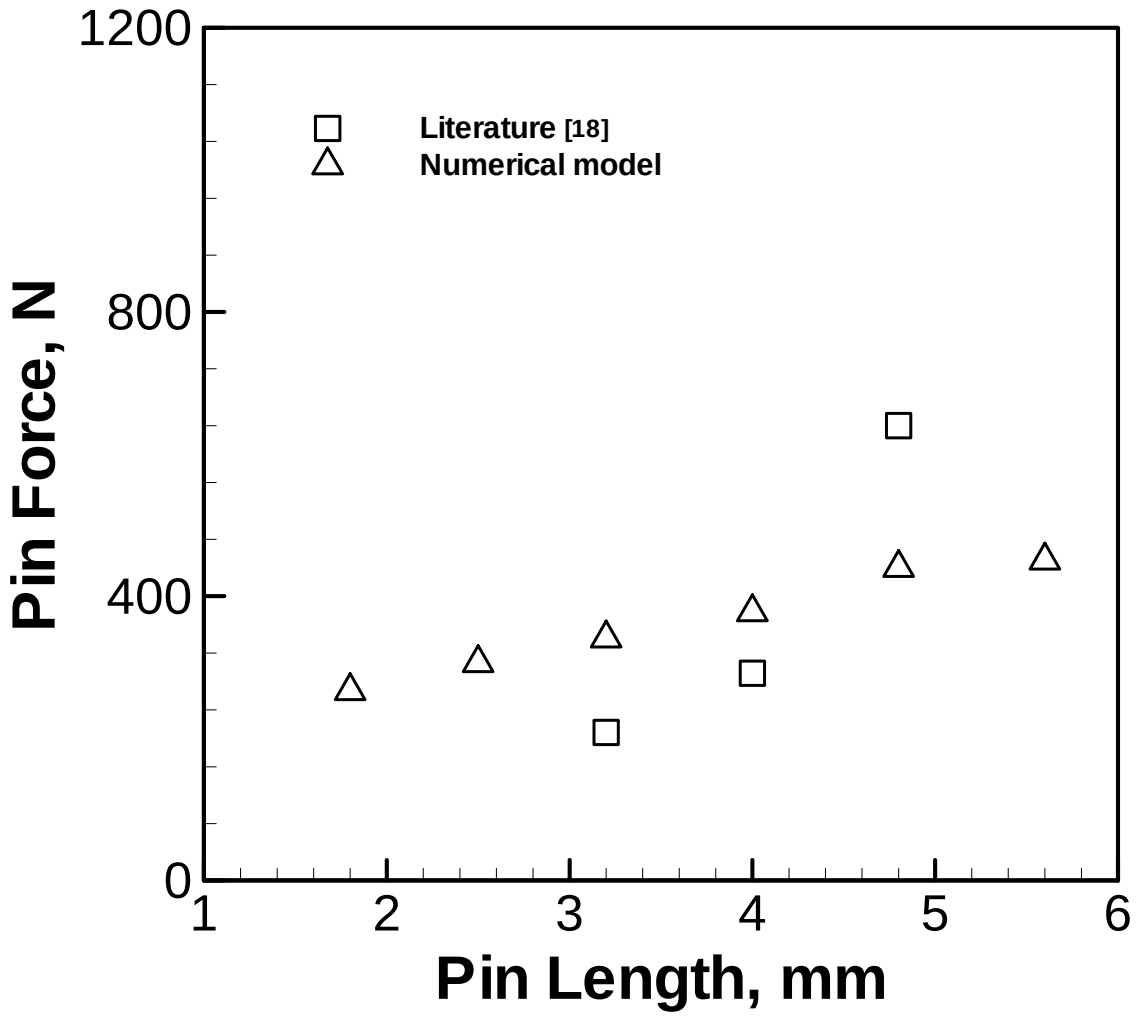

Figure 4.7 A comparison of the force on the tool pin computed and the estimated values based on regression analysis model [18] for different pin lengths. The welding velocity is 3.33 mm/s, tool rotational speed is 650 RPM and the pin diameter is 7.6 mm. [18]

Figure 4.8 shows the distribution of the computed tool pin forces along the length of the tool pin for FSW of AA6061. A tool pin with a diameter of 7.6 mm and length of 3.8 mm is considered. The welding is done with a tool rotational speed of 650 RPM and a welding speed of 3.33 mm/s. The computed force on the pin continuously increases from the root of the pin to the tip of the pin. Since the tip of the tool pin is moving, the material

at lower temperature compared to the material near the root, the pin experiences greater resistance near the tip compared to the root. In terms of structure, the tool pin can be compared with a cantilever beam with one end fixed. The distribution of the force on the pin leads to bending moment on the pin resulting in bending stress (σ_B) and shear stress (τ_B) along and perpendicular to the axis of the pin, respectively. In addition to the traverse force, the pin also experiences shear stress (σ_T) due to torque on the pin resulting from the resistance to tool rotation. The load bearing capacity of the tool pin during FSW can be determined from the total stress resulting from the stresses due to both bending and torsion.

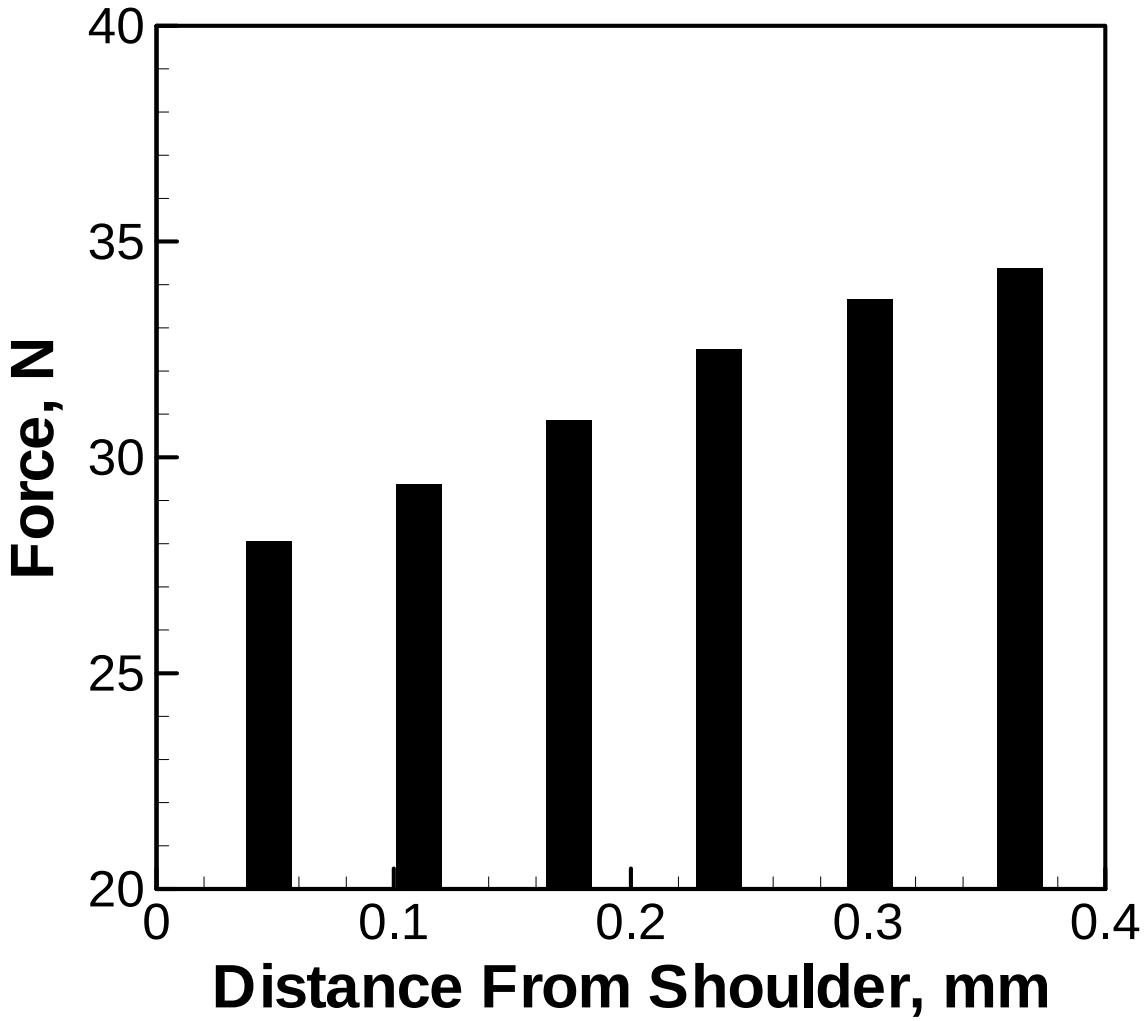

Figure 4.8 Typical distribution of traverse force from the root to the tip of a tool pin for a given pin geometry. The welding velocity is 3.33 mm/s, tool rotational speed is 650 RPM, the pin diameter is 7.6 mm and the pin length is 3.8 mm.

The maximum shear stress, τ_{MAX}, acting at any point on the surface of a tool pin with circular cross-section can be computed as shown in Equation 4.9. Figures 4.9 and 4.10 show the computed maximum shear stress, τ_{MAX}, as a function of the length and the diameter of the tool pin. For the tools with longer pins, the tool pin moves relatively harder workpiece at lower temperature, resulting in greater tool pin force and higher computed values of τ_{MAX}. Therefore, a tool with a longer pin, with all other parameters constant, would require a stronger tool material for longer lasting performance of the FSW tool. As the tool pin diameter increases, the maximum shear stress on the tool pin decreases as shown in figure 4.10. The lower maximum shear stress on the tool pin with larger diameter shows that the tool with larger diameter pin would be able to sustain greater bending and torsion moments with all other parameters remaining constant. The maximum shear stress experienced by the tool pin is in the range of 29-65 MPa. Considering the shear strength of the tool material (H13 tool steel) at the corresponding temperature [24], the maximum shear stress on the tool pin is within the factor of safety of 14 for FSW of AA6061.

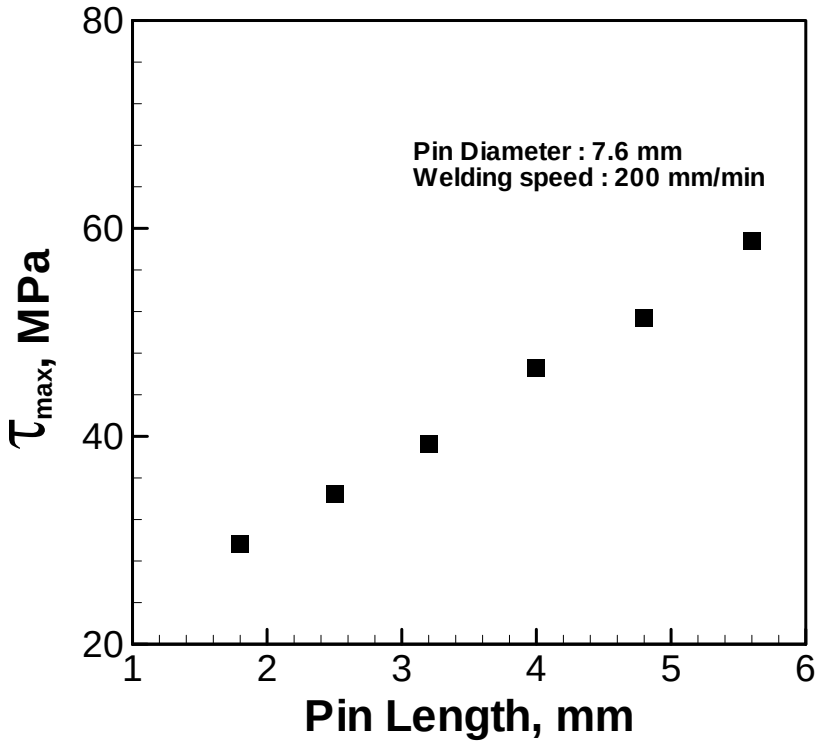

Figure 4.9 The computed maximum shear stress (τ_{max}) on the tool pin as a function of the pin length during FSW of AA6061. The welding velocity is 3.33 mm/s, tool rotational speed is 650 RPM and the pin diameter is 7.6 mm.

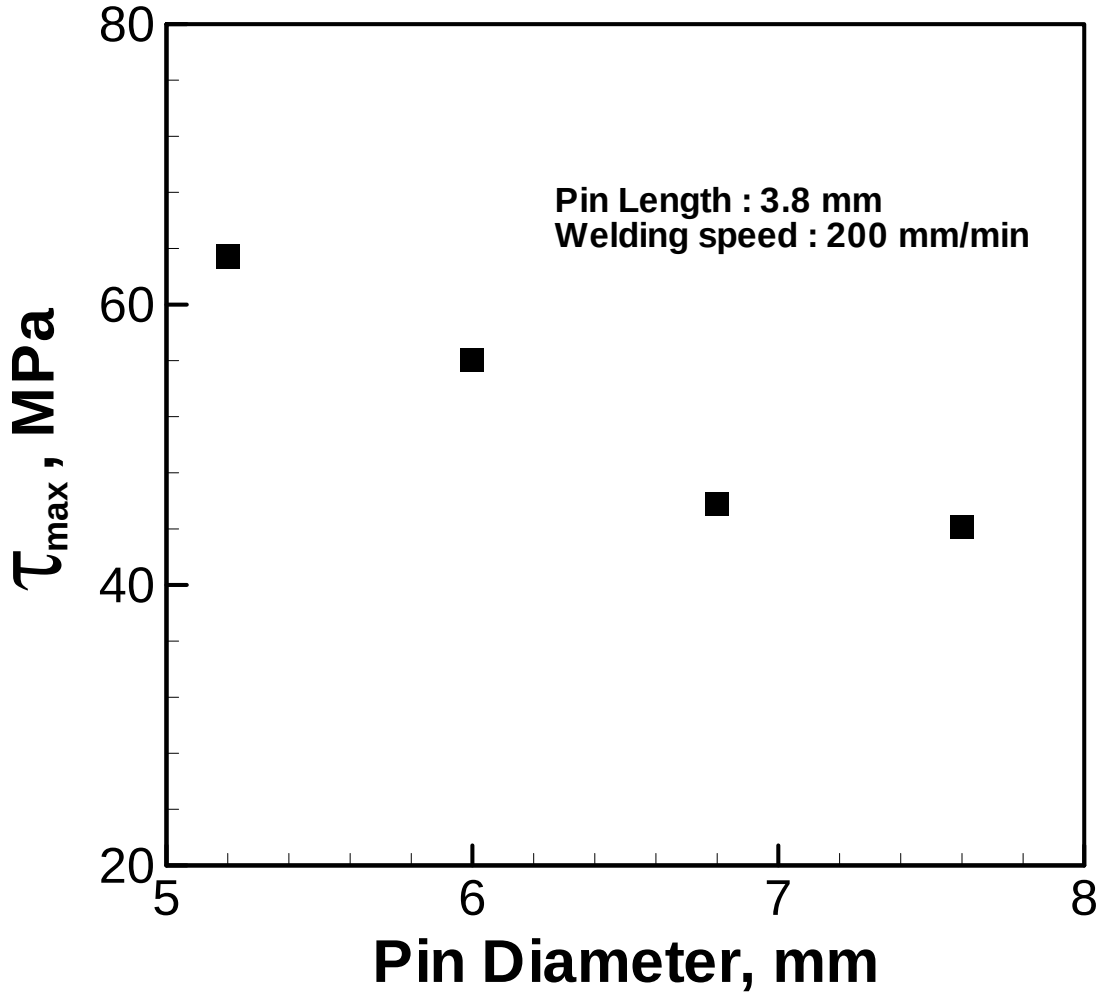

Figure 4.10 The computed maximum shear stress (τ_{max}) on the tool pin as a function of the pin diameter during FSW of AA6061. The welding velocity is 3.33 mm/s, tool rotational speed is 650 RPM and the pin length is 3.8 mm.

Gan et al. [25] reported severe deformation and reduction in pin length in the pure tungsten tool used for FSW of L80 steel plates. The torque and traverse force are computed using the tool dimensions and the welding parameters given in table 4.2. Figure 4.11 shows the tool pin force distribution along the length of the tool pin as a function of the distance from the root of the pin. As in other calculations, the force on the tool pin increases with the distance from the pin root. The maximum shear stress, τ_{MAX}, on the tool pin is computed using the force distribution and the torque on the tool pin. The computed value of the maximum shear stress, τ_{MAX}, on the tool pin at the pin root is 85 MPa. The approximate peak temperature during FSW is reported as 1273 K. [25] As shown in Figure 4.12, the shear strength of the tool material, tungsten, at this temperature

is 214 MPa. [26] Based on the computed maximum shear stress, the FSW tool in this case was operating with a factor of safety of approximately 2.5 (~214/85) which is much smaller than that used during FSW of AA6061 discussed earlier. With such a low factor of safety, the tool pin experienced severe deformation and about 12.5% reduction in length as reported by Gan et al. [25]

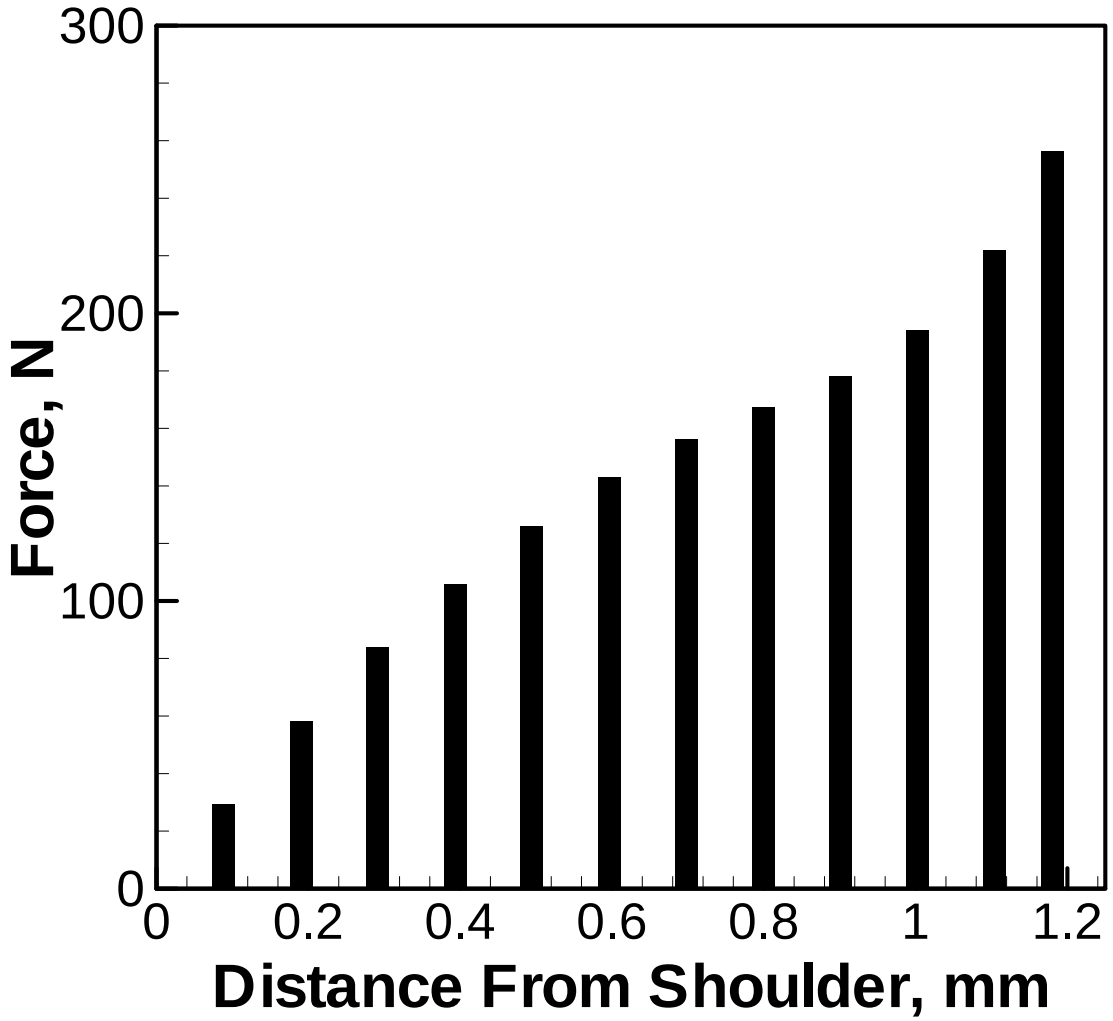

Figure 4.11 The force distribution on the tool pin during FSW of L80 steel. The welding velocity is 1.7 mm/s and the tool rotational speed is 170 RPM. [25]

Table 4.2 The tool material, dimensions and welding variables used for calculation of force and torque

Workpiece material	AA2524 [27]	Ti-6Al-4V [28]	AA-6061 [19]	L80 Steel [29]	AA 7075 [20]
Tool material	Steel	Tungsten	H13 tool steel	Commercially pure tungsten	H13 tool steel
Tool shoulder diameter, mm	20.3	25.0	25.4	35.0	26.4
Pin diameter at root, mm	7.1	19.8	5.2-7.6	20.0	5.2
Pin diameter at tip, mm	7.1	0.2	5.2-7.6	20.0	1.5
Pin length, mm	6.2	9.9	1.8-5.6	12.0	5.1
Workpiece thickness, mm	6.4	10.3	9.5	12.7	6.0
Tool rotational speed, RPM	150-800	120-800	650	170	800
Welding speed, mm s^{-1}	2.11	0.85-3.4	3.33	1.7	2.1
Axial pressure, MPa	130.7	40-137	20.0	92.5	20.0
*Specific heat, J kg^{-1} K^{-1}	$25.82 + 0.38\ T + 2.9\times10^{-5}\ T^2 + 2.7\times10^{-7}\ T^3$	$628.03 - 3.93\times10^{-1}\ T + 5.95\times10^{-4}T^2$	$9.29\times10^{2} - 6.27\times10^{-1}T + 1.48\times10^{-3}T^2 - 4.33\times10^{-8}T^3$	$3.30\times10^{+2} \times\exp(9.56\times10\text{-}^{4}T)$	$853.5 - 1.25\ T + 4.2\times10^{-4}\ T^2 - 1.3\times10^{-8}T^3$
*Thermal conductivity, W m^{-1} K^{-1}	$929.3 - 6.2\times10^{-1}\ T - 1.4\times10^{-3}\ T^2 + 4.3\times10^{-8}\ T^3$	$4.44 + 4.3\times10^{-3}\ T + 1.05\times10^{-5}\ T^2$	$2.52\times10^{1} + 3.98\times10^{-1}T + 7.36\times10^{-6}T^2 - 2.52\times10^{-7}T^3$	$47.28 - 4.2\times10^{-2}\ T + 1.1\times10^{-4}\ T^2 - 4.6\times10^{-8}\ T^3$	$74.52 + 2.5\times10^{-1}\ T - 4.2\times10^{-5}\ T^2$

* Temperature, T, in K.

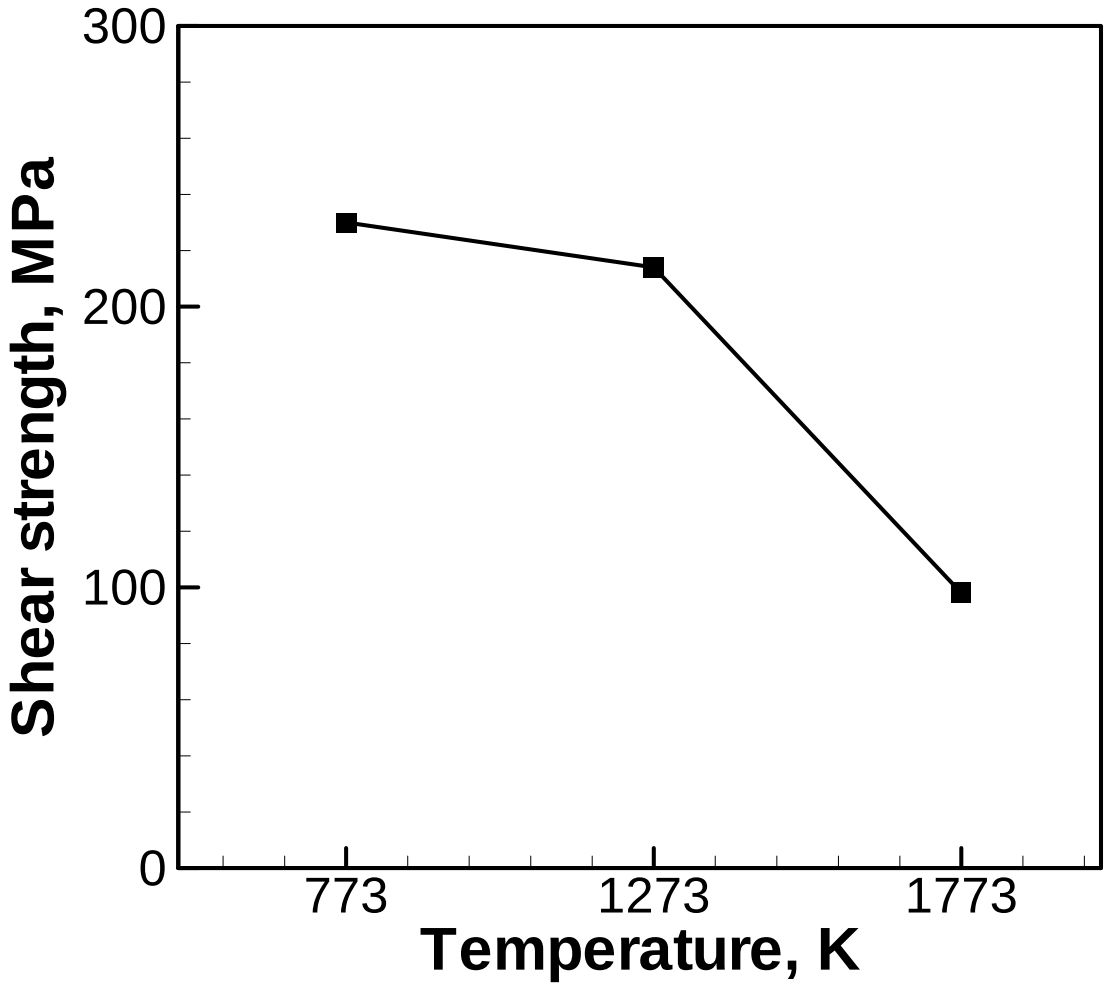

Figure 4.12 Temperature dependent shear strength of the commercially pure tungsten as reported by Kravchenko et al. [26]

Nielsen [30] used a convex scrolled shoulder step spiral (CS4) tool to study the effect of tool geometry on tool performance during FSW of AA7075 alloy. Figure 4.13 shows the tools after the use by Nielsen for FSW of AA7075 alloy. One of the pins shown sheared off at its mid-length during welding. Table 4.2 shows the welding variables and tool dimensions used in the welding experiments. [19-20,27-29] Figure 4.14 shows the computed distribution of pin force as a function of the distance from the root of the tool pin. As the tool pin failed at the mid-length, the computed value of maximum shear stress on the tool pin at its mid-length is 488 MPa. Figure 4.15 shows the shear strength of the tool material, H13 tool steel, as a function of temperature. The computed approximate peak temperature during FSW of AA7075 is 720 K. The shear strength of the H13 tool steel at this temperature is 534 MPa. [24] Since the safety factor based

on the calculations is approximately 1.1 (~534/488), the failure of the tool pin can be ascertained to such low factor of safety during FSW of AA7075.

Figure 4.13 The tools used by Neilsen during FSW of AA7075 after the use. The tool pin in the second tool from the left sheared off during welding. [30]

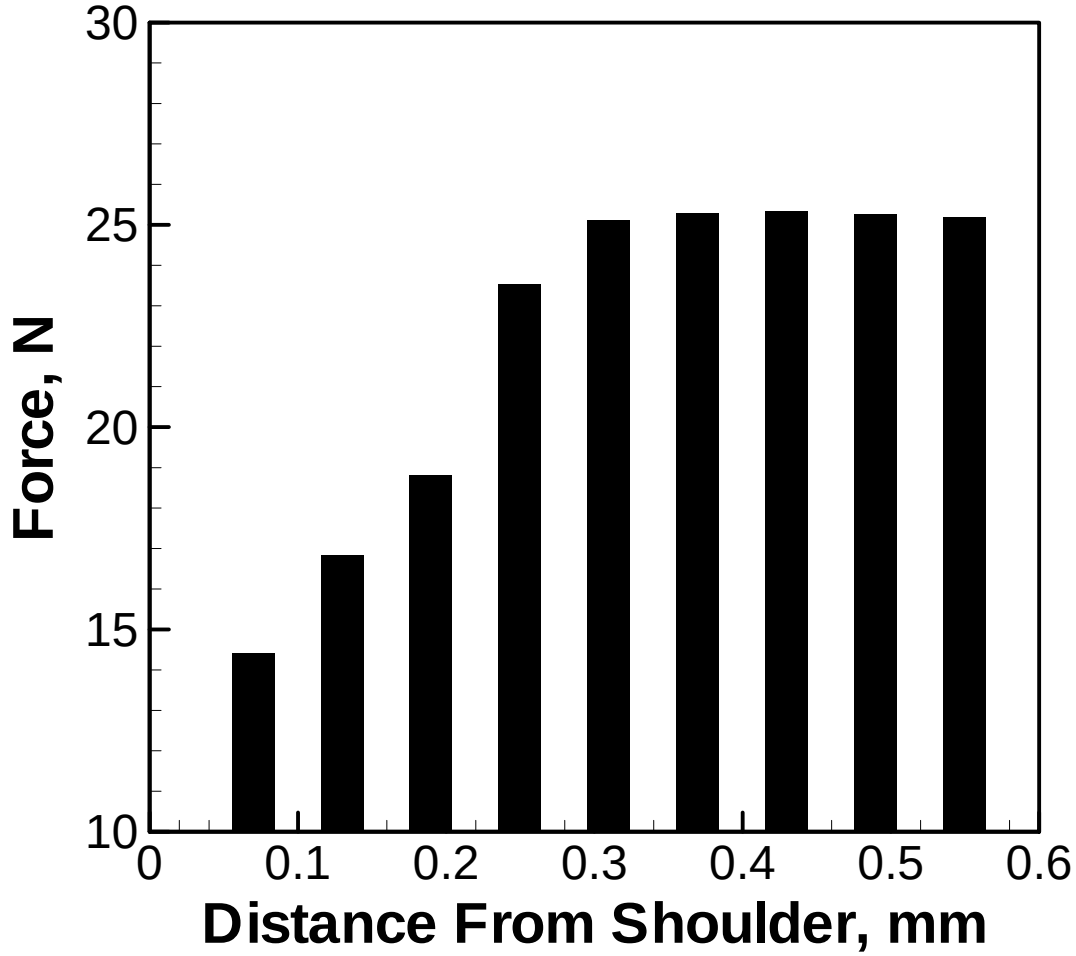

Figure 4.14 The computed force distribution of the tool pin during FSW of AA7075 alloy. The tool rotational speed is 800 RPM and welding speed is 4.66 mm/s.

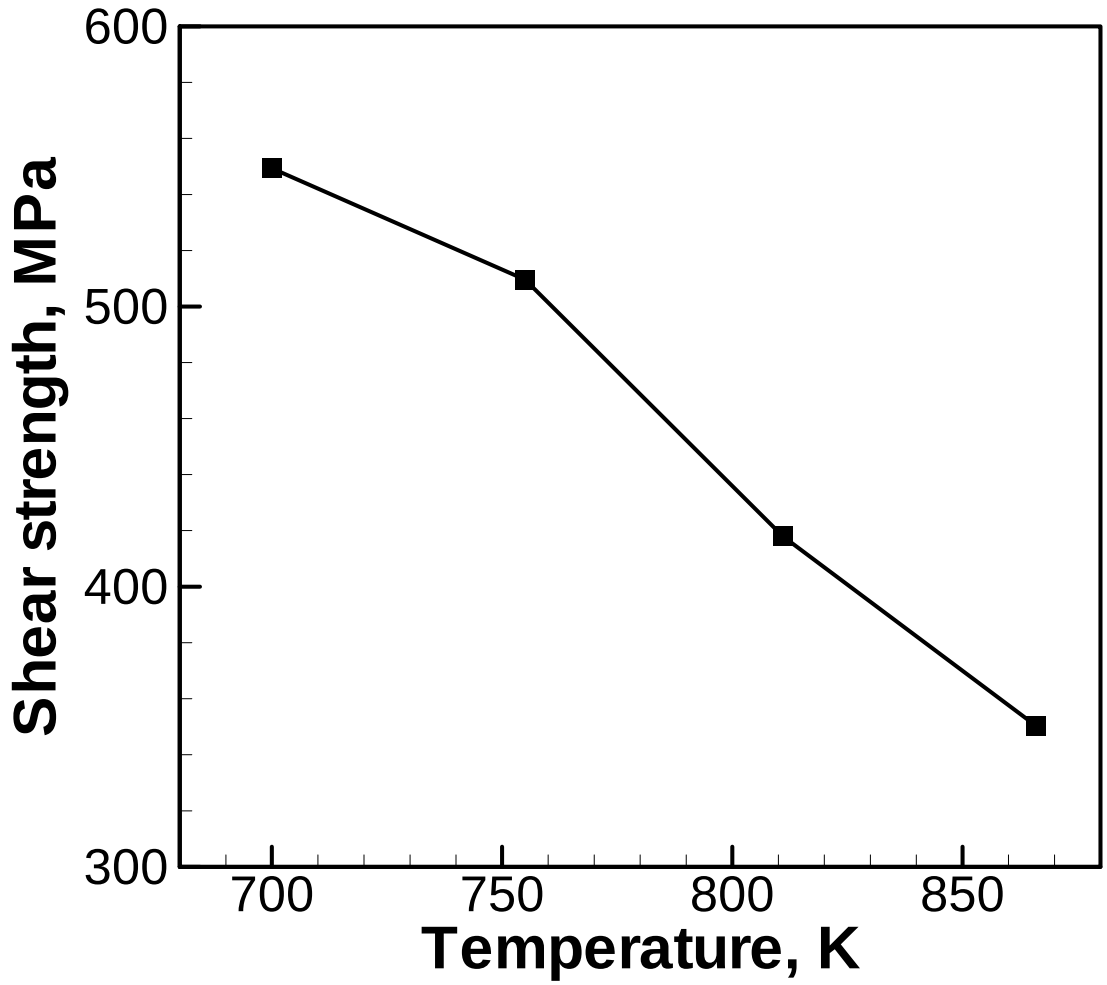

Figure 4.15 The temperature dependent shear strength of the H13 tool steel. [24]

4.3. Conclusions

The tool traverse force is computed using a three dimensional heat transfer and visco-plastic material flow model. Effects of changing welding parameters and tool dimensions on the tool traverse force are analyzed. The traverse force increases with increase in pin length, however it is not significantly affected by change in the pin diameter for the welding conditions considered. Maximum stress on the tool pin due to a combined bending and torsion is calculated by considering the pin as a cantilever beam fixed at one end. The computed maximum shear stress defines the load bearing capacity of the tool pin. With an increase in the pin length, the maximum shear stress increases. The increase in pin diameter reduces the maximum shear stress

on the tool pin when keeping all other parameters constant. The proposed methodology is used to calculate the factor of safety for different welding conditions based on the computed load bearing capacity and the shear strength of the tool material. The failure of a commercially pure tungsten tool during FSW of L80 steel and a H13 tool steel during FSW of AA7075 alloy are explained by showing very low safety factor used during welding.

4.4. References

1. H.K.D.H. Bhadeshia and T. DebRoy, Sci. Technol. Weld. Join. 14(3) (2009) 193-196.
2. R. Nandan, T. DebRoy, H.K.D.H. Bhadeshia, Prog. Mater. Sci. 53 (2008) 980-1023.
3. S. Hirasawa, H. Badarinarayan, K. Okamoto, T. Tomimura, T. Kawanami, J Mater Process Technol 210(2010) 1455-1463.
4. K. Elangovan, V. Balasubramanian, J Mater Process Technol 200(2008) 163-175.
5. D.G. Hattingh, C. Bignaut, T.I.van Niekerk and M.N. James, J Mater Process Technol 203 (2008) 46-57.
6. H. Badarinarayan, Y. Shi, X. Li, K. Okamoto, Int. J. Mach. Tools Manuf. 49 (2009) 814-823.
7. Y. Tozaki, Y. Uematsu, K. Tokaji, Int. J. Mach. Tools Manuf. 47 (2007) 2230-2236.
8. W.M. Thomas, K.I. Johnson, C.S. Wiesner, Adv. Eng. Mater. 5 (2003) 485-490.
9. W.M. Thomas, Mater. Sci. Forum 426-432 (2003) 229-236.
10. Y.H. Zhao, S.B. Lin, L. Wu, F.X. Qu, Mater. Lett. 59 (2005) 2948-2952.
11. Y.H. Zhao, S.B. Lin, F.X. Qu, L. Wu, Mater. Sci. Technol. 22 (2006) 45-50.
12. G. Buffa, J. Hua, R. Shivpuri, Mater. Sci. Eng. A. 419 (2006) pp. 381-388.
13. H. Fujii, L. Cui, M. Maeda, Mater. Sci. Eng. A. 419 (2006) 25-31.
14. K. Kumar and S. V. Kailas, Mater. Sci. Eng. A. 485 (2008) 367-374.
15. P.A. Colegrove, H.R. Shercliff, Sci. Technol. Weld. Join. 9 (2004) 345-351.
16. P.A. Colegrove, H.R. Shercliff, Sci. Technol. Weld. Join. 9 (2004) 352-361.
17. P.A. Colegrove, H.R. Shercliff, J. Mater. Process. Technol. 169 (2005) 320–327.
18. C.D. Sorensen and A.L. Stahl, Metall. Mater. Trans. B 38B (2007) 451-459.
19. A. Arora, A. De, T. DebRoy, Scr. Mater. 64(1) (2011) 9-12.
20. M. Mehta, A. Arora, A. De, T. DebRoy, Metall. Mater. Trans. A. 42A (2011) 2716-2722.
21. E.P. Popov, "Engineering Mechanics of Solids", 2nd Edition, Pearson Education, 2003, (sections 10.9, 11.4 and 13.10).
22. J.H. Yan, M.A. Sutton and A.P. Reynolds, Sci. Technol. Weld. Join. 10 (2005) 725–736
23. Jason Boyles, Process Development for and Property Evaluation of Friction Stir Welded Titanium Alloys, Master's Thesis, University of South Carolina, Columbia, SC, 2008.
24. Q. Shi, "Prediction of thermal distortion and thermal fatigue in shot sleeves", Masters thesis, 2002, The Ohio State University.
25. W. Gan, Z.T. Li, S. Khurana, Sci. Technol. Weld. Join. 12 (2007) 610–613
26. V.S. Kravchenko, I.V. Sheina, V.S. Gnuchev, E.E. Zasimchuk, V.K. Kharchenko, A.N. Vashchenko, Strength Mater. 11 (1979) 175-178.
27. A. Arora, R. Nandan, A. P. Reynolds, T. DebRoy, Scr. Mater. 60 (2009) 13-16.
28. R. Nandan, T.J. Lienert, T. DebRoy, Int. J. Mater. Res. 99(4) (2008) 434-444.
29. R. Nandan, G.G. Roy, T.J. Lienert, T. DebRoy, Acta Mater. 55 (2007) 883-895.

30. Bryce Nielsen, Developing response surfaces based on tool geometry for a convex scrolled shoulder step spiral (CS4) friction stir processing tool used to weld AL 7075, Master's Thesis, Bringham Young University, Provo, Utah, 2009.

Chapter 5. Artificial neural networks and tool safety maps in FSW

Phenomenological models [1-4] have provided detailed insight into the complex welding processes without conducting a lot of expensive experiments. Friction stir welding is a relatively new process and the understanding of the thermo-mechanical conditions around the tool and the stress on the FSW tool is still developing. For advancement of FSW as a commercial process for welding of hard alloys, there is a need to find the safe zone of operating parameters that would result in low stresses on the tool leading to longer life of the tool. Interaction of several complex physical processes in FSW results in every process parameter affecting the thermo-mechanical conditions and stress in a complex manner. The phenomenological model explained in chapters (3) and (4) has provided an understanding of the effect of process parameters on the various stresses experienced by the tool. These models are comprehensive in nature and require significant computing time. To obtain an atlas of safe working range of operating parameters for FSW as defined by low stresses on the tool, we would require repeated use of the phenomenological model to understand the effect of each process parameter on the tool stresses. However, the large amount of computing time required for the phenomenological models restricts the repeated use of these models in real time. For various other welding processes, researchers have shown the capability of the artificial neural network models to represent the complex relationships between the welding variables and material properties to the weld characteristics such as the weld geometry and the cooling rate. [5-12] These artificial neural network (ANN) models take significantly less computing time, can be used in real time and can explain the complex relationship between the input and the output variables of complex welding processes. These ANN models can be used to generate large amount of data rapidly to make an atlas of safe operating parameters for FSW which would results in lower stresses on the tool.

In case of FSW, researchers have reported use of ANN to estimate various weld properties and microstructural features for a given set of welding parameters. Atharifar [13] used the neural network to estimate optimum parameters for friction stir spot welding process. He used tool rotational speed, penetration and dwell time for friction stir spot welding as the input parameters and tensile force, plunging load and process duration as output parameters. However,

the important parameters such as welding speed and axial pressure were not considered in the input variables. Fleming et al [14] used the measured values of both axial force and traverse force to predict the tool offset position during FSW. Fratini et al [15-17] used ANN in conjunction with the finite element model to predict average grain size in FSW as function of local equivalent plastic strain, strain rate, temperature and Zener-Hollowmon parameters. Okuyucu et al [18] and Tansel et al [19] developed ANN to understand the correlation between the FSW parameters of aluminum plates and mechanical properties. They considered tool rotational speed and welding speed as the input parameters and used the ANN model to predict the tensile strength, yield strength, elongation, weld metal hardness and heat affected zone hardness. Lakshminarayanan and Balasubramanian [20] used the Response Surface methodology (RSM) and ANN to predict tensile strength of friction stir welds as function of welding speed, tool rotational speed and axial force. The ANN results were found to be better compared to RSM model. The ANN model can have better predictions for highly non-linear relationships and requires less number of experiments for training. Based on the results from the two models they concluded that the ANN model was more robust and accurate than the RSM model. [20]

These ANN models give a good understanding about how the welding variables affect weld properties. However, none of the existing models considers tool dimensions such as shoulder diameter, pin diameter, pin length as the input variables. These models also have not considered the stresses on the tool as an output. An estimation of the stresses on the FSW tool is very important to design reliable long lasting tools. The input variable ranges used for training of these ANN models were very limited and the selection of these training cases was not based on any scientific reasoning. Furthermore these models do not provide any information about the possible error in the estimated values of the output variables. A comprehensive artificial neural network model is required which uses tool dimensions and the welding parameters, such as tool rotational speed, welding velocity and axial pressure, as input and is able to predict the torque, traverse force, torque peak temperature and stresses on the FSW tool. The availability of such model will be a useful addition to the welding community to understand the thermo-mechanical conditions experienced by the tool and help in prolonging tool life based on the analysis of stresses on the tool pin.

A set of multiple artificial neural networks for FSW are developed to predict the total torque, torque components – sticking and sliding, traverse force, peak temperature and maximum

shear stress on the tool pin for a given set of input variables. The six most important welding variables, tool rotation speed, welding velocity, axial pressure, tool shoulder radius, tool pin radius and tool pin length, are considered as the input variables for the ANN model. In these calculations a tool with cylindrical pin is considered, meaning the pin radius is constant along the length of the pin. A large amount of data is required to train and test the ANN models. Some of the output parameters of these ANN models, such as sticking and sliding components of torque and maximum shear stress, cannot be determined from experiments only. These output parameters are selected because the sticking torque provides a measure of the grip of the tool on the plasticized material and the stresses on the tool determine the life of the tool. The heat transfer and visco-plastic flow model is used to generate the large amount of results to train and test the ANN models. The results of the heat transfer and visco-plastic flow model have been validated using results from independent experiments as shown previously in the chapters 3 and 4. Thus, the ANN models developed with the results of heat transfer and fluid flow model will conform to the experimental observations as well as satisfy the fundamental scientific principles. The developed neural networks are material specific. These models are used to estimate the traverse force, torque, peak temperature, maximum shear stress and bending stress on the tool pin for a large amount of input variable ranges for the welding of a given material. The peak temperature is then used to calculate the temperature dependent shear strength of the tool for those welding parameters. Based on the bending stress and fatigue calculations, it has been shown that the FSW tool failure will not occur by fatigue mechanism for the welding of thin plates as represented in Appendix B. The tool failure is thus believed to occur by shear. The tool safety factor is defined as the ratio of the tool shear strength and the maximum shear stress on the tool pin. For a given set of welding parameters the tool safety factor is calculated. These values of tool safety factor are then plotted in form of contours with respect to the shoulder radius and tool rotational speeds. These plots explain the effect of various input variables on the tool safety factor during FSW and can be used as tool durability maps to determine safe operating parameters.

5.1. Artificial Neural Network (ANN) model:

A set of artificial neural network (ANN) based models are developed to understand the effect of the friction stir welding process parameters and the tool dimensions on the peak

temperature, torque, traverse force, and stresses on the tool pin. Neural networks are a representation of the non-linear relationship between the input and the output variables. In the present work, neural networks with three-layers are considered. These three layers consist of different nodes where the input layer is made of the input nodes, output layer consists of output nodes and the hidden layer has a variable number of nodes depending on the non-linearity of the relationship between the input and the output variables. The input layer is connected to the hidden layer and the hidden layer is connected to the output layer. A schematic of the neural network based model, as used in the present work, is shown in Figure 5.1. The basic structure of the ANN model was developed by Professor Amitava De's group at Indian Institute of Technology, Bombay and is used here with their permission.

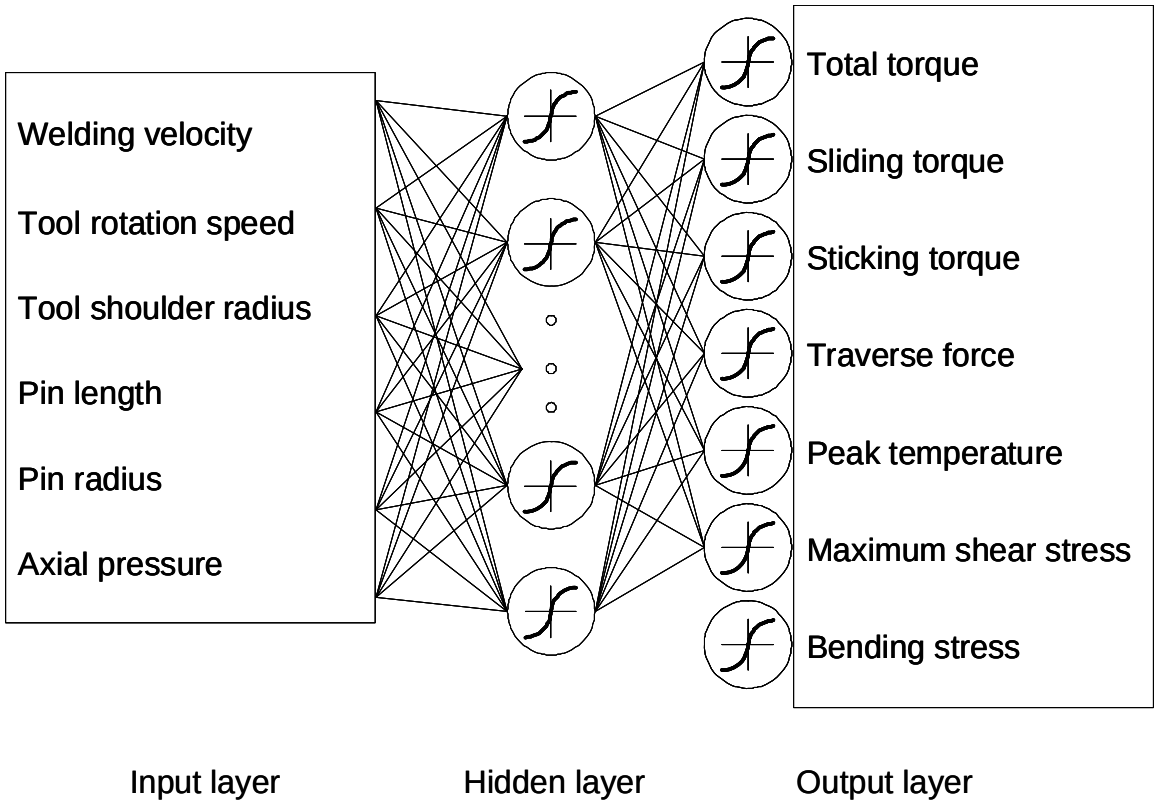

Figure 5.1 Architecture of the artificial neural network (ANN) model.

The input variables are connected to the output of the model via the nodes in the hidden layer as shown in Figure 5.1. The output of a specific node in either the hidden layer or in the output layer is computed using a hyperbolic tangent function, which is a symmetrical sigmoid function, as

$$y = \tanh\left(\sum_{i=1}^{N} w_i x_i + \theta_i\right) \tag{5.1}$$

where y is the output of a node, x_i is the input, w_i is the weight and θ_i is the bias attached to the i^{th} input node and N is the total number of input nodes contributing to the output node. Corresponding to each output in Figure 5.1, a separate neural network model is developed. The feed forward back propagation algorithm with the gradient descent approach is used for the optimization of the weights for the nodes by minimizing the following objective function, E,

$$\mathrm{E} = \frac{1}{\mathrm{N}}\left(\sum_{\mathrm{i=1}}^{\mathrm{N}} (\mathrm{d_i} - \mathrm{y_i})^2\right) \tag{5.2}$$

where E is the squared error between the desired and the corresponding predicted outputs, N is the number of training datasets, d_i and y_i are the desired and the corresponding estimated output for the i^{th} data-set. The weights are typically updated as

$$\mathrm{w_{i+1}} = \mathrm{w_i} - \left(\eta \frac{\partial \mathrm{E}}{\partial \mathrm{w}} + \varphi \frac{\partial^2 \mathrm{E}}{\partial \mathrm{w}^2}\right) \tag{5.3}$$

where η and φ refer to learning rate and momentum transfer constant, respectively, and w_{i+1} and w_i refer to the weights for the nodes in two successive iterations. The training of the neural network models are performed in batch mode to ensure equal importance of all the training data-sets.

The methodology outlined above for the optimization of the weights (i.e. the training of neural network models) cannot provide the uncertainty in the final predictions. The predictions from a neural network model would be useful in real design purpose only if the uncertainty or the reliability in prediction is also known. Hence, the Bayesian approach [21-23] for the training of the neural network models is adopted that facilitates the estimation of the uncertainty of the prediction from neural network models. In the Bayesian approach, the objective function, E, is expressed as

$$\mathrm{E} = \beta \mathrm{E_D} + \alpha \mathrm{E_W} \tag{5.4}$$

where β and α are two regularizer terms referring to the inverse of error variance due to presumed noise in training data-set and in weight distribution, respectively. The terms E_D and E_W refer to the noise or error in data and in weight distributions, and are expressed as

$$E_D = \frac{1}{N}\left(\sum_{i=1}^{N}(d_i - y_i)^2\right) \tag{5.5}$$

$$E_W = \frac{1}{2}\sum_{j=1}^{M} w_i^2 \tag{5.6}$$

where M refers to the number of weights in a neural network model. [21-23] The two regularizer terms, β and α, are also optimized along with the weights to enhance the posterior probability of the weights of the nodes for a neural network model. The posterior probability of the weights, $P(W \mid D)$, is estimated using the Bayesian theorem of conditional probability as

$$P(W \mid D) = \frac{P(D \mid W)P(W)}{P(D)} \tag{5.7}$$

where P(W) refers to the prior distribution of weights and is expressed as

$$P(W) = \frac{1}{\int \exp(-\alpha E_W)dw}\exp(-\alpha E_W) = \frac{\exp(-\alpha E_W)}{(2\pi/\alpha)^{M/2}} \tag{5.8}$$

where M is the total number of weights. The term, $P(D \mid W)$, refers to the conditional probability of a data-set for a given weight distribution and is expressed as

$$P(D \mid W) = \frac{1}{\int \exp(-\beta E_D)dD}\exp(-\beta E_D) = \frac{\exp(-\beta E_D)}{(2\pi/\beta)^{N/2}} \tag{5.9}$$

where N is the total number of training data-set. The term P(D) in equation (5.7) acts as a normalizing factor since it is defined as $P(D) = \int P(D \mid W)P(W)dw$. Hence, equation (5.7) can be rewritten as

$$P(W \mid D) \approx P(D \mid W)P(W) = \frac{\exp(-\beta E_D - \alpha E_W)}{(2\pi/\beta)^{N/2}(2\pi/\alpha)^{W/2}} \tag{5.10}$$

Equation (5.10) depicts that the posterior probability of the weights of the nodes of the neural network model and can be maximized by minimizing the negative logarithm of the squared error, E, as given in equation (5.4), with respect to the regularizer terms, β and α. The optimum values of β and α corresponding to the most probable weight distribution with the maximum posterior probability are given as [21-23]

$$\beta^{MP} = \frac{M - \gamma}{2E_D^{MP}} \tag{5.11}$$

$$\alpha^{MP} = \frac{\gamma}{2E_W^{MP}} \quad (5.12)$$

where M is the total number of weights, and E_D^{MP} and E_W^{MP} refer to the to the noise or error in data and in weight distributions corresponding to the most probable weights with the maximum posterior probability. The term γ is referred to the effective number of parameters in the neural network model and is expressed as $\gamma = N_P - 2\alpha^{MP}\text{trace}(H^{MP})^{-1}$. The term N_P refers to the total number of parameters in the neural network model and typically considered as $N_P = N_H + M + 1$, where N_H is the number of hidden nodes and M is the number of weights. The term, H^{MP} is computed as

$$H^{MP} = \beta^{MP}\nabla^2 E_D^{MP} + \alpha^{MP}\nabla^2 E_W^{MP} \quad (5.13)$$

Following equations (5.4) to (5.13), several neural network models with the number of hidden nodes from one to eighteen (three times the number of input nodes) are trained for a given training data-set. The performance of these neural network models are compared based on the respective log-predictive error (LPE) which is computed as

$$\text{LPE} = \frac{1}{2(1/\beta^{MP})^2}(N \times E_D^{MP}) + \log\left(\sqrt{2\pi\frac{1}{\beta^{MP}}}\right) \quad (5.14)$$

The neural network model architecture with the least LPE is selected as the best and is expected to provide a balance between over- or under-fitting and the complexity of model. The variance or the uncertainty corresponding to the outputs of the neural network model is calculated as [21-23]

$$\sigma_w^2 = g^T(H^{MP})^{-1}g \quad (5.15)$$

where g refers to the sensitivity of the output of the neural network model with respect to the corresponding individual weights and is computed as $g = \partial y_i / \partial w_i$ considering the weights with the maximum posterior probability.

The heat transfer and visco-plastic material flow model is used to generate the data sets to train the ANN model. The important input variables during FSW process are identified as the tool rotational speed, welding speed, axial pressure, tool shoulder radius, tool pin radius and tool pin length. In FSW experiments the length of the FSW tool pin is usually considered based on the thickness of the workpiece material to obtain full penetration and good weld characteristics. Thus the workpiece thickness is considered as a variable and the length of the tool pin is taken as 90% of the thickness of the workpiece.

Training of the ANN models is done using datasets generated considering two different design of experiment concepts. *Taguchi's design of experiments* and *central composite rotatable design* (*CCD*), which facilitates a significant reduction in the total number of required calculations for a quantitative understanding of the influence of a large number of unknown input variables on a response parameter in comparison to *full factorial design of experiments*. [24-25] Ten levels of values are considered for these input variables to train the ANN models, five for Taguchi's L50 array and five for CCD array. The ANN models are then tested for five different levels of these input parameters which lie in the same range as the training variable levels. Table 5.1 lists these input variable levels for both training and testing of ANN models for FSW of AA7075.

Table 5.1 Levels of the six input variables used for training and testing of the ANN models for FSW of AA7075

Input variable	Shoulder Radius (cm)	Pin radius (cm)	Pin length (cm)	Weld velocity (cm/s)	Rotational Speed (RPM)	Axial Pressure (MPa)
Levels for training (L50)	0.75	0.200	0.27	0.1	300	18
	1.00	0.225	0.35	0.2	420	20
	1.25	0.250	0.43	0.3	570	22
	1.50	0.275	0.55	0.4	750	25
	1.75	0.300	0.93	0.5	900	27
Levels for training (CCD)	0.75	0.25	0.27	0.1	300	18
	0.99	0.28	0.41	0.23	494	22.53
	1.1	0.3	0.5	0.3	600	25
	1.26	0.32	0.56	0.37	706	27.47
	1.5	0.35	0.7	0.5	900	32
Levels for testing (L50)	0.9	0.21	0.306	0.15	360	19
	1.1	0.24	0.387	0.25	480	21
	1.3	0.26	0.468	0.33	630	23
	1.4	0.27	0.513	0.36	680	24
	1.6	0.29	0.594	0.45	820	26

Table 5.2 Combinations of input variables and corresponding output parameters for the training of ANN models for FSW of AA7075

Training data for AA7075												
Shoulder radius, cm	Pin radius, cm	Pin length, cm	Welding velocity, cm/s	Tool rotational speed, rpm	Axial pressure, Mpa	Total torque, Nm	Sticking torque, Nm	Sliding torque, Nm	Peak temperature, K	Total force, N	Max shear90, Mpa	Bending stress, MPa
0.75	0.200	0.27	0.1	300.0	18.0	18.19	14.40	3.79	549.68	1403.80	273.90	164.46
0.75	0.225	0.35	0.2	420.0	20.0	16.33	12.51	3.83	569.16	1636.80	287.59	203.78
0.75	0.250	0.43	0.3	570.0	22.0	15.26	11.81	3.44	591.13	1778.50	281.61	221.88
0.75	0.275	0.55	0.4	750.0	25.0	15.67	12.39	3.28	613.97	2211.10	301.71	316.19
0.75	0.300	0.63	0.5	900.0	27.0	15.92	12.75	3.18	601.11	2899.20	292.33	417.02
1.00	0.200	0.35	0.4	570.0	27.0	22.57	13.07	9.50	637.19	1922.50	182.56	143.64
1.00	0.225	0.43	0.5	750.0	18.0	19.13	14.01	5.11	636.96	1473.20	211.22	186.35
1.00	0.250	0.55	0.1	900.0	20.0	16.34	11.81	4.53	671.17	1500.60	184.53	189.82
1.00	0.275	0.63	0.2	300.0	22.0	42.97	31.47	11.50	589.98	3521.80	393.85	429.13
1.00	0.300	0.27	0.3	420.0	25.0	26.62	15.45	11.17	632.48	2005.20	91.26	36.59
1.25	0.200	0.43	0.2	900.0	25.0	22.27	11.70	10.56	712.02	1715.50	109.51	113.52
1.25	0.225	0.55	0.3	300.0	27.0	60.07	35.16	24.91	619.47	3926.30	301.51	345.09
1.25	0.250	0.63	0.4	420.0	18.0	47.29	32.42	14.87	631.68	3085.80	309.67	377.81
1.25	0.275	0.27	0.5	570.0	20.0	30.46	16.93	13.53	690.66	1946.10	70.08	29.24
1.25	0.300	0.35	0.1	750.0	22.0	24.27	12.66	11.62	712.76	1717.10	53.07	30.03
1.50	0.200	0.55	0.5	420.0	22.0	68.17	36.49	31.69	678.18	3829.10	242.42	296.13
1.50	0.225	0.63	0.1	570.0	25.0	50.61	21.06	29.55	709.09	3591.40	147.40	210.45
1.50	0.275	0.35	0.3	900.0	18.0	27.37	13.85	13.52	734.43	1623.70	34.09	20.17
1.50	0.300	0.43	0.4	300.0	20.0	79.88	46.49	33.39	663.29	3859.90	131.56	78.31
1.75	0.200	0.63	0.3	750.0	20.0	49.31	20.82	28.49	733.80	3037.60	116.46	197.56
1.75	0.250	0.35	0.5	300.0	25.0	105.66	43.00	62.66	717.56	5624.00	80.99	47.72
1.75	0.275	0.43	0.1	420.0	27.0	79.69	19.93	59.76	738.73	5373.70	40.72	29.69
1.75	0.300	0.55	0.2	570.0	18.0	59.38	26.22	33.16	723.03	3356.90	68.92	66.66
0.75	0.200	0.27	0.5	750.0	25.0	10.27	7.36	2.91	604.50	1073.40	182.29	115.54

0.75	0.225	0.35	0.1	900.0	27.0	9.27	6.69	2.58	631.95	1067.20	170.57	122.00
0.75	0.250	0.43	0.2	300.0	18.0	23.30	19.23	4.07	548.33	2270.00	392.14	301.36
0.75	0.275	0.55	0.3	420.0	20.0	22.46	18.14	4.32	572.80	2860.70	407.24	408.75
0.75	0.300	0.63	0.4	570.0	22.0	20.83	16.59	4.23	569.61	3540.50	363.42	495.39
1.00	0.200	0.35	0.3	300.0	22.0	34.69	23.90	10.79	588.38	2234.80	268.04	207.27
1.00	0.225	0.43	0.4	420.0	25.0	30.60	19.69	10.92	607.88	2448.80	268.28	232.60
1.00	0.250	0.55	0.5	570.0	27.0	28.17	18.45	9.72	630.97	2691.20	283.14	315.32
1.00	0.275	0.63	0.1	750.0	18.0	20.19	14.98	5.21	656.67	1887.40	225.66	243.34
1.00	0.300	0.27	0.2	900.0	20.0	13.64	8.98	4.66	690.14	1000.00	58.27	25.24
1.25	0.200	0.43	0.1	570.0	20.0	30.87	17.56	13.31	676.67	2114.60	171.10	160.05
1.25	0.225	0.55	0.2	750.0	22.0	27.45	15.94	11.51	687.06	2083.30	171.18	202.20
1.25	0.250	0.63	0.3	900.0	25.0	26.12	15.47	10.65	703.88	2129.30	166.28	209.53
1.25	0.275	0.27	0.4	300.0	27.0	52.02	27.05	24.97	656.38	3262.70	90.13	35.82
1.25	0.300	0.35	0.5	420.0	18.0	41.48	26.25	15.22	648.38	2346.10	114.61	57.98
1.50	0.200	0.55	0.4	900.0	18.0	32.41	18.95	13.46	714.40	1905.80	134.43	196.10
1.50	0.225	0.63	0.5	300.0	20.0	89.59	56.56	33.03	638.26	4322.80	336.82	441.34
1.50	0.250	0.27	0.1	420.0	22.0	52.49	20.90	31.59	714.55	3336.90	42.76	19.51
1.50	0.275	0.35	0.2	570.0	25.0	45.05	15.48	29.57	731.24	3202.10	38.70	22.32
1.50	0.300	0.43	0.3	750.0	27.0	38.57	13.58	24.99	739.47	2808.50	39.32	28.72
1.75	0.200	0.63	0.2	420.0	27.0	87.97	28.29	59.69	724.26	5660.40	151.95	238.46
1.75	0.225	0.27	0.3	570.0	18.0	49.75	16.94	32.81	743.99	3053.60	26.17	13.08
1.75	0.250	0.35	0.4	750.0	20.0	42.57	14.09	28.47	753.20	2771.50	21.45	14.48
1.75	0.275	0.43	0.5	900.0	22.0	39.87	14.27	25.60	755.90	2573.00	27.54	22.67
1.75	0.300	0.55	0.1	300.0	25.0	107.52	44.47	63.05	700.82	5876.50	101.57	90.38
0.99	0.28	0.41	0.23	494.0	22.53	24.95	16.15	8.80	629.84	2048.40	166.09	105.61
1.26	0.28	0.41	0.23	494.0	22.53	37.89	20.36	17.53	680.43	2620.20	117.01	72.61
0.99	0.32	0.41	0.23	494.0	22.53	25.57	16.58	8.99	636.41	2103.00	135.93	79.10
1.26	0.32	0.41	0.23	494.0	22.53	38.41	20.72	17.69	684.98	2647.30	97.03	54.79
0.99	0.28	0.56	0.23	494.0	22.53	38.41	20.72	17.69	684.98	2647.30	97.03	54.79
1.26	0.28	0.56	0.23	494.0	22.53	41.17	23.53	17.63	672.20	2954.10	177.87	156.61
0.99	0.32	0.56	0.23	494.0	22.53	28.68	19.55	9.13	626.93	2709.00	200.52	182.09

1.26	0.32	0.56	0.23	494.0	22.53	41.88	24.06	17.82	671.71	3039.10	145.82	119.66
0.99	0.28	0.41	0.37	494.0	22.53	26.10	17.22	8.88	626.70	2118.20	178.76	115.04
1.26	0.28	0.41	0.37	494.0	22.53	39.35	21.76	17.60	676.09	2655.60	124.74	76.11
0.99	0.32	0.41	0.37	494.0	22.53	26.83	17.74	9.09	630.48	2186.10	146.89	86.64
1.26	0.32	0.41	0.37	494.0	22.53	39.99	22.22	17.78	678.72	2691.50	104.79	57.80
0.99	0.28	0.56	0.37	494.0	22.53	29.51	20.50	9.01	623.41	2693.90	270.80	263.14
1.26	0.28	0.56	0.37	494.0	22.53	43.16	25.43	17.73	665.92	3036.60	193.99	173.98
0.99	0.32	0.56	0.37	494.0	22.53	30.46	21.18	9.28	622.69	2890.30	219.99	205.28
1.26	0.32	0.56	0.37	494.0	22.53	24.95	16.15	8.80	629.84	2048.40	166.09	105.61
0.99	0.28	0.41	0.23	706.0	22.53	18.90	12.35	6.55	659.32	1609.40	136.59	84.47
1.26	0.28	0.41	0.23	706.0	22.53	29.36	16.21	13.15	700.39	2069.00	96.29	63.23
0.99	0.32	0.41	0.23	706.0	22.53	20.36	13.62	6.74	661.45	1702.80	120.37	68.83
1.26	0.32	0.41	0.23	706.0	22.53	29.81	16.53	13.28	703.27	2084.20	79.41	47.65
0.99	0.28	0.56	0.23	706.0	22.53	22.37	15.67	6.70	652.12	2119.80	218.46	212.07
1.26	0.28	0.56	0.23	706.0	22.53	32.50	19.27	13.23	692.42	2393.40	154.42	142.17
0.99	0.32	0.56	0.23	706.0	22.53	23.17	16.29	6.87	650.47	2261.70	178.45	164.59
1.26	0.32	0.56	0.23	706.0	22.53	18.90	12.35	6.55	659.32	1609.40	136.59	84.47
0.99	0.28	0.41	0.37	706.0	22.53	28.20	15.07	13.13	704.14	2019.20	86.41	56.75
1.26	0.28	0.41	0.37	706.0	22.53	19.46	12.79	6.66	668.81	1645.90	112.79	63.13
0.99	0.32	0.41	0.37	706.0	22.53	28.55	15.31	13.25	708.15	2026.60	70.73	42.61
1.26	0.32	0.41	0.37	706.0	22.53	28.55	15.31	13.25	708.15	2026.60	70.73	42.61
0.99	0.28	0.56	0.37	706.0	22.53	30.91	17.75	13.16	697.24	2327.70	140.29	131.50
1.26	0.28	0.56	0.37	706.0	22.53	21.81	15.05	6.77	654.76	2120.60	163.06	145.73
0.99	0.32	0.56	0.37	706.0	22.53	31.37	18.08	13.29	695.59	2395.40	113.20	101.15
1.26	0.32	0.56	0.37	706.0	22.53	20.44	12.50	7.94	662.90	1830.50	139.39	87.78
0.99	0.28	0.41	0.23	494.0	27.47	25.88	15.28	10.60	636.49	2274.00	158.42	100.85
1.26	0.28	0.41	0.23	494.0	27.47	39.93	18.65	21.28	689.91	3022.20	107.08	68.37
0.99	0.32	0.41	0.23	494.0	27.47	26.50	15.73	10.78	642.40	2314.50	130.20	75.55
1.26	0.32	0.41	0.23	494.0	27.47	40.41	18.97	21.44	693.29	3033.00	88.45	51.34
0.99	0.28	0.56	0.23	494.0	27.47	40.41	18.97	21.44	693.29	3033.00	88.45	51.34
1.26	0.28	0.56	0.23	494.0	27.47	43.27	21.90	21.37	680.61	3348.80	167.22	148.28

0.99	0.32	0.56	0.23	494.0	27.47	29.62	18.70	10.92	633.00	2900.90	194.11	175.10
1.26	0.32	0.56	0.23	494.0	27.47	43.94	22.39	21.54	680.41	3417.80	136.93	113.38
0.99	0.28	0.41	0.37	494.0	27.47	27.02	16.35	10.67	633.10	2343.40	171.06	110.23
1.26	0.28	0.41	0.37	494.0	27.47	41.43	20.10	21.33	685.63	3064.50	116.40	72.60
0.99	0.32	0.41	0.37	494.0	27.47	27.74	16.86	10.88	636.74	2397.60	140.89	83.08
1.26	0.32	0.41	0.37	494.0	27.47	42.02	20.53	21.50	687.49	3084.70	97.42	55.00
0.99	0.28	0.56	0.37	494.0	27.47	30.42	19.61	10.81	628.53	2905.70	261.75	254.36
1.26	0.28	0.56	0.37	494.0	27.47	45.28	23.82	21.46	674.45	3430.00	183.51	164.06
0.99	0.32	0.56	0.37	494.0	27.47	31.37	20.30	11.07	628.35	3082.20	213.11	198.25
1.26	0.32	0.56	0.37	494.0	27.47	25.88	15.28	10.60	636.49	2274.00	158.42	100.85
0.99	0.28	0.41	0.23	706.0	27.47	19.64	11.75	7.89	667.11	1784.70	131.08	80.82
1.26	0.28	0.41	0.23	706.0	27.47	30.70	14.74	15.96	709.20	2366.00	86.20	57.51
0.99	0.32	0.41	0.23	706.0	27.47	21.07	12.99	8.07	667.94	1863.40	115.72	65.95
1.26	0.32	0.41	0.23	706.0	27.47	31.14	15.04	16.10	710.86	2366.30	71.29	43.41
0.99	0.28	0.56	0.23	706.0	27.47	23.06	15.01	8.04	658.64	2278.90	211.96	204.26
1.26	0.28	0.56	0.23	706.0	27.47	33.91	17.88	16.02	699.93	2691.60	144.25	135.40
0.99	0.32	0.56	0.23	706.0	27.47	23.84	15.63	8.21	657.01	2404.20	172.81	158.50
1.26	0.32	0.56	0.23	706.0	27.47	19.64	11.75	7.89	667.11	1784.70	131.08	80.82
0.99	0.28	0.41	0.37	706.0	27.47	29.51	13.59	15.93	712.73	2315.20	76.15	50.83
1.26	0.28	0.41	0.37	706.0	27.47	20.17	12.16	8.00	675.13	1811.70	108.07	60.76
0.99	0.32	0.41	0.37	706.0	27.47	29.84	13.81	16.03	715.73	2307.90	62.51	38.25
1.26	0.32	0.41	0.37	706.0	27.47	29.84	13.81	16.03	715.73	2307.90	62.51	38.25
0.99	0.28	0.56	0.37	706.0	27.47	32.30	16.34	15.96	704.81	2622.10	129.42	124.56
1.26	0.28	0.56	0.37	706.0	27.47	22.49	14.38	8.11	661.34	2268.70	157.39	140.06
0.99	0.32	0.56	0.37	706.0	27.47	32.75	16.65	16.10	703.69	2675.70	104.61	96.40
1.26	0.32	0.56	0.37	706.0	27.47	20.44	12.50	7.94	662.90	1830.50	139.39	87.78
0.75	0.3	0.5	0.3	600.0	25	16.93	12.73	4.20	581.97	2524.70	243.92	250.68
1.5	0.3	0.5	0.3	600.0	25	48.93	20.27	28.66	718.13	3360.00	75.38	66.60
1.1	0.25	0.5	0.3	600.0	25	27.99	16.66	11.33	662.46	2342.20	188.52	173.13
1.1	0.35	0.5	0.3	600.0	25	29.91	18.26	11.65	678.31	2488.10	122.56	81.96
1.1	0.3	0.27	0.3	600.0	25	24.07	12.55	11.52	685.51	1839.20	63.29	25.98

1.1	0.3	0.7	0.3	600.0	25	32.82	20.91	11.91	647.22	3129.20	240.99	310.43
1.1	0.3	0.5	0.1	600.0	25	27.24	15.69	11.55	664.45	2329.30	131.39	108.02
1.1	0.3	0.5	0.5	600.0	25	31.32	19.45	11.87	646.06	2598.90	169.89	148.45
1.1	0.3	0.5	0.3	300.0	25	49.07	31.86	17.21	602.06	3514.00	222.86	190.29
1.1	0.3	0.5	0.3	900.0	25	20.76	13.09	7.68	685.04	1787.50	112.78	101.21
1.1	0.3	0.5	0.3	600.0	18	27.42	18.78	8.64	645.21	2108.70	158.98	135.46
1.1	0.3	0.5	0.3	600.0	32	30.67	15.92	14.75	668.79	2775.10	137.71	115.41

Table 5.3 Combinations of input variables and corresponding output parameters for the testing of ANN models for FSW of AA7075

Testing data for AA7075												
Shoulder radius, cm	Pin radius, cm	Pin length, cm	Tool rotational speed, rpm	Welding velocity, cm/s	Axial pressure, Mpa	Total torque, Nm	Sticking torque, Nm	Sliding torque, Nm	Peak temperature, K	Total force, N	Max shear90, MPa	Bending stress, MPa
0.90	0.210	0.306	0.15	360.0	19.0	23.08	16.59	6.48	589.33	1632.60	215.39	135.25
0.90	0.240	0.387	0.25	480.0	21.0	21.05	14.75	6.30	607.51	1803.70	216.21	156.26
0.90	0.260	0.468	0.33	630.0	23.0	19.60	13.76	5.84	624.34	1954.10	225.78	202.69
0.90	0.270	0.513	0.36	680.0	24.0	19.77	14.07	5.69	631.67	2059.90	235.63	222.96
0.90	0.290	0.594	0.45	820.0	26.0	19.62	14.51	5.11	650.55	2198.90	239.12	250.82
1.10	0.210	0.387	0.36	630.0	26.0	25.21	14.01	11.20	666.84	2035.40	162.95	126.01
1.10	0.240	0.468	0.45	680.0	19.0	24.70	16.90	7.80	652.72	1833.00	191.19	177.39
1.10	0.260	0.513	0.15	820.0	21.0	20.59	13.47	7.12	682.18	1671.90	153.03	140.21
1.10	0.270	0.594	0.25	360.0	23.0	43.32	28.66	14.66	616.37	3306.40	301.58	313.24
1.10	0.290	0.306	0.33	480.0	24.0	29.35	16.44	12.90	663.29	2161.90	94.92	40.76
1.30	0.210	0.468	0.25	820.0	24.0	27.21	14.10	13.10	709.51	2011.70	114.96	129.22
1.30	0.240	0.513	0.33	360.0	26.0	57.12	30.69	26.43	649.98	3769.30	212.05	203.72
1.30	0.260	0.594	0.36	480.0	19.0	45.83	28.74	17.10	657.02	2935.90	232.94	244.79
1.30	0.270	0.306	0.45	630.0	21.0	31.75	16.59	15.16	703.57	2057.50	66.86	32.71
1.30	0.290	0.387	0.15	680.0	23.0	30.17	14.77	15.40	712.77	2147.90	63.82	38.27
1.40	0.210	0.513	0.45	480.0	23.0	52.26	27.65	24.61	676.76	3302.90	207.22	224.16
1.40	0.240	0.594	0.15	630.0	24.0	40.36	19.35	21.01	703.24	2956.80	145.01	182.83
1.40	0.260	0.306	0.25	680.0	26.0	33.17	11.95	21.22	733.07	2502.50	33.30	17.69
1.40	0.270	0.387	0.33	820.0	19.0	28.36	15.46	12.90	719.76	1745.10	62.21	40.52
1.40	0.290	0.468	0.36	360.0	21.0	61.75	35.44	26.31	666.50	3500.60	147.43	100.55
1.60	0.210	0.594	0.33	680.0	21.0	48.14	22.41	25.73	718.85	3028.60	139.62	201.49
1.60	0.260	0.387	0.45	360.0	24.0	80.00	35.12	44.88	706.02	4527.60	97.97	62.50
1.60	0.270	0.468	0.15	480.0	26.0	62.84	20.91	41.93	725.33	4273.70	65.22	53.36
1.60	0.290	0.513	0.25	630.0	19.0	48.08	22.93	25.15	721.42	2865.40	76.12	65.12

0.90	0.210	0.306	0.45	680.0	24.0	15.62	10.27	5.35	630.35	1361.30	159.85	103.18
0.90	0.240	0.387	0.15	820.0	26.0	13.98	9.19	4.79	660.28	1344.40	148.12	102.99
0.90	0.260	0.468	0.25	360.0	19.0	28.47	21.38	7.09	584.61	2435.20	305.66	266.33
0.90	0.270	0.513	0.33	480.0	21.0	25.08	18.40	6.69	604.80	2441.50	290.76	270.75
0.90	0.290	0.594	0.36	630.0	23.0	22.75	16.83	5.93	629.00	2475.80	269.52	278.06
1.10	0.210	0.387	0.33	360.0	23.0	37.51	23.41	14.10	616.38	2513.70	227.36	181.84
1.10	0.240	0.468	0.36	480.0	24.0	32.82	19.99	12.84	636.07	2554.80	210.51	195.98
1.10	0.260	0.513	0.45	630.0	26.0	28.50	16.95	11.55	664.46	2369.20	188.96	171.20
1.10	0.270	0.594	0.15	680.0	19.0	24.86	16.94	7.92	664.58	2037.70	204.73	206.47
1.10	0.290	0.306	0.25	820.0	21.0	18.14	11.06	7.08	697.26	1308.60	65.19	30.24
1.30	0.210	0.468	0.15	630.0	21.0	32.57	17.60	14.97	691.02	2261.00	146.05	157.25
1.30	0.240	0.513	0.25	680.0	23.0	32.94	17.60	15.34	696.31	2409.30	136.76	145.22
1.30	0.260	0.594	0.33	820.0	24.0	30.70	17.38	13.32	704.98	2287.20	149.94	168.63
1.30	0.270	0.306	0.36	360.0	26.0	51.40	24.90	26.50	677.38	3341.90	92.77	43.39
1.30	0.290	0.387	0.45	480.0	19.0	41.86	24.94	16.93	675.02	2494.30	114.45	63.32
1.40	0.210	0.513	0.36	820.0	19.0	30.79	18.02	12.77	705.11	1949.80	140.14	173.18
1.40	0.240	0.594	0.45	360.0	21.0	66.72	40.52	26.20	640.76	3803.80	271.70	315.61
1.40	0.260	0.306	0.15	480.0	23.0	43.08	18.40	24.69	708.58	2878.90	56.58	28.62
1.40	0.270	0.387	0.25	630.0	24.0	37.27	16.19	21.08	717.75	2613.60	64.49	41.59
1.40	0.290	0.468	0.33	680.0	26.0	38.43	17.08	21.35	719.37	2800.30	77.63	61.09
1.60	0.210	0.594	0.25	480.0	26.0	67.60	25.81	41.79	714.30	4500.40	156.15	217.17
1.60	0.240	0.306	0.33	630.0	19.0	41.84	16.88	24.96	734.80	2600.20	35.00	19.54
1.60	0.260	0.387	0.36	680.0	21.0	43.19	17.34	25.86	734.85	2738.70	46.81	31.90
1.60	0.270	0.468	0.45	820.0	23.0	40.11	16.77	23.33	738.70	2614.00	55.39	47.80
1.60	0.290	0.513	0.15	360.0	24.0	79.55	34.69	44.87	700.96	4699.80	106.51	85.69

5.2. Results and discussion

The combinations of the input variables for training, based on an aggregation of L50 array and CCD array, are shown in Table 5.2. Testing of the ANN models is done using input combinations based on L50 array with five levels of input variables. These input variable combinations are listed in Table 5.3. The heat transfer and visco-plastic flow model is used to calculate the output parameters for each case. The seven specific outputs from heat transfer and visco-plastic flow model used for the ANN models are total torque, sliding torque, sticking torque, peak temperature, traverse force, maximum shear stress on the tool pin and bending stress on the pin. These output parameters are selected since they define the thermo-mechanical conditions around the FSW tool. Tables 5.2 and 5.3 list the input variable combinations and values of corresponding output variables for training and testing of AA7075, respictvely.

Several artificial neural network models are trained and tested using the outputs of the heat transfer and visco-plastic flow model. Since an ANN model is a collection of weights representing the relationship between the input parameters and a specific output parameter, there will be an independent ANN model for every output parameter for each of the two materials considered. Thus for seven output parameters for the two materials selected, 14 different ANN models are developed.

Figures 5.2(a) through (f) show the comparison of the predicted values using ANN model and the desired values computed using the three dimensional heat transfer and visco-plastic flow model for FSW of AA7075 alloy using H13 steel tool. The output variables shown in figure 5.2 (a) to (g) are total torque, sliding torque, sticking torque, traverse force, peak temperature, the maximum shear stress, and bending stress, respectively. The error bars calculated based on the uncertainty in the prediction from the ANN model are shown in these plots for 95% of confidence interval. The plots show a fair agreement of the predicted and desired values of the output parameters for both training and testing cases. The input variables considered in the Tables 5.2 and 5.3 cover a considerable range of welding parameters and tool dimensions.

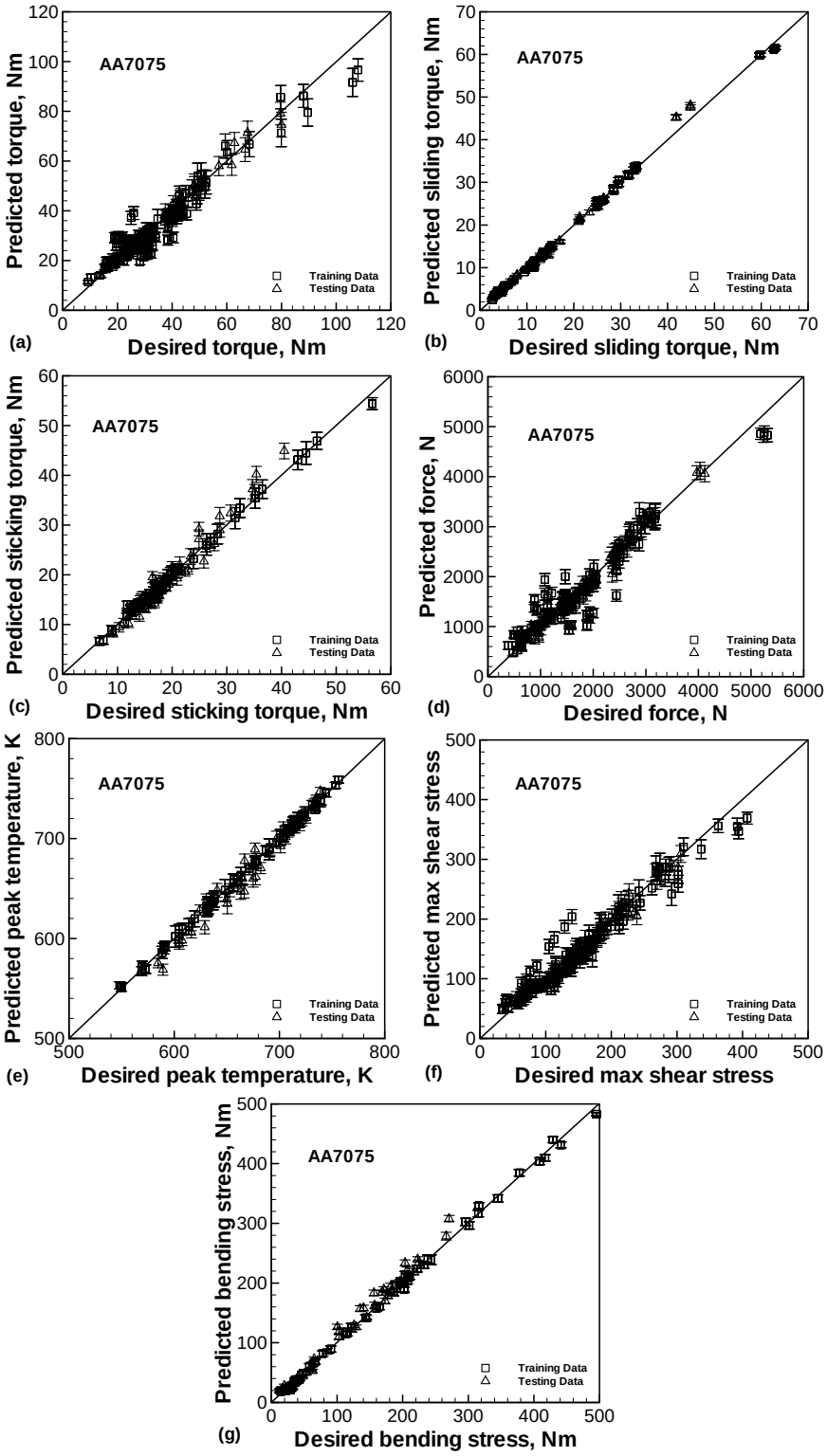

Figure 5.2 Comparison of the predicted and the desired values of output parameters for FSW of AA7075, (a) total torque, (b) sliding torque, (c) sticking torque, (d) traverse force, (e) peak temperature, (f) maximum shear stress and (g) bending stress.

These developed ANN models for AA7075 are now used to predict the outputs, such as peak temperature, torque, traverse force, maximum shear stress and bending stress, that define the thermo-mechanical conditions around the tool. The values of these outputs are predicted for a large range of input parameters. These ANN model predictions are used to understand the effect of tool shoulder radius, tool rotational speed, pin radius, pin length, welding velocity and axial pressure on these outputs. The predicted values of the peak temperature, total torque, traverse force, maximum shear stress and bending stress for the FSW of AA7075 are shown in figure 5.3 to 5.7, respectively. In all these four figures, sub-figure (a) shows the effect of shoulder diameter and tool rotational speed on the predicted value of the output parameter, while other four input variables are kept constant. Sub-figure (b) shows the effect of increase in tool pin radius when compared with sub-figure (a) for the same values of tool pin length, welding velocity and axial pressure. The comparison of sub-figures (a) and (c) reflects the effect of change in tool pin length while tool pin radius, welding velocity and axial pressure are kept constant. The sub-figure (a) and (d) can be compared to understand the effect of increase in the welding velocity on the values of the output parameter as the values of tool pin radius, pin length and axial pressure are for the two cases. The comparison of sub-figures (a) and (e) shows the effect of increase in axial pressure while pin radius, pin length and welding velocity remains constant.

The predicted values of peak temperature for five different combinations of the input variables indicated in Figure 5.3 are shown in Figure 5.3 (a) to (e). Figure 5.3(a) shows the effect of tool shoulder radius and tool rotational speed on the predicted peak temperature for constant values of other input variables, pin radius, pin length, welding velocity and axial pressure. For any constant value of tool rotational speed, increase in tool shoulder radius results in higher peak temperatures. The larger tool shoulder radius results in increased heat generation at the tool shoulder workpiece interface and thus leads to higher peak temperature as all other variables are kept constant. For a constant tool shoulder radius, the increase in tool rotational speed results in higher predicted value of peak temperature while other input variables are kept constant. The increased tool rotational speed also results in higher heat generation and thus leads to higher peak temperature during FSW of AA7075. Figure 5.4 shows experimentally measured temperatures as function of time during FSW of aluminum 6063 alloy for various tool rotational speeds. [26] Sato et al [26] has experimentally shown that the measured values of peak temperatures increase continuously with increase in tool rotational speed. Although these results are for a different alloy, the

similar trend shows that the results from ANN model conform to the available experimental results of peak temperature in literature.

A comparison of Figure 5.3(a) and 5.3(b) shows the effect of increase in tool pin radius on the predicted peak temperature during FSW of AA7075. For any combination of tool shoulder radius and tool rotational speed, as the tool pin radius increases the peak temperature during FSW also increases. The increase in tool pin radius results in higher surface area at the tool-workpiece interface. This increased surface area results in higher heat generation and thus leads to higher peak temperature during FSW which other pin length, welding velocity and axial pressure are constant. The effect of increase in tool pin length and increase in workpiece plate thickness can be seen by comparison of Figure 5.3(a) and 5.3(c). As the tool pin length increases, the generated heat is dispersed into larger volume of the workpiece material and thus the generated heat results in peak temperature lower compared to the thinner plate. For a specific combination of tool shoulder diameter and tool rotational speed, the peak temperature is lower for thicker plates as shown in Figure 5.3(c) while pin radius, welding velocity and axial pressure remains same as used in Figure 5.3(a).

A comparison of Figure 5.3(a) and Figure 5.3(d) shows the effect of increase in welding velocity while other welding variables, pin radius, pin length and axial pressure are kept constant. The increase in the welding velocity results in lower heat input per unit length during FSW of AA7075. This reduced heat input per unit length results in decrease in the peak temperature when compared with the predicted peak temperature at lower welding speed shown in Figure 5.3(a). The training data also show the same trend, when the welding velocity is increased from 0.1 to 0.5 cm/s, the peak temperature decreases from 664.45 to 646.06K. However, the peak temperature in Figure 5.3(d) for larger tool shoulder diameter and high tool rotational speed the peak temperature increases with increase in welding velocity. This trend might be a result of poor training of ANN model at high welding velocity, large shoulder and high rpm combination and can be improved in future. A comparison of the Figure 5.3(a) and Figure 5.3(e) shows the effect of increase in axial pressure on the computed values of peak temperature while other input parameters, pin radius, pin length and welding velocity, are kept constant. The increase in axial pressure results in higher heat generation during FSW and thus the peak temperature increases for higher axial pressure.

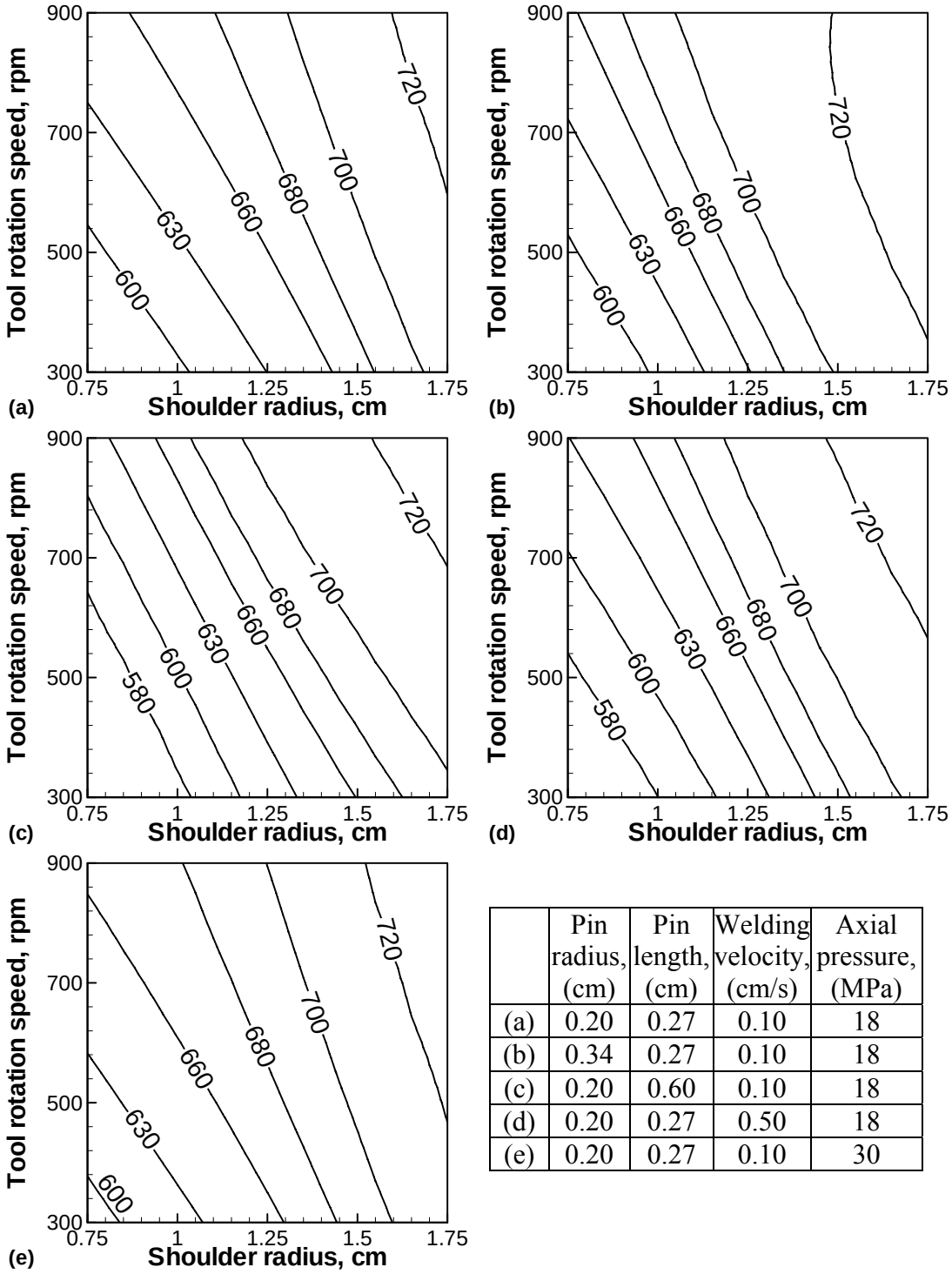

	Pin radius, (cm)	Pin length, (cm)	Welding velocity, (cm/s)	Axial pressure, (MPa)
(a)	0.20	0.27	0.10	18
(b)	0.34	0.27	0.10	18
(c)	0.20	0.60	0.10	18
(d)	0.20	0.27	0.50	18
(e)	0.20	0.27	0.10	30

Figure 5.3 The predicted values of peak temperature (K) by ANN model for FSW of AA7075 as function of tool shoulder radius and tool rotational speed for the combinations of input variables listed in the table shown here.

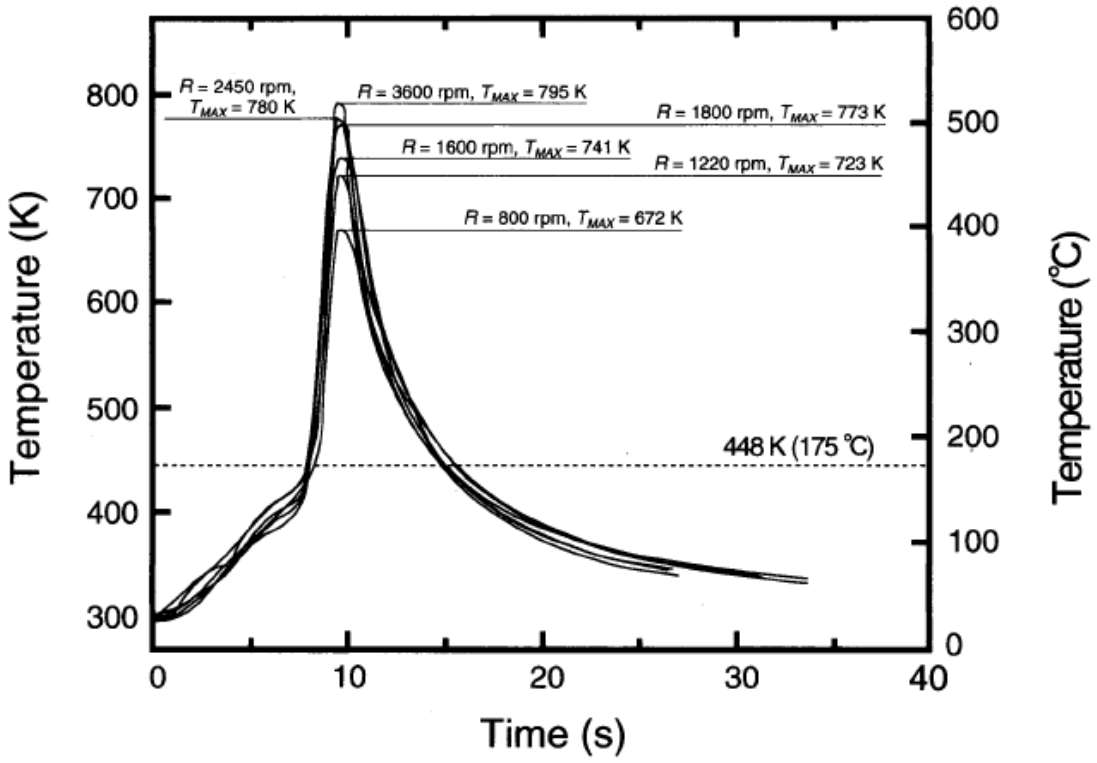

Figure 5.4 Experimentally measured values of temperatures as function of the time for FSW of aluminum 6063 alloy at various tool rotational speeds. [26]

The predicted values of the torque for large number of combination of tool shoulder diameter and tool rotational speed values are shown in Figure 5.5(a) to (e). The combination of input variables considered for total torque predictions are listed in the table shown in the Figure. Figure 5.5(a) shows the effects of tool shoulder radius and tool rotational speed on the predicted values of torque as tool pin radius, pin length, welding velocity and axial pressure are kept constant. The predicted value of torque increases with increase in tool shoulder radius for a constant value of tool rotational speed. As the tool shoulder radius remains constant, the predicted torque decreases with increase in tool rotational speed for FSW of AA7075. Increase in tool rotational speed increases the amount of heat generated during FSW. The increased heat softens the workpiece material and the torque decreases. Yan et al [27] has experimentally measured the torque during FSW of AA2524 for various tool rotational speeds as shown in Figure 5.6. The measured value of torque decreases with increase in tool rotational speed as the welding speed is 2.11 mm/s and axial force is 42.3kN and the tool dimensions are same in all cases. [27] Also, the effect of welding speed was studied experimentally by Yan et al. [27]. They showed that the measured value of torque is nearly unchanged with change in welding speed.

The comparison of Figure 5.5(a) and 5.5(b) show the effect of increase in tool pin radius on the predicted value of total torque as other input variables, i.e., pin length, welding velocity and axial pressure, are kept constant. For any specific combination of tool shoulder radius and tool rotational speed, the increase in pin radius results in higher predicted value of total torque. The increase in pin radius results in higher surface area at the tool-workpiece interface. The increased tool-workpiece interface area results in higher resistance to the tool rotation from the workpiece material. This results in higher torque for increase tool pin radius.

Comparison of Figure 5.5(a) and 5.5(c) shows the effect of increase in tool pin length on the predicted value of total torque. The total torque increases with increase in tool pin length as all other input variables are same. The increase in tool pin length increases the part of the pin in contact with material at lower temperature, thus increasing the total torque. Figure 5.5(a) and 5.5(d) can be compared to understand the effect of welding speed on the predicted values of total torque as function of the tool shoulder radius and tool rotational speed. The higher welding speed results in higher predicted values of total torque for any specific combination of tool shoulder radius and tool rotational speed. The increase in welding velocity results in lower heat input per unit length and thus lower peak temperature as shown previously in Figure 5.3(d). The reduced temperatures during FSW at higher welding speed results in higher total torque values. The comparison of Figure 5.5(a) and 5.5(e) shows the effect of increase in axial pressure on the predicted values of total torque while other input variables, pin radius, pin length and welding velocity, are constant. The increase in axial pressure results in increased predicted values of total torque for all other variables being constant. The increase in axial pressure results in higher frictional resistance to the rotation of the FSW tool thus, resulting in higher predicted values of total torque.

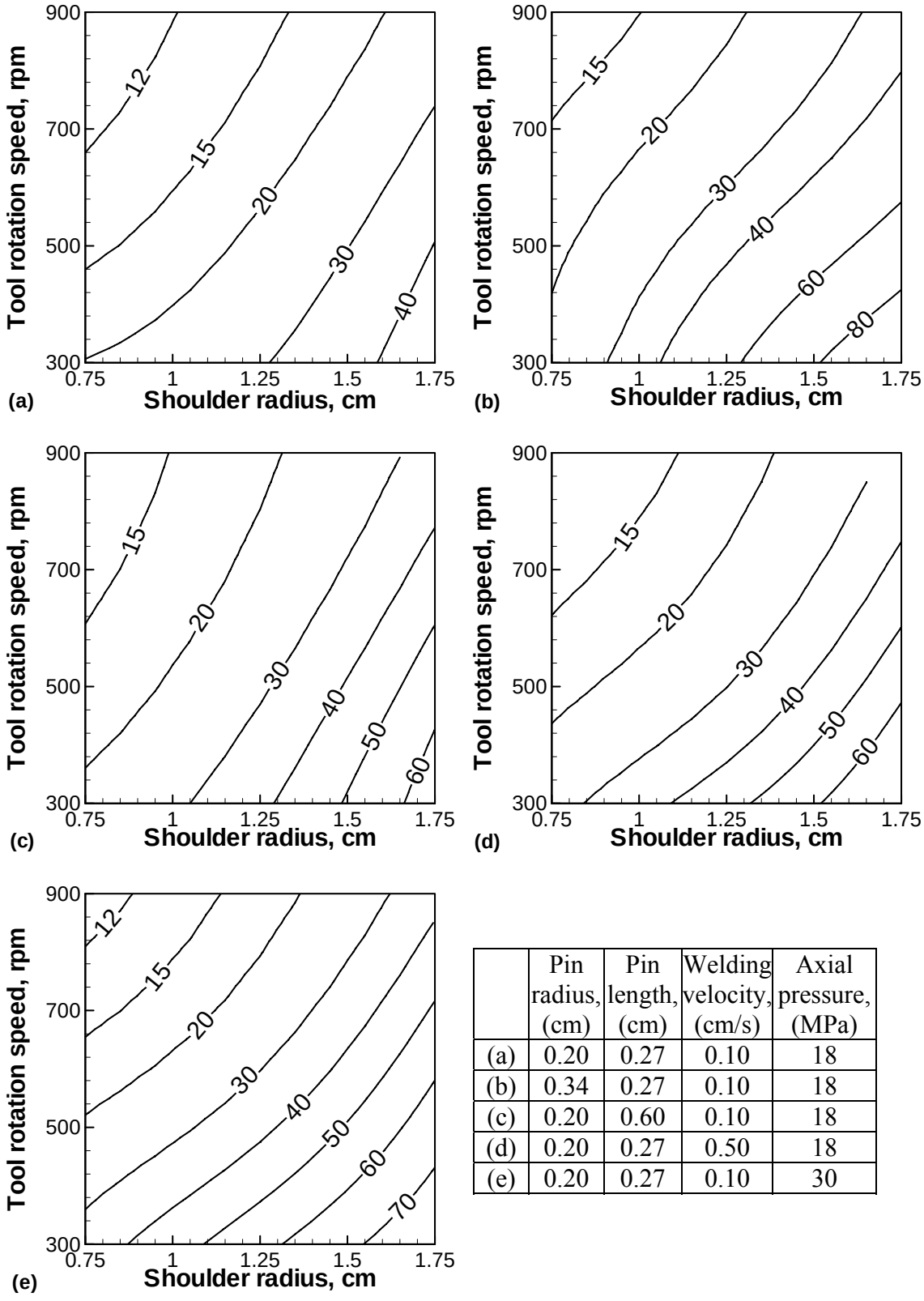

	Pin radius, (cm)	Pin length, (cm)	Welding velocity, (cm/s)	Axial pressure, (MPa)
(a)	0.20	0.27	0.10	18
(b)	0.34	0.27	0.10	18
(c)	0.20	0.60	0.10	18
(d)	0.20	0.27	0.50	18
(e)	0.20	0.27	0.10	30

Figure 5.5 The predicted values of total torque (Nm) by ANN model for FSW of AA7075 as function of tool shoulder radius and tool rotational speed for the combinations of input variables listed in the table shown here.

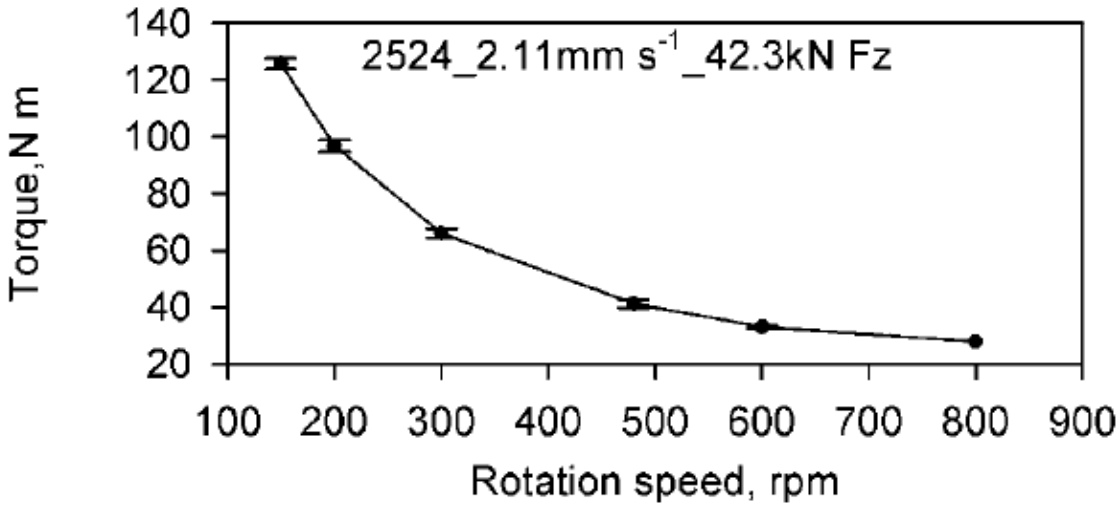

Figure 5.6 Measured values of torque as function of tool rotational speed during FSW of AA2524 as the welding velocity is 2.11 mm/s and axial force is 42.3kN. [27]

The ANN model to predict traverse force for the FSW of AA7075 is used to predict the values of traverse force as function of tool shoulder diameter values and tool rotational speeds. These predicted values are shown in Figure 5.7(a) to (f) for various combinations of pin radius, pin length, welding velocity and axial pressure shown in the Table attached to Figure 5.7. The effects of tool shoulder radius and tool rotational speed are shown in Figure 5.7(a) at constant pin radius, pin length, welding velocity and axial pressure. At constant tool rotational speed, the increase in tool shoulder radius increases the tool traverse force. The increase in tool shoulder radius increases the friction force on the tool thus increasing the tool traverse force. The larger tool shoulder also increases the temperature, thus decreasing the force on the tool pin. However, the force on the shoulder is a much larger component of the total traverse force in comparison with the force on the pin. Thus the increase in the shoulder force dominates the decrease in pin force leading to higher traverse force for larger shoulder radius tool. With increase in tool rotational speed the traverse force decreases. The increase in tool rotational speed increases the temperature thus leading to lower traverse force for a specific value of tool shoulder radius.

On comparison of Figures 5.7(a) and 5.7(b) show the effect of pin radius on the tool traverse force. The increase in pin radius slightly decreases the force on the tool pin. The larger tool pin results in higher temperatures in the workpiece, thus leading to lower force on

the tool. Comparison of Figure 5.7(a) and 5.7(c) shows that the increase in tool pin length slightly increases the traverse force. The longer tool pin is in contact with the workpiece material at lower temperature and thus the force on the tool increases with increase in pin length. The effect of welding velocity on the traverse force is shown in figure 5.7(d). The comparison of Figure 5.7(d) with Figure 5.7(a) shows that the traverse force is nearly unchanged with increase in the welding velocity. Although the peak temperature decreases with increase in welding velocity, the force remains nearly unchanged as the temperature affects the force on tool pin, which is very small at high temperatures. The comparison of Figure 5.7(a) and 5.7(e) show the effect of axial pressure on the tool traverse force. Figure 5.7(e) shows that increase in axial pressure results in higher traverse force on the tool. The increased axial pressure leads to higher frictional force on the tool shoulder which results in higher tool traverse force during FSW of AA7075.

Sorensen and Stahl [28] experimentally studied the effect of tool pin dimensions on the measured value of traverse force during FSW of AA6061. They [28] showed that the traverse force increases with increase in the tool pin length. The increase in the tool pin radius slightly decreases the traverse force experienced by the FSW tool as shown by the experimental measurements.[28]

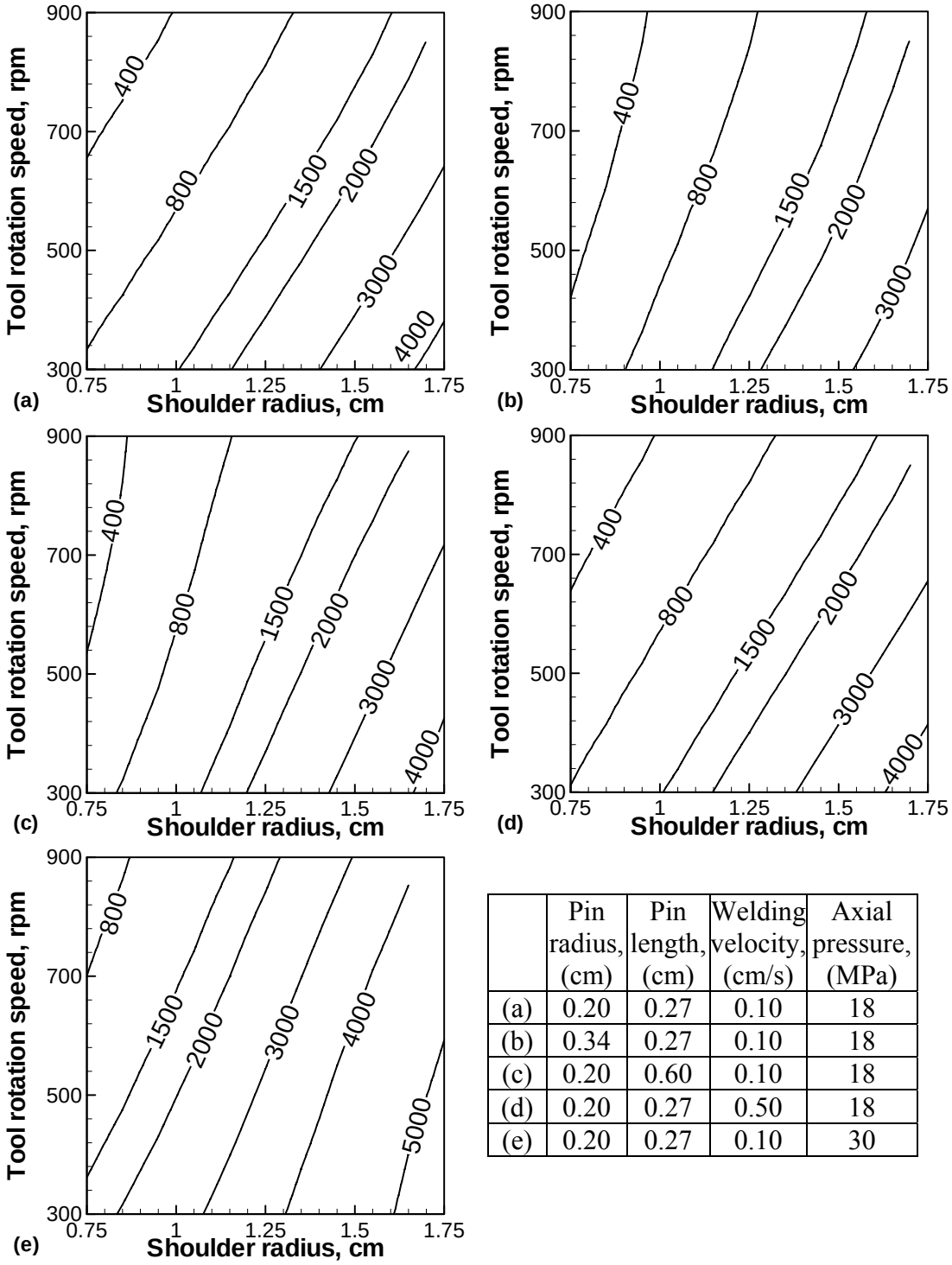

	Pin radius, (cm)	Pin length, (cm)	Welding velocity, (cm/s)	Axial pressure, (MPa)
(a)	0.20	0.27	0.10	18
(b)	0.34	0.27	0.10	18
(c)	0.20	0.60	0.10	18
(d)	0.20	0.27	0.50	18
(e)	0.20	0.27	0.10	30

Figure 5.7 The predicted values of traverse force (N) by the ANN model for FSW of AA7075 as function of tool shoulder radius and tool rotational speed for the combinations of input variables listed here.

The ANN model is used to predict maximum shear stress for various input variables for the FSW of AA7075. Figure 5.8 shows the predicted values of maximum shear stress as function of the tool rotational speed and tool shoulder diameter for five different

combinations of pin radius, pin length, welding velocity and axial pressure. These combinations are shown in the table attached to the Figure. The effects of tool shoulder radius and tool rotational speed can be seen in Figure 5.8(a). For a constant tool rotational speed, as the tool shoulder radius increases, the maximum shear stress decreases. As the tool shoulder radius increases, the total heat generation also increase leading to higher temperature and lower maximum shear stress. At any specific value of tool shoulder radius, the maximum shear stress decreases with increase in tool rotational speed. For higher tool rotational speed also, there is more heat generated at the tool-wokrpiece interface that results in higher workpiece temperature and lower maximum shear stress. A comparison of Figure 5.8(a) and 5.8(b) shows that the increase in pin radius decreases the maximum shear stress on the pin for any selected combination of tool shoulder radius and tool rotational speed. The increase in the pin radius results in lower stresses on the tool pin thus leading to lower maximum shear stress value.

Figures 5.8(a) and 5.8(c) can be compared to show that increase in pin length increases the predicted value of maximum shear stress, as other input variables, pin length, welding velocity and axial pressure, are kept constant. The increase in tool pin length increases the stresses on the tool pin and thus leads to higher maximum shear stress. Comparison of Figure 5.8(a) and Figure 5.8(d) shows the effect of welding velocity on the maximum shear stress. For any given tool shoulder radius and tool rotational speed, higher welding speed results in lower temperatures and thus higher stresses on the tool pin. A comparison of Figure 5.8(a) and Figure 5.8(e) shows that increase in axial pressure results in slight decrease in the predicted value of maximum shear stress on the tool pin. The increase in axial pressure results in higher temperature and thus the stresses on the tool pin decreases.

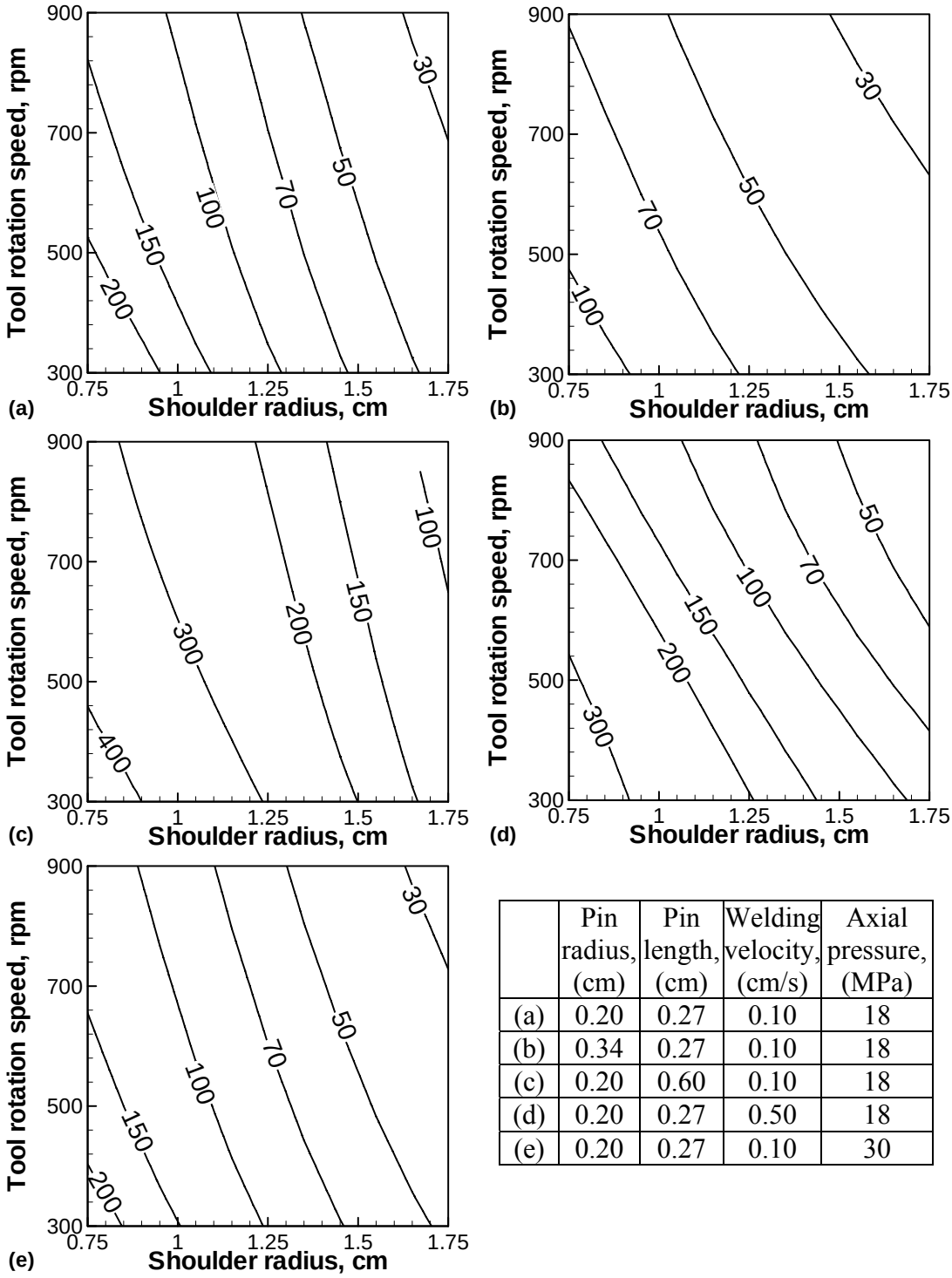

	Pin radius, (cm)	Pin length, (cm)	Welding velocity, (cm/s)	Axial pressure, (MPa)
(a)	0.20	0.27	0.10	18
(b)	0.34	0.27	0.10	18
(c)	0.20	0.60	0.10	18
(d)	0.20	0.27	0.50	18
(e)	0.20	0.27	0.10	30

Figure 5.8 The predicted values of maximum shear stress on the tool pin (MPa) by the ANN model for FSW of AA7075 as function of tool shoulder radius and tool rotational speed for the combinations of input variables listed here.

The ANN model is used to predict bending stress values for FSW of AA7075 for various input variables. The predicted values of the bending stress are plotted in Figure 5.9

as function of tool shoulder radius and tool rotational speed. The combinations of values of pin radius, pin length, welding velocity and axial pressure are shown in the attached Table. Figure 5.9(a) shows that increase in tool shoulder radius for a constant tool rotational speed results in lower predicted values of bending stress. The larger shoulder radius results in higher heat generation during FSW thus lead to higher workpiece temperatures and lower force on the tool pin. Thus the bending stress is lower in case of larger shoulder radius tools. For a given tool shoulder radius, the bending stress decreases with increase in tool rotational speed. The higher tool rotational speed also results in higher heat generation, thus leading to increased temperature and lower bending stress. The effect of increase in pin radius is shown in Figure 5.9(b) when compared with Figure 5.9(a). The increase in pin radius decreases the bending stress on the tool pin. A thicker pin experiences lower bending stress when all other variables are kept the same.

A comparison of Figure 5.9(a) and 5.9(c) shows the effect of increase in tool pin length while pin radius, welding velocity and axial pressure are kept same for the two sub-figures. The predicted values of bending stress are higher for a longer tool pin and thicker workpiece plate. The increase in the tool pin length and the plate thickness increases the force on the tool pin, thus results in higher bending stress during FSW of AA7075. The higher welding velocity slightly increases the bending stress on the tool pin as shown in Figure 5.9(d). The increased welding velocity means lower heat input per unit length thus lower workpiece temperature and higher bending stress on the tool pin. As also shown in training data the bending stress increases from 108.02 to 148.45 MPa when the welding velocity is increased from 0.1 to 0.5 cm/s. However, the ANN model results for large shoulder radius and high tool rotational speed do not have the same trend. These results can possibly be improved in future by better training of ANN model for large shoulder radii, high tool rotational speed and high welding velocity. Comparison of Figure 5.9(a) and 5.9(e) shows the effect of change in axial pressure on the predicted values of bending stress. As the axial pressure increases, the predicted value of bending stress slightly decreases for same combination of tool shoulder radius and tool rotational speed. The increase in axial pressure results in higher frictional heat generation thus higher temperature and lower force on the tool pin. This results in lower bending stress at higher axial pressure.

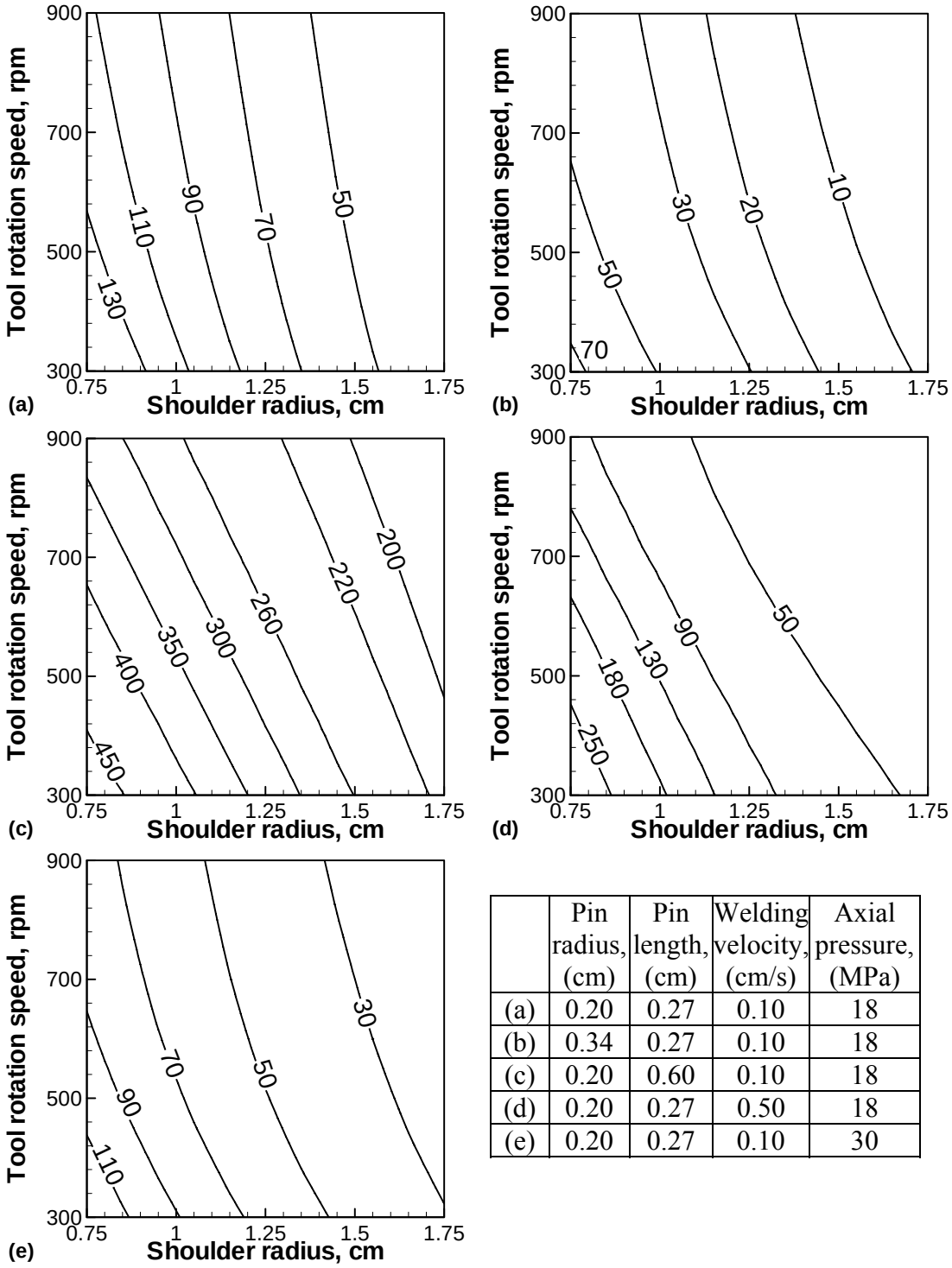

	Pin radius, (cm)	Pin length, (cm)	Welding velocity, (cm/s)	Axial pressure, (MPa)
(a)	0.20	0.27	0.10	18
(b)	0.34	0.27	0.10	18
(c)	0.20	0.60	0.10	18
(d)	0.20	0.27	0.50	18
(e)	0.20	0.27	0.10	30

Figure 5.9 The predicted values of bending stress on the tool pin (MPa) by the ANN model for FSW of AA7075 as function of tool shoulder radius and tool rotational speed for the combinations of input variables listed here.

Figures 5.3, 5.5, 5.7, 5.8 and 5.9 show the capability of the ANN models to predict the trends for peak temperature, torque, traverse force, maximum shear stress and bending stress as function of the input parameters tool shoulder radius, tool rotational speed, pin radius, pin length, welding velocity and axial pressure. It is showed that the ANN model results can reproduce the results obtained from the phenomenological model. Now, these ANN models are used to estimate the stresses on the tool pin and in turn have an estimate of the safe working parameters for FSW of these alloys. The FSW tool experiences both shear stress and bending stress on the tool pin. The bending stress based calculation presented in appendix A show that it is unlikely for fatigue failure to occur in the tool for FSW of thin AA7075 plates except when the stresses are large. Based on the shear failure mechanism, the safety factor criterion is defined as the ratio of the shear strength of the tool material and the maximum shear stress on the tool pin. The maximum shear stress on the tool pin is calculated based on Tresca's criteria as explained in Equation 4.9 in chapter 4. The developed ANN model for maximum shear stress for FSW of AA7075 is used to calculate the maximum shear stress on the tool pin for various combinations of the input variables. The ANN model for peak temperature is used to estimate the corresponding shear strength of the tool material. The calculated value of the safety factor is the ratio of the strength of the tool material and the maximum shear stress on the tool. The shear strength of the commonly used tool material for aluminum alloys, H13 tool steel, as function of temperature is shown in Figure 5.10. [29] Since the peak temperature for the FSW of AA7075 lies below 750K, the shear strength of the tool material will always be more that 500MPa.

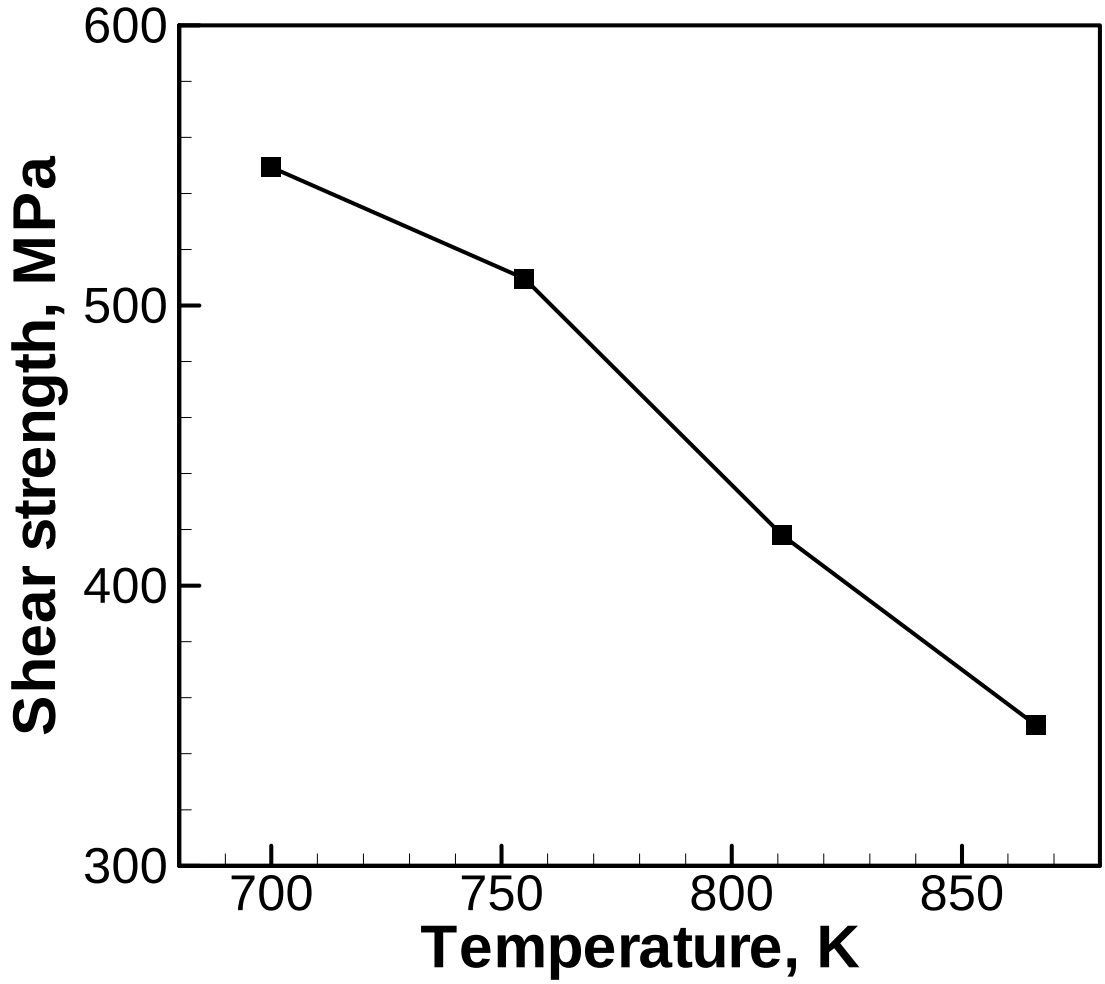

Figure 5.10 The temperature dependent shear strength of the H13 tool steel. [29]

The contours of the calculated safety factor for different combinations of the values of tool shoulder radius and the tool rotational speed, are plotted for FSW of AA7075 alloy in Figure 5.11 (a)-(f). The combinations of the remaining input variables used to predict the safety factor shown in these figures are given in Table attached in Figure 5.11. For a given set of values of other input parameters, Figure 5.11(a) shows that the safety factor increases with increase in the tool shoulder radius. A larger tool radius results in higher temperature thus lower stresses on the tool pin resulting in higher safety factor value. With increase in tool rotational speed, the safety factor increases. The increase in tool rotational speed also increases the workpiece temperature and thus decreases the stresses on the tool pin resulting in higher value of safety factor. A comparison of figure 5.11(a) and 5.11(b) show the effect of increase in tool pin radius while all other input variables are kept same. As the tool pin radius increases, the stresses on the tool pin decreases and the safety factor is higher for the thicker tool pin radius for same combination of tool shoulder radius and tool rotation speed.

This observation is consistent with the observations made in chapter 4, where in figure 4.10 showed that the maximum shear stress on the tool pin decreases with increase in the tool pin radius thus leading to higher safety factor values.

Figure 5.11(c) shows the effect of increase in tool pin length when compared with Figure 5.11(a). As the tool pin length increases, the stresses on the tool increases as the longer tool pin faces material farther away from the tool shoulder which is at much lower temperature and is much stronger. This increased resistance from the stronger material increases the stresses on the tool material decreasing the safety factor for the tool. Thus for the same combinations of the tool shoulder radius and tool rotational speed, the safety factor is much less in Figure 5.11(c) compared to the same in Figure 5.11(a). Comparison of Figure 5.11(a) and 5.11(d) shows the effect of welding velocity on the safety factor for the tool. As shown in Figure 5.8(d) the maximum shear stress on the tool pin increases with increase in welding speed. Thus increase in welding speed decreases the tool safety factor for FSW of AA7075. Figure 5.11(e) shows the effect of increase in the axial pressure while other input parameter values are kept constant. As the axial pressure increases, the total heat generation increases decreasing the stresses on the tool. The decreased stresses result in the increase in tool safety factor while other parameters are kept constant. Figure 5.11(b) also shows the symbols representing the successful FSW experimental conditions. These plots of safety factor can be used as tool durability map to determine safe operating parameters for FSW of AA7075.

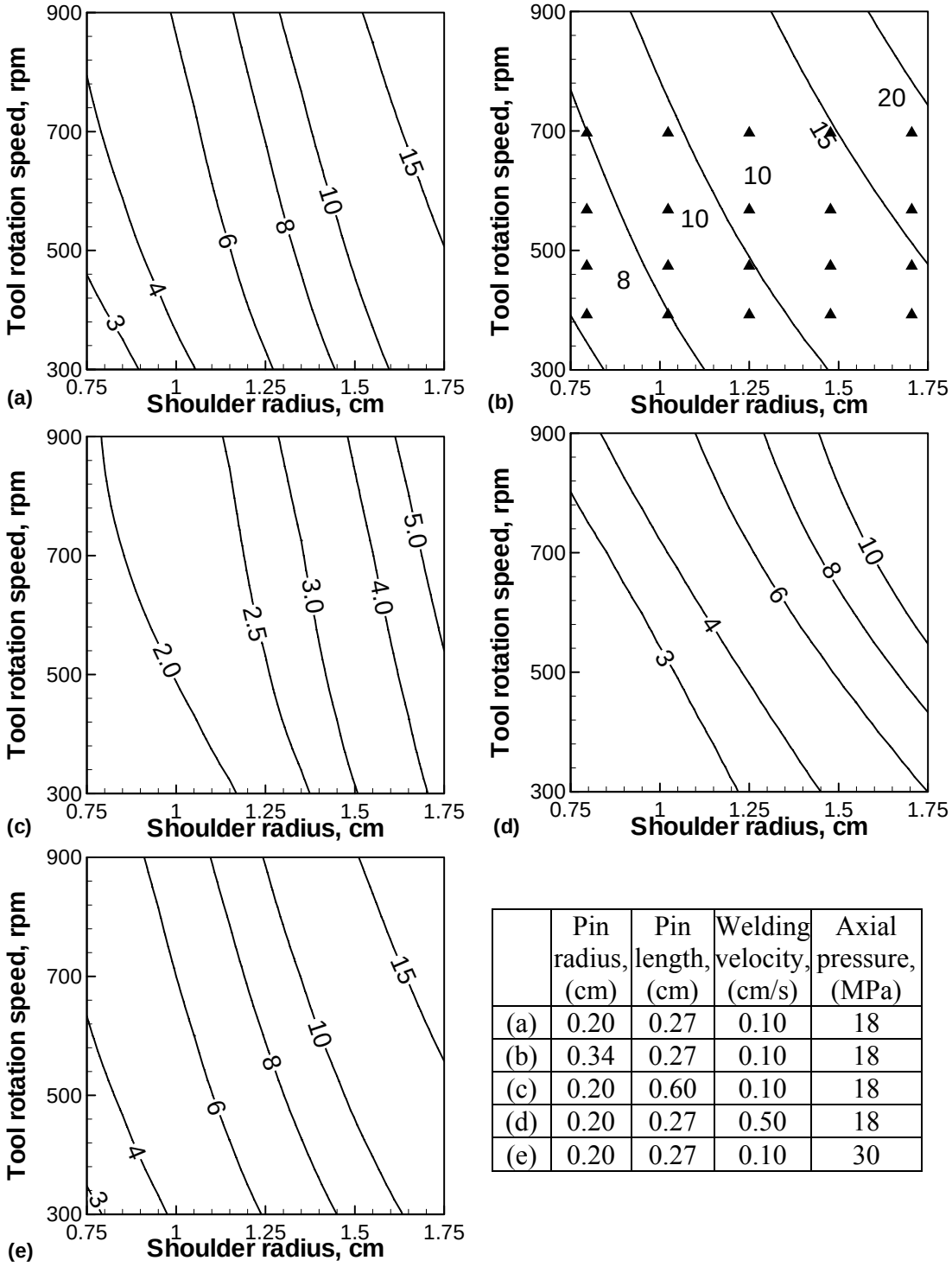

	Pin radius, (cm)	Pin length, (cm)	Welding velocity, (cm/s)	Axial pressure, (MPa)
(a)	0.20	0.27	0.10	18
(b)	0.34	0.27	0.10	18
(c)	0.20	0.60	0.10	18
(d)	0.20	0.27	0.50	18
(e)	0.20	0.27	0.10	30

Figure 5.11 Computed contours of safety factor for FSW of AA7075 alloy.

5.3. Conclusion

The artificial neural network (ANN) models based on Bayesian method has been used to predict the total torque, sliding torque, sticking torque, traverse force, peak temperature and maximum shear stress for the FSW of AA7075. These ANN models are shown to be able to predict these variables and the errors in the predictions. The ANN models are used to predict the peak temperature, total torque, traverse force, maximum shear stress and bending stress for a wide range of input parameters. These predicted results explain the effects of various input parameters on these output parameters for the FSW of AA7075. The increase in shoulder diameter increases the peak temperature, torque, and traverse force whereas the maximum shear stress and bending stress decreases. The increase in tool rotational speed increases the peak temperature whereas decreases the torque, traverse force, maximum shear stress and bending stress.

The larger tool pin radius is shown to result in higher peak temperature and torque. The traverse force, maximum shear stress and bending stress decreases with increase in tool pin radius. The longer pin is used for thicker plates, for which the peak temperature is lower and torque, traverse force, maximum shear stress and bending stress are higher compared to thinner plate workpiece. Similar to the effect of increase in pin length, increase in welding velocity also results in lower peak temperature, and higher torque, traverse force, maximum shear stress and bending stress for the FSW of AA7075. Increase in axial pressure results in higher peak temperature, torque and traverse force but lower maximum shear stress and bending stress.

Based on bending stress calculations, it is shown that the possibility of fatigue failure during FSW of AA7075. Considering shear failure as the possible mode of failure, the safety factor is defined as the ratio of the tool shear strength and the maximum shear stress on the tool pin. The predicted values of the peak temperature are used to estimate the tool shear strength. The maximum shear stress on the tool pin is predicted using the ANN model. The computed safety factors are plotted as function of tool shoulder radius and tool rotational speed for various combinations of other four input variables, tool pin radius, pin length, welding velocity and axial pressure. The plots provide significant information about what would be the value of safety factor for a specific combination of the input variables. This information would be very useful in developing long lasting tools.

5.4. References

1. T. DebRoy, S.A. David, Rev Mod Phys 67(1995) 85-112.
2. W. Zhang, G.G. Roy, J.W. Elmer, T. DebRoy, J Appl Phys 93(2003) 3022-3033.
3. X. He, P.W. Fuerschbach, T. DebRoy, J Phys D Appl Phys 36(2003) 1388-1398.
4. C.L. Kim, W. Zhang, T. DebRoy, J Appl Phys 94(2003) 2667-2679.
5. I.S. Kim, S.H. Lee and P.K.D.V. Yarlagadda, Sci Technol Weld Join 8(2003) 347-352.
6. H.B. Smartt and J.A. Johnson, Proceedings of 'Artificial neural networks in engineering, 'ANNIE'91', St Louis, MO, (ed. C. H. Dagli, S. R. T. Kumara and Y. C. Shin), 711–716; New York, ASME, 1991.
7. G.E. Cook, K. Andersen, G. Karsai, K. Ramaswamy, IEEE Trans Indust Applic 26(1990) 824–830.
8. X. Li, S.W. Simpson, M. Rados, Sci Technol Weld Join 5(2000) 71–79.
9. H.K.D.H. Bhadeshia, ISIJ Int 39(1999) 966–979.
10. S. Mishra, T. DebRoy, Mat Sci Eng A 454(2007) 477-486.
11. A. Kumar, T. DebRoy, Sci Technol Weld Join 11(2006) 106-119.
12. A. Kumar, T. DebRoy, Weld J 86(2007) 26s-33s.
13. H. Atharifar, Proc Inst Mech Eng Part B-J Eng Manuf 224(2010) 403-418.
14. P.A. Fleming, D.H. Lammlein, D.M. Wilkes, G.E. Cook, A.M. Strauss, D.R. DeLapp, D.A. Hartman, Sci Technol Weld Join 14(2009) 93-96.
15. L. Fratini, G. Buffa, D. Palmeri, Comput Struct 87(2009) 1166–1174.
16. L. Fratini, G. Buffa, J Eng Mater Technol 130(2008) 031001-1- 031001-6.
17. L. Fratini, G. Buffa, Proc Inst Mech Eng Part B-J Eng Manuf 221(2007) 857-864.
18. H. Okuyucu, A. Kurt, E. Arcaklioglu, Mater Des 28(2007) 78–84.
19. I.N. Tansel, M. Demetgul, H. Okuyucu, A. Yapici, Int J Adv Manuf Technol 48(2010) 95-101.
20. A. K. Lakshminarayanan, V. Balasubramanian, Trans Nonferrous Met Soc China 19(2009) 9-18.
21. D. J. C. MacKay, Neural Computation 4(1992) 415-447.
22. V. Strijov, G. W. Weber, Computers and Mathematics with Applications 60(2010) 981-988.
23. C. G. Chua, A. T. C. Goh, Int J Numer Anal Meth Geomech 27(2003) 651–667.
24. G. Taguchi, System of Experimental Design, Kraus, White Plains, NY (1987).
25. D. C. Montgomery, Design and analysis of experiments, 7th Ed. John Wiley & Sons Inc.
26. Y.S. Sato, M. Urata, H. Kokawa, Metal. Mater. Trans. A 33A(2002) 625-635.
27. J. H. Yan, M. A. Sutton and A. P. Reynolds, Sci Techno Weld Join 10(6) (2005) 725–736.
28. C. D. Sorensen, A. L. Stahl, Metal Mater Trans B 38B(2007) 451-459.
29. Q. Shi, "Prediction of thermal distortion and thermal fatigue in shot sleeves", Masters Thesis, 2002, The Ohio State University.

Chapter 6. Strains and strain rates

Currently the three dimensional heat transfer and material flow model available at Penn State uses temperature dependent thermo mechanical properties of work-piece material. However, during FSW the material properties are also affected by the strains and strains rates. These updated material properties can be estimated by use of a dynamic recrystallization model which would consider the changes in material properties due to strain, strain rate and temperature. The lack of strain and strain rate data limit the development of a dynamic recrystallization based heat transfer and visco plastic flow model for prediction of the weld joint properties. Also, the microstructure and mechanical properties of FSW joints are affected by local gradients of strain and strain rates in the stir zone (SZ) and the thermo mechanically affected zone (TMAZ). [1] In processes involving large amounts of deformation, the accumulated strain is a significant factor in determining the nucleation and dynamic recrystallization rates. [2-7] The critical nuclei diameter and the nucleation rate are also affected by the local strain values. [3-6] The accumulated strain values also affect the final grain structure and the extent of low angle grain boundary formation in the SZ. [3-7]

Buffa et al. [8-9] and Schmidt and Hattel [10] adopted a continuum solid mechanics based approach to compute the equivalent strains in FSW. The equivalent strain values reported by these researchers varies from 6 [8-9] to 1.33×10^2 [10]. Bastier et al. [11] used a local computational fluid dynamics based model for FSW to estimate the values of strain components in the SZ. They reported that the computed normal strain (ε_{33}) to be tensile in nature and transverse strain (ε_{22}) to be compressive in nature. They also reported that the computed values of longitudinal strain (ε_{11}) were significantly small compared to the other two components. However, in terms of effective strain, the values reported by Bastier et al. [11] were significantly smaller than the same reported earlier. [8-10] The computed values reported by various researchers vary significantly and thus is it important to understand the values of not only the effective or equivalent strains but also the distribution of the strain and strain rate components in the SZ and TMAZ during FSW.

In recent years, a three dimensional visco-plastic material flow and heat transfer based numerical model has been used to explain the heat generation rate, temperature fields, materials flow and strain rates during FSW. [12-16] The results from this model have been

validated by comparing with the experimentally measured temperature profiles and the size of TMAZ for a wide range of materials and process conditions. [12-16] The material flow fields computed from this model can be used to compute the strain rates and strains during FSW. This chapter explains a methodology to compute strains and strain rates from a computed three dimensional velocity field. The methodology is first tested against the experimental observations during an extrusion process, which is similar to FSW in terms of the amount of material deformation involved. The methodology is then used to examine the strain and strain rate distributions during FSW of AA2524 alloy.

6.1. Numerical model

The three-dimensional visco-plastic flow and heat transfer model explained in chapter 2 is used to compute the three dimensional distribution of the temperature and the velocity fields. [15-17] The computed local velocity fields can then be used to compute the strain rates by the following relation:

$$\dot{\varepsilon}_{ij} = \frac{1}{2}\left(\frac{\partial u_i}{\partial x_j} + \frac{\partial u_j}{\partial x_i}\right) \tag{6.1}$$

where $\dot{\varepsilon}_{ij}$ is the strain rate tensor and $\frac{\partial u_i}{\partial x_j}$ is the velocity gradient in the computed velocity field. The integration of strain rate components with time results in the strain components: [18]

$$\varepsilon_{ij} = \int_0^t \dot{\varepsilon}_{ij} dt \tag{6.2}$$

where ε_{ij} is the strain tensor, and dt is the time step for integration. Since steady state flow is assumed in the heat transfer and visco-plastic flow model for the calculation of velocity fields, time is not a variable in the calculations. To perform the integration shown in Equation 6.2, the time variable is obtained by performing the integration along the streamlines. Since a streamline represents the path a particle is expected to follow in the flow field. If the streamlines are divided into various points, for any two nearby points on a streamline the ratio of the local velocity and the distance between the points will represent the time taken by a particle to travel between these two points.

$$dt = \frac{\Delta x_s}{u_s} \tag{6.3}$$

where dx_s is the distance between two points on the streamline and u_s is the resultant velocity along the streamline between the two points. From Equations 6.1, 6.2 and 6.3, for n (= 60) points on a streamline, the strain tensor can now be computed as follows:

$$\varepsilon_{ij} = \sum_{k=1}^{n-1} \frac{1}{2}\left(\frac{\partial u_i}{\partial x_j} + \frac{\partial u_j}{\partial x_i}\right)^k \times \left(\frac{\Delta x_s}{u_s}\right)^k \qquad (6.4)$$

where k is the counter of points along the streamline, Δx_s is the distance between point k and k+1, and u_s is the velocity at point k on the streamline. The local strain computed by Equation 6.4 will depict the total strain experienced by the particle at a spatial location.

6.2. Results and discussion

The results from the method explained above to compute the strain and strain rate components are validated by comparing with the experimentally determined strain values in an extrusion experiment reported by Berghaus et al. [18] They used an ink-stamped grid on the axial plane of an aluminum billet to experimentally measure the strain values. The aluminum billet is extruded at 430°C with an extrusion ratio of 12.4 to 1. Figure 6.1 shows a comparison of the experimentally measured strain values using the ink-grid method and computed values of strain using the streamline integration method. The fair agreement of these values shows that the method can be used to compute local strain values in a similar process, such as FSW, involving large amounts of strain.

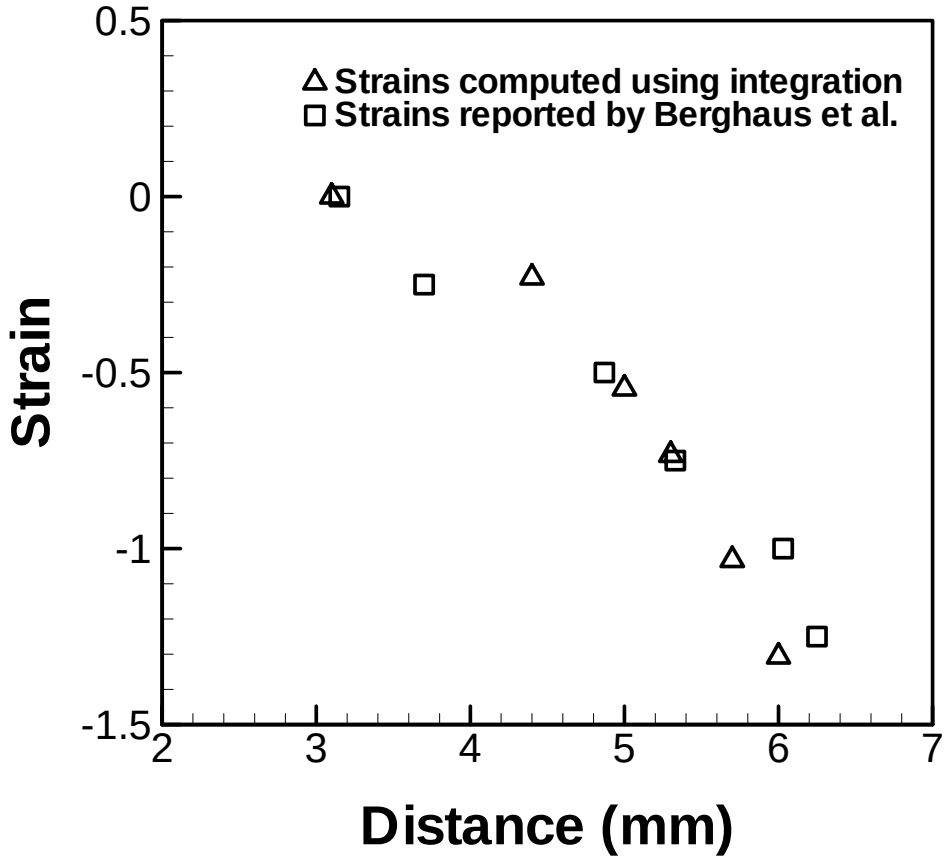

Figure 6.1 The strain values computed for the extrusion of an aluminum billet to verify the formulation of streamline integration method. The values shown by the squares are from the experimental results of Berghaus et al. [14] and the values shown by the triangles are from the methodology adapted in this work.

The heat transfer and visco-plastic flow model is used to compute the three dimensional temperature and material flow fields during FSW of Aluminum alloy AA2524. The material properties and experimental conditions used for these calculations are presented in Table 6.1. The computed velocity fields in two different horizontal planes, 0.13 and 2.0 mm away from the top surface, are shown in figure 6.2. These two planes are parallel to the top surface of the work piece. The figure also shows the direction of linear and rotational motion of the FSW tool. The computed velocity fields are used to find the streamlines representing the flow of material in FSW. Five streamlines shown in figure 6.2(a) are considered, since they represent the material flow in both the SZ and TMAZ. The x-axis represents the direction of the weld joint line and y axis is the transverse direction. The tool location is taken as x=0 and y=0.

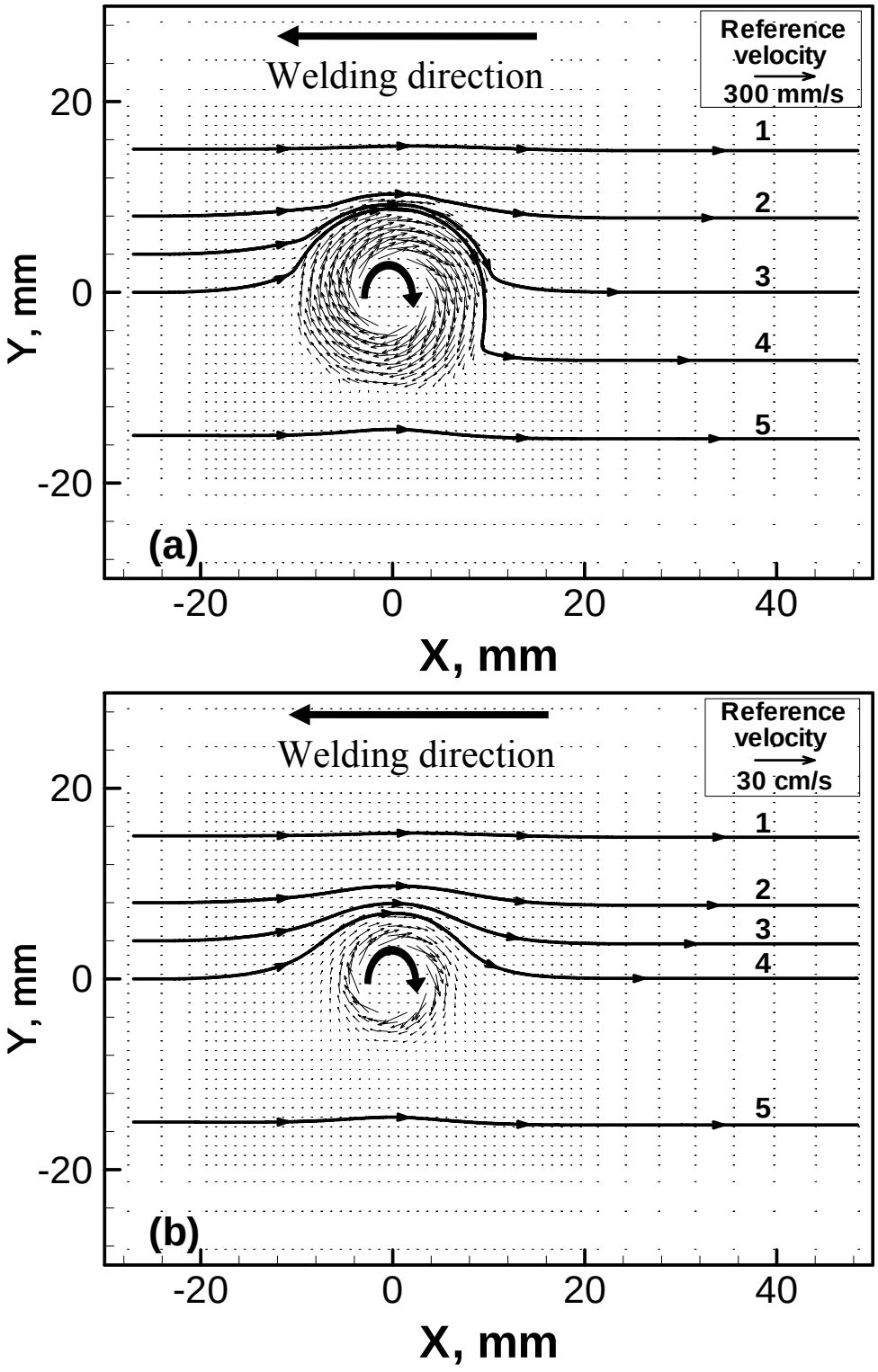

Figure 6.2. The computed velocity fields and streamlines in two horizontal planes parellal to the work-piece top surface. (a) Plane 1 – 0.13mm away from top and (b) plane 2 – 2.0mm away from top.

Table 6.1 The experimental conditions and material properties used for calculating the temperature and velocity fields.

Experimental conditions	
Workpiece length, cm	30
Workpiece width, cm	21
Workpiece depth, cm	0.64
Workpiece material	AA2524
Tool material	1018 steel
Shoulder radius, cm	1.015
Pin radius, cm	0.355
Pin length, cm	0.62
Welding velocity, cm-s^{-1}	0.211
Tool rotation velocity, rpm	300
Axial pressure, MPa	130.7
Tilt angle	2.5°
Thread pitch, cm	0.079
Work piece material properties	
Density, kg/m^3	2700
Specific heat capacity, J/kg-K	$929.3 - 0.627\,T + 1.48\times10^{-3}\,T^2 - 4.33\times10^{-8}\,T^3$
Thermal conductivity, W/m-K	$25.2 + 0.398\,T + 7.36\times10^{-6}\,T^2 - 2.52\times10^{-7}\,T^3$
Yield Strength: Temperature (K) 297 373 421 476 533 589 644 855 Yield Strength (MPa) 340 305 245 145 65 35 25 0	
Tool material properties	
Density	7860 kg/m^3
Specific heat capacity, J/kg-K	$468.3 - 8.5\,T + 3.0\times10^{-4}\,T^2 + 1.8\times10^{-7}\,T^3$
Thermal conductivity, W/m-K	$3.8 + 9.2\times10^{-2}\,T - 1.8\times10^{-4}\,T^2 + 7.8\times10^{-8}\,T^3$

The velocity gradients shown in Figure 6.2(a) are used to compute the strain rate components ($\dot{\varepsilon}_{ij}$) along the streamlines. The strain rate components computed along the streamlines are then integrated using Equation 6.2 to compute the strain components (ε_{ij}). Figure 6.3(a) and (b) shows the computed values of the two strain rate components $\dot{\varepsilon}_{11}$ and $\dot{\varepsilon}_{22}$, respectively. For streamlines 1 to 4 in Figure 6.2(a), which pass through the retreating side, as the material moves from the front of the tool to the back of the tool, the x-component of velocity, u, initially increases and then decreases with distance x. The strain rate component, $\dot{\varepsilon}_{11}$, that is calculated from the velocity gradient $\partial u/\partial x$ is positive in front of the tool as shown in Figure 6.3(a). The strain rate component is negative behind the tool as the velocity gradient becomes negative for the material in the back of the tool. The y component of velocity, v, decreases with an increase in the y distance for the material in

front of the tool and decreases with a decrease in the y distance for the material behind the tool. This results in the velocity gradient $\partial v/\partial y$ being negative in front of the tool and positive behind the tool. The strain rate component, $\dot{\varepsilon}_{22}$, as calculated from the velocity gradient $\partial v/\partial y$ also show this change along x axis as shown in Figure 6.3(b).

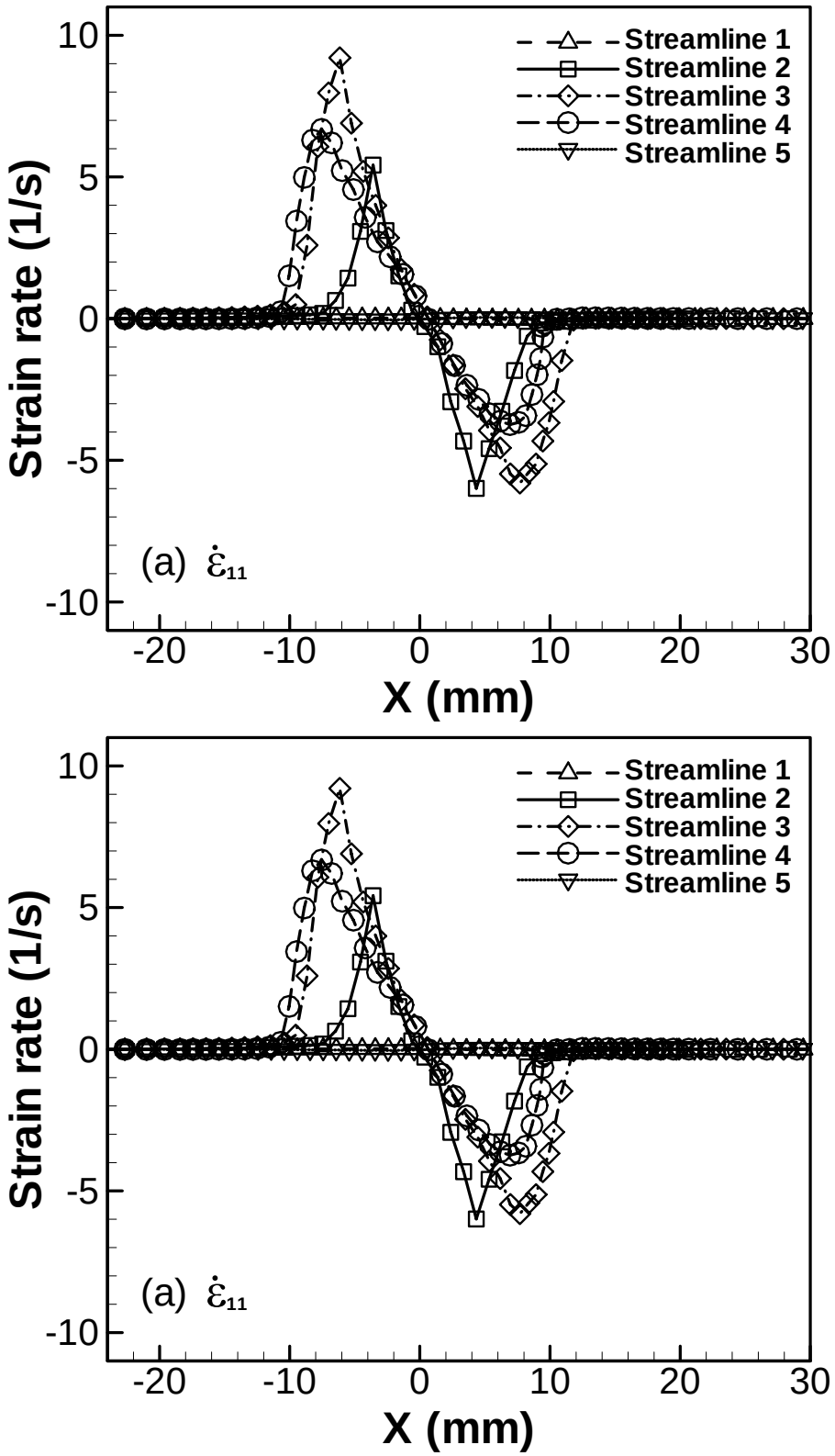

Figure 6.3 Computed strain rate components (a) $\dot{\varepsilon}_{11}$, and (b) $\dot{\varepsilon}_{22}$.

The computed strain rate values are integrated using Equation 6.4 to estimate the strain components at various spatial locations. Figure 6.4(a) and (b) show the computed

values of two normal strain components, ε_{11} and $\varepsilon_{22,}$ respectively. The calculation of strain rate components is cumulative in nature, as shown in Equation 6.4. The value of the strain components at any spatial location represent the overall effect of all the deformations experienced by the particle before reaching that location. The positive value of the normal strain component, ε_{11}, shown in Figure 6.4(a), represents elongation of the material as it moves along the streamline. This tensile nature of strain component ε_{11} increases as the material reaches the tool and reduces behind the tool as the material moves away. The final value of this strain component towards the end of streamlines 2 and 3 become compressive in nature. However, in the case of streamline 4, ε_{11} retains a positive value (tensile strain) towards the end.

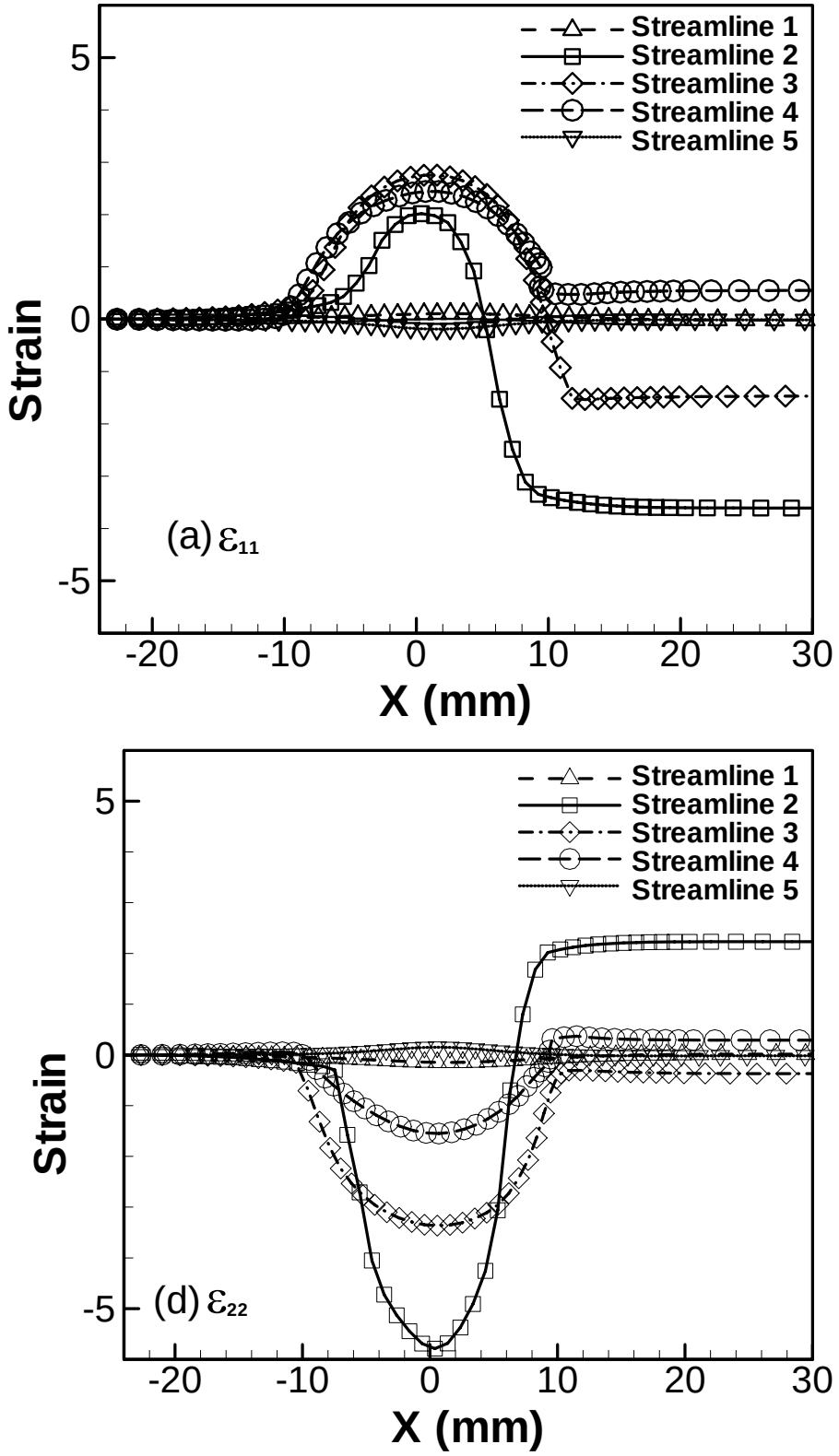

Figure 6.4 Computed strain components (c) ε_{11}, and (d) ε_{22}

Figure 6.4(b) shows that the computed values of the transverse strain component, ε_{22}, are negative for the material in front of the tool and increase as the material moves behind

the tool. The transverse strain component is compressive in nature in front of the tool and the accumulation of tensile strain behind the tool reduces the compressive nature of the total transverse strain component. For the streamlines 2 and 4 in Figure 6.2(a), the transverse strain component is positive (tensile). However, for the material following streamline 3, the transverse strain component is negative (compressive). For the streamlines 1 and 5, since the material is very near to the end of the deformation zone, the strain component values are very small and can be considered insignificant.

The spatial variations of the computed values of the strain components along the x axis are realistic in nature. For example, as the material moves from the front of the tool to the back of the tool through the retreating side, the material adjacent to the tool elongates in the longitudinal direction and therefore, compress in the transverse direction. Thus, for the material in front of the tool, the transverse strain component, ε_{22}, is compressive (-ve) in nature and the longitudinal strain, ε_{11}, is tensile (+ve) in nature. However, behind the tool, the transverse strain is tensile and the longitudinal strain is compressive.

For the welding conditions investigated, the computed values of components of strain rate lies between -9 /s to 9 /s, whereas the computed values of strain components are between -10 to 5. These computed values of strain and strain rates are comparable to the earlier reported values for strain and strain rates.[3,19] The computed strain and strain rate values can be used to estimate the material properties resulting from dynamic recrystallization. These updated values of material properties would strengthen the heat transfer and visco-plastic flow model to design reliable, long lasting tools.

6.3. Summary and conclusion

The strain rate and strain components during FSW of AA2524 can be computed using a coupled three dimensional visco-plastic flow and heat transfer model. As the material moves from the leading to the trailing edge through the retreating side, it experiences a tensile strain in the welding direction and compressive strain in the transverse direction. The nature of the strain reverses as the material reaches the trailing edge and is forced to consolidate behind the advancing tool. In the retreating side, the volumetric strain increases as the material reaches close to the tool and decreases behind the tool. The maximum strain occurs close to the welding tool. In the advancing side, the volumetric strains are small. For the

condition of FSW investigated, the computed strains and strain rates were in the ranges -10 to 5 and -9 /s to 9 /s, respectively.

6.4. References

1. M. D. Fuller, S. Swaminathan, A. P. Zhilyaev, T. R. McNelley, Materials Science & Engineering A 463 (2007) 128–137.
2. F. J. Humphreys, P. B. Prangnell, J. R. Bowen, A. Gholinia And C. Harris, Philosophical Transactions of the Royal Society A 357 (1999) 1663–1681.
3. T. R. McNelley, S. Swaminathan and J. Q. Su, Scripta Materialia 58 (2008) 349–354.
4. P. B. Prangnell, C. P. Heason, Acta Materialia 53 (2005) 3179–3192.
5. L. E. Murr, G. Liu, J. C. McClure, Journal of Materials Science Letters 16 (1997) 1801–1803.
6. K. Oh-Ishi, A. P. Zhilyaev, T. R. McNelley, Metallurgical and Materials Transactions A 37A (2006) 277–286.
7. J. Q. Sua, T. W. Nelson and C. J. Sterling, Materials Science and Engineering A 405 (2005) 277–286.
8. G. Buffa, J. Hua, R. Shivpuri, L. Fratini, Materials Science and Enginnering A 419 (2006) 381-388
9. G. Buffa, J. Hua, R. Shivpuri, L. Fratini, Materials Science and Enginnering A 419 (2006) 389-396
10. H. Schmidt, J. Hattel, Modelling and Simulation in Materials Science and Engineering 13 (2005) 77-93
11. A. Bastier, M. H. Maitournam, K. Dang Van, F. Roger, Science and Technology of Welding and Joining 11(3) (2006) 278-288
12. R. Nandan, T. DebRoy, H. K. D. H. Bhadeshia, Progress in Materials Science (2008) 980–1023.
13. R. Nandan, G. G. Roy and T. DebRoy, Metallurgical and Materials Transactions A 37(4) (2006) 1247–1259.
14. R. Nandan, G. G. Roy, T. J. Lienert and T. DebRoy, Science and Technology of Welding and Joining 11(5) (2006) 526–537.
15. R. Nandan, G. G. Roy, T. J. Lienert and T. DebRoy, Acta Materialia 55 (2007) 883–895.
16. R. Nandan, T. J. Lienert and T. DebRoy, International Journal of Materials Research 99(4) (2008) 434–444.
17. A. Arora, R. Nandan, A. P. Reynolds and T. DebRoy, Scripta Materialia 60 (2009) 13–16.
18. D.G. Berghaus and H.B. Peacock, Experimental Mechanics 25(3) (1985) 301–307.
19. P. Heurtier, C. Desrayaud, F. Montheillet, Mater. Sci. Forum 396–402 (2002) 1537–1542.

Chapter 7. Back of envelope calculations in FSW

Recently developed numerical models of heat transfer, materials flow, torque and other parameters in friction stir welding (FSW) have been tested against experimental data for the joining of aluminum alloys [1-24], steels [25-29] and titanium alloys. [30] The numerical models have been applied for the solution of several problems. For example, the computed temperature and material flow fields have been useful in understanding the heating and cooling rates [7,23], improvement of tool design [13,15,17-19,30-34] and in the estimation of torque and traverse force [16-18,21-22,31-32,35-36]. However, most of these numerical models require the solution of the Navier Stokes equations and the energy equation together with the constitutive equations to obtain the viscosity of the plasticized materials. These calculations are complex and computationally intensive.

In the case of fusion welding, sophisticated numerical models also exist [37-40] in parallel with simple but insightful methods that can be easily implemented by practicing engineers. For example, those based on the Rosenthal equations [41] or carbon equivalents [42] are two common analytical tools that are used widely and form the basis for many practical judgments. Further analytical methods are being developed to include the effect of convection in the existing cooling rate estimations in fusion welding. [43] A similar scenario does not exist for the much younger friction stir process. Heurtier et al [44] and Jacquin et al [16] have proposed semi-analytical models where they have used a mix of three different analytical methods to estimate the material flow in FSW. There is a need for a simpler method where just one analytical method can explain the material flow in FSW. A set of analytical methods to calculate important parameters such as peak temperature, and torque are also needed, but not currently available.

Several simplified methodologies to approximately estimate these important variables are proposed and tested in this chapter. Material flow during friction stir welding is driven mainly by the rotation of the tool shoulder. Therefore, an approximate analytical technique for the calculation of this flow in three dimensions is developed and tested, based on viscous flow of an incompressible fluid induced by a solid rotating disk. The computed velocity fields for the welding of an aluminum alloy, a steel and a titanium alloy are compared with those obtained from a well tested and comprehensive numerical model. An

improved non-dimensional correlation to estimate the peak temperature, and an analytical method to estimate torque are also presented in this chapter. The proposed correlation for the peak temperature is tested against experimental data for different weld pitch (distance moved by tool per rotation) for three aluminum alloys. The computed torque values are tested against corresponding measurements for various tool rotational speeds.

7.1. Velocity field

In order to develop an analytical solution for the three dimensional velocity field, the following assumptions are made. First, a relatively simple tool geometry with a straight cylindrical tool pin is considered. Second, the flow is assumed to result primarily from the rotation of the tool shoulder. Third, a known geometry of the flow domain based on many experiments is assumed. The material flow field is estimated by appropriately modifying an analytical solution for the steady state flow of an incompressible fluid between two solid disks, one rotating and the other stationary. [45] The three components of velocity, u, v, w in r, θ and z directions, respectively in cylindrical polar coordinates are given by:

$$u = r\omega F,\ v = r\omega G,\ \text{and}\ w = d\omega H \tag{7.1}$$

where r is the radial distance, ω is the rotational velocity, d is the distance between the two disks, and F, G and H are functions of z/d where z is the vertical distance under the rotating disk. The expressions for F, G and H are explained in detail in the appendix. In order to adapt the above mentioned solution for FSW, it is necessary to define the material flow domain. The experimentally observed domain for material flow is shown schematically in Figure 7.1. This zone has the shape of an inverted cone, truncated near the tip of the tool pin. The velocity field in the entire three dimensional flow region can be readily calculated using Equation 7.1 if the velocity field at the tool shoulder is specified.

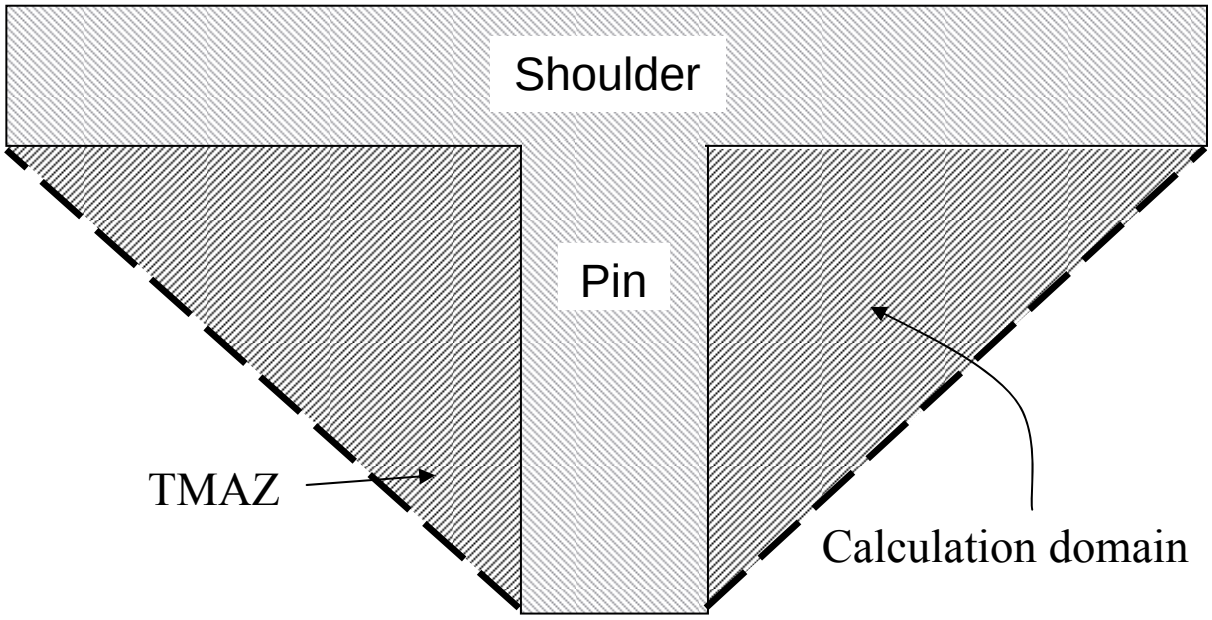

Figure 7.1 Schematic diagram showing the domain for velocity field calculation. An approximate thermomechanically affected zone (TMAZ) geometry is shown by cross hatched region in the figure.

In order to specify the local velocities of plasticized materials at the tool shoulder – material interface, a condition of partial slip is considered. For a tool shoulder velocity of ωr, the velocity of material in contact with the tool shoulder surface is considered as $(1\text{-}\delta)\omega r$ where δ is the fraction of slip at the interface. The fraction of slip is considered to be function of the tool rotation speed and can be expressed as: [36]

$$\delta = 0.2 + 0.8 \times \left(1 - \exp(-\delta_0 \frac{\omega}{\omega_0} \frac{R_M}{R_S}) \right) \qquad (7.2)$$

where δ_0 and ω_0 are constants, R_S is the radius of shoulder and R_M is the average of the pin and shoulder radius. The data used for calculations of velocities are presented in Table 7.1. [26,30,36]

Table 7.1 Material properties and welding process parameters used in the velocity and torque estimation

Alloy	**AA2524** [36]	**304L SS** [26]	**Ti-6Al-4V** [30]
Shoulder radius, R_S	10.15 mm	9.5 mm	12.5 mm
Pin radius, R_P	3.55 mm	3 mm	5 mm
Pin length	6.2 mm	6.4 mm	9.9 mm
Rotating velocity, ω	31.42 rad/s	47.12 rad/s	20.94 rad/s
Density, ρ	2700 kg/m^3	7800 kg/m^3	4420 kg/m^3
Axial pressure, P_N	130.7 MPa	130.7 MPa	37.75 MPa
Constant for slip, δ_0	3.0	2.0	2.5

Constant for slip, ω_0	40 rad/s	40 rad/s	40 rad/s
Yield Strength, Y (Temperature, T in K)	$0.0062xT^2$ - 7.61xT+ 2371.5 MPa	-	-0.1406xT + 271.83 MPa

7.2. Peak Temperature

It has been recently shown that an existing dimensionless correlation of the following form can be useful for the estimation of non-dimensional peak temperature from the non-dimensional heat input: [46]

$$T^* = \alpha \log_{10}(Q^*) + \beta \tag{7.3}$$

where α and β are constants, and the non-dimensional peak temperature, T^*, is defined as: [46]

$$T^* = \frac{T_P - T_{in}}{T_S - T_{in}} \tag{7.4}$$

where T_P is the peak temperature, T_{in} is the initial temperature and T_S is the solidus temperature, Q^* is the non-dimensional heat input defined as: [46]

$$Q^* = \frac{\sigma_8 A \omega C_P \phi}{kU^2} \tag{7.5}$$

where σ_8 is the yield stress of the material at a temperature of $0.8T_S$, A is the cross sectional area of the tool shoulder, ω is the tool rotation velocity, C_P is the specific heat capacity of the workpiece material, k is the thermal conductivity of the workpiece, U is the traverse velocity and ϕ is the ratio in which heat generated at the shoulder workpiece interface is transported between the tool and the workpiece, and is defined as: [46]

$$\phi = \left[(k\rho C_P)_W / (k\rho C_P)_T\right]^{1/2} \tag{7.6}$$

where ρ is the density, and the subscripts W and T are used to describe the material properties of workpiece and the tool respectively. All the material properties are taken at a temperature average between the initial temperature and the solidus temperature.

Because of the availability of many recently reported values of peak temperatures in the literature, the coefficients α and β in Equation **7.3** can now be based on a larger volume of reported peak-temperature data. As a result, the correlation is now more accurate than before.

7.3. Torque

The torque required during FSW determines the energy input to the workpiece and is also an important parameter in tool design. It is calculated from the shear stress at yielding, τ, which is given by: [26-27,35-36]

$$\tau = Y/\sqrt{3} \tag{7.7}$$

where Y is the yield stress at an average temperature on the tool shoulder workpiece interface. The average temperature, in turn, is calculated from the peak temperature. Previous research [35] has shown that the average temperature at the shoulder work piece interface is approximately 95% of the peak temperature (T_P). The value of T_P is estimated from the dimensionless correlation shown in equation **7.**3. The total shear stress, τ_t, on the tool can be given as [27,36]

$$\tau_t = [(1-\delta)\tau + \delta\mu_f P_N] \tag{7.8}$$

where δ is the fraction of slip computed from equation **7.**2, μ_f is the friction coefficient and P_N is the axial pressure. Similar to the fraction of slip in equation **7.**2, μ_f, is computed as [36]

$$\mu_f = 0.25 \times \left(1 - \exp(-\delta \frac{\omega}{\omega_0} \frac{R_M}{R_S})\right) \tag{7.9}$$

The torque, T, can be computed from the total shear stress as follows: [27,36]

$$T = \oint_A r \times (\tau_t dA) = \tau_t \int_0^{R_S} 2\pi r^2 dr = \frac{2\pi R_S^3 \tau_t}{3} \tag{7.10}$$

where r is the distance from tool axis, dA is the infinitesimal area on the shoulder workpiece contact surface and dr is the infinitesimal distance along the radial direction.

7.4. Results and discussion

The first step in the proposed analytical calculation of three dimensional materials flow field in FSW is to estimate the material velocities at the interface between the shoulder and the workpiece. The maximum velocities at the top surface are $(1-\delta)\omega r$ where δ is the spatially dependent slip given by Equation 7.2, ω is the rotational speed and r is the distance from the tool rotation axis. Once the velocities at the shoulder-workpiece interface are known, the velocity field in the entire flow domain is given by Equation 7.1. For aluminum alloy AA2524 containing 4.3Cu, 1.4Mg, 0.58Mn wt% and small quantities of Si, Fe and Zn,

the computed velocity fields in different horizontal planes parallel to the tool shoulder surface are compared with those in the same planes computed by three dimensional heat transfer and visco-plastic flow model [26-27,35-36] in Figure 7.2. The heat transfer and visco-plastic flow model uses the partial slip condition at the tool workpiece interface similar to the consideration in proposed analytical model. [26-27,35-36] A fair agreement in the flow pattern is observed between the numerically and analytically computed results in Figure 7.2, The material velocity is maximum at z = 0 (the tool shoulder workpiece interface) and decreases as the distance from the tool shoulder increases. The analytically computed velocities at various locations are quantitatively compared with the correspondingly numerically computed results as explained below.

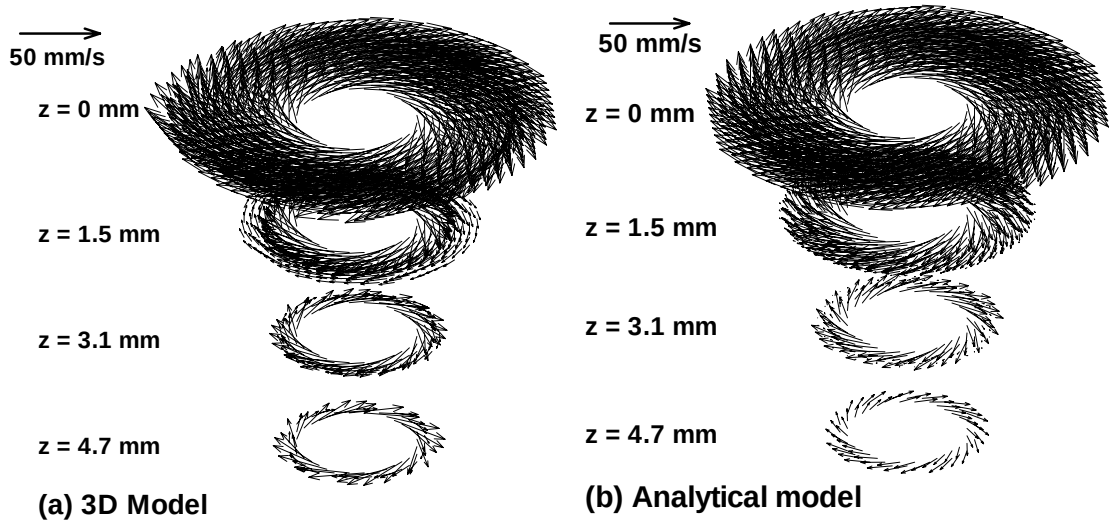

Figure 7.2 The computed velocity fields in various horizontal planes for the FSW of AA2524. (a) results from a well tested numerical heat transfer and visco plastic flow code, and (b) from the proposed analytical solution.

Figure 7.3 shows the velocities, computed from both analytical solution and 3D comprehensive numerical visco-plastic flow and heat transfer model, as a function of the vertical distance below the tool shoulder. The velocity *u'* in this figure is the square root of the sum of the three velocity components squared. The velocities in the three plots for the welding of an aluminum alloy, a steel, and a titanium alloy are made non-dimensional by dividing with the maximum velocity (u*). These velocities are plotted against the non-dimensional vertical distance from the shoulder defined by *z/d*, where *d* is the pin length. The velocities in the three cases are maximum at the tool workpiece interface where *z/d* is zero and decrease as the distance from the tool shoulder increases. The results from the analytical solution are in fair agreement with the 3D heat transfer and visco-plastic flow

model for FSW of AA2524, Ti-6Al-4V and 304L SS alloys. In each case, at horizontal planes near the mid-height of the tool pin, the analytical solutions predict about 10 to 17% higher velocities than the corresponding numerically computed velocities. This discrepancy can be attributed, at least in part, due to the difference between the computational and the physical flow domains. The actual wall of the flow domain is often closer than the wall of the inverted truncated cone assumed in the calculations. Other possible sources of this discrepancy include the effects of the presence of the tool pin and the welding velocity which are not considered directly in the analytical model.

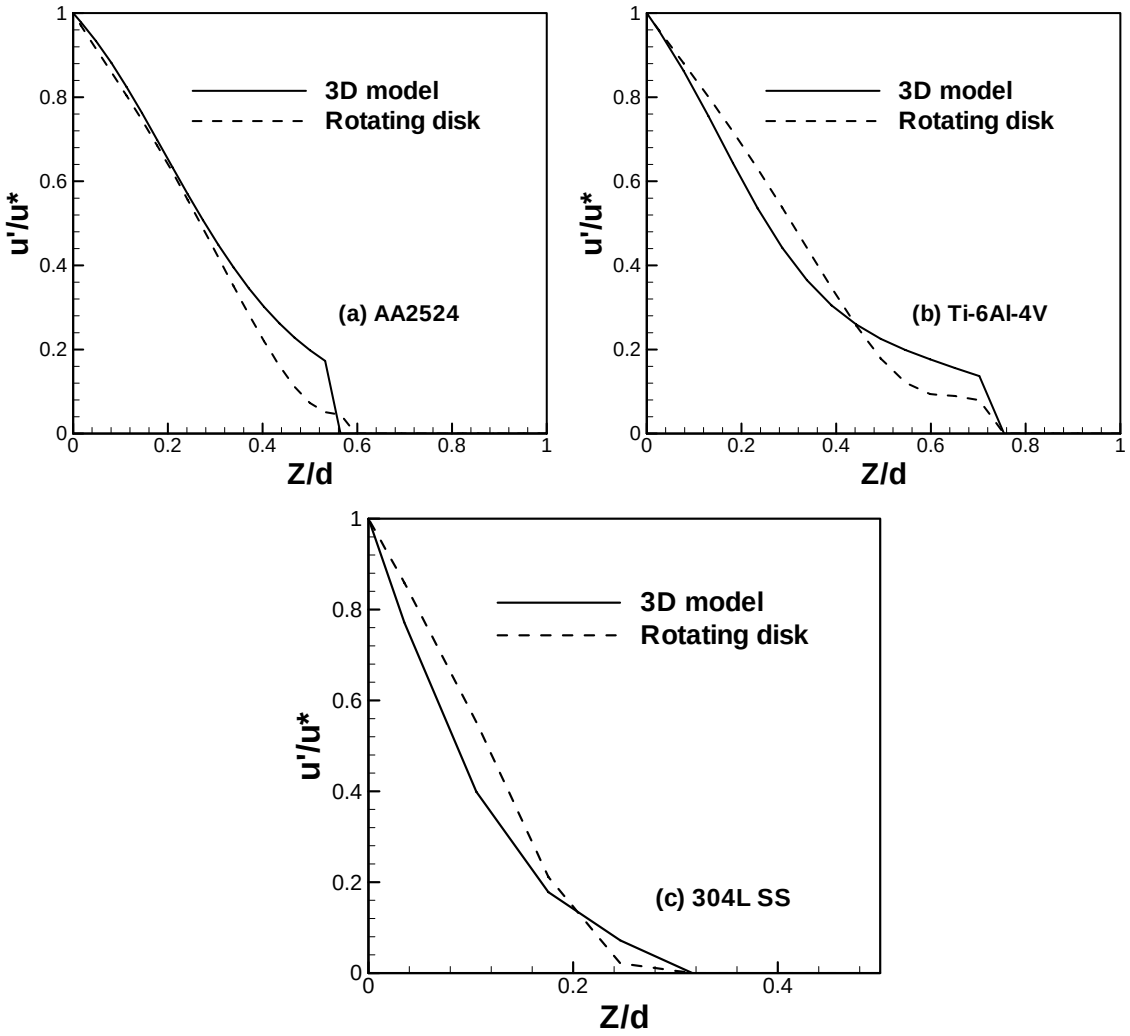

Figure 7.3 The analytically computed velocities relative to the maximum velocity as a function of the dimensionless distance from the tool shoulder. (a) AA2524 (b) Ti-6Al-4V, (c) 304L SS. u' is the square root of sum of the three velocity components squared and u* is the maximum velocity.

The non-dimensional temperature, defined by Equation 7.3, is plotted as a function of the non-dimensional heat input using various experimental and numerically computed results obtained from the literature. [22,26,46-47] The experimental values of peak

temperatures are measured at the edge of the tool shoulder. The numerical model is used to estimate the peak temperature where temperature was measured farther away from the edge of tool shoulder. [48] The coefficients α and β for Equation 7.3 are recalculated from experimental results, including recently published experimental results. The following correlation is proposed to estimate the non-dimensional peak temperature from the non-dimensional heat input on the basis of the results shown in figure 7.4:

$$T^* = 0.151 \ \log_{10}\left(Q^*\right) + 0.097 \qquad (7.12)$$

This relationship is valid in the range of Q^* between $4x10^2$ and $3.7x10^5$. It should be noted that the correlation has a standard deviation of 0.01 which is an improvement over the previous results [48] because of the inclusion of many recently published results. Furthermore, Equation 7.12 is now valid for a larger range of Q^*.

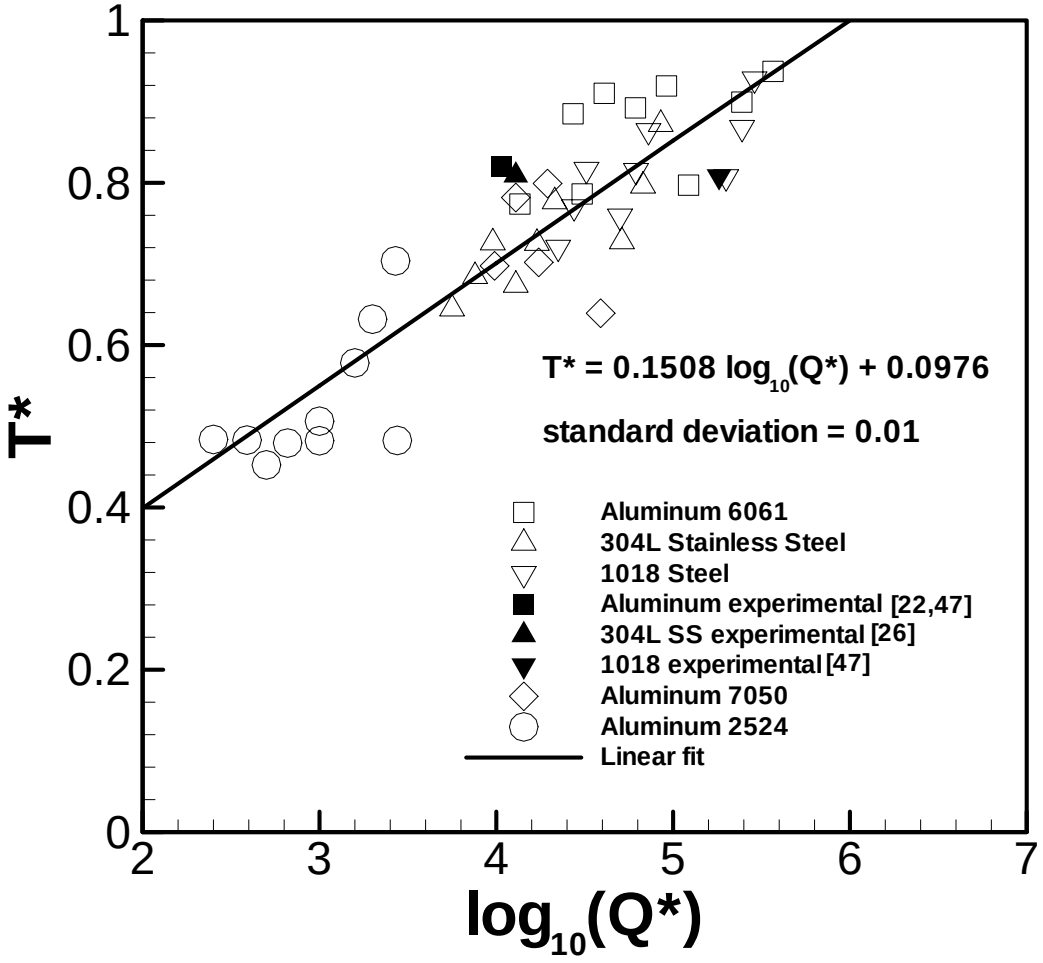

Figure 7.4 Linear relationship between dimensionless temperature and log of dimensionless heat input.

The accuracy of the correlation developed in Equation 7.12 is evaluated by estimating the peak temperatures at different weld pitch values and comparing the estimated results with corresponding experimental observations. Figure 7.5(a) shows the experimentally measured peak temperatures for various welding pitch values for aluminum 2024, 5083 and 7075 alloys. [49] The estimated values of peak temperature for the same alloys are shown in Figure 7.5(b). The data used for the computation is shown in Table 7.2. Since the tool dimensions and welding speed are not provided by Nakata et al. [49], commonly used tool dimensions (25 mm shoulder diameter and 6 mm pin diameter) and 400 mm/min welding velocity have been used for the calculations. It can be observed that the slopes of the estimated peak temperatures for the three alloys are similar to the slopes for experimental results. In both the experimental [49] and the analytical results, the peak temperature is highest for AA5083 and lowest for AA7075 for a specific weld pitch. The computed peak temperatures for various cases are 3 to 9% different from the corresponding experimentally determined values.

Table 7.2 The data used for calculation of the peak temperature at different weld pitch values for various aluminum alloys. [50]

Material	Solidus temperature,T_s, K	Thermal conductivity,k, W m^{-1} K^{-1}	Specific heat,C_P, J kg^{-1} K^{-1}	Shoulder radius, m	Pin radius, m	σ_8, MPa	F
AA7075	749	130	1200	0.0125	0.006	26.88	0.95
AA2024	775	110	1200	0.0125	0.006	19.27	0.95
AA5083	852	109	1200	0.0125	0.006	16.70	0.95

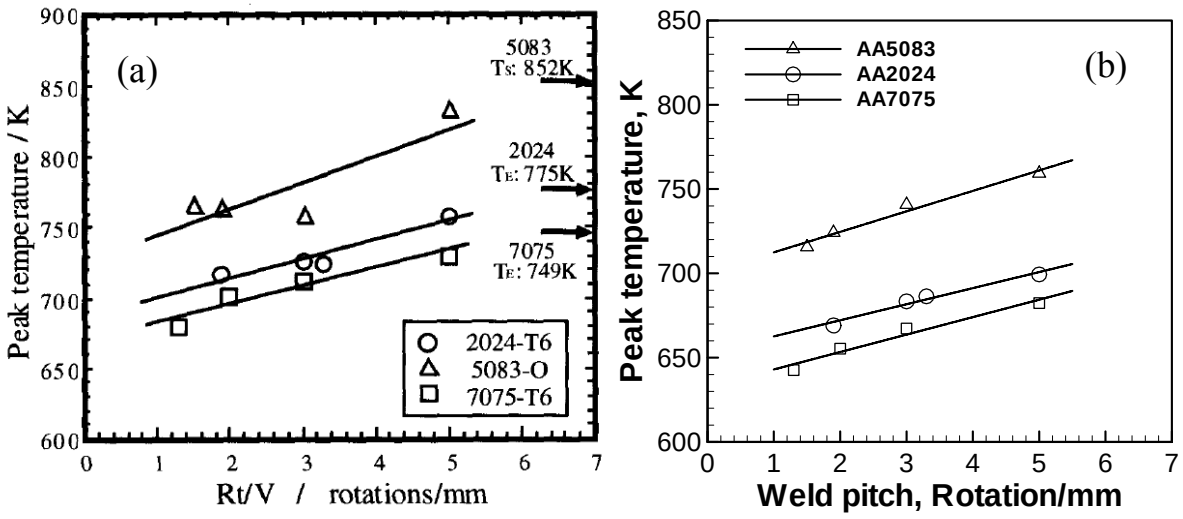

Figure 7.5 Peak temperature against weld pitch for friction stir welding of various aluminum alloys. (a) Experimentally measured peak temperature [49] (b) Peak temperature from the proposed correlation.

The experimentally measured values of the torque for friction stir welding of AA2524 and Ti-6Al-4V alloys are compared with the estimated torque from Equation 7.10. Figure 7.6 compares the analytically estimated and the experimentally measured torque values for FSW at various tool rotational speeds. It is observed that the torque required decreases with increase in the tool rotational speed for the FSW of both AA2524 and Ti-6Al-4V alloys. The material becomes softer with increase in temperature as the tool rotational speed increases, making it easier for the tool to rotate the material around. The analytically estimated values of the torque are in close agreement with the experimentally observed values of torque for both AA2524 and Ti-6Al-4V alloys. The torque values for Ti-6Al-4V are higher compared to AA2524 as the former is a harder material.

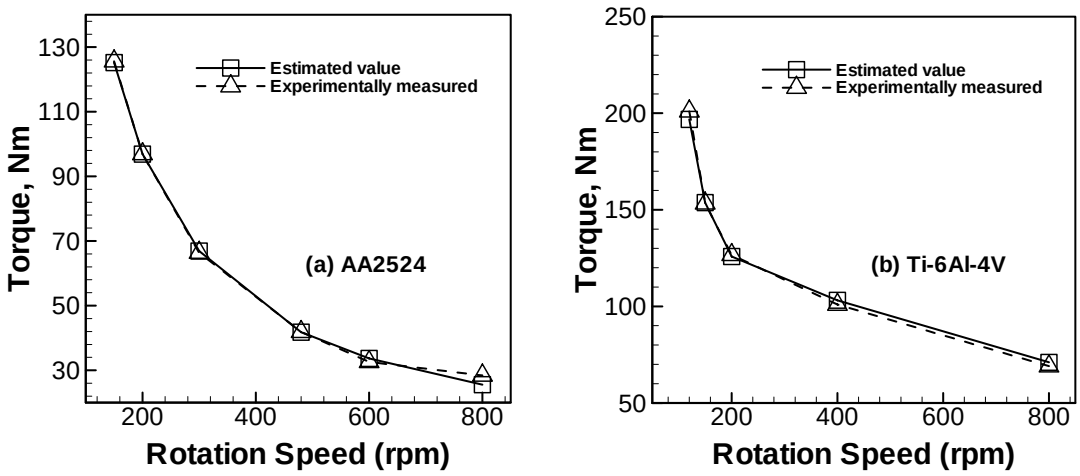

Figure 7.6 Estimated and experimental torque values for FSW of (a) AA2524 [36] and (b) Ti-6Al-4V alloy. [51] The data used for the calculations are available in table 7.1.

7.5. Summary and conclusion

Analytical models of materials flow, peak temperatures, and torque for friction stir welding (FSW) are proposed and tested. The analytical solution for the calculation of three dimensional materials flow velocities during FSW is adapted from the analytical solution of the viscous flow of an incompressible fluid induced by a solid rotating disk. It is shown that such calculations are straightforward and fairly accurate for the FSW of an aluminum alloy, a steel and a titanium alloy. An existing correlation for the estimation of peak temperature is improved using a large volume of recently published data. The improved correlation for peak temperature is tested against experimental peak temperatures for different welding pitch for three aluminum alloys. The torque required for FSW at various tool rotational

speeds were computed analytically from the yield stress of the materials using the peak temperature estimation proposed in this chapter. The methodologies proposed and tested in this chapter allow calculation of important parameters in FSW without time-consuming and complex calculations.

7.6. References

1. M.J. Russell, H. Shercliff, Analytical modelling of friction stir welding. In: Russell MJ, Shercliff R (Eds.). INALCO'98: 7th international conference on joints in aluminium. Cambridge, UK: TWI; 1999. 197–207.
2. L. Fratini, G. Buffa, R. Shivpuri, Acta Mater 58(2010) 2056-2067.
3. M. Song, R. Kovacevic, Int J Mach Tools Manuf 43(2003) 605-615.
4. M. Song, R. Kovacevic, J Eng Manuf 218(2004) 17-33.
5. A. Simar, Y. Brechet, B. de Meester, A. Denquin, T. Pardoen, Acta Mater 55(2007) 6133-6143.
6. H.W. Zhang, Z. Zhang, J.T. Chen, Acta Metall Sin 41(2005) 853-857.
7. C.M. Chen, R. Kovacevic, Int J Mach Tools Manuf 43(2003) 1319-1326.
8. H. Schmidt, J. Hattel, J. Wert, Modell Simul Mater Sci Eng 12(2004) 143-157.
9. H. Schmidt, J. Hattel, Int J Offshore Polar Eng 14(2004) 296-304.
10. H. Schmidt, J. Hattel, Sci Technol Weld Join 10(2005) 176-186.
11. H. Schmidt, J. Hattel, Modell Simul Mater Sci Eng 13(2005) 77-93.
12. N. Kamp, A. Sullivan, R. Tomasi, J.D. Robson, Acta Mater 54(2006) 2003-2014.
13. G. Buffa, J. Hua, R. Shivpuri, L. Fratini, Mater Sci Eng A 419(2006) 381-388.
14. A. Arora, Z. Zhang, A. De, T. DebRoy, Scr Mater 61(2009) 863-866.
15. A. Arora, A. De, T. DebRoy, Scr Mater 64(2011) 9-12.
16. D. Jacquin, B. de Meester, A. Simar, D. Deloison, F. Montheillet, C. Desrayaud, J Mater Process Technol 211(2011) 57-65.
17. P.A. Colegrove, H.R. Shercliff, Sci Technol Weld Join 9(2004) 345-351.
18. P.A. Colegrove, H.R. Shercliff, Sci Technol Weld Join 9(2004) 352-361.
19. Y.H. Zhao, S.B. Lin, F. Qu, L. Wu, Mater Sci Technol 22(2006) 45-49.
20. P.A. Colegrove, H.R. Shercliff, J Mater Process Technol 169(2005) 320-327.
21. M.Z.H Khandkar, J.A. Khan, J Mater Process Manuf Sci 10(2001) 91-105.
22. M.Z.H. Khandkar, J.A. Khan, A.P. Reynolds, Sci Technol Weld Join 8(2003) 165-174.
23. A. Simar, J. Lecomte-Beckers, T. Pardoen, B. de Meester, Sci Technol Weld Join 11(2006) 170-177.
24. R. Nandan, B. Prabu, A. De, T. DebRoy, Weld J 86(2007) 331s-322s.
25. Z. Feng, J.E. Gould, T.J. Lienert, A heat flow model for friction stir welding of steel. In: Bieler TR (Eds.). Hot deformation of aluminium alloys. Warrendale, PA, USA: TMS–AIME; 1998. 149–158.
26. R. Nandan, G.G. Roy, T.J. Lienert, T. DebRoy, Sci Technol Weld Join 11(2006) 526-537.
27. R. Nandan, G.G. Roy, T.J. Lienert, T. DebRoy, Acta Mater 55(2007) 883-895.
28. S. Bruschi, S. Poggio, F. Quadrini, M.E. Tata, Mater Lett 58(2004) 3622-3629.
29. H.K.D.H. Bhadeshia, T. DebRoy, Sci Technol Weld Join 14(2009) 193-196.
30. R. Nandan, T.J. Lienert, T. DebRoy, Int J Mater Res 99(2008) 434-444.

31. W.M. Thomas, K.I. Johnson, C.S. Wiesner, Adv Eng Mater 5(2003) 485-490.
32. W.M. Thomas, Mater Sci Forum 426-432(2003) 229-236.
33. W.M. Thomas, D.G. Staines, K.I. Johnson and, P. Evans, Adv Eng Mater 5(2003) 273-274.
34. A. Mandal, P. Roy, J Mater Process Technol 180(2006) 167-173.
35. R. Nandan, G.G. Roy, T. DebRoy, Metall Mater Trans A 37(2006) 1247-1259.
36. A. Arora, R. Nandan, A.P. Reynolds, T. DebRoy, Scr Mater 60(2009) 13-16.
37. A. De, T. DebRoy, Weld J 84(2005) 101s-112s.
38. A. Kumar, T. DebRoy, Metall Mater Trans A 38(2007) 506-519.
39. W. Zhang, C.L. Kim, T. DebRoy, J Appl Phys 95(2004) 5220-5229.
40. A. Kumar, T. DebRoy, Int J Heat Mass Transfer 47(2004) 5793-5806.
41. D. Rosenthal, Weld. J. 20(1941) 220s-234s.
42. H. Suzuki, Carbon equivalent and maximum hardness, IIW Document IX-1279-1283, 1983.
43. A. Arora, G.G. Roy, T. DebRoy, Sci Technol Weld Join 15(2010) 423-427.
44. P. Heurtier, M.J. Jones, C. Desrayaud, J.H. Driver, F. Montheillet, D. Allehaux, J Mater Process Technol 171(2006) 348-357.
45. A.C. Srivastava, Q J Mech Appl Math 14(1961) 353-358
46. X. K. Zhu, Y. J. Chao, J Mater Process Technol 146(2004) 263-272.
47. T. U. Seidel, A. P. Reynolds, Sci Technol Weld Join 8(2003) 175-183.
48. G.G. Roy, R. Nandan, T. DebRoy, Sci Technol Weld Join 11(2006) 606-608.
49. K. Nakata, Y.G. Kim, M. Ushio, T. Hasimoto, S. Jyogan, ISIJ Int. 40(2000) S15-S19.
50. E.A. Brandes and G.B. Brook, eds., Smithells Metals Reference Book, 7th ed., Butterworth Heinemann, Woburn, MA, 1992, pp. 8–51.
51. Bryce Nielsen, Developing response surfaces based on tool geometry for a convex scrolled shoulder step spiral (CS4) friction stir processing tool used to weld AL 7075, Master's Thesis, Bringham Young University, Provo, Utah, 2009.

Chapter 8. Concluding Remarks

8.1. Summary and conclusions

Friction stir welding is a solid state joining process that avoids several difficulties associated with fusion welding processes, such as liquation cracking, porosity and loss of alloying elements. The FSW process has been commercially adopted to join soft alloys such as aluminum, magnesium and copper alloys. However, this process has not been considered for commercial application due to the lack of cost effective, long lasting tools. The tools required to friction stir weld hard materials use very costly materials and have shown small life of use. Development of understanding of the thermo-mechanical conditions experienced by the FSW tools would be of great help to develop reliable and long lasting FSW tools.

Here the aim was to improve the understanding of thermo-mechanical conditions experienced by the tool, such as peak temperature, torque, traverse force, shear stresses on the tool. The heat transfer and visco-plastic model was developed to estimate these parameters and to understand the effect of various input parameters on these thermo-mechanical conditions. The artificial neural networks (ANN) were developed to make use of these phenomenological model findings in real time with limited computing resources. These ANN models were used to develop process maps of safe operating parameters for FSW of AA7075 and 1018 mild steel. Several simplified and analytical models were also developed to quickly estimate certain FSW parameters, such as velocity fields, peak temperature, and torque. The main features of the work and important findings of this research are the following:

- The effect of tool shoulder diameter on peak temperature, torque and spindle power requirements in the FSW of AA7075-T6 and AA6061 at various rotational speeds is investigated using a three dimensional heat transfer and visco-plastic flow model. For all rotational speeds considered, the increase in shoulder diameter resulted in higher peak temperature, spindle power and torque requirements. With increase in tool shoulder diameter, the state of the deforming material changes from high flow stress and low temperature to low flow stress and high temperature.
- A design criterion for the selection of an optimum tool shoulder diameter is proposed based on the optimum use of the torque and maximum grip of the material on the

plasticized material. The optimum tool shoulder diameter identified for 355, 560 and 710 RPM are 30 mm, 25 mm, and 20 mm, respectively for FSW of AA7075. The mechanical energy provided by the tool is also shown to have a maximum for these combinations of optimal shoulder diameter and rotational speed. The optimum shoulder diameters were determined for FSW of AA6061 for rotational speeds of 900, 1200 and 1500 RPM. The 18 mm optimum shoulder diameter at 1200 RPM has resulted in superior tensile properties in independent tests reported in the literature.

- The three dimensional heat transfer and visco-plastic material flow model is use d to compute the tool traverse force for various welding parameters and tool dimensions. The traverse force increases with increase in pin length, however it is not significantly affected by change in the pin diameter for the welding conditions considered.
- Based on the calculated torque and traverse force, the maximum stress on the tool pin due to a combined bending and torsion is calculated by considering the pin as a cantilever beam fixed at one end. The computed maximum shear stress defines the load bearing capacity of the tool pin. With an increase in the pin length, the maximum shear stress increases. The increase in pin diameter reduces the maximum shear stress on the tool pin when keeping all other parameters constant.
- The proposed methodology of maximum shear stress is used to calculate the factor of safety for different welding conditions based on the computed load bearing capacity and the shear strength of the tool material. The failure of a commercially pure tungsten tool during FSW of L80 steel and a H13 tool steel during FSW of AA7075 alloy are explained by showing very low tool safety factor used during welding.
- The artificial neural network (ANN) models are developed to successfully predict total torque, sliding torque, sticking torque, traverse force, peak temperature, maximum shear stress and bending stress for the FSW of AA7075 and 1018 mild steel. The ANN model is used to predicted values of total torque and traverse force for wide range of input parameters to explain the effect of these input parameters. Based on bending stress calculations, it is shown that the possibility of fatigue failure during FSW of AA7075. Considering shear failure as the possible mode of failure, the tool safety factor is defined as the ratio of the tool shear strength and the maximum shear stress on the tool pin. The predicted values of the peak temperature

are used to estimate the tool shear strength. The maximum shear stress on the tool pin is predicted using the ANN model. The computed tool safety factors are plotted as function of tool shoulder radius and tool rotational speed for various combinations of other four input variables, tool pin radius, pin length, welding velocity and axial pressure. These plots will be of great use to predict the tool safety factor for a combination of input parameters. The estimation of tool safety factor will be useful to develop long lasting FSW tools.

- The strain rate and strain components during FSW of AA2524 are computed using a three dimensional heat transfer and visco-plastic flow model. As the material moves from the leading to the trailing edge through the retreating side, it experiences a tensile strain in the welding direction and compressive strain in the transverse direction. The nature of the strain reverses as the material reaches the trailing edge and is forced to consolidate behind the advancing tool. In the retreating side, the volumetric strain increases as the material reaches close to the tool and decreases behind the tool. The maximum strain occurs close to the welding tool. In the advancing side, the volumetric strains are small. For the condition of FSW investigated, the computed strains and strain rates were in the ranges -10 to 5 and -9 /s to 9 /s, respectively.
- Simplified models of materials flow, peak temperatures, and torque for friction stir welding (FSW) are proposed and tested. The analytical solution for the calculation of three dimensional materials flow velocities during FSW is adapted from the analytical solution of the viscous flow of an incompressible fluid induced by a solid rotating disk. It is shown that such calculations are straightforward and fairly accurate for the FSW of an aluminum alloy, a steel and a titanium alloy. An existing correlation for the estimation of peak temperature is improved using a large volume of recently published data. The improved correlation for peak temperature is tested against experimental peak temperatures for different welding pitch for three aluminum alloys.

8.2. Future work

This research provides insight about the thermo-mechanical conditions around the tool and enable development of long lasting FSW tools based on the stresses on the tool pin. However, several important questions yet remain unanswered in the field of FSW.

- What are the wear rates of FSW tools and can these rates be estimated using numerical modeling?
- Can numerical modeling improve the process understanding of FSW of two dissimilar alloys?
- Can numerical modeling explain the grain structure evolution during FSW?

FSW is a very promising technique to join difficult-to-weld materials and advanced materials. Further advancement of the process need a fair understanding of the tool degradation and tool failure. Numerical modeling has improved understanding of the basic physical processes in FSW. Development of numerical models explaining wear rates of FSW tools will be of great help to further the cause of FSW.

In recent years FSW has shown promise in joining dissimilar materials that is becoming a growing demand in aerospace applications. Welds such as aluminum-magnesium or aluminum-steel are being formed at experimental level. Even welding of combinations never thought before such as aluminum with aluminum-metal-matrix composites can be done using FSW. Numerical modeling has contributed significantly in the knowledge development of FSW process for welding of similar materials. Development of numerical models can improve the process understanding of FSW of dissimilar materials.

Monte Carlo simulations have provided useful insight about the grain structure evolution during fusion welding processes. Although, final weld properties of FSW joints are a strong function of grain structure in stir zone (SZ) and thermo mechanically affected zone (TMAZ), no insightful numerical model is available to explain and estimate the grain structure evolution in SZ and TMAZ. The strain and strain rate calculation model in combination with dynamic recrystallization models will be useful to understand the grain structure development in SZ and TMAZ for FSW.

Appendix A. Sensitivity of uncertain parameters in flow stress equation

Heat transfer and visco-plastic flow model for friction stir welding uses input variables such as welding variables and tool dimensions. The model also considers several empirical constants to represent physical processes in the numerical model, such as conversion of mechanical energy to heat, heat transfer at bottom surface or partial slip at shoulder workpiece interface. These empirical constants include the heat transfer coefficient at the bottom surface, h_{b0}, coefficient for slip, δ_0, friction coefficient, μ_0, mechanical efficiency, η, and the fraction of plastic deformational heat generation, β, as discussed in chapter 2. Their values cannot be determined from fundamental scientific principles or from straight-forward experiments. Since these parameters are estimated by fitting an empirical equation to a limited voloume of data, their values are somewhat uncertain.. Nandan et al [1] used available experimental data from friction stir welding experiments to optimize the values of the above mentioned five uncertain empirical constants in the FSW model. However, there are some parameters in the following material constitutive equation which are empirically determined by fitting experimental data in equation A.1.

$$\sigma_e = \frac{1}{\alpha}\sinh^{-1}\left[\left(\frac{1}{A}\dot{\varepsilon}\exp\left(\frac{Q}{RT}\right)\right)^{1/n}\right] \qquad (A.1)$$

where α, A, Q and n are material constants, $\dot{\varepsilon}$ is the strain rate and T is the temperature in K. Depending on the material composition and heat treatment conditions, different values of these four variables have been reported in literature. [2] Table 1 lists the values of the four material constants for a few selected aluminum alloys and steels. [2-4] Since the constitutive relation depends on the state of the material such as the heat treatment and microstructure and processing conditions such as the temperature and strain rate, the accuracy of these variables are open to question. Therefore, it is important to examine the effects of the values of these four materials constants in the constitutive equations on the visco-plastic flow and temperature model output parameters, such as torque, traverse force and peak temperature.

Table A.1 Reported values of the four uncertain parameters for selected aluminum alloys and steels with different heat treatments [2-4]

Material	**A, s^{-1}**	**Q, J mol^{-1}**	**n**	**α, $(MPa)^{-1}$**
AA1050 [2]	3.9×10^{11}	1.57×10^{5}	3.84	0.037
AA1100 [2]	5.2×10^{10}	1.58×10^{5}	5.66	0.045
AA3003 [2]	4.8×10^{11}	1.65×10^{5}	4.45	0.0316
AA3004 [2]	1.8×10^{12}	1.94×10^{5}	3.60	0.0344
AA7075H1 [2]	1.0×10^{9}	1.29×10^{5}	5.41	0.0141
AA7075H2 [2]	2.7×10^{11}	1.58×10^{5}	6.14	0.010
AA7075H3 [2]	9.1×10^{11}	1.55×10^{5}	7.80	0.012
AA7075H4 [2]	6.1×10^{11}	1.56×10^{5}	8.50	0.010
AA7075H5 [2]	2.8×10^{11}	1.56×10^{5}	6.32	0.011
1018 C-Mn steel [3]	3.1×10^{7}	3.72×10^{5}	0.75	0.86
1003 C-Mn steel [4]	1.6×10^{11}	3.12×10^{5}	5.10	0.012

The heat transfer and visco-plastic flow model for FSW of AA7075 was used to calculate the three important output parameters, torque, traverse force and peak temperature. The input conditions for these calculations are considered for which the model results have already been validated with the experimental results. The data used for these calculations are listed in Table 2.

Table A.2 Data used for the calculation of temperature and velocity fields, torque and traverse force for FSW of AA7075

Workpiece material	AA 7075
Tool material	EN24 tool steel
Tool shoulder diameter, mm	20
Pin diameter at root, mm	6.0
Pin diameter at tip, mm	4.66
Pin length, mm	3.325
Workpiece thickness, mm	3.5
Tool rotational speed, RPM	355
Welding speed, mm s^{-1}	0.67
Axial pressure, MPa	30.0
Workpiece solidus temperature, K [5]	749
Specific heat*, J kg^{-1} K^{-1} [5]	$0.20 - 3.0\times10^{-4}T + 1.0\times10^{-7}T^2 - 3.0\times10^{-12}T^3$
Thermal conductivity*, W m^{-1} K^{-1} [5]	$0.18 + 6.0\times10^{-4}T - 1.0\times10^{-7}T^2$
Yield stress, MPa [5]	$6.97\times10^{3}\times e^{(-0.0087\times T)}$ for $T < 644$ K $0.285\times(749-T)$ for $644 < T < 749$ K

The values of torque, traverse force and peak temperature are computed using the heat transfer and visco-plastic flow model for various combinations of the four uncertain

parameters. These combinations are shown in Table 3. The case 1 uses the values available in the literature. [2] Case 2 and case 3 consider 20% lesser and 20% higher value of the parameter A, respectively in comparison with case 1, keeping all other variables the same as case 1. The value of activation energy, Q, is considered 20% lower and 20% higher, for cases 4 and 5, respectively compared with the value of Q in case 1, keeping all other parameters constant. Case 6 and case 7 consider 20% lower and 20% higher values of n, respectively for same values of other parameters as case 1. Similarly, the case 8 and case 9 are the combinations where value of α is 20% lower and 20% higher, respectively, while keeping other variables unchanged compared to case 1. The heat transfer and visco-plastic flow model is used to calculate the values of torque, traverse force and peak temperature for these nine combinations of the uncertain parameters. The computed values of these output variables are listed in Table 4.

Table A.3 Nine different combinations of the four uncertain parameters for the sensitivity analysis

Case #	**A, s^{-1}**	**Q, J**	**n**	**α, $(MPa)^{-1}$**
Case 1	2.9×10^{11}	1.57×10^{5}	6.32	0.011
Case 2	2.32×10^{11}	1.57×10^{5}	6.32	0.011
Case 3	3.48×10^{11}	1.57×10^{5}	6.32	0.011
Case 4	2.9×10^{11}	1.26×10^{5}	6.32	0.011
Case 5	2.9×10^{11}	1.88×10^{5}	6.32	0.011
Case 6	2.9×10^{11}	1.57×10^{5}	5.056	0.011
Case 7	2.9×10^{11}	1.57×10^{5}	7.584	0.011
Case 8	2.9×10^{11}	1.57×10^{5}	6.32	0.0088
Case 9	2.9×10^{11}	1.57×10^{5}	6.32	0.0132

Table A.4 Calculated values of torque, traverse force, and peak temperature for the nine combinations of uncertain parameters in flow stress equation.

Case #	**Torque, Nm**	**Traverse force, kN**	**Peak temperature, K**
Case 1	30.24	2.460	625.5
Case 2	30.21	2.459	625.7
Case 3	30.37	2.461	625.3
Case 4	31.20	2.495	619.3
Case 5	29.26	2.424	632.2
Case 6	29.89	2.448	627.7
Case 7	30.48	2.468	623.9
Case 8	29.71	2.441	628.9
Case 9	30.60	2.473	623.1

From the comparison of the calculated values of peak temperature, torque and traverse force for cases 1, 2 and 3, it can be seen that 20% change in value of A does not significantly change the computed values of the three variables. Comparing cases 1 and 2, as

the value of parameter A is reduced by 20%, the calculated values of torque, traverse force and peak temperature change by -0.1%, -0.04% and +0.03%, respectively. When the value of A is increased by 20%, the calculated values of the torque, traverse force and peak temperature change by +0.1%, +0.04%, -0.03%, respectively. The changes in the three output parameters are very small as the parameter A in Equation A.1 is changed by 20%. The effect of change in activation energy, Q, can be understood by comparison of results for cases 1, 4, and 5. As the activation energy, Q, is increased by 20%, the torque, traverse force and peak temperature changes by +3.17%, +1.42%, -0.99%, respectively. A 20% decrease in activation energy results in -3.24%, -1.46%, and +1.07% change in calculated values of torque, traverse force and peak temperature, respectively. The changes in these output parameters are much more pronounced due to change in Q than due to the variation in A. However, the change in the values of these variables were always less than 3.5% when Q was changed by 20%.

A comparison of cases 1, 6, and 7 shows the effect of the parameter n in equation A.1 on the computed values of these variables. As the value of parameter n decreases by 20%, the calculated values of torque, traverse force and peak temperature change by -1.16%, -0.49% and +0.35%, respectively. When n is increased by 20%, the calculated values of torque, traverse force and peak temperature changes by +0.79%, +0.33% and -0.24%. The effect of change in parameter α can be examined by comparing the calculated values of output results for cases 1, 8 and 9. A decrease of 20% in the value of parameter α leads to calculated values of torque, traverse force and peak temperature to change by -1.75%, -0.77% and +0.56%, respectively. When the value of parameter α increases by 20%, the calculated values of torque, traverse force and peak temperature change by +1.19%, +0.53% and -0.38%, respectively.

These calculations show that the output parameters, torque, traverse force and peak temperatures, show maximum sensitivity to the change in the activation energy. For example, when the activation energy was decreased by 20%, the calculated value of torque decreased by 3.24%. The change of 20% in the values of all other parameters show very small (1.75% or less) change in the calculated values of torque, traverse force and peak temperature. Thus, the overall effect of all the four uncertain parameters, A, Q, n, and α, is not very significant on the computed values of important parameters such as torque, traverse

force and peak temperature. These four uncertain parameters affect the flow stress, σ, of the material which is used to compute the viscosity, μ, as shown in Equation A.2.

$$\mu = \frac{\sigma}{3\dot{\varepsilon}} \qquad \text{(A.2)}$$

where $\dot{\varepsilon}$ is the computed strain rate. The viscosity value is used in the momentum conservation equation to compute the material flow fields. However, the material flow field in friction stir welding is mainly affected by the tool rotational speed and the distance from the tool shoulder workpiece interface. As shown in the analytical model presented in chapter 7, the computed velocity fields are not significantly affected by the viscosity of the plasticized material. The maximum velocity in the plasticized workpiece material is at the tool shoulder-workpiece interface and is a fraction of the rotational velocity of the FSW tool. As shown in equation 7.1 in chapter 7, the material velocity away from the shoulder-workpiece interface continuously decreases and is zero at the workpiece bottom surface. Since the material flow during FSW is restricted by between top and bottom of the workpiece and the maximum and minimum velocities are externally forced on the material flow, the effect of viscosity on the material flow is very small. Thus the change in the four uncertain parameters, which lead to change in viscosity, do not affect the important output parameters, such as torque, traverse force, and peak temperature.

A.1. References

1. R. Nandan, B. Prabu, A. De and T. DebRoy, Weld J 86(2007) 313s-322s.
2. T. Sheppard, A. Jackson, Mater Sci Technol 13(1997) 203-209.
3. P.F. Kozlowski, B.G. Thomas, J.A. Azzi, H. Wang, Metal Trans A 23A(1992) 903-918.
4. A. Laasraoui, J.J. Jonas, Metal Trans A 22A(1991) 1545-1558.
5. J.G. Sessler, V. Weiss, Aerospace structural metals handbook, vol. II, Wright-Patterson Air Force Base, Ohio, pp. 3207(1-3).

Appendix B. Recent calculations of fatigue failure in FSW tools

DebRoy and Bhadeshia has used the Paris-Erdogan law relating the stress intensity factor range to the sub-critical crack growth rate to calculate the fatigue crack growth during FSW. [1] According to the Paris-Erdogan Law

$$\frac{da}{dN} = A\Delta K^{m} \tag{B.1}$$

where a is the crack length, N is the number of load cycles, da/dN is the crack growth rate, ΔK is the range of stress intensity factor and A and m are the Paris parameters. The range of stress intensity factor is calculated as following:

$$\Delta K = \Delta\sigma(\pi a)^{1/2} \tag{B.2}$$

where $\Delta\sigma$ is the range of stress on the tool pin. The crack growth rate can be expressed as following:

$$\frac{da}{dN} = A\ \Delta\sigma^{m}\pi^{m/2}a^{m/2} \tag{B.3}$$

The crack growth rate can be integrated to obtain the following correlation:

$$a^{-m/2}da = A\ \Delta\sigma^{m}\pi^{m/2}dN \tag{B.4}$$

The number of cycles to failure can be calculated as follows:

$$N_f = \left(\frac{2}{2-m}\right)\left[a_f^{1-\frac{m}{2}} - a_0^{1-\frac{m}{2}}\right] \Big/ A\ \Delta\sigma^{m}\pi^{m/2} \tag{B.5}$$

The critical crack size for the tool can be calculated as following:

$$a_f = \left(K_I / 1.12\tau_m\right)^2 / \pi \tag{B.6}$$

where K_I is the toughness of the tool, and τ_m is the maximum bending stress. The toughness of the tool is 40 MPa-$m^{1/2}$. The Paris parameter A for the tool material is 1.93 x 10^{-13} m^{-1} and the value of Paris exponent, m, is 3.05. For the tool steel material, the initial crack size is considered equal to the carbide particle in the tool. The range of the initial crack size is considered in the range of 0-25 μm. For the bending stress range of 0-1500 MPa, the number of cycled required for failure is calculated and plotted in Figure B.1.

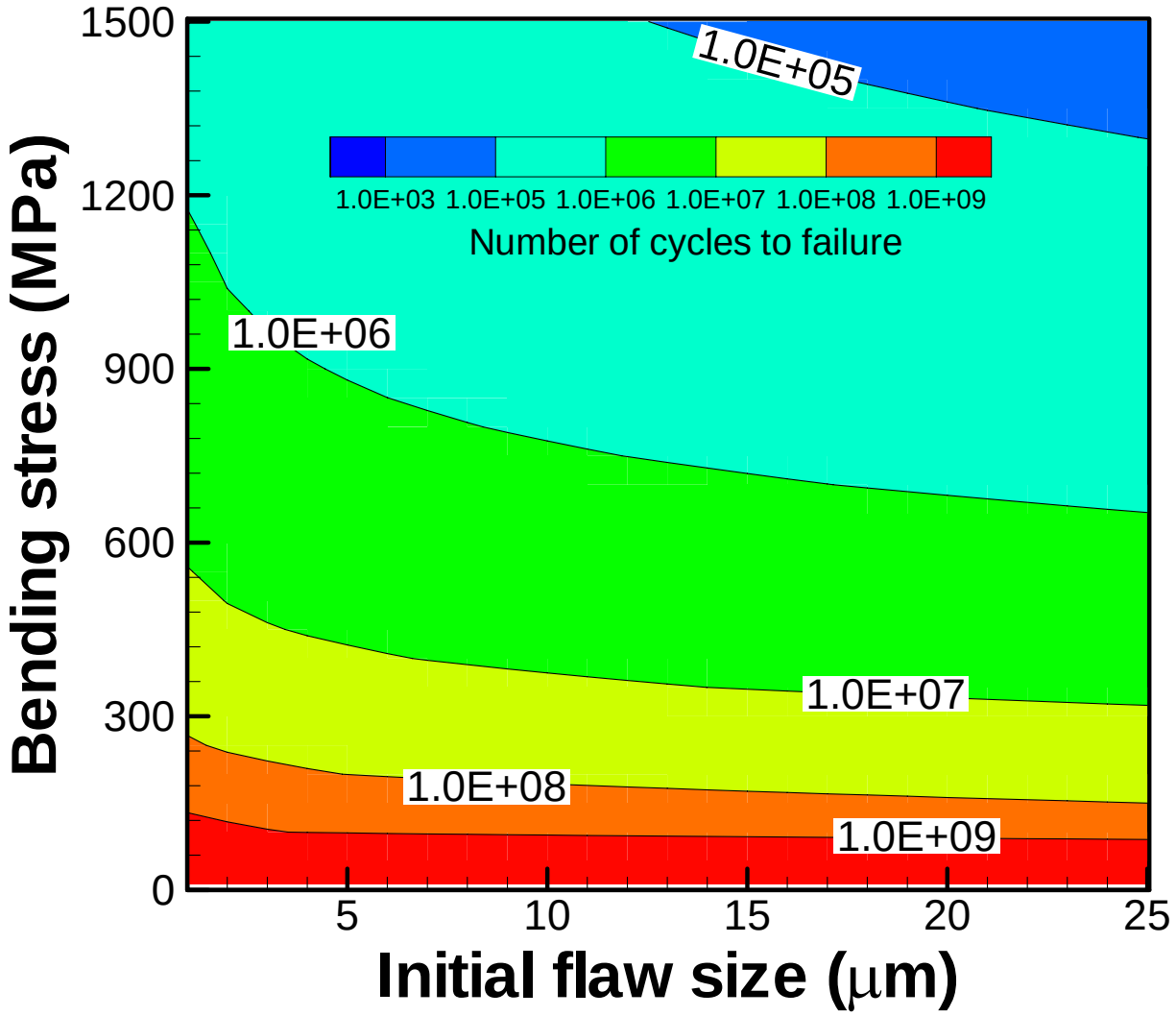

Figure B.1 The calculated number of cycles for failure of the steel tool for toughness of 40 MPa-$m^{1/2}$.

If the stress concentration factor, which depends on the radius of curvature at the joint and to a much lesser extent to the pin radius is about 2, the bending stress considered is up to about 750 MPa without considering any stress concentration. This value of bending stress is somewhat higher that the values calculated for 7 mm thick plates. However, if the thickness of the plates are higher such as 12.5 mm thick, the bending stress values can be higher than 1000 PMa considering the stress concentration factor. For such high bending stress values, fatigue is likely to be the main mechanism of tool failure for the welding of 7075 aluminum alloy because the number of cycles to failure may be less than $3x10^5$ cycles if the toughness remains at 40 MPa $m^{1/2}$

The results show that for the welding of aluminum alloys using a tool steel (define) up to a bending stress of about 350 MPa, the tool should endure at least about 10 million cycles before fatigue failure. At 0.5 cm/sec welding speed and 600 tool rpm, it should be able to weld about $(10^7 \times 60/600) \times 0.5 \times 10^{-2}) = 5000$ m = 5 km of the alloy before fatigue failure. For a conservative estimate, if the bending stress is about 1200 MPa and the initial flaw size is about 15 μm, the tool will endure 1.5×10^5 cycles before fatigue failure. For welding velocity of 0.5 cm/s, the tool will last 150 m of FSW before fatigue failure.

Since the toughness data at high temperatures are not accurately known, a look at the sensitivity of the computed number of cycles to failure on the toughness value is necessary. If the toughness of the tool material is taken 5 MPa $m^{1/2}$, which is a fairly low value, the number of cycles to failure reduces somewhat from what was calculated assuming a toughness value of 40MPa $m^{1/2}$. But Fig. 2 shows that up to a bending stress of about 300 MPa, the failure will not occur until about 10 million cycles. In other words, it would still be possible to weld 5 km long at 0.5 cm/sec welding speed and 600 rpm rotational speed before the tool fails. However, for a bending stress of 600 MPa and the initial flaw size of 15 μm, the tool will endure only 5000 cycles before fatigue failure.

These calculations show that fatigue failure in FSW tools is highly unlikely for low stresses and high toughness values, as would be expected for welding of thin plates of soft materials. The fatigue failure becomes important at high stress values that would be expected for FSW of thick plates of hard materials.

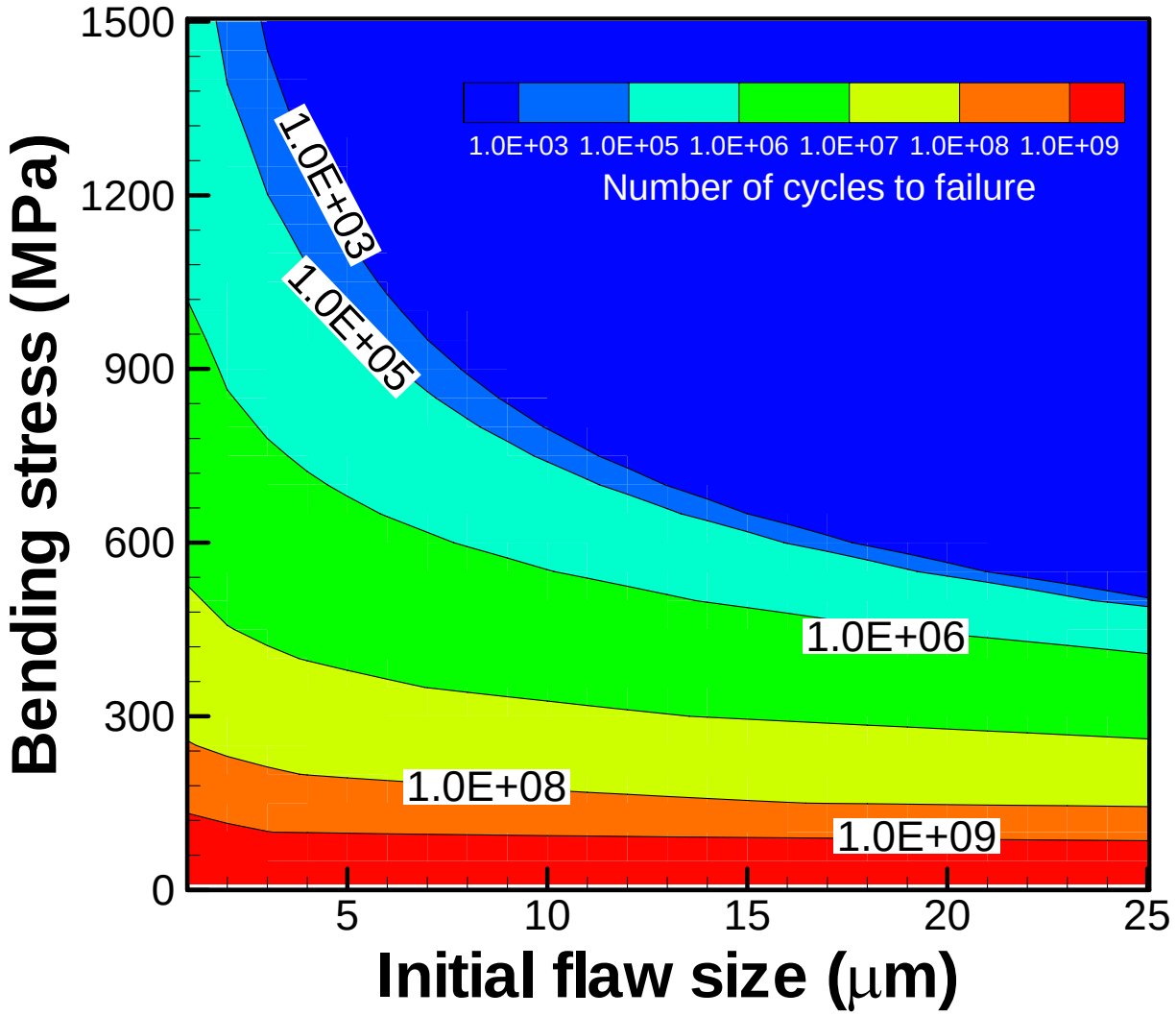

Figure B.2 The calculated number of cycles for failure of the steel tool for toughness of 5 MPa-$m^{1/2}$.

Thus the results show that the uncertainty in the toughness values do not seriously affect our ability to do the calculations. More important, fatigue failure of the tool is unlikely to occur during FSW of 7075 aluminum alloy for the conditions considered here.

A.2. References

1. T. DebRoy, H.K.D.H. Bhadeshia, Unpublished research, Aug 2011, Cambridge University, UK.

Appendix C. Artificial neural network models for 1018 mild steel

Similar to AA7075, seven sets of artificial neural networks are developed to predict total torque, sliding torque, sticking torque, traverse force, peak temperature, maximum shear stress and bending stress for FSW of 1018 mild steel. The comparison of desired and predicted values for the training and testing data for these output variables for FSW of 1018 steels is shown in Figure C.1. The error bars as calculated from Bayesian method for 95% confidence interval are shown in this Figure.

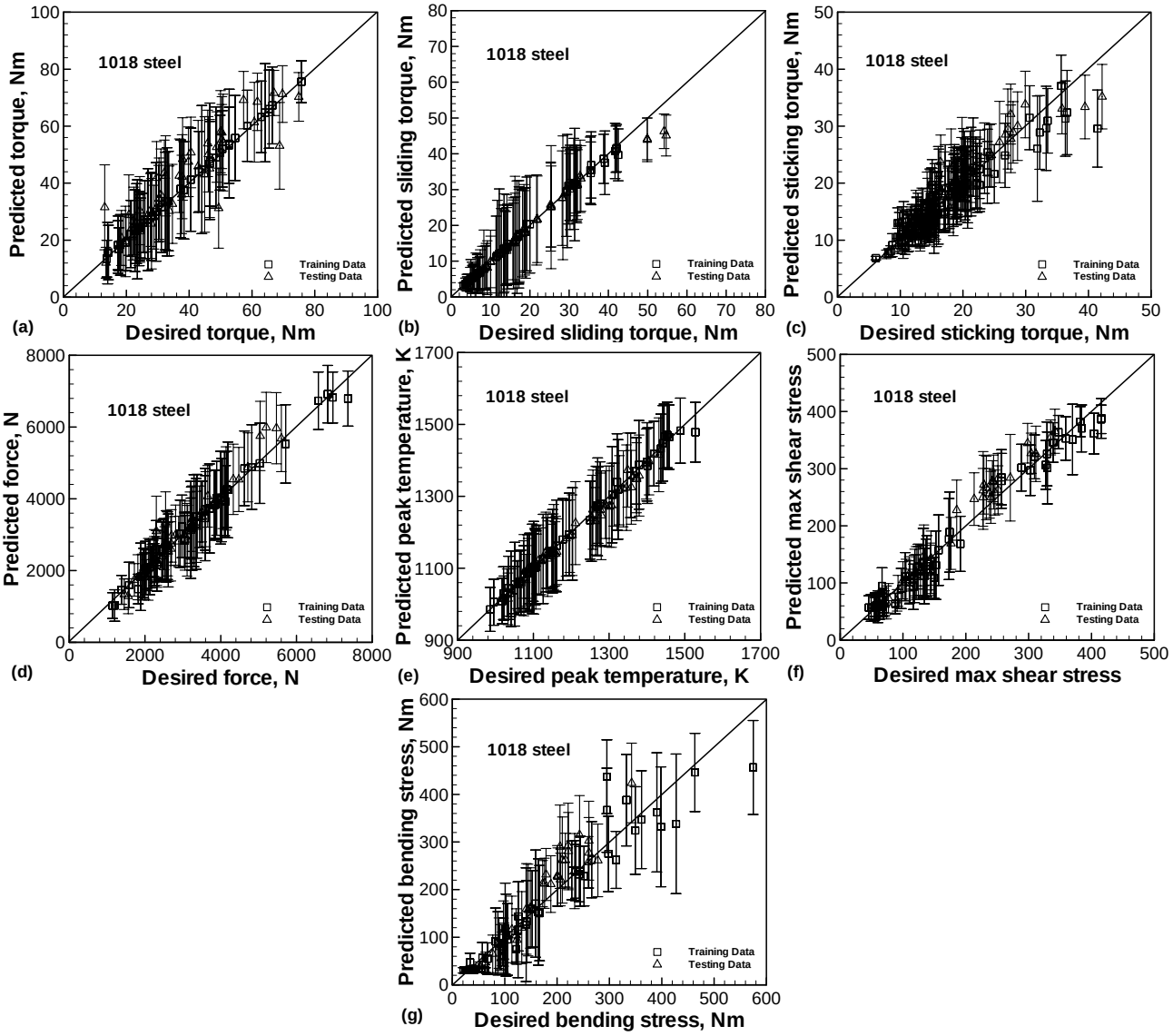

Figure C.1 Comparison of desired and predicted values of output parameters for training and testing datasets for FSW of 1018 mild steel.

The developed neural networks are used to understand the effect of various input variables on the output variables such as peak temperature, total torque, traverse force, maximum shear stress and bending stress. Figure C.2 shows the effect of input variables pin radius, pin length, welding velocity and axial force on the predicted values of peak temperature for FSW of 1018 mild steel. The calculated values are shown as function of tool shoulder radius and tool rotational speed. Similar to the calculations shown for AA7075 the peak temperature decreases with increase in tool shoulder diameter and tool rotational speed. The peak temperature also increases with increase in pin radius as can be seen by comparison of Figure C.2(a) and C.2(b). However, at small shoulder radius, the peak temperature increases with increase and then decreases. For small shoulder radii, the increase in pin radii increases the heating due to sticking friction but decreases the heating due to sliding friction at shoulder workpiece interface. This comparative increase and decrease in heat generation due to increase in pin radii results the increase and decrease in peak temperatures at low shoulder radii.

A comparison of Figure C.2(a) and C.2(c) shows that the peak temperature slightly increases with increase in tool pin length and plate thickness. This trend is different from the corresponding trend for AA7075 where the peak temperature decreases with increase in tool pin length. Thermal conductivity of 1018 mild steel is much lower compared to AA7075, thus the heat generated at the shoulder workpiece interface is not completely dissipated towards the workpiece bottom similar to AA7075. Also, an increase in pin length increases the plastic work done by the tool pin, thus reducing the temperature gradient in the plate thickness direction. Possibly, both these reasons act against the decrease in peak temperature in 1018 steel with increase in plate thickness for the range of variables considered for these calculations. Figure C.2(a) and C.2(d) can be compared to understand the effect of welding velocity on the predicted value of peak temperature. The peak temperature slightly increases with increase in welding velocity. As the axial pressure on the tool increases the peak temperature also increases as can be seen by comparing Figure C.2(a) and C.2(e). The increase in axial pressure increases the frictional heating at the shoulder-workpiece interface and thus increases the peak temperature. This trend is same as the corresponding trend observed for AA7075.

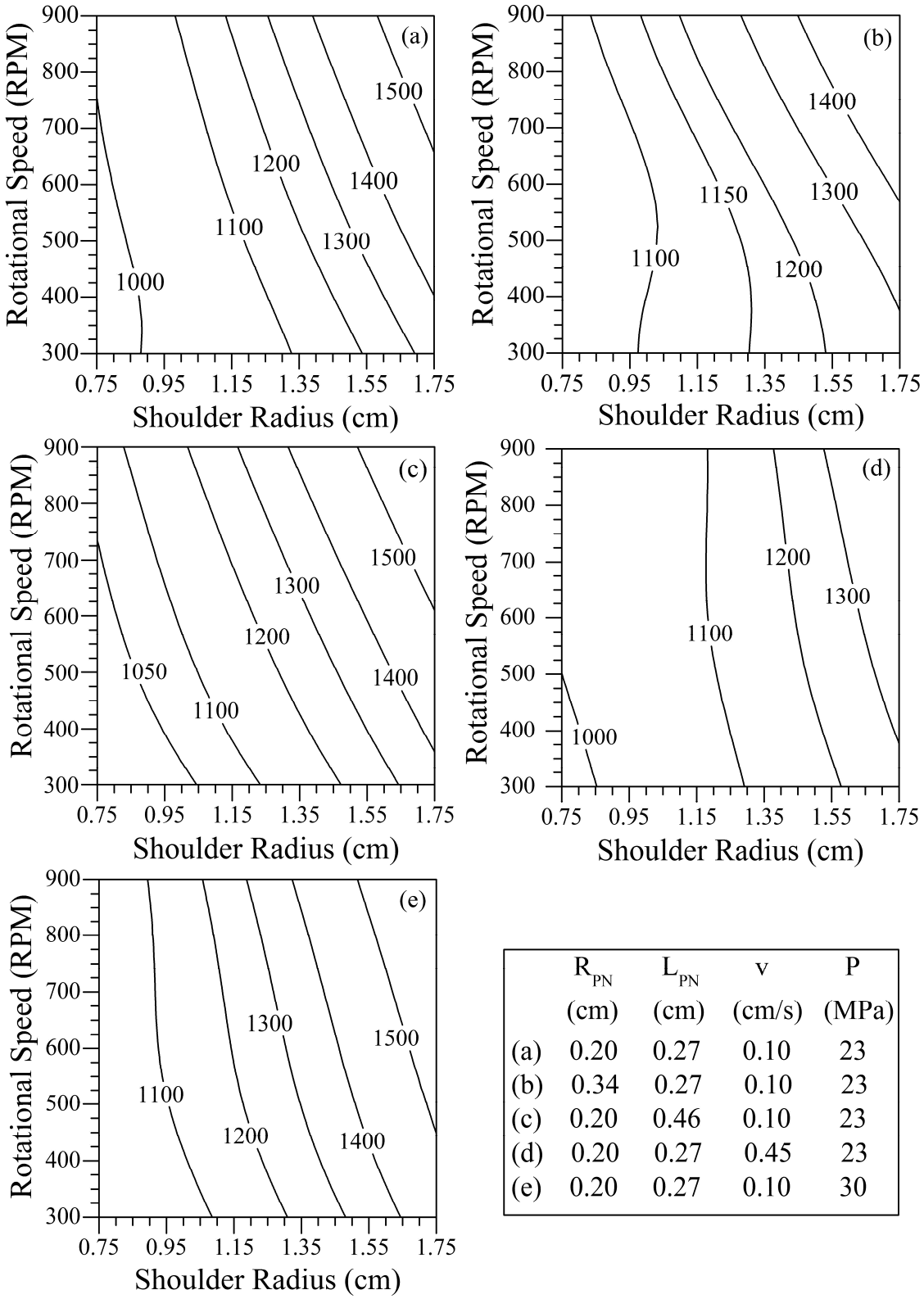

	R_{PN} (cm)	L_{PN} (cm)	v (cm/s)	P (MPa)
(a)	0.20	0.27	0.10	23
(b)	0.34	0.27	0.10	23
(c)	0.20	0.46	0.10	23
(d)	0.20	0.27	0.45	23
(e)	0.20	0.27	0.10	30

Figure C.2 The predicted values of peak temperature (K) by ANN model for FSW of 1018 mild steel as function of tool shoulder radius and tool rotational speed for the combinations of input variables listed in the table shown here.

Predicted values of torque are plotted in Figure C.3 as function of tool shoulder radii and tool rotational speed for various combinations of other input variables, pin radius, pin length, welding velocity and axial pressure. Similar to the results from AA7075, it can be seen in Figure C.3(a) that as the tool shoulder radius increases, the torque also increases whereas the torque decreases with increase in tool rotational speed. Comparison of Figure C.3(a) and C.3(b) shows that the torque increases with increase in tool pin radius. However, for low tool rotational speed and larger tool radius, the torque decreases. The effect of increase in tool pin length and plate thickness can be understood by comparing Figure C.3(a) and C.3(c). The total torque increases as the tool pin length and the plate thickness is increased. Increase in pin length increases the surface of the tool pin in contact with the workpiece material, thus the torque increases.

Increase in welding velocity decreases the total heat generation during FSW. Thus higher welding velocity results in increase in torque that can be concluded by comparing Figure C.3(a) and C.3(d). Comparison of Figure C.3(a) and C.3(e) shows the effect of axial pressure of the torque during FSW of 1018 steel. Increase in the axial pressure increases the frictional resistance at the shoulder workpiece interface. This increase resistance results in higher sliding torque and also higher heat generation. The increased heat generation softens the workpiece material and decreases the sticking torque. The combined effect of the increase in axial pressure is a slight increase in the total torque as can be seen in Figure C.3(e).

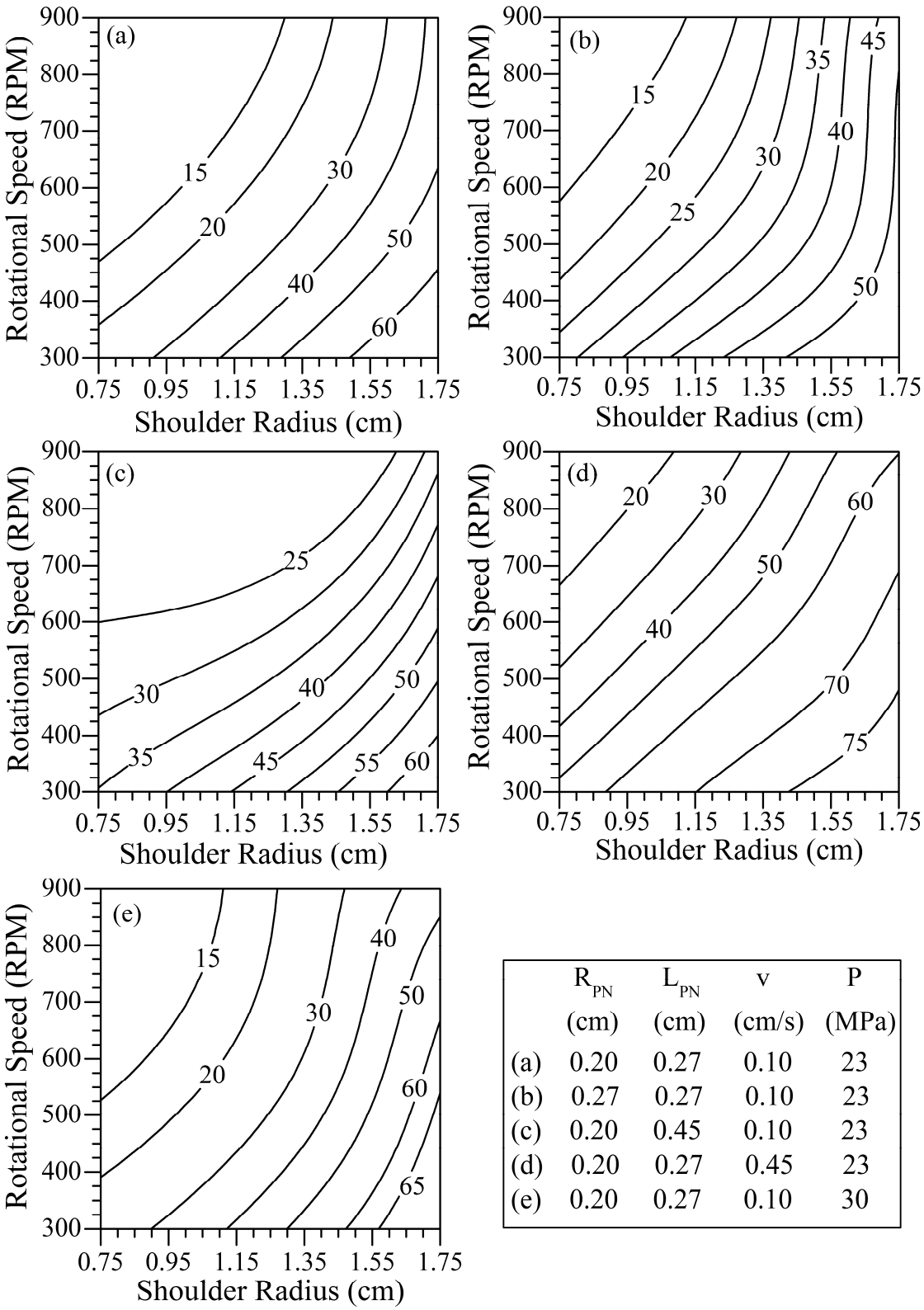

	R_{PN} (cm)	L_{PN} (cm)	v (cm/s)	P (MPa)
(a)	0.20	0.27	0.10	23
(b)	0.27	0.27	0.10	23
(c)	0.20	0.45	0.10	23
(d)	0.20	0.27	0.45	23
(e)	0.20	0.27	0.10	30

Figure C.3 The predicted values of total torque (Nm) by ANN model for FSW of 1018 mild steel as function of tool shoulder radius and tool rotational speed for the combinations of input variables listed in the table shown here.

The traverse force during FSW of 1018 mild steel predicted as function of tool rotational speed and tool shoulder radius is shown in Figure C.4(a) through (e). Figure C.4(a) shows the effect of tool rotational speed and tool shoulder radius as all other input variables, pin radius, pin length, welding velocity and axial pressure, are kept constant. For a constant tool rotational speed, the predicted traverse force increase with increase in tool shoulder radius. The increase in shoulder radius results in higher frictional force on the tool shoulder, thus resulting in higher traverse force value. Predicted values of traverse force decreases with increase in tool rotational speed for a constant tool shoulder radius. As the tool rotational speed increases, the workpiece material softens due to greater heat generation resulting lower value of traverse force.

Comparison of Figure C.4(a) and C.4(b) shows the effect of tool pin radius on the predicted values of traverse force. As the pin radius increases, the surface of the tool in contact with the worpiece also increases, thus resulting in higher traverse force on the FSW tool. Effect of tool pin length can be examined by comparison of Figure C.4(a) and C.4(c). For all the other variables, pin radius, welding velocity and axial pressure, constant the traverse force increases with increase in tool pin length. As the tool pin length increases, the pin comes into contact with colder and harder material, resulting in higher traverse force. Figure C.4(a) and C.4(d) can be compared to examine the effect of welding velocity, as all other variables are kept constant. As the welding velocity increases, the traverse force also increases. Higher welding velocity result in lower heat input per unit length and thus lower temperatures and higher workpiece strength. This greater resistance from harder material results in the higher traverse force. Comparison of Figure C.4(a) and C.4(e) shows the effect of increase in axial pressure on the predicted value of traverse force. The increased axial pressure results in significant increase in frictional force on the tool shoulder workpiece interface. Thus higher axial pressure leads to higher traverse force while all other variables are kept constant.

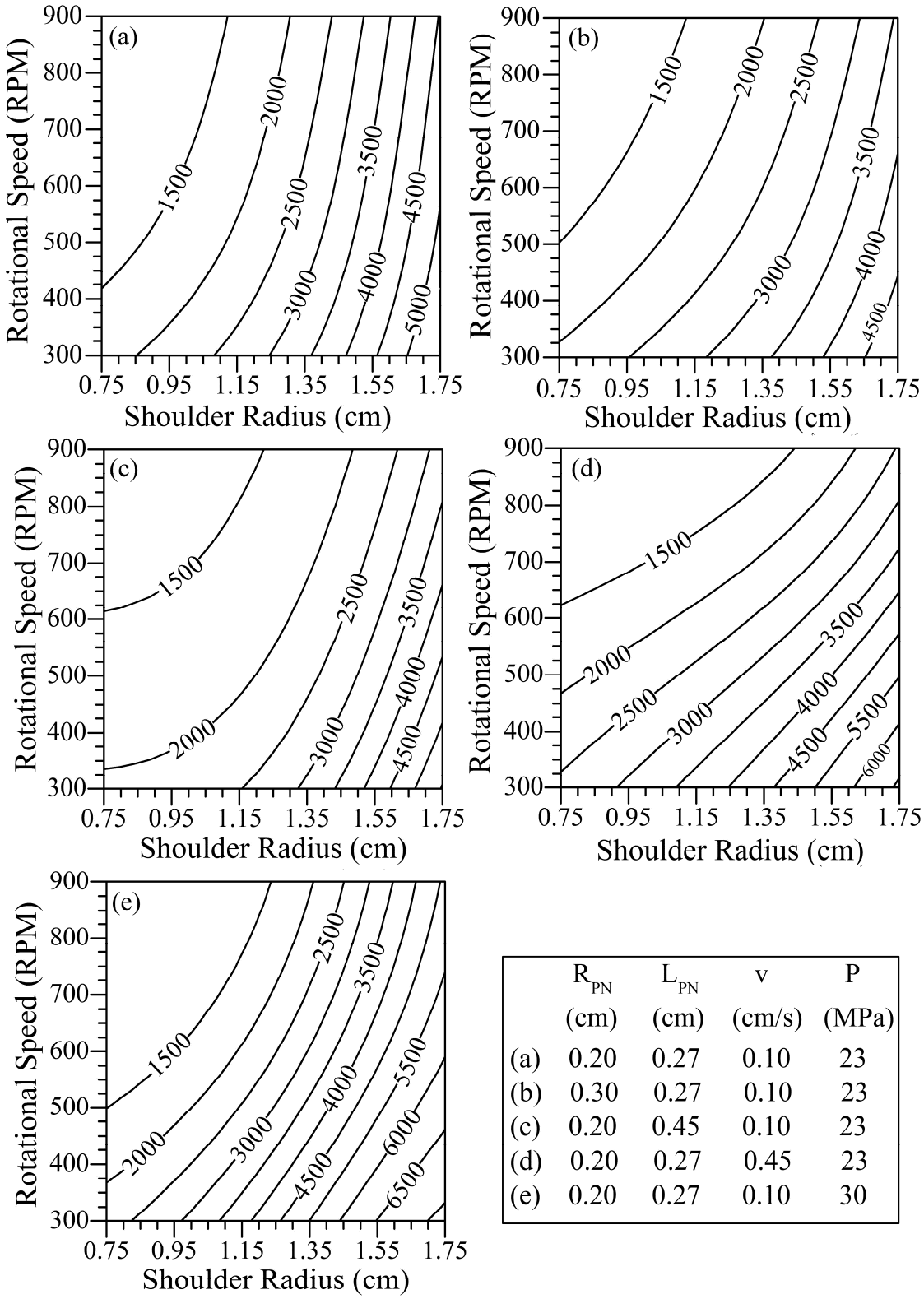

	R_{PN} (cm)	L_{PN} (cm)	v (cm/s)	P (MPa)
(a)	0.20	0.27	0.10	23
(b)	0.30	0.27	0.10	23
(c)	0.20	0.45	0.10	23
(d)	0.20	0.27	0.45	23
(e)	0.20	0.27	0.10	30

Figure C.4 The predicted values of traverse force (N) by the ANN model for FSW of 1018 mild steel as function of tool shoulder radius and tool rotational speed for the combinations of input variables listed here.

Figure C.5 shows the effect of the input parameters on the predicted values of maximum shear stress on the tool pin. The predicted values of maximum shear stress are shown as function of tool rotational speed and tool shoulder radius for combinations of the input variables, pin radius, pin length, welding velocity and axial pressure, as shown in the table attached to the Figure. Figure C.5(a) shows the effect of tool rotational speed and tool shoulder radius as all other input variables, pin radius, pin length, welding velocity and axial pressure, are kept constant. For a constant tool rotational speed, the predicted maximum shear stress decreases with increase in tool shoulder radius. The increase in shoulder radius results in higher heat generation, thus resulting in lower stresses on the pin. Predicted values of the maximum shear stress decrease with increase in tool rotational speed for a constant tool shoulder radius. As the tool rotational speed increases, the workpiece material softens due to greater heat generation resulting lower value of stresses.

Comparison of Figure C.5(a) and C.5(b) shows the effect of tool pin radius on the predicted values of maximum shear stress. As the pin radius increases, the stresses on the pin decreases, thus resulting in lower maximum shear stress on the tool pin. Effect of tool pin length can be examined by comparison of Figure C.5(a) and C.5(c). For all the other variables, pin radius, welding velocity and axial pressure, constant the maximum shear stress increases with increase in tool pin length. As the tool pin length increases, the pin comes into contact with colder and harder material, resulting in higher stresses on the pin. Figure C.5(a) and C.5(d) can be compared to examine the effect of welding velocity, as all other variables are kept constant. As the welding velocity increases, the maximum shear stress also increases. Higher welding velocity result in lower heat input per unit length and thus lower temperatures and higher workpiece strength. The pin experiences higher stresses while deforming such harder material. Comparison of Figure C.5(a) and C.5(e) shows the effect of increase in axial pressure on the predicted value of maximum shear stress. The increased axial pressure results in increase in frictional heating, resulting higher temperatures and lower stresses on the pin.

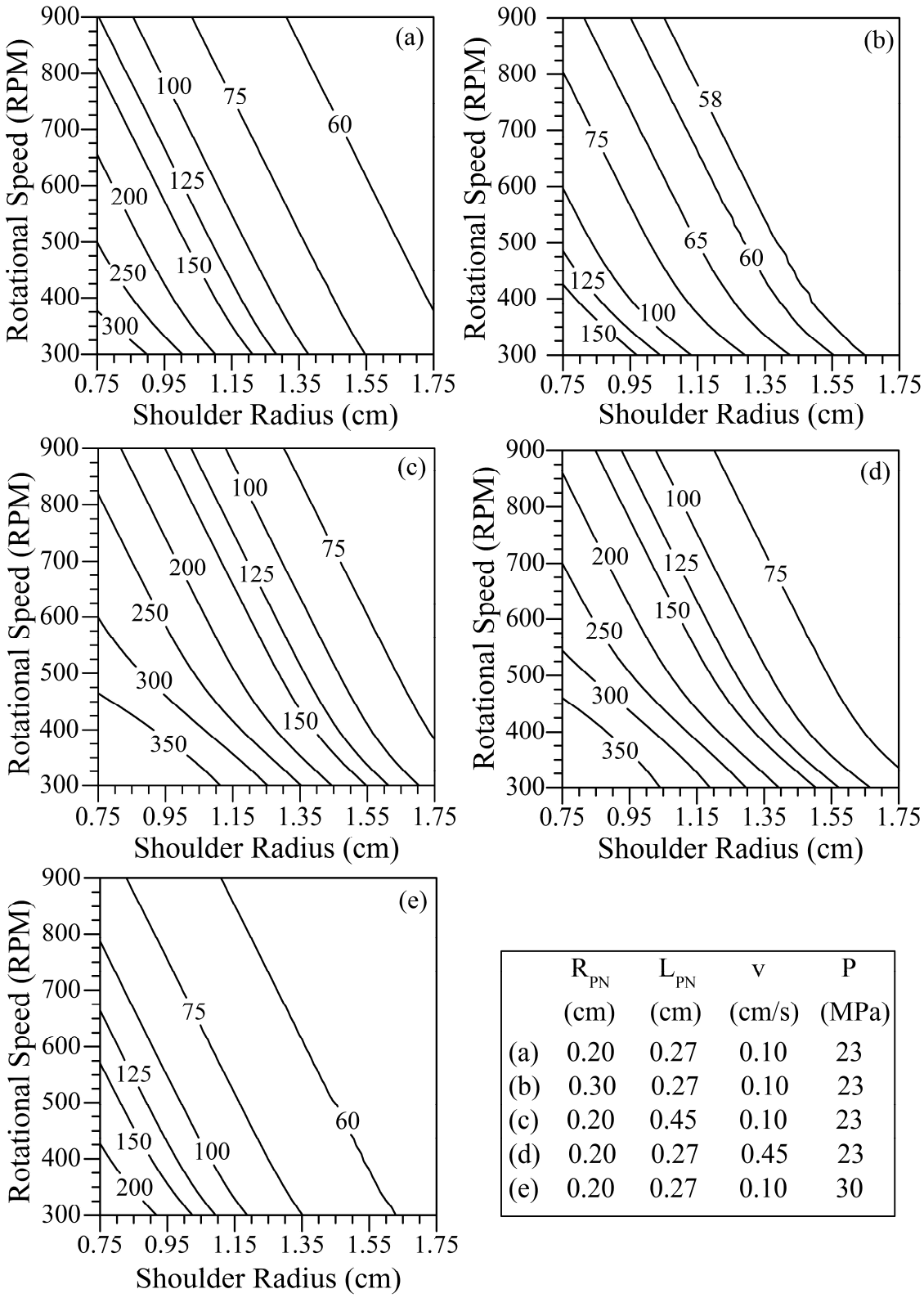

	R_{PN} (cm)	L_{PN} (cm)	v (cm/s)	P (MPa)
(a)	0.20	0.27	0.10	23
(b)	0.30	0.27	0.10	23
(c)	0.20	0.45	0.10	23
(d)	0.20	0.27	0.45	23
(e)	0.20	0.27	0.10	30

Figure C.5 The predicted values of maximum shear stress on the tool pin (MPa) by the ANN model for FSW of 1018 mild steel as function of tool shoulder radius and tool rotational speed for the combinations of input variables listed here.

Figure C.6 shows the effect of the input parameters on the predicted values of bending stress on the tool pin. The predicted values of bending stress are shown as function of tool rotational speed and tool shoulder radius for combinations of the input variables, pin radius, pin length, welding velocity and axial pressure, as shown in the table attached to the Figure. Figure C.6(a) shows the effect of tool rotational speed and tool shoulder radius as all other input variables, pin radius, pin length, welding velocity and axial pressure, are kept constant. For a constant tool rotational speed, the predicted bending stress decreases with increase in tool shoulder radius. The increase in shoulder radius results in higher heat generation, thus resulting in lower force on the pin. Predicted values of the bending stress decrease with increase in tool rotational speed for a constant tool shoulder radius. As the tool rotational speed increases, the workpiece material softens due to greater heat generation resulting lower tool pin force.

Comparison of Figure C.6(a) and C.6(b) shows the effect of tool pin radius on the predicted values of bending stress. As the pin radius increases, the stress on the pin decreases, thus resulting in lower bending stress on the tool pin. Effect of tool pin length can be examined by comparison of Figure C.6(a) and C.6(c). For all the other variables, pin radius, welding velocity and axial pressure, constant the bending stress increases with increase in tool pin length. As the tool pin length increases, the pin comes into contact with colder and harder material, resulting in higher force on the pin. Figure C.6(a) and C.6(d) can be compared to examine the effect of welding velocity, as all other variables are kept constant. As the welding velocity increases, the bending stress also increases. Higher welding velocity result in lower heat input per unit length and thus lower temperatures and higher workpiece strength. The pin experiences higher force while shearing such harder material. Comparison of Figure C.6(a) and C.6(e) shows the effect of increase in axial pressure on the predicted value of bending stress. The increased axial pressure results in increase in frictional heating, resulting higher temperatures and lower force on the pin.

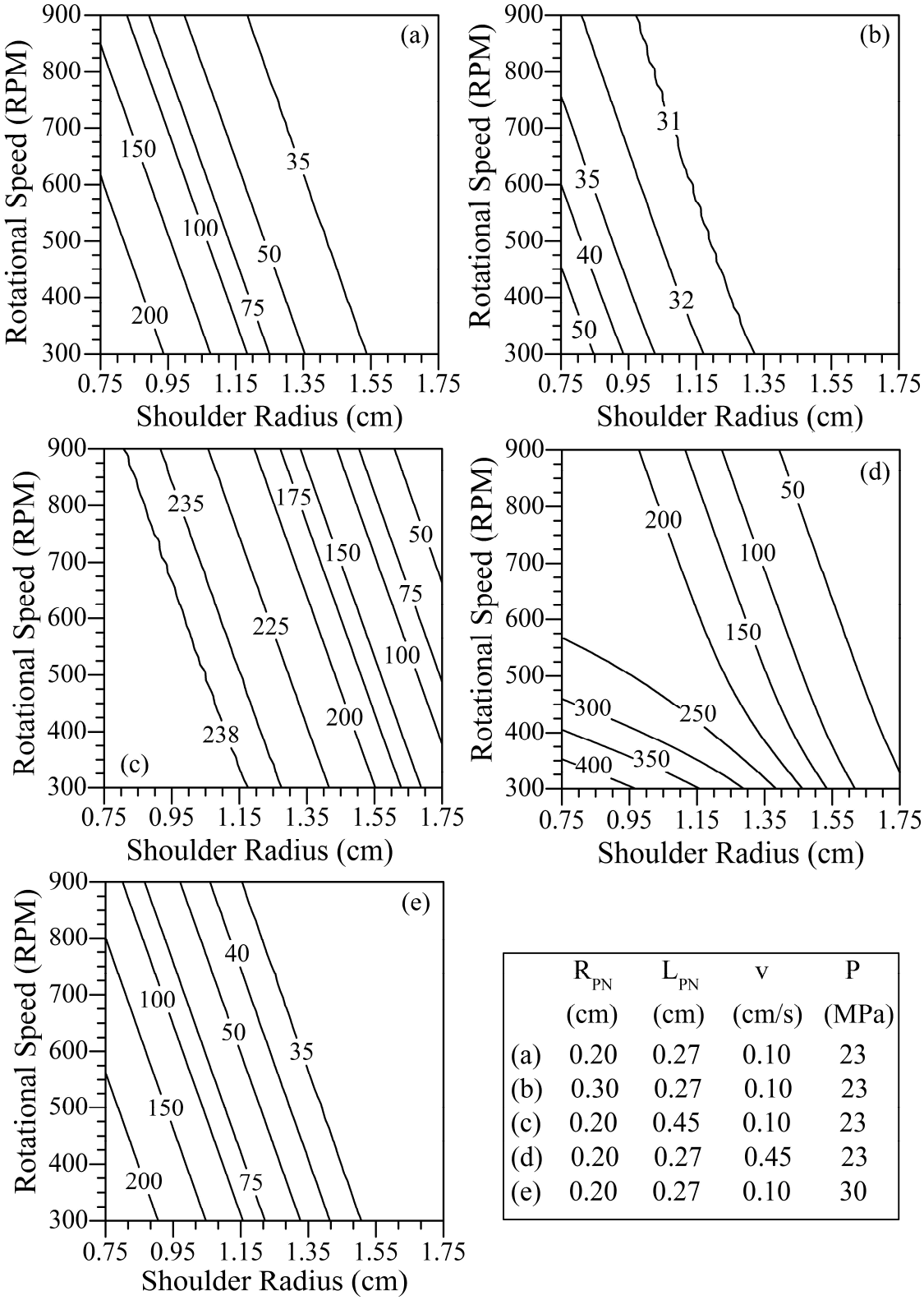

	R_{PN} (cm)	L_{PN} (cm)	v (cm/s)	P (MPa)
(a)	0.20	0.27	0.10	23
(b)	0.30	0.27	0.10	23
(c)	0.20	0.45	0.10	23
(d)	0.20	0.27	0.45	23
(e)	0.20	0.27	0.10	30

Figure C.6 The predicted values of bending stress on the tool pin (MPa) by the ANN model for FSW of 1018 mild steel as function of tool shoulder radius and tool rotational speed for the combinations of input variables listed here.

Appendix D. Analytical calculation of the flow field

Here an analytical solution for the steady state flow of an incompressible fluid between two parallel discs, one rotating with a constant angular speed and the other at rest, is described. The two discs are separated by a distance d, the rotating disk is at $z = 0$ and the stationary disc is at $z = d$. In the cylindrical coordinate system, the continuity and momentum equations are as follows: [1]

$$2F + H' = 0 \tag{D.1}$$

$$R(F^2 - G^2 + F'H) = F'' + \alpha_c R(F'^2 - 2FF' - G'^2) - 2P_1 \tag{D.2}$$

$$R(2FG + G'H) = G'' + 2\alpha_c R(F'G' - FG'') \tag{D.3}$$

$$R(HH') = P' + H'' + \alpha_c R(8H'H'' - 4FF') + \frac{r^2}{d^2}[2\alpha_c R(G'G'' + F'F'') - P_1'] \tag{D.4}$$

where R is Reynolds number $R = \frac{\omega d^2}{\upsilon_v}$, and $\alpha_c = \frac{\upsilon_c}{d^2}$, with υ_v and υ_c as the kinematic coefficients of viscosity and cross-viscosity. [1] The function F, G and H are functions of a dimensionless parameter η and define the velocity components u, v, w in the r, θ, z direction respectively. The velocity components are taken in the following form for the above mentioned simplification: [1]

$$u = r\omega F(\eta), \quad v = r\omega G(\eta), \quad w = d\omega H(\eta) \quad \text{for } \eta = z/d \tag{D.5}$$

where ω is the angular velocity of the rotating disc. By solving (D.2) and (D.4) we can obtain [1]

$$R(F^2 - G^2 + F'H) = F'' - \alpha_c R(F'^2 + 2FF'' + 3G'^2) - 2\lambda \tag{D.6}$$

where λ is an integration constant. For small values of R, a regular perturbation scheme for the equation (D.1), (D.3), and (D.6) can be developed by expanding F, G, H, λ in powers of R: [1]

$$\begin{aligned} F &= f_0 + f_1 R + f_2 R^2 + f_3 R^3 + \ldots \\ G &= g_0 + g_1 R + g_2 R^2 + g_3 R^3 + \ldots \\ H &= h_0 + h_1 R + h_2 R^2 + h_3 R^3 + \ldots \\ \lambda &= \lambda_0 + \lambda_1 R + \lambda_2 R^2 + \lambda_3 R^3 + \ldots \end{aligned} \tag{D.7}$$

Substituting F, G, H and λ from (D.7) in (D.3), (D.6) and equating the coefficients of different powers of R on both sides of these equations reduces the boundary conditions to [1]

$$f_0 = 0, \quad g_0 = 1, \quad h_0 = 0 \quad \text{at} \quad \eta = 0,$$
$$f_0 = 0, \quad g_0 = 0, \quad h_0 = 0 \quad \text{at} \quad \eta = 1, \tag{D.8}$$

and for n = 1,2,3 … [1]

$$f_n = 0, \quad g_n = 0, \quad h_n = 0 \quad \text{at} \quad \eta = 0,$$
$$f_n = 0, \quad g_n = 0, \quad h_n = 0 \quad \text{at} \quad \eta = 1, \tag{D.9}$$

Solution for f_n, g_n, h_n and λ_n for n = 1, 2, 3 … can be found and F, G and H can be expressed in terms of f_n, g_n, h_n, λ_n and R as follows: [1]

$$\begin{aligned} F = {} & R\left(\frac{1}{10}\eta - \frac{7}{20}\eta^2 + \frac{1}{3}\eta^3 - \frac{1}{12}\eta^4\right) + \\ & R^3\begin{bmatrix} -0.000115\eta + 0.000219\eta^2 + 0.000714\eta^3 - 0.000714\eta^4 - 0.002167\eta^5 \\ +0.003639\eta^6 - 0.002619\eta^7 + 0.001262\eta^8 - 0.000243\eta^9 + 0.000024\eta^{10} \\ +\alpha_c\begin{pmatrix} -0.004161\eta + 0.021661\eta^2 - 0.046667\eta^3 + 0.065\eta^4 \\ -0.063333\eta^5 + 0.037222\eta^6 - 0.011111\eta^7 + 0.001389\eta^8 \end{pmatrix} \\ +\alpha_c^2\left(0.018095\eta - 0.001428\eta^2 - 0.2\eta^3 + 0.35\eta^4 - 0.2\eta^5 + 0.033333\eta^6\right) \end{bmatrix} \end{aligned} \tag{D.10}$$

$$G = (1-\eta) + R^2\begin{bmatrix} -\frac{3}{700}\eta + \frac{1}{30}\eta^3 - \frac{1}{15}\eta^4 + \frac{17}{300}\eta^5 - \frac{1}{45}\eta^6 + \frac{1}{315}\eta^7 \\ +\alpha_c\left(\frac{1}{10}\eta^2 - \frac{7}{30}\eta^3 + \frac{1}{6}\eta^4 - \frac{1}{30}\eta^5\right) \end{bmatrix} \tag{D.11}$$

$$\begin{aligned} F = {} & R\left(-\frac{1}{10}\eta^2 + \frac{7}{30}\eta^3 - \frac{1}{6}\eta^4 - \frac{1}{30}\eta^5\right) + \\ & R^3\begin{bmatrix} -0.000105\eta^2 - 0.000146\eta^3 - 0.000357\eta^4 + 0.000286\eta^5 + 0.000722\eta^6 \\ -0.00103\eta^7 + 0.000655\eta^8 - 0.00028\eta^9 + 0.000049\eta^{10} - 0.000004\eta^{11} \\ +\alpha_c\begin{pmatrix} 0.004162\eta^2 - 0.014441\eta^3 + 0.023334\eta^4 - 0.026\eta^5 \\ +0.021111\eta^6 - 0.010635\eta^7 + 0.002778\eta^8 - 0.000309\eta^9 \end{pmatrix} \\ +\alpha_c^2\left(-0.018095\eta^2 + 0.000952\eta^3 + 0.1\eta^4 - 0.14\eta^5 + 0.066667\eta^6 - 0.009524\eta^7\right) \end{bmatrix} \end{aligned} \tag{D.12}$$

In cartesian coordinate system r and η can be computed as follows:

$$r = \left(x^2 + y^2\right), \ \eta = z/d \tag{D.13}$$

The computed velocity components are in cylindrical coordinates, and can be converted to the Cartesian coordinate system as follows:

$$u_{cart} = u_{cyl}\, cos(\theta) - v_{cyl}\, sin(\theta) \tag{D.14}$$

$$v_{cart} = u_{cyl}\, sin(\theta) + v_{cyl}\, cos(\theta) \text{ where } tan(\theta) = {}^{y}\!/_{x} \quad \text{(D.15)}$$

$$w_{cart} = w_{cyl} \quad \text{(D.16)}$$

D.1. References

1. A.C. Srivastava, Q J Mech Appl Math 14(1961) 353-358

Vita

Amit Arora

Amit Arora was born in Jodhpur (Rajasthan), India on 17th November, 1982 to school teacher and a rural bank employee. After gaining his early education in a small school in the village he transferred to the Government School, Housing Board, Pali. Later he attended Bangur Senior Secondary School, Pali-Marwar (Rajasthan).

In July 2000, he joined the prestigious Indian Institute of Technology, Kharagpur, India to pursue a five year dual-degree program. He graduated with B.Tech. in Metallurgical and Materials Engineering and M. Tech. in Metallurgical Engineering in May 2005.

He worked with IBM India Pvt. Ltd. for one year as Associate System Engineer before joining The Pennsylvania State University, University Park to pursue graduate research under the guidance of Professor Tarasankar DebRoy.

His work during graduate research resulted in several publications in well-cited journals such as Acta Materialia, Scripta Materialia, and Metallurgical and Materials Transactions A etc. The work was also presented at various international conferences and gatherings of peer researchers. His publications during Ph.D. are listed below:

1. Scripta Materialia, 2009, vol. 60, pp. 13-16.
2. Scripta Materialia, 2009, vol. 61, pp. 863-866.
3. Scripta Materialia, 2009, vol. 60, pp. 68-71.
4. Science and Technology of Welding and Joining, 2010, vol. 15(5), pp. 423-427.
5. Mathematical Modeling of Weld Phenomena 9, 2010, pp. 3-19.
6. Scripta Materialia, 2011, vol. 64, pp. 9-12.
7. Acta Materialia, 2011, vol. 59(5), pp. 2020-2028.
8. Metallurgical and Materials Transactions A, 2011, vol. 42A, pp. 2716-2722.
9. International Journal of Advanced Manufacturing Technology, 2011, DOI: 10.1007/s00170-011-3759-7.